Institut für
Kontinuumsmechanik

Peridynamic Galerkin methods for nonlinear solid mechanics

Tobias Bode

Leibniz
Universität
Hannover

ISBN 978-3-941302-45-7

Simulation-driven product development is nowadays an essential part in the industrial development process and the interest in realistic high-fidelity simulations is significant. As a versatile tool, meshfree methods have gained attention in the last decades. However, along with their flexibility in discretization, meshfree Galerkin methods often endure a decrease in accuracy, efficiency and stability compared to mesh-based methods. While satisfying certain shape function requirements, the Peridynamic Galerkin methods provide a sound approach for the modeling of highest deformations on arbitrarily distributed point clouds. This work comprises a detailed introduction into the theory, analysis and application of these methods and outlines future research areas.

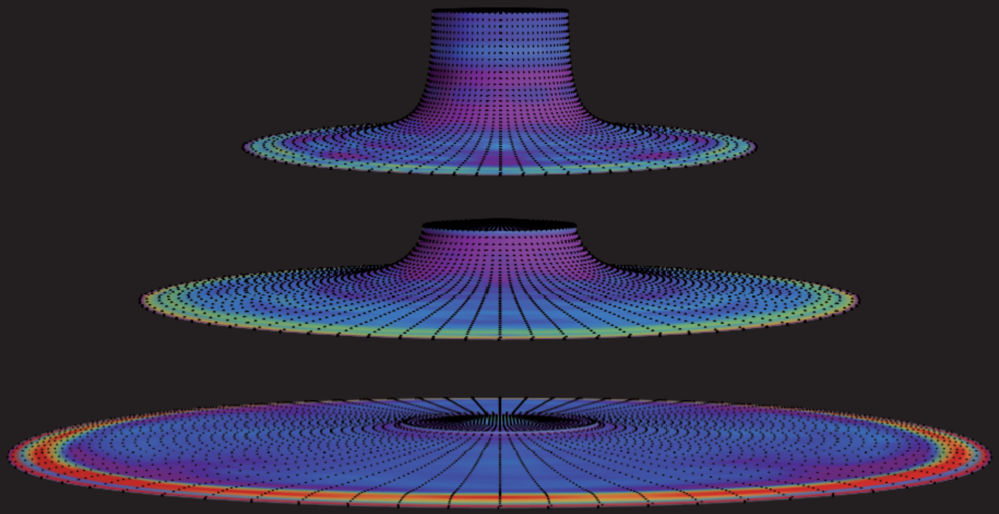

B21/6

Tobias Bode | Peridynamic Galerkin methods for nonlinear solid mechanics

Peridynamic Galerkin methods for nonlinear solid mechanics

B21/6

Tobias Bode

Leibniz
Universität
Hannover

Institut für
Kontinuumsmechanik

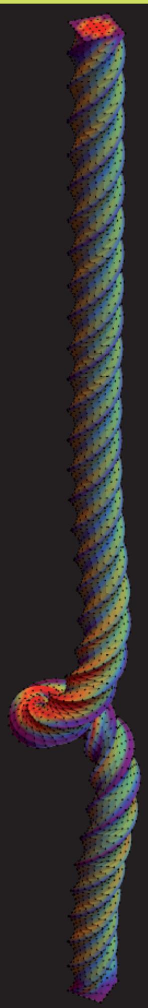

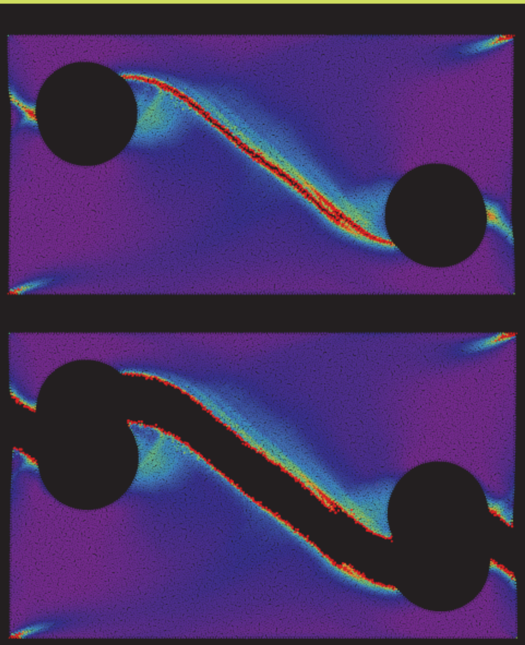

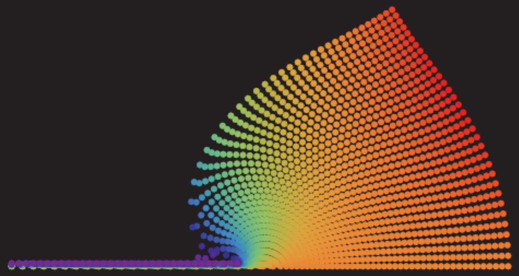

Peridynamic Galerkin methods for nonlinear solid mechanics

Von der Fakultät für Maschinenbau
der Gottfried Wilhelm Leibniz Universität Hannover

zur Erlangung des akademischen Grades
Doktor-Ingenieur

genehmigte Dissertation
von

M. Sc. Tobias Bode

geboren am 04.04.1994 in Hannover

2021

Herausgeber:
Prof. Dr.-Ing. habil. Dr. h.c. mult. Dr.-Ing. E.h. Peter Wriggers

Verwaltung:
Institut für Kontinuumsmechanik
Gottfried Wilhelm Leibniz Universität Hannover
An der Universität 1
30823 Garbsen

Tel: +49 511 762 3220
Fax: +49 511 762 5496
Web: www.ikm.uni-hannover.de

© M. Sc. Tobias Bode
Institut für Kontinuumsmechanik
Gottfried Wilhelm Leibniz Universität Hannover
An der Universität 1
30823 Garbsen

Alle Rechte, insbesondere das der Übersetzung in fremde Sprachen, vorbehalten. Ohne Genehmigung des Autors ist es nicht gestattet, dieses Heft ganz oder teilweise auf photomechanischem, elektronischem oder sonstigem Wege zu vervielfältigen.

ISBN 978-3-941302-45-7

1. Referent: Prof. Dr.-Ing. habil. Dr. h.c. mult. Dr.-Ing. E.h. Peter Wriggers
2. Referent: Prof. Dr.-Ing. habil. Christian Weißenfels

Tag der Promotion: 13.12.2021

To my family

Zusammenfassung

Die simulationsgesteuerte Produktenwicklung ist heutzutage ein wesentlicher Bestandteil des industriellen Digitalisierungsprozesses. Insbesondere im stark wachsenden Gebiet der additiven und abtragenden Fertigungsverfahren gibt es ein steigendes Interesse an realistischen und hochgenauen Simulationsverfahren. Dank ihrer Flexibilität eigenen sich netzfreie Lösungsmethoden besonders für das Simulieren dieser Fertigungsprozesse, welche oftmals von großen Verformungen, veränderlichen Diskontinuitäten oder Phasenwechseln begleitet werden. Darüber hinaus stellt im industriellen Bereich das Vernetzen von komplexen Geometrien einen wesentlichen Arbeitsaufwand dar, welcher bei netzfreien Verfahren für gewöhnlich weniger bedeutsam ist.

Im Laufe der Jahre wurden viele netzfreie Verfahren entwickelt. Einhergehend mit ihrer Flexibilität in der Diskretisierung leiden netzfreie Methoden oftmals jedoch an einer Verminderung der Genauigkeit, Effizienz und Stabilität oder einer wesentlich erhöhten Rechenzeit. Die Peridynamik ist eine zur lokalen Kontinuumsmechanik alternative Theorie zur Beschreibung von partiellen Differentialgleichungen in einer nicht-lokalen integro-differentialen Form. Die Kombination der sogenannten peridynamischen Korrespondenzformulierung mit einer Partikeldiskretisierung ergibt eine flexible netzfreie Simulationsmethode, führt jedoch ohne weitere Behandlung nicht zu zuverlässigen Ergebnissen.

Um eine verlässliche, robuste und dennoch flexible netzfreie Simulationsmethode zu entwickeln, wird in dieser Arbeit die klassische Korrespondenzformulierung in den Peridynamischen Galerkin (PG)-Methoden generalisiert. Anhand dieser werden Bedingungen an die netzfreien Formfunktionen der virtuellen und tatsächlichen Verschiebung vorgestellt, die eine genaue Aufbringung von Kraft- und Verschiebungsrandbedingungen ermöglichen und zu Stabilität und optimalen Konvergenzraten führen. Auf Basis sich mit dem Auswertepunkt bewegender Taylor-Entwicklungen werden spezielle Formfunktionen eingeführt, die alle zuvor genannten Anforderungen unter Verwendung von Korrekturschemen erfüllen. Neben verschiebungsbasierten Formulierungen werden unterschiedliche stabilisierte, gemischte und angereicherte Varianten entwickelt, die in ihrer Anwendung auf die nahezu inkompressible und elasto-plastische finite Deformation von Festkörpern zugeschnitten sind und den großen Gestaltungsspielraum der PG-Methoden hervorheben.

Es werden umfangreiche numerische Validierungen und Benchmark-Simulationen durchgeführt, um die Auswirkungen der Verletzung verschiedener Formfunktionsanforderungen aufzuzeigen und die Eigenschaften der verschiedenen PG-Formulierungen zu demonstrieren. Im Vergleich zu verwandten Finite-Elemente-Formulierungen weisen die PG-Methoden ähnliche Konvergenzeigenschaften auf. Darüber hinaus steht einer durch die Nichtlokalität erhöhten Rechenzeit eine erheblich gesteigerte Robustheit bei schlecht vernetzten Diskretisierungen gegenüber.

Schlagworte: Netzfreie Partikelmethode, Galerkin-Verfahren, Konsistenz, Peridynamik, Smoothed Particle Hydrodynamics, Gemischte Methoden, Stabiliserte Methoden, Angereicherte Methoden

Abstract

Simulation-driven product development is nowadays an essential part in the industrial digitalization. Notably, there is an increasing interest in realistic high-fidelity simulation methods in the fast-growing field of additive and ablative manufacturing processes. Thanks to their flexibility, meshfree solution methods are particularly suitable for simulating the stated processes, often accompanied by large deformations, variable discontinuities, or phase changes. Furthermore, in the industrial domain, the meshing of complex geometries represents a significant workload, which is usually minor for meshfree methods.

Over the years, several meshfree schemes have been developed. Nevertheless, along with their flexibility in discretization, meshfree methods often endure a decrease in accuracy, efficiency and stability or suffer from a significantly increased computation time. Peridynamics is an alternative theory to local continuum mechanics for describing partial differential equations in a non-local integro-differential form. The combination of the so-called peridynamic correspondence formulation with a particle discretization yields a flexible meshfree simulation method, though does not lead to reliable results without further treatment.

In order to develop a reliable, robust and still flexible meshfree simulation method, the classical correspondence formulation is generalized into the Peridynamic Galerkin (PG) methods in this work. On this basis, conditions on the meshfree shape functions of virtual and actual displacement are presented, which allow an accurate imposition of force and displacement boundary conditions and lead to stability and optimal convergence rates. Based on Taylor expansions moving with the evaluation point, special shape functions are introduced that satisfy all the previously mentioned requirements employing correction schemes. In addition to displacement-based formulations, a variety of stabilized, mixed and enriched variants are developed, which are tailored in their application to the nearly incompressible and elasto-plastic finite deformation of solids, highlighting the broad design scope within the PG methods.

Extensive numerical validations and benchmark simulations are performed to show the impact of violating different shape function requirements as well as demonstrating the properties of the different PG formulations. Compared to related Finite Element formulations, the PG methods exhibit similar convergence properties. Furthermore, an increased computation time due to non-locality is counterbalanced by a considerably improved robustness against poorly meshed discretizations.

Keywords: Meshfree particle method, Galerkin method, Consistency, Peridynamic theory, Smoothed Particle Hydrodynamics, Mixed methods, Stabilized methods, Enriched methods

Acknowledgements

At this point I would like to express my sincere thanks to all those who made the production of this work possible. First and foremost, I thank Prof. Dr.-Ing. habil. Dr. h.c. mult. Dr.-Ing. E.h. Peter Wriggers for the opportunity to work at the Institute of Continuum Mechanics and for giving me the greatest possible freedom in the focus of my research. The environment he has created at the Institute has provided the possibility to have countless discussions and gain broad insight beyond one's own topic through the regular institute seminars and external lectures. The opportunity to participate in further courses and international conferences was a special and wonderful experience for me. Furthermore, I would like to thank Prof. Dr.-Ing. habil. Christian Weißenfels, who motivated, supported and supervised me since my master studies when I attended his really great continuum mechanics I lecture. During the course of my doctoral studies we had many long discussions and he had always an open door for questions.

I would also like to thank my great current and former colleagues for the good and harmonic atmosphere in the institute and the enjoyable joint activities. The exchange with my colleagues also working in the field of meshfree methods, especially with Dr.-Ing. Henning Wessels, Dr.-Ing. Philipp Hartmann, Dr.-Ing. Jan-Philipp Fürstenau and Dr.-Ing. Meisam Soleimani, was a lot of fun and advanced my work. Special thanks also go to Vera Halfar for her constant support in bureaucratic matters, Jens Bsdok for always quickly solving all my IT problems and Volker Meine for making most of the drawings in this work.

Finally, and most importantly, I would like to express my heartfelt gratitude to my parents, siblings, relatives and friends for their constant support and understanding in all respects.

Hannover, December 2021 Tobias Bode

Contents

1 **Introduction** **1**
  1.1 Meshfree Methods . . . 2
  1.2 Numerical challenges . . . 3

2 **Local continuum mechanics** **5**
  2.1 Kinematics of the continuum . . . 5
    2.1.1 Deformation and strain measures . . . 5
    2.1.2 Multiplicative decomposition . . . 7
  2.2 Balance principles . . . 8
    2.2.1 Conservation of mass . . . 9
    2.2.2 Momentum balances . . . 9
    2.2.3 Conservation of energy . . . 10
    2.2.4 Entropy inequality . . . 11
  2.3 Constitutive models . . . 12
    2.3.1 Hyperelasticity . . . 12
    2.3.2 Finite elasto-plasticity . . . 13
  2.4 Variational principles . . . 14
    2.4.1 D'Alembert's principle . . . 14
    2.4.2 Hu-Washizu principle . . . 15

3 **Fundamentals of peridynamic theory** **17**
  3.1 States and non-local kinematics . . . 18
  3.2 Integro-differential momentum balance . . . 19
  3.3 Peridynamic constitutive models . . . 20
  3.4 Correspondence theory . . . 22

4 **Peridynamic Galerkin methods** **23**
  4.1 Particle discretization . . . 24
  4.2 Bridging peridynamic and local quantities . . . 26
    4.2.1 Classical correspondence formulation . . . 26
    4.2.2 From states to tensors: A general shape function approach . . . 28
    4.2.3 Inverse non-local averaging . . . 30
  4.3 Treatment of boundary conditions . . . 33
    4.3.1 Dirichlet boundaries . . . 33
    4.3.2 Neumann boundaries . . . 34

4.4 Temporal discretization . . . 34
    4.4.1 Integration of motion . . . 35
    4.4.2 Evolution of plastic variables . . . 36
4.5 Residual or discretized strong form . . . 36
4.6 Linearization of the global equations . . . 38
    4.6.1 Finite Difference approximation . . . 40
    4.6.2 Consistent linearization . . . 40
    4.6.3 Automatic Differentiation . . . 41
4.7 Local conservation properties . . . 42

5 The role of shape functions 45
5.1 Requirements on test and trial shape functions . . . 45
    5.1.1 Consistency criteria . . . 46
    5.1.2 Interpolation condition . . . 47
    5.1.3 Bond mapping criterion . . . 48
    5.1.4 Integration constraints . . . 49
5.2 Specific meshfree shape functions . . . 51
    5.2.1 Shape functions of least square regressions . . . 52
    5.2.2 A Moving Taylor Expansion . . . 56
5.3 Modification of shape function derivatives . . . 57
    5.3.1 Restoration of bond mapping . . . 57
    5.3.2 Restoration of variational consistency . . . 59

6 Specific Peridynamic-Galerkin formulations 63
6.1 Displacement based formulations . . . 63
6.2 Mixed displacement–pressure–dilation approaches . . . 64
    6.2.1 Constant pressure and dilation . . . 66
    6.2.2 Higher order approaches . . . 67
    6.2.3 A bubble-enriched formulation . . . 67
6.3 Underintegration and stabilization . . . 68
    6.3.1 Full integration stabilization . . . 69
    6.3.2 Stabilization with implicit gradients . . . 70

7 Numerical illustrations, verifications and examples 73
7.1 Errors in practice . . . 73
7.2 Isolation of pitfalls and verifications . . . 78
    7.2.1 Eigen mode analysis . . . 78
    7.2.2 Patch tests . . . 80
    7.2.3 Convergence in a manufactured 2-D problem . . . 84
    7.2.4 Comparison of total and updated Lagrange . . . 85
    7.2.5 Numerical inf-sup test . . . 89
7.3 Numerical benchmarks . . . 90
    7.3.1 2-D punch problem . . . 91
    7.3.2 Torsion of square hyperelastic prism . . . 93
    7.3.3 3-D Punch problem . . . 94

7.3.4 Cook’s membrane 95
7.3.5 Cylindrical necking 96
7.3.6 Dynamic torsion of square elasto-plastic prism 98
7.3.7 Taylor anvil impact benchmark 101
7.3.8 Coupling with Finite Elements and symmetry boundary conditions . 108

8 Conclusion and outlook 111
8.1 Back to the origin of peridynamics: Fracture 112
8.2 Fluid flows 113

A Exemplary derivation of the global tangent stiffness matrix 117

B Momentum preservation of mixed approaches 123

Bibliography 125

List of Figures 137

List of Tables 142

CURRICULUM VITAE 144

Chapter 1

Introduction

In last decades many different methods for the approximate solution of partial differential equations were developed and applied to various engineering problems. The Finite Element Method (FEM) is well accepted for the solution of a wide range of problems in industry, and simulation-driven product development is nowadays an important part of the industrial development process. Especially in the fast growing field of additive and ablative manufacturing processes there is an increasing interest in realistic high fidelity simulation methods. However, for complex lifelike simulations it is advantageous to have more flexible discretization schemes as with large distortions the FEM needs a remeshing which is prone to errors, cf. HABRAKEN & CESCOTTO (1990). Due to their flexibility, meshfree solution methods are particularly suitable for simulating these processes, which often exhibit large deformations, variable discontinuities or phase changes (see e.g. WESSELS (2019), HARTMANN (2019), HUANG (2020) and FÜRSTENAU (2021)). Furthermore, in the industrial domain, the meshing of complex geometries represents a significant workload, which is usually less significant for meshfree methods. Besides the advantage of flexibility in discretization and oftentimes an exceptional robustness, the efficiency and accuracy of the mesh-based FEM is hard to achieve. Some reasons include the consistency, stability and the imposition of boundary conditions which are challenging aspects in the scope of meshfree methods.

The target of this work is to introduce a new class of meshfree formulations that have a comparable accuracy and reliability as the FEM, but are less sensitive to a poor meshing or mesh distortion. Thereby, the nature of a particle method shall be retained to pave the way for further developments for the usage within phase changes and moving surfaces where the neighborhoods change and the connectivities have to be updated. In the further course of this thesis, a brief overview into the variety of meshfree methods and the challenges in their design is given in the following sections. With chapters 2 and 3, an introduction to the theory of classical local continuum mechanics and the nonlocal peridynamic theory is given, which provide the physical foundation for the further development of the numerical methods. This is followed in chapter 4 by a detailed motivation and introduction into the basic Peridynamic Galerkin (PG) methods as a generalization of the peridynamic theory of correspondence materials. Inter alia, the application of boundary conditions, the linearization of the weak form and the residual, and the local conservation properties are discussed in more detail. The special requirements for the meshfree shape functions and a possible construction technique based on manipulations of a particular interpolating Moving Taylor Expansion procedure are in depth addressed in chapter 5. Further on, an example for more advanced PG formulations is given customized for the use within the region of volumetric kinematic constraints as occurs in incompressibility or isochoric plastic flow. Therefore, several mixed and stabilized approaches are designed in chapter 6. Examples of pitfalls arising from the use of unsuitable meshfree schemes are demonstrated in chapter 7, followed by a selection of verification problems isolating their different appearance and a set of benchmarks demonstrating the performance and competitiveness of proper PG formulations. Finally, chapter 8 concludes the findings of this work and reveals two areas for future developments, namely the modeling of fracture and the application to fluid dynamics, and provides possible realization options. Parts of the current thesis have been published previously in the original articles BODE ET AL. (2020a), BODE ET AL. (2020b) and BODE ET AL. (2021) or are in preparation for submission.

1.1 Meshfree Methods

Discretization schemes that assemble a global algebraic system without previous meshing have been developed since the 1930s, cf. LIU (2009) and LIU & GU (2005). While numerous methods were introduced, some more prominent of them include the Smoothed Particle Hydrodynamics (SPH) introduced by GINGOLD & MONAGHAN (1977) and LUCY (1977), the Reproducing Kernel Particle Method (RKPM, LIU ET AL. (1995a) and LIU ET AL. (1995b)), the Element Free Galerkin (EFG) method (BELYTSCHKO ET AL., 1994), the Material Point Method (MPM, SULSKY ET AL. (1994)) and the more recent peridynamic approach, combined with a particle discretization (see SILLING & ASKARI (2005)). A good overview over the developments of meshfree methods and challenges therein can be found in FRIES ET AL. (2003) and CHEN ET AL. (2017).

Peridynamics is a non-local field theory based on integro-differential equations which is idealized and widely used to model discontinuities as occurring in fracture simulations (see e.g. SILLING (2000) and SILLING (2003)), but in recent years the area of applications rapidly increased. By now, the range of applications includes multifield and multiscale, as well as complex flow, impact problems and wave dispersion (JAVILI ET AL., 2018). Applied to the momentum equation, two fundamental modeling approaches are present. On the one hand, a non-local balance equation can be directly combined with a non-locally defined constitutive model, which results in the bond- and state-based peridynamic formulations. On the other hand, utilizing a material model of the local continuum mechanics theory, the so-called correspondence formulation was introduced, whereby the reduction operation established the link between non-local and local measures. Together with a particle discretization, a flexible meshfree method can be set up (WARREN ET AL., 2009). In BESSA ET AL. (2014) the similarity of the peridynamic correspondence theory to the RKPM and other meshfree methods with polynomial basis was shown. Further, in GANZENMÜLLER ET AL. (2015), the peridynamic correspondence formulation was found to be equivalent to the corrected SPH in the total Lagrangian perspective. Hence, it can suffer from the typical problems of meshfree methods which are further addressed and include:

- Rank deficiency and instability due to nodal-, particle- or rather underintegration
- Tensile instability resulting from Lagrange updates
- Inaccurate imposition of Dirichlet and Neumann boundaries
- Lack of consistency and the fulfillment of a patch test
- Erroneous convergence and reduced convergence rates
- Locking in the range of geometric constraints

1.2 Numerical challenges

Accompanied with the flexibility in discretization, a rank deficiency arises when particle integration is used which results in spurious zero or low energy modes. Oftentimes, this is addressed by corrections to restore stability (see e.g. the works of MONAGHAN (2000) in SPH and WEISSENFELS & WRIGGERS (2018) in the Optimal Transportation Meshfree (OTM) method). In terms of the peridynamic correspondence formulation, oscillations occur due to the locally averaged deformation gradient, which is a reduction of the possibly nonlinear peridynamic deformation state (see e.g. SILLING (2016) and FOSTER (2016)). In the last years, this issue was suspect to extensive research and several stabilization schemes have been introduced. One approach is, to apply correction forces, see e.g. LITTLEWOOD (2010), BREITENFELD ET AL. (2014) and SILLING (2017). However, unphysical parameters have to be determined that can be case sensitive and reduce the accuracy of the solution. TUPEK & RADOVITZKY (2014) proposed an extended correspondence formulation based on Seth-Hill strains. A higher order approximation using modified weight functions has been developed in YAGHOOBI & CHORZEPA (2017). CHOWDHURY ET AL. (2019) addressed the low-energy modes by means of a separation of the neighborhood of a particle into subdivisions which was studied and extended in HARTMANN ET AL. (2020) and HARTMANN ET AL. (2021). The use of bond-level and bond-associated deformation gradients is studied in BREITZMAN & DAYAL (2018), CHEN (2018), GU ET AL. (2019), MADENCI ET AL. (2019) and CHEN & SPENCER (2019). A stress-point method to overcome the rank deficiency was presented in LUO & SUNDARARAGHAVAN (2018) and ZHANG ET AL. (2020). Within this work, a unified Galerkin type shape function approach is pursued which provides the basis for a variety of formulations within a generalized framework and is generally stable without the use of further artificial stabilization techniques. Furthermore, this allows to shift the most crucial aspects of the method to a matter of shape functions, which than have to fulfill certain conditions.

The tensile instability, which also produces displacement oscillations, should not be mixed up with the presence of a rank deficiency, cf. BELYTSCHKO ET AL. (2000) and BONET & KULASEGARAM (2001), as it is a result of updating the perspective in which the kernel or shape functions are computed. This inconsistency arises when the actual deformation of a neighborhood is not contained in the ansatz space, i.e. the actual current configuration of a neighborhood and its pushed forward counterpart differ. Hence, the tensile instability has to be treated separately from the rank deficiency or rather avoided by using a total Lagrangian formulation. Here, a shape function condition is stated that ensures an accurate and bijective mapping.

If the rank deficiency and tensile instability are sufficiently treated, the resulting meshfree method may be stable and robust, however, a disturbed convergence or the failure in satisfying the patch test can oftentimes be observed. These issues apply for different kinds of weak form methods where either the numerical integration is inaccurate, or the ansatz spaces are not conforming such that the Galerkin orthogonality does not hold and the solution is not anymore the optimal Galerkin solution. A criterion for the test shape functions, later termed integration constraint, was developed that is needed to enable these properties (cf. KRONGAUZ & BELYTSCHKO (1997)) and to ensure an accurate imposition of Neumann boundary conditions. Different methodologies were presented to fulfill the requirements for the test functions. See e.g. in Smoothed Particle Hydrodynamics (SPH) BONET & LOK (1999), BONET & KULASEGARAM (2000) and FERNÁNDEZ-MÉNDEZ ET AL. (2005) and for the nodal strain method PUSO ET AL. (2008). In CHEN ET AL. (2013) the integration constraint was generalized in the more general variational consistency for polynomials of higher order. Further, variationally consistent integration methods were introduced and applied for the Stabilized Conforming Nodal Integration (SCNI, (HILLMAN ET AL., 2014)), Stabilized Nonconforming Nodal Integration (SNNI, (HILLMAN & CHEN, 2016)) and Element-Free Galerkin (EFG, (DUAN ET AL., 2014)) method. In the present thesis, a shape function derivative correction is presented that is compatible to Bubnov- and Petrov-Galerkin methods and to all other shape function conditions that ensure consistency and prevent tensile instabilities.

Like in the FEM, mere displacement-based meshfree approaches can exhibit locking phenomena, as e.g. a stiffer response or divergence, when the problem is subject to geometric constraints (see e.g. DOLBOW & BELYTSCHKO (1999) and CHEN ET AL. (2000)). In the range of near incompressibility or isochoric plastic flow, a volumetric locking arises. Next to other techniques, like selective reduced integration, projection methods or the promising enhanced assumed strain elements (cf. KORELC ET AL. (2010)), mixed displacement–pressure–dilation formulations on the basis of a Hu-Washizu potential are known to overcome these problems and possess increased robustness. Whether a specific formulation underlies a volumetric locking or spurious pressure modes can be verified by means of an inf-sup condition, see FORTIN & BREZZI (1991). Although not fulfilling this condition, the popular Q1P0 element of SIMO ET AL. (1985) usually leads to good results in practice. The technique of underintegration and selective integration as well as the formulation of mixed and enriched approaches will be addressed in the remainder of this work.

Chapter 2

Local continuum mechanics

In this chapter, the simplified fundamentals of the local continuum mechanics are stated that provide the local part of the physical basis for the discretization within the PG methods. A complete set of equations for the modeling of finite strain solid mechanics include, next to initial and boundary conditions, a kinematic description, the balance equations and a constitutive model. For the numerical solution, variational principles are further deployed. An extensive overview can be found e.g. in TRUESDELL & TOUPIN (1960) and HOLZAPFEL (2002).

2.1 Kinematics of the continuum

In continuum mechanics, the macroscopic behavior of a body is described (see e.g. HOLZAPFEL (2002)). Therefore, the body $\mathcal{B}$ consists of a continuous set of material particles $X \in \mathcal{B}$, which are embedded in the Euclidean space $\mathbb{E}^3$. The geometric region occupied by the collection of the particles at a specific time t is called configuration Ω. In the initial, i.e. undeformed, configuration Ω_0, the position of particle X is given by $\mathbf{X} \in \Omega_0$. The motion $\mathcal{X}$ of body $\mathcal{B}$ is a mapping that assigns each particles initial position to a deformed position $\mathbf{x} \in \Omega$ (see Figure 2.1). With the geometric difference between the initial position and its current position to a time t, the displacement vector field is defined as

$$\mathbf{u}(\mathbf{X}, t) = \mathbf{x}(\mathbf{X}, t) - \mathbf{X}\,. \tag{2.1}$$

2.1.1 Deformation and strain measures

For the objective, i.e. observer independent, description of the state of deformation in the incremental neighborhood of a material particle, i.e. in the local theory, a linear mapping operator can be defined. The two-field second order tensor field $\mathbf{F}(\mathbf{X}, t)$ is termed material deformation gradient and computes as the derivative of the current position $\mathbf{x}(\mathbf{X}, t)$ with respect to its initial position $\mathbf{X}$. For convenience, the dependency $(\mathbf{X}, t)$ is further omitted.

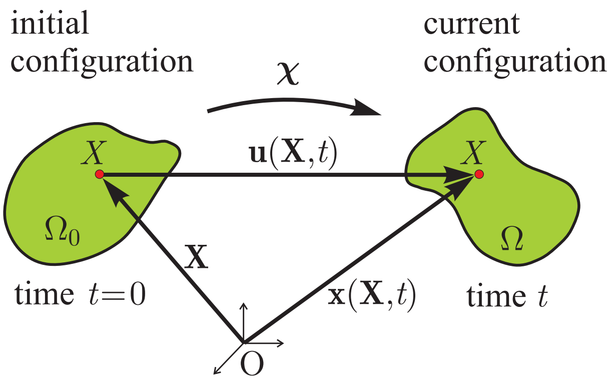

Figure 2.1. Motion of body $\mathcal{B}$ from initial to current configuration.

$$\mathbf{F} = \frac{\partial \mathbf{x}}{\partial \mathbf{X}} = \frac{\partial\left(\mathbf{X}+\mathbf{u}\right)}{\partial \mathbf{X}} = \mathbf{1} + \frac{\partial \mathbf{u}}{\partial \mathbf{X}} = \mathbf{1} + \mathbf{H} \tag{2.2}$$

with the unity tensor $\mathbf{1}$ and the displacement gradient $\mathbf{H}$. While the deformation gradient $\mathbf{F}$ maps the incremental material distance vector $d\mathbf{X}$ into the incremental spatial distance vector $d\mathbf{x}$, the inverse mapping is performed by the spatial deformation gradient $\mathbf{F}^{-1}$. The incremental initial volume element dV around a particle can be transferred with the Jacobian J to its current counterpart:

$$dv = J dV \quad \text{with} \quad J = \det \mathbf{F}\,. \tag{2.3}$$

To ensure the bijectivity of the linear mapping, the inverse $\mathbf{F}^{-1}$ has to exist, which yields in the condition $J \neq 0$. Further, the self-penetration of material additionally restricts the physical range of the Jacobian to $J > 0$, which serves as a criterion for the constitutive modeling. In the case of incompressibility, the incremental volume element does not change during deformation, which constraints the Jacobian to $J = 1$.

In the hyperelastic modeling of solids, further deformation measures are relevant. The symmetric right Cauchy-Green tensor, defined with respect to the initial configuration, states

$$\mathbf{C} = \mathbf{F}^T \cdot \mathbf{F}\,. \tag{2.4}$$

Analogously, the symmetric left Cauchy-Green tensor can be defined with respect to the current configuration:

$$\mathbf{b} = \mathbf{F} \cdot \mathbf{F}^T\,. \tag{2.5}$$

A nonlinear strain measure can now be derived as the Green-Lagrange strain tensor in the initial configuration

$$\mathbf{E} = \frac{1}{2}\left(\mathbf{C} - \mathbf{1}\right)\,, \tag{2.6}$$

while its push-forward (transformation to the basis of the current configuration), the Euler-Almansi strain tensor, yields with respect to the current configuration

$$\mathbf{e} = \mathbf{F}^{-T} \cdot \mathbf{E} \cdot \mathbf{F}^{-1} = \frac{1}{2}\left(\mathbf{1} - \mathbf{b}^{-1}\right) . \tag{2.7}$$

For linear analyses, the strain measure can be linearized as

$$\boldsymbol{\epsilon} = \frac{1}{2}\left(\mathbf{H} + \mathbf{H}^{T}\right) . \tag{2.8}$$

2.1.2 Multiplicative decomposition

For the application of geometric constraints or the numerical treatment of the deformation, it can be advantageous to separate the deformation into consecutive parts. The polar decomposition of the deformation gradient

$$\mathbf{F} = \mathbf{R} \cdot \mathbf{U} = \mathbf{v} \cdot \mathbf{R} \tag{2.9}$$

decomposes the rotational and the stretching part. Herein, $\mathbf{R}$ is the second order orthogonal rotation tensor and $\mathbf{U}$ and $\mathbf{v}$ are the symmetric positive definite stretching tensors with respect to the initial and current configuration, respectively. Alternatively, the deformation gradient can be decomposed into a volume changing volumetric part $\mathbf{F}_{vol}$ and a shape changing isochoric part $\mathbf{F}_{iso}$:

$$\mathbf{F} = \mathbf{F}_{vol} \cdot \mathbf{F}_{iso} \quad \text{with} \quad \mathbf{F}_{vol} = J^{\frac{1}{3}}\mathbf{1} \quad \text{and} \quad \mathbf{F}_{iso} = J^{-\frac{1}{3}}\mathbf{F} . \tag{2.10}$$

Accordingly, the isochoric part of the right and left Cauchy-Green tensor write

$$\mathbf{C}_{iso} = \mathbf{F}_{iso}^{T} \cdot \mathbf{F}_{iso} = J^{-\frac{2}{3}}\mathbf{F}^{T} \cdot \mathbf{F} = J^{-\frac{2}{3}}\mathbf{C} \quad \text{and} \quad \mathbf{b}_{iso} = J^{-\frac{2}{3}}\mathbf{b} . \tag{2.11}$$

For the modeling of elasto-plasticity within the range of finite deformations, the elastic and plastic deformation can be separated and a stress-free plastic intermediate configuration is introduced (see Figure 2.2). Hence, the deformation gradient splits consecutively into a purely plastic and an elastic mapping:

$$\mathbf{F} = \mathbf{F}_{e} \cdot \mathbf{F}_{p} . \tag{2.12}$$

While the plastic deformation is assumed to be perfectly isochoric, i.e.

$$\mathbf{F}_{p} = \mathbf{F}_{p\,iso} \quad \text{and} \quad J_{p} = \det \mathbf{F}_{p} = 1, \tag{2.13}$$

the elastic part can again be split into an isochoric and a volumetric deformation

$$\mathbf{F}_{e} = J_{e}^{\frac{1}{3}}\,\mathbf{F}_{e\,iso} \quad \text{with} \quad J_{e} = \det \mathbf{F}_{e} = J . \tag{2.14}$$

If the elastic response is considered in terms of an hyperelastic strain energy potential, based on the left Cauchy-Green tensor, the elastic part of it can be written as

$$\mathbf{b}_{e} = \mathbf{b}_{e\,iso} \cdot \mathbf{b}_{e\,vol} \quad \text{with} \quad \mathbf{b}_{e\,vol} = \mathbf{F}_{e\,vol} \cdot \mathbf{F}_{e\,vol}^{T} = J^{\frac{2}{3}}\mathbf{1} \tag{2.15}$$

and the isochoric part of the elastic left Cauchy-Green tensor

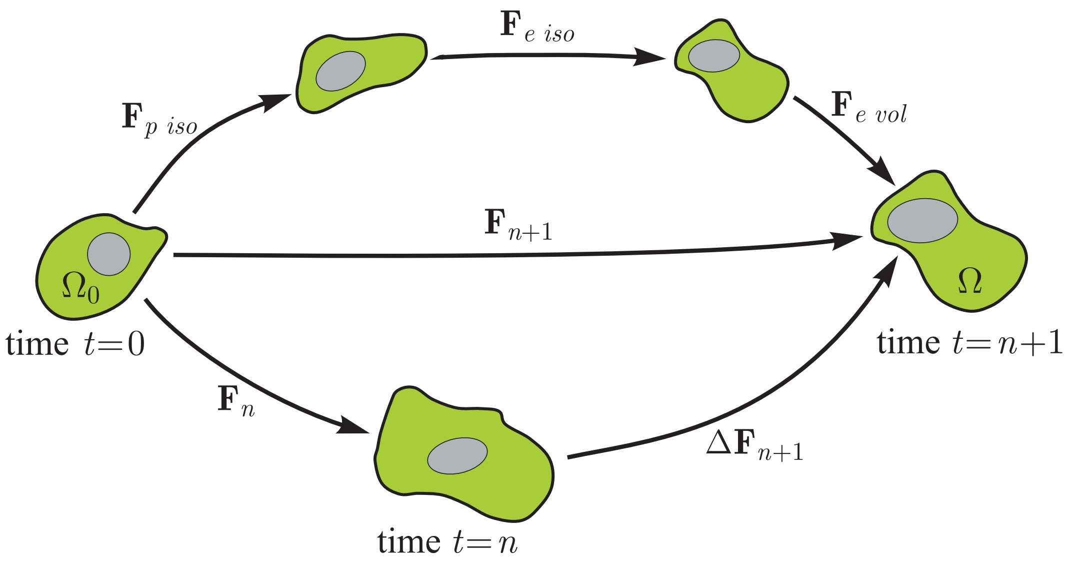

Figure 2.2. At the top: Superposition of isochoric plastic, isochoric elastic and volumetric plastic deformation with intermediate configurations. At the bottom: Updated Lagrangian decomposition of the deformation gradient mapping. The successive deformation of an infinitesimal spherical region by a single multiplicatively split deformation gradient is shown in gray.

$$\mathbf{b}_{e\ iso} = J_e^{-\frac{2}{3}}\,\mathbf{F}_e \cdot \mathbf{F}_e^T = J_e^{-\frac{2}{3}}\,\mathbf{F} \cdot \mathbf{F}_p^{-1} \cdot \mathbf{F}_p^{-T} \cdot \mathbf{F}^T = J^{-\frac{2}{3}}\,\mathbf{F} \cdot \mathbf{C}_p^{-1} \cdot \mathbf{F}^T\,, \tag{2.16}$$

where the plastic deformation is only considered with the symmetric (isochoric) plastic right Cauchy-Green tensor

$$\mathbf{C}_p = \mathbf{F}_p^T \cdot \mathbf{F}_p\,. \tag{2.17}$$

In the numerical treatment, it can be beneficial to describe the current configuration with respect to a reference configuration. This can either be constant in time, as done for isoparametric Finite Elements, or consisting of the configuration of the last load or time step $t = n$. In this updated Lagrangian description, the deformation gradient of the time $t = n + 1$ can be composed of the old part $\mathbf{F}_n$ and an incremental part $\Delta\mathbf{F}_{n+1}$:

$$\mathbf{F}_{n+1} = \Delta\mathbf{F}_{n+1} \cdot \mathbf{F}_n\,. \tag{2.18}$$

2.2 Balance principles

The motion of body $\mathcal{B}$ underlies physical laws of axiomatic character which are stated in this section in its Lagrangian description, i.e. with respect to the initial configuration. These include, the mass balance, the balance of linear and angular momentum and the first and second law of thermodynamics.

2.2.1 Conservation of mass

First, the mass balance states, that the density integrated over the region of a closed system is invariant to motion. This conservation states

$$\frac{Ddm}{Dt} = 0 \tag{2.19}$$

with the infinitesimal mass

$$dm = \rho_0 dV = \rho dv, \tag{2.20}$$

where ρ_0 denotes the initial density, ρ is the current density and dv the infinitesimal current volume.

2.2.2 Momentum balances

Cauchy's first law of motion derives from the principle of the conservation of linear momentum, which states that the change of linear momentum

$$\mathbf{I} = \int_{\Omega_0} \rho_0 \dot{\mathbf{u}} \, d\Omega_0 \tag{2.21}$$

of a body $\mathcal{B}$ equals the sum of external forces acting on it:

$$\frac{D\mathbf{I}}{Dt} = \int_{\Omega_0} \rho_0 \overline{\mathbf{b}} \, d\Omega_0 + \int_{\partial\Omega_0} \mathbf{T} \, d\partial\Omega_0 \,, \tag{2.22}$$

where $\rho_0\overline{\mathbf{b}}$ is an external body force density and $\mathbf{T}$ are external surface tractions acting on the initial surface $\partial\Omega_0$ of Ω_0. With the initial outward unit vector $\mathbf{n}_0$, Cauchy's theorem states with respect to the initial configuration

$$\mathbf{T} = \mathbf{N}^T \cdot \mathbf{n}_0 = \mathbf{P} \cdot \mathbf{n}_0 \tag{2.23}$$

where $\mathbf{N}$ is the nominal stress tensor (cf. OGDEN (1997)) and $\mathbf{P} = \mathbf{N}^T$ denotes the first Piola-Kirchhoff stress tensor. By inserting Cauchy's theorem into the change of linear momentum equation (2.22) and applying Gauß's theorem, the surface integral can be transformed into a volume integral, and the change of linear momentum yields

$$\int_{\Omega_0} \rho_0 \ddot{\mathbf{u}} \, d\Omega_0 = \int_{\Omega_0} \rho_0 \overline{\mathbf{b}} \, d\Omega_0 + \int_{\Omega_0} \operatorname{Div} \mathbf{P} \, d\Omega_0 \,, \tag{2.24}$$

where $\operatorname{Div}(\bullet)$ stands for the divergence with respect to the initial configuration. As the control region on which the linear momentum has to be fulfilled is arbitrary, Cauchy's first law of motion can be written in its local Lagrangian form

$$-\operatorname{Div} \mathbf{P} + \rho_0 \left(\ddot{\mathbf{u}} - \overline{\mathbf{b}}\right) = \mathbf{0} \,. \tag{2.25}$$

Analogous to the linear momentum, an angular momentum with respect to a position $\mathbf{x}_0$ can be computed as

$$\mathbf{L} = \int_{\Omega_0} \rho_0 \, (\mathbf{x} - \mathbf{x}_0) \times \dot{\mathbf{u}} \, d\Omega_0 \, . \tag{2.26}$$

Considering non-polar materials, the change of angular momentum results from the moment resulting from the acting external volume and surface forces:

$$\frac{D\mathbf{L}}{Dt} = \int_{\Omega_0} \rho_0 \, (\mathbf{x} - \mathbf{x}_0) \times \overline{\mathbf{b}} \, d\Omega_0 + \int_{\partial\Omega_0} (\mathbf{x} - \mathbf{x}_0) \times \mathbf{T} \, d\partial\Omega_0 \, . \tag{2.27}$$

Again, it can be simplified and reduced to a local form, which yields Cauchy's second law of motion in its material description

$$\mathbf{F} \cdot \mathbf{P}^T = \left(\mathbf{F} \cdot \mathbf{P}^T\right)^T \, , \tag{2.28}$$

which can be implicitly fulfilled by a constitutive model.

2.2.3 Conservation of energy

The first law of thermodynamics states, that the change of total energy E of body $\mathcal{B}$, consisting of kinetic energy K and inner energy U, is driven by the external force power P_{ext} and thermal power Q:

$$\frac{DE}{Dt} = \frac{DK}{Dt} + \frac{DU}{Dt} = P_{ext} + Q \, , \tag{2.29}$$

where the change of kinetic energy computes via the conservation of mechanical energy to

$$\frac{DK}{Dt} = P_{ext} - P_{int} \tag{2.30}$$

with the force power of the internal forces

$$P_{int} = \int_{\Omega_0} \mathbf{P} : \dot{\mathbf{F}} \, d\Omega_0 \, . \tag{2.31}$$

Therefore, the change of inner energy can be written as

$$\dot{U} = P_{int} + Q \tag{2.32}$$

where the thermal power

$$Q = -\int_{\partial\Omega_0} \mathbf{Q} \cdot \mathbf{n}_0 \, d\partial\Omega_0 + \int_{\Omega_0} \rho_0 r \, d\Omega_0 \tag{2.33}$$

is composed of the Piola-Kirchhoff heat flux $\mathbf{Q}$ across the surface and the volumetric heat source density $\rho_0 r$. Utilizing Gauß's theorem, and the arbitrariness of the control volume, the local form of the first law of thermodynamics in material description reduces to

$$\rho_0 \dot{u} = \mathbf{P} : \dot{\mathbf{F}} - \operatorname{Div} \mathbf{Q} + \rho_0 r \tag{2.34}$$

with the mass specific inner energy u. By applying the Legendre transformation $\psi = u - \eta\theta$, where ψ is the specific free Helmholtz energy, η denotes the entropy and θ stands for the absolute temperature ($\theta > 0$), the first law of thermodynamics can alternatively be written as

$$\rho_0 \dot{\psi} = \mathbf{P} : \dot{\mathbf{F}} + \rho_0 r - \operatorname{Div} \mathbf{Q} - \dot{\eta}\theta - \eta\dot{\theta}\,. \tag{2.35}$$

2.2.4 Entropy inequality

The second law of thermodynamics stipulates a condition for the direction of a physical process. It requires the entropy production Γ, which is the difference between the change in entropy $\dot{S}$ and the entropy insertion rate $\bar{Q}$, never to be negative:

$$\Gamma = \dot{S} - \bar{Q} \geq 0 \tag{2.36}$$

with

$$\dot{S} = \frac{D}{Dt} \int_{\Omega_0} \rho_0 \eta \, d\Omega_0 \quad \text{and} \quad \bar{Q} = -\int_{\partial\Omega_0} \mathbf{H} \cdot \mathbf{n}_0 \, d\partial\Omega_0 + \int_{\Omega_0} \rho_0 \bar{r} \, d\Omega_0\,, \tag{2.37}$$

where $\mathbf{H}$ is an entropy flux with respect to the initial surface and $\rho_0 \bar{r}$ denotes a volumetric entropy density source. Inserting the postulation $\mathbf{H} = \frac{\mathbf{Q}}{\theta}$ and $\bar{r} = \frac{r}{\theta}$ into the second law of thermodynamics yields

$$\frac{D}{Dt} \int_{\Omega_0} \rho_0 \eta \, d\Omega_0 + \int_{\partial\Omega_0} \frac{\mathbf{Q}}{\theta} \cdot \mathbf{n}_0 \, d\partial\Omega_0 - \int_{\Omega_0} \rho_0 \frac{r}{\theta} \, d\Omega_0 \geq 0\,, \tag{2.38}$$

known as the Clausius-Duhem inequality. Transforming the surface into a volume integral by means of Gauß's theorem, prescribing the heat to flow from warmer to colder regions and considering the independence of the control volume, the Clausius-Planck inequality states in the local material description

$$\mathcal{D}_{int} = \rho_0 \theta \dot{\eta} + \mathbf{P} : \dot{\mathbf{F}} - \rho_0 \dot{u} = \rho_0 \theta \dot{\eta} + \operatorname{Div} \mathbf{Q} - \rho_0 r \geq 0 \tag{2.39}$$

with the internal dissipation $\mathcal{D}_{int}$. Equation (2.39) has to be fulfilled by the constitutive models to be thermodynamically consistent. Considering isothermal processes ($\dot{\Theta} = 0$), the internal dissipation can further be simplified via the Legendre transformation to

$$\mathcal{D}_{int} = \mathbf{P} : \dot{\mathbf{F}} - \rho_0 \dot{\psi} = \boldsymbol{\tau} : \mathbf{d} - \rho_0 \dot{\psi} \geq 0. \tag{2.40}$$

Here, the internal stress power can be expressed by other work conjugated pairs of stress and strain measures as e.g., with respect to the initial configuration, via the second Piola-Kirchhoff stress $\mathbf{S} = \mathbf{F}^{-1} \cdot \mathbf{P}$ and the Green Lagrange strain: $\mathbf{P} : \dot{\mathbf{F}} = \mathbf{S} : \dot{\mathbf{E}}$. Alternatively, it can be written with respect to the current configuration which later serves for the concept of maximal plastic dissipation. Therefore, the first Piola Kirchhoff stress $\mathbf{P}$ is pushed forward to the symmetric Kirchhoff stress $\boldsymbol{\tau} = \mathbf{P} \cdot \mathbf{F}^T$ and, exploiting the symmetry of $\boldsymbol{\tau}$, the remaining part is transformed to the rate of deformation tensor $\mathbf{d} = \frac{1}{2}\left(\operatorname{grad} \dot{\mathbf{u}} + \operatorname{grad}^T \dot{\mathbf{u}}\right)$.

2.3 Constitutive models

Next to the kinematic description of the continuum and the conservation laws, a description of the response of a specific material, the constitutive model, is needed to set up a complete initial boundary value problem. In the constitutive modeling, several aspects have to be taken into account besides the fulfillment of the entropy inequality and the objectivity, which include the determinism, material symmetry, equi-presence, multiplicative decomposition, the concept of internal variables and fading memory (see e.g. TRUESDELL & TOUPIN (1960), MALVERN (1969) and BECKER & BÜRGER (2013)).

2.3.1 Hyperelasticity

When considering an isentropic material behavior, the stored strain energy density can be expressed in terms of a conservative potential function $W(\mathbf{F}) = \rho_0 \psi(\mathbf{F})$. Thus, the relation between the deformation gradient and the resulting stress computes via the Coleman-Noll procedure with $\mathcal{D}_{int} = 0$ from equation (2.40) to

$$\mathbf{P} = \frac{\partial W}{\partial \mathbf{F}}\,, \tag{2.41}$$

which is the two-field first Piola-Kirchhoff stress tensor. With the first Lamé constant λ and the shear modulus (or second Lamé constant) μ, the strain energy density function of a nonlinear isotropic neo-Hookean solid (cf. CIARLET (1988)) states

$$W = \frac{\mu}{2}\left(\mathrm{tr}\left[\mathbf{C}\right] - 3 - 2\ln\left[J\right]\right) + \frac{\lambda}{4}\left(J^2 - 1 - 2\ln\left[J\right]\right)\,. \tag{2.42}$$

In the region of nearly incompressible or incompressible material behavior, it can be more convenient to split the strain energy density additively into a purely isochoric part W_{iso} and volumetric part W_{vol} as

$$W = W_{iso}\left(\mathbf{b}_{iso}\right) + W_{vol}\left(J\right) = \frac{\mu}{2}\left(\mathrm{tr}\left[\mathbf{b}_{iso}\right] - 3\right) + \frac{K}{4}\left(J^2 - 1 - 2\ln\left[J\right]\right)\,, \tag{2.43}$$

where the bulk modulus K is related to the Lamé constants via

$$K = \lambda + \frac{2}{3}\mu\,. \tag{2.44}$$

For the numerical analysis of polynomial displacement fields in terms of a patch test, a model describing linearly elastic material behavior can be necessary. Therefore, the Saint Venant-Kirchhoff model for the geometrically nonlinear regime provides a linear relationship between the Green-Lagrange strain tensor $\mathbf{E}$ and the second Piola-Kirchhoff stress tensor $\mathbf{S}$:

$$\mathbf{S} = \frac{\partial^2 W}{\partial \mathbf{E}^2} : \mathbf{E} \quad \text{with} \quad W = \mu\,\mathrm{tr}\left[\mathbf{E}^2\right] + \frac{\lambda}{2}\,\mathrm{tr}\left[\mathbf{E}\right]^2\,. \tag{2.45}$$

In case of a linear analysis, the Green-Lagrange strain tensor has to be substituted with the linearized strain measure (equation (2.8)).

2.3.2 Finite elasto-plasticity

In an elasto-plastic material, the resistance against further deformation abruptly decreases if a certain limit of stress is reached. When this yield limit is reached, the material starts to deform irreversibly and the deformation can be split into a consecutive plastic and elastic part (see section 2.1). To the reversible elastic part a neo-Hookean strain energy density function can be assigned:

$$W = W_{iso}\left(\mathbf{b}_{e\,iso}\right) + W_{vol}\left(J_e\right) = \frac{\mu}{2}\left(\mathrm{tr}\left[\mathbf{b}_{e\,iso}\right] - 3\right) + \frac{K}{4}\left({J_e}^2 - 1 - 2\ln\left[J_e\right]\right) \,. \qquad (2.46)$$

The resulting first Piola-Kirchhoff stress tensor

$$\mathbf{P} = \frac{\partial W}{\partial \mathbf{F}_e} \qquad (2.47)$$

has one of its basis in the plastic intermediate configuration. Hence, for a push-forward to the current configuration, only the elastic part of the deformation gradient has to be considered. Thus, the symmetric Kirchhoff stress tensor states

$$\boldsymbol{\tau} = \mathbf{P} \cdot \mathbf{F}_e^T \,. \qquad (2.48)$$

Considering standard von Mises J_2 plasticity (see e.g. SIMO (1988) and SIMO & HUGHES (2006)) with nonlinear isotropic hardening, the yield limit that bounds the elastic regime writes

$$\mathcal{F} = \sigma_{vM} - \left[\sigma_{y0} + H\alpha + \left(\sigma_{y\infty} - \sigma_{y0}\right)\left(1 - e^{-\delta\alpha}\right)\right] \qquad (2.49)$$

where σ_{y0} is the initial yield stress, H is the linear hardening modulus, α the hardening variable and $\sigma_{y\infty}$ and δ define the nonlinearity of the isotropic hardening. The von Mises stress computes from the second main invariant of the deviatoric part of the Kirchhoff stress tensor:

$$\sigma_{vM} = \sqrt{3J_2\left(\boldsymbol{\tau_{dev}}\right)} = \sqrt{\frac{3}{2}\,\mathrm{tr}\left(\boldsymbol{\tau}_{dev} \cdot \boldsymbol{\tau}_{dev}\right)} \quad \text{with} \quad \boldsymbol{\tau}_{dev} = \boldsymbol{\tau} - \frac{\mathrm{tr}\left(\boldsymbol{\tau}\right)}{3}\mathbf{1} \,. \qquad (2.50)$$

For the evolution of the plastic deformation, a flow rule is further necessary. The Clausius-Planck inequality (2.40) leads with the concept of maximal plastic dissipation to a constraint optimization problem and the resulting thermodynamically consistent associative plastic flow rule

$$\mathbf{d}_p = \dot{\lambda}_{\mathcal{F}}\mathbf{n}_{\mathcal{F}} \quad \text{with} \quad \mathbf{n}_{\mathcal{F}} = \frac{\partial \mathcal{F}}{\partial \boldsymbol{\tau}} \quad \text{and} \quad \dot{\alpha} = \dot{\lambda}_{\mathcal{F}} \,, \qquad (2.51)$$

where $\mathbf{d}_p$ is the spatial plastic rate of deformation tensor, $\mathbf{n}_{\mathcal{F}}$ is the normal on the yield surface and $\lambda_{\mathcal{F}}$ the plastic Lagrange multiplier. By neglecting the plastic spin, the evolution equation can alternatively be expressed in terms of the rate of the plastic right Cauchy-Green tensor $\dot{\mathbf{C}}_p$ (cf. KORELC & STUPKIEWICZ (2014)) as

$$\dot{\mathbf{C}}_p^{-1} = -2\dot{\lambda}_{\mathcal{F}}\,\mathbf{F}^{-1} \cdot \mathbf{n}_{\mathcal{F}} \cdot \mathbf{F} \cdot \mathbf{C}_p^{-1} \qquad (2.52)$$

The flow conditions can be summarized in the Karush-Kuhn-Tucker form

$$\dot{\lambda}_{\mathcal{F}} \geq 0\,, \quad \mathcal{F} \leq 0 \quad \text{and} \quad \dot{\lambda}_{\mathcal{F}} \mathcal{F} = 0\,. \tag{2.53}$$

with the consistency condition

$$\dot{\lambda}_{\mathcal{F}} \dot{\mathcal{F}} = 0 \quad \text{for} \quad \mathcal{F} = 0\,. \tag{2.54}$$

2.4 Variational principles

With the kinematic description of section 2.1, the fundamental balance laws of section 2.2, a constitutive model of section 2.3, conditions on the Dirichlet and Neumann boundary and imposed initial conditions, the coupled system of nonlinear partial differential equations is complete. However, the solution of it can only be done analytically in idealized special cases. The application to nonlinear material behavior within finite deformations on a complex geometry needs a numerical treatment. Among other approaches (see e.g. BATHE (2006)), the general weak form and the principle of Hu-Washizu are further listed.

2.4.1 D'Alembert's principle

The general weak form of the linear momentum balance with respect to the initial configuration is based on the principle of virtual displacements applied to equation (2.25). Multiplying with a virtual displacement $\delta\mathbf{u}$, also known as test function, and integration over the initial region Ω_0 of $\mathcal{B}$ yields

$$\int_{\Omega_0} \left[-\operatorname{Div}\mathbf{P} + \rho_0 \left(\ddot{\mathbf{u}} - \overline{\mathbf{b}} \right) \right] \cdot \delta\mathbf{u} \, d\Omega_0 = 0 \tag{2.55}$$

which rewrites by doing integration by parts to the principle of d'Alembert in its Lagrangian description

$$\int_{\Omega_0} \mathbf{P} : \delta\mathbf{F} - \operatorname{Div}\left(\delta\mathbf{u} \cdot \mathbf{P}\right) + \rho_0 \left(\ddot{\mathbf{u}} - \overline{\mathbf{b}} \right) \cdot \delta\mathbf{u} \, d\Omega_0 = 0\,, \tag{2.56}$$

where $\delta\mathbf{F} = \operatorname{Grad}\delta\mathbf{u}$ can be interpreted as the variation of the deformation gradient. With the application of Gauß's theorem, the second term in the volume integral can be shifted to an integral over the boundary $\partial\Omega_0$ of Ω_0, leading to the weak form:

$$\int_{\Omega_0} \mathbf{P} : \delta\mathbf{F} + \rho_0 \left(\ddot{\mathbf{u}} - \overline{\mathbf{b}} \right) \cdot \delta\mathbf{u} \, d\Omega_0 - \int_{\partial\Omega_0} \left(\mathbf{P} \cdot \mathbf{n}_0 \right) \cdot \delta\mathbf{u} \, d\partial\Omega_0 = 0 \tag{2.57}$$

or equivalently with Cauchy's theorem of equation (2.23) written as

$$\int_{\Omega_0} \mathbf{P} : \delta\mathbf{F} + \rho_0 \left(\ddot{\mathbf{u}} - \overline{\mathbf{b}} \right) \cdot \delta\mathbf{u} \, d\Omega_0 - \int_{\partial\Omega_0} \mathbf{T} \cdot \delta\mathbf{u} \, d\partial\Omega_0 = 0\,. \tag{2.58}$$

As in the derivation no further assumptions were made, the weak form is generally valid, also for non-conservative inelastic constitutive models.

2.4.2 Hu-Washizu principle

In the numerical processing of the weak form (2.57) in terms of a Galerkin method with displacement degrees of freedom, an over-stiff behavior, called locking, can be observed in certain situations. The phenomenon of volumetric locking occurs when the material behaves incompressible or nearly incompressible, i.e. the bulk modulus approaches infinity. In these situations, the Hu-Washizu principle (WASHIZU (1968)) showed to be advantageous where next to the displacements, the strain measure and stress tensor are used as variables. Within a special Hu-Washizu potential with respect to the displacement $\mathbf{u}$, pressure p and dilation Θ, cf. SIMO ET AL. (1985), the strain energy density can be decoupled by equation (2.43) and independently processed. While the isochoric part as well as external and inertia forces are directly handled via the general weak form (2.57), the volumetric part is treated separately:

$$\Pi = \Pi_{iso}\left(\mathbf{b}_{iso}\right) + \Pi_{vol}\left(\mathbf{u}, p, \Theta\right) = \int_{\Omega_0} \left[W_{iso}\left(\mathbf{b}_{iso}\right) + W_{vol}\left(\Theta\right) + p\left(J - \Theta\right)\right] \, d\Omega_0 \,, \tag{2.59}$$

where the pressure can be interpreted as a Lagrangian multiplier. The variation of Π, including additionally the external and inertia forces, leads to

$$\begin{aligned}
\frac{\partial \Pi}{\partial \mathbf{u}} \cdot \delta \mathbf{u} = \int_{\Omega_0} \left(\underbrace{\frac{\partial W_{iso}}{\partial \mathbf{F}_{iso}}}_{\mathbf{P}_{iso}} + \underbrace{J p \mathbf{F}^{-T}}_{\mathbf{P}_{vol}} \right) : \delta \mathbf{F} + \rho_0 \left(\ddot{\mathbf{u}} - \overline{\mathbf{b}} \right) \cdot \delta \mathbf{u} \, d\Omega_0 - \int_{\partial \Omega_0} \mathbf{T} \cdot \delta \mathbf{u} \, d\partial\Omega_0 = 0 \,, \\
\frac{\partial \Pi}{\partial p} \delta p = \int_{\Omega_0} \left(J - \Theta\right) \delta p \, d\Omega_0 = 0 \quad \text{and} \\
\frac{\partial \Pi}{\partial \Theta} \delta \Theta = \int_{\Omega_0} \left(\frac{\partial W_{vol}}{\partial \Theta} - p \right) \delta \Theta \, d\Omega_0 = 0 \,.
\end{aligned} \tag{2.60}$$

Chapter 3

Fundamentals of peridynamic theory

Starting with the pioneering work of Silling (2000), the peridynamic theory has been developed. The adjective *peridynamic* is composed of the two greek words *peri* and *dyna* meaning the *near field* and *forces*, respectively. In relation to solids, the noun *peridynamics* is used as an abbreviation for the peridynamic theory of solid mechanics. Therefore, the peridynamic theory is a non-local field theory and it provides, as an extension to the local theory, an alternative way to model partial differential equations in terms of an integro-differential form. The initial motivation was, to provide a consistent way of modeling non-local effects and discontinuities by avoiding the use of spatial derivatives. In the present chapter, an introduction to the peridynamic fundamentals is given, whereby the classical peridynamic notation is partly adjusted for the sake of compatibility to the local description of chapter 2. A comprehensive overview on the peridynamic theory can be found in Bobaru et al. (2016), Madenci & Oterkus (2016a) and Gerstle (2015).

In the peridynamic theory, a particle $X \in \mathcal{B}$ with initial position $\mathbf{X} \in \Omega_0$ does not solely interact with particles in an infinitesimal distance, but within its non-local neighborhood, whereby the interaction beyond a radius δ, called horizon, is assumed to be negligible. The collective material particles within the distance of δ form the region of the neighborhood, the so-called family $\mathcal{H}_0$ of X (see Figure 3.1). Neighbor particle X' thereby exerts the force $\mathbf{f}\left(X, X'\right) dV_X dV_{X'}$ on particle X, further called master particle, where dV_X and $dV_{X'}$ denote the infinitesimal volume of X and X', respectively.

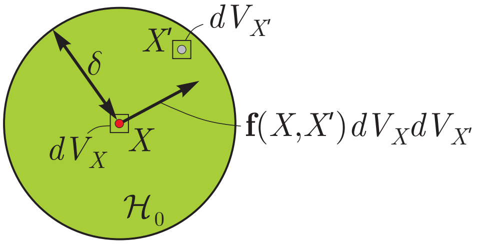

Figure 3.1. The infinitesimal master particle X with volume dV_X interacts with each neighbor particle X' within its family $\mathcal{H}_0$.

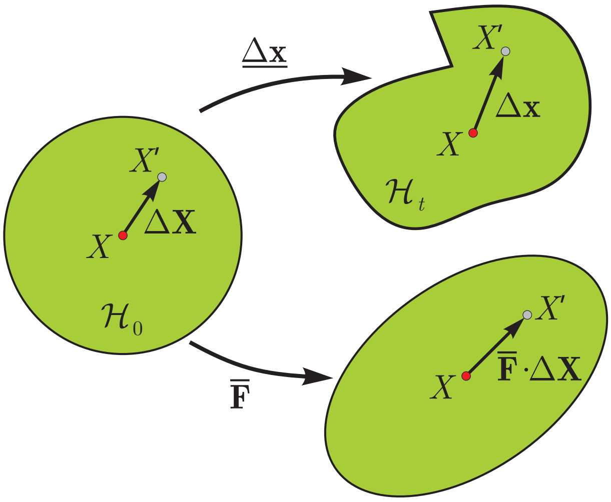

Figure 3.2. The current bond vector state $\underline{\Delta \mathbf{x}}$ performs a generally nonlinear and possibly non-smooth mapping of the initial family $\mathcal{H}_0$ into the current configuration, while its reduction $\bar{\mathbf{F}}$ is its linearized weighted average.

3.1 States and non-local kinematics

The kinematic description of a family can be established by the position $\mathbf{X}$ of the master particle X and the relative position of each infinitesimal particle within $\mathcal{H}_0$. With the initial position $\mathbf{X}'$ of particle X', the so-called bond $\Delta\mathbf{X}$ defines the distance vector with respect to $\mathbf{X}$:

$$\Delta\mathbf{X} = \mathbf{X}' - \mathbf{X} \tag{3.1}$$

and with respect to the current configuration the bond computes accordingly

$$\Delta\mathbf{x} = \mathbf{x}' - \mathbf{x}\,. \tag{3.2}$$

In SILLING ET AL. (2007) the concept of scalar, vector and tensor states was introduced as operators that assign each particle X' within $\mathcal{H}_0$ a scalar, vectorial or tensorial value, respectively. With regard to the bonds in initial and current configuration, the collective bonds of $\mathcal{H}_0$ can thus be stored in the vector states, marked with an underline,

$$\underline{\Delta\mathbf{X}} : X' \mapsto \Delta\mathbf{X}, \quad X' \in \mathcal{H}_0 \quad \text{and} \quad \underline{\Delta\mathbf{x}} : X' \mapsto \Delta\mathbf{x}, \quad X' \in \mathcal{H}_0\,, \tag{3.3}$$

where the evaluation for a single neighbor particle X' gives $\underline{\Delta\mathbf{X}}\,(X') = \Delta\mathbf{X}$. In relation to a second order tensor, a vector state is a generalization of the linear mapping to a nonlinear mapping of a non-local neighborhood (see illustration in Figure 3.2).

The further abbreviations are frequently used in state calculus. The inner and outer product of two states $\underline{\mathbf{a}}$ and $\underline{\mathbf{b}}$ are defined as the weighted integral of the inner and outer product for each particle within $\mathcal{H}_0$:

$$\underline{\mathbf{a}} \bullet \underline{\mathbf{b}} = \int_{\mathcal{H}_0} \underline{\mathbf{a}}\,(X') \cdot \underline{\mathbf{b}}\,(X')\; d\mathcal{H}_0 \tag{3.4}$$

and

$$\underline{\mathbf{a}} * \underline{\mathbf{b}} = \int_{\mathcal{H}_0} \underline{\omega}\,(X')\,\underline{\mathbf{a}}\,(X') \otimes \underline{\mathbf{b}}\,(X')\ d\mathcal{H}_0 \tag{3.5}$$

where $\underline{\omega}$ denotes an influence function. Applied to the initial bond vector state, the outer product with itself yields the symmetric shape tensor

$$\mathbf{K} = \underline{\Delta\mathbf{X}} * \underline{\Delta\mathbf{X}} \tag{3.6}$$

which is a measure for the shape of a family. An averaged second order tensor can then be gained via the so-called peridynamic reduction. With respect to the current bond vector state (see Figure 3.2), the reduction leads to an averaged deformation gradient

$$\mathcal{R}\,\{\underline{\Delta\mathbf{x}}\} = (\underline{\Delta\mathbf{x}} * \underline{\Delta\mathbf{X}}) \cdot \mathbf{K}^{-1} = \bar{\mathbf{F}}\,. \tag{3.7}$$

Note, that the definition of the peridynamic reduction is strongly related to the Weighted Least Square fitting technique, which is further explained in chapter 4. For a non-local constitutive modeling, the deformation of each bond is relevant. Therefore, the scalar extension state

$$\underline{e} = \underline{x} - \underline{X} \quad \text{with} \quad \underline{X} = |\underline{\Delta\mathbf{X}}| \quad \text{and} \quad \underline{x} = |\underline{\Delta\mathbf{x}}| \tag{3.8}$$

stores the change in length of each bond. Further, the extension state can be decomposed into an isotropic and deviatoric part as $\underline{e} = \underline{e}_i + \underline{e}_d$. With the weighted volume $m = (\underline{\omega}\underline{X}) \bullet \underline{X}$, the peridynamic dilation computes

$$\hat{\Theta} = \frac{3\,(\underline{\omega}\underline{X}) \bullet \underline{e}}{m}\,. \tag{3.9}$$

Hence, the isotropic and deviatoric part of the extension state write

$$\underline{e}_i = \frac{\hat{\Theta}}{3}\underline{X} \quad \text{and} \quad \underline{e}_d = \underline{e} - \underline{e}_i\,. \tag{3.10}$$

3.2 Integro-differential momentum balance

In the peridynamic counterpart to the local momentum equation (2.25) the internal force density is expressed in terms of an integral over the interactions with neighboring material points. The force $\mathbf{f}\,(X, X')\,dV_X dV_{X'}$, that neighbor particle X' exerts on X, can be decoupled into a part $\mathbf{t}dV_X dV_{X'}$ resulting from the deformation of the family $\mathcal{H}_0$ and a part $\mathbf{t}' dV_X dV_{X'}$ arising from the deformation of $\mathcal{H}_0'$. In this state-based formulation, $\underline{\mathbf{t}}$ and $\underline{\mathbf{t}}'$ are called the pairwise force density vector states. With an external body force density $\rho_0\tilde{\mathbf{b}}$, the relation of inner, inertia and external forces leads to the peridynamic linear momentum balance

$$-\int_{\mathcal{H}_0} (\mathbf{t} - \mathbf{t}')\ d\mathcal{H}_0 + \rho_0 \left(\ddot{\mathbf{u}} - \tilde{\mathbf{b}}\right) = \mathbf{0}\,. \tag{3.11}$$

Analogous to the local momentum balance, the principle of virtual displacements can be applied to equation (3.11) by multiplication with a virtual displacement $\delta\mathbf{u}$ and integration over the region Ω_0 of $\mathcal{B}$:

$$\int_{\Omega_0} \left[-\int_{\mathcal{H}_0} (\mathbf{t} - \mathbf{t}')\ d\mathcal{H}_0 + \rho_0 \left(\ddot{\mathbf{u}} - \tilde{\mathbf{b}}\right)\right] \cdot \delta\mathbf{u}\, d\Omega_0 = 0\,. \tag{3.12}$$

For the derivation of a correspondence formulation that allows the usage of local material models, it is more convenient to rewrite equation (3.12). Taking into account that the pairwise force densities $\mathbf{t}$ and $\mathbf{t}'$ are zero outside the scope of family $\mathcal{H}_0$, the family integral can be extended to Ω_0, the indices changed $(\ ) \leftrightarrow (\ )'$ and the integral again reduced to $\mathcal{H}_0$:

$$\begin{aligned}
\int_{\Omega_0} \left[-\int_{\Omega_0} (\mathbf{t}\cdot\delta\mathbf{u} - \mathbf{t}'\cdot\delta\mathbf{u})\ d\Omega_0 + \rho_0 \left(\ddot{\mathbf{u}} - \tilde{\mathbf{b}}\right)\cdot\delta\mathbf{u}\right]\ d\Omega_0 &= 0 \\
\int_{\Omega_0} \left[-\int_{\Omega_0} (\mathbf{t}'\cdot\delta\mathbf{u}' - \mathbf{t}'\cdot\delta\mathbf{u})\ d\Omega_0 + \rho_0 \left(\ddot{\mathbf{u}} - \tilde{\mathbf{b}}\right)\cdot\delta\mathbf{u}\right]\ d\Omega_0 &= 0 \\
\int_{\Omega_0} \left[-\int_{\mathcal{H}_0} \mathbf{t}'\cdot(\delta\mathbf{u}' - \delta\mathbf{u})\ d\mathcal{H}_0 + \rho_0 \left(\ddot{\mathbf{u}} - \tilde{\mathbf{b}}\right)\cdot\delta\mathbf{u}\right]\ d\Omega_0 &= 0
\end{aligned} \tag{3.13}$$

or alternatively by means of the same procedure (cf. MADENCI & OTERKUS (2016a))

$$\int_{\Omega_0} \left[\int_{\mathcal{H}_0} \mathbf{t}\cdot(\delta\mathbf{u}' - \delta\mathbf{u})\ d\mathcal{H}_0 + \rho_0 \left(\ddot{\mathbf{u}} - \tilde{\mathbf{b}}\right)\cdot\delta\mathbf{u}\right]\ d\Omega_0 = 0\,. \tag{3.14}$$

The conservation of angular momentum for non-polar peridynamic materials is fulfilled locally, provided that the resulting moment of each force state vanishes (see SILLING ET AL. (2007)):

$$\int_{\mathcal{H}_0} \Delta\mathbf{x} \times \mathbf{t}\, d\mathcal{H}_0 = 0\,. \tag{3.15}$$

3.3 Peridynamic constitutive models

Besides the non-local kinematics and balance laws, the constitutive response needs to be defined. Instead of a locally defined strain energy density function, the peridynamic momentum equation allows directly the consideration of non-local effects by defining the strain energy density function with respect to peridynamic states. Generally, with a non-local strain energy density function $\hat{W}\left(\underline{\Delta\mathbf{x}}\right)$, the pairwise force density state computes as the derivative of $\hat{W}$ with respect to $\underline{\Delta\mathbf{x}}$:

$$\underline{\mathbf{t}} = \frac{\partial \hat{W}}{\partial \underline{\Delta \mathbf{x}}} \,. \tag{3.16}$$

Dependent on the relation and direction of $\mathbf{t} = \underline{\mathbf{t}}\,(X)$, it is distinguished between three different types of materials: In a bond-based material, the pairwise force densities only depend on the deformation of the corresponding bond ($\mathbf{t} = \mathbf{t}\,(\Delta\mathbf{x})$). State-based materials additionally consider the deformation of the entire family ($\mathbf{t} = \mathbf{t}\,(\underline{\Delta \mathbf{x}})$). While in ordinary state-based materials, the force density vector $\mathbf{t}$ shows in the same direction as the current bond $\Delta\mathbf{x}$, which fulfills the local angular momentum balance (3.15) a priori, in non-ordinary state-based materials, the direction of $\mathbf{t}$ can be arbitrary. An elastic bond-based peridynamic strain energy density function $\hat{W}$ can be set up by the composition of spring-like micro-potentials w of each of the bonds within a family (see e.g. BOBARU ET AL. (2016)):

$$\hat{W} = \int_{\mathcal{H}_0} \frac{1}{2} w \; d\mathcal{H}_0 \quad \text{with} \quad w = \frac{1}{2} C e^2 \,. \tag{3.17}$$

Here the $1/2$ in the assembled strain energy density potential comes from the separation of the bond strain energy to both families of the two concerning particles. e measures the lengthening of the bond (see equation (3.8)) and C is a material parameter. The calibration of C can be done by equating the strain energy density with the one of a local linear elastic model (equation (2.45)) for a homogeneous deformation. This results for the non-discretized interior apart from the influence of the surface in three dimensions in

$$C = \frac{45K}{2\pi\delta^5} \,. \tag{3.18}$$

with the horizon or radius δ of a spherical neighborhood. From the fact, that only one material parameter is used, an implicit assumption is included, that restricts the Poisson's ratio to $\nu = 0.25$ in 3-D. A more general modeling approach can be gained via an ordinary state-based formulation by utilizing the isotropic deviatoric decomposition of the scalar extension state of equations (3.8) to (3.10). Accordingly, the peridynamic strain energy density potential (cf. SILLING ET AL. (2007) and LE ET AL. (2014)) writes

$$\hat{W} = \frac{K}{2}\hat{\theta}^2 + \frac{\alpha}{2}\left(\underline{\omega}\underline{e}_d\right) \bullet \underline{e}_d \tag{3.19}$$

with the bulk modulus K and a peridynamic shear modulus α. Again, a calibration of α can be done by means of a comparison of strain energy within homogeneous deformation which yields in the interior with the shear modulus μ and the weighted volume m

$$\alpha = \frac{15\mu}{m} \,. \tag{3.20}$$

As a consequence of the split of the extension state, the resulting force density decouples to

$$\mathbf{t} = (t_i + t_d)\,\frac{\Delta\mathbf{x}}{|\Delta\mathbf{x}|} \quad \text{with} \quad t_i = \frac{\partial \hat{W}}{\partial e_i} \quad \text{and} \quad t_d = \frac{\partial \hat{W}}{\partial e_d} \,. \tag{3.21}$$

Since the isotropic part of the pairwise force-density depends on the averaged peridynamic dilation $\hat{\Theta}$, strain energy (3.19) corresponds to a state-based material. Further, the direction

$\Delta\mathbf{x}/|\Delta\mathbf{x}|$ of the pairwise bond force density $\mathbf{t}$ makes it an ordinary state-based material.

The development of non-locally defined peridynamic constitutive models has been an active research area since the last decade (cf. Javili et al. (2018)). Among other works, a selection of progressing approaches include higher gradient expansions in Šilhavý (2017), a state-based plasticity (Madenci & Oterkus (2016b)) and viscoplasticity Foster et al. (2010) model and the peridynamic crystal plasticity model of Sun & Sundararaghavan (2014).

3.4 Correspondence theory

Next to constitutive models that depend directly on the non-local kinematics, local material models can be adopted for the peridynamic momentum equation (Silling et al., 2007). Therefore, the peridynamic reduction operation (see equation (3.7)) is classically used to average the current bond vector state to a second order tensor, the averaged deformation gradient $\bar{\mathbf{F}}$. With this, a strain energy function of the local continuum mechanics theory $W\left(\bar{\mathbf{F}}\right)$ can be applied to define the stress response in terms of the averaged first Piola-Kirchhoff stress $\bar{\mathbf{P}}$. Finally, the second order stress tensor has to be redistributed to the pairwise force density state which can be done, analogous to a peridynamic material model, via the derivative with respect to the current bond vector state:

$$\underline{\mathbf{t}}\left(\mathbf{P}\left(\bar{\mathbf{F}}\right)\right) = \frac{\partial W\left(\bar{\mathbf{F}}\right)}{\partial \underline{\Delta\mathbf{x}}} = \frac{\partial W\left(\bar{\mathbf{F}}\right)}{\partial \bar{\mathbf{F}}} : \frac{\partial \mathcal{R}\left\{\underline{\Delta\mathbf{x}}\right\}}{\partial \underline{\Delta\mathbf{x}}} = \underline{\omega}\bar{\mathbf{P}} \cdot \mathbf{K}^{-1} \cdot \underline{\Delta\mathbf{X}}\,, \tag{3.22}$$

where the chain rule was applied and the averaged deformation gradient (3.7) inserted. This so-called correspondence formulation leads to a generally non-ordinary state-based model that still conserves the angular momentum balance in accordance with equation (3.15) (see Silling et al. (2007)). Though flexible, the correspondence formulation suffers from low-energy modes that manifest in oscillations in a numerical setting (see e.g. Littlewood et al. (2012)).

Chapter 4

Peridynamic Galerkin methods

The correspondence formulation of equation (3.22) is the underlying principle for the further derivation of the Peridynamic Galerkin methods. Thereby, the integral over a family is discretized in a finite sum of collocated particles. In a generalized Galerkin framework, this yields a powerful unified particle method that reduces, on the one hand, to the classical peridynamic correspondence formulation or rather the corrected SPH. On the other hand, a strong relationship to other well established Galerkin methods as the FEM is produced.

In the FEM, the region Ω_0 is separated into adjacent elements and numerically integrated at Gauß points. The shape functions can be defined on a reference configuration for a fixed set of nodes, dependent on the element formulation, and isoparametrically mapped into the initial or current configuration. Instead of elements, the PG methods utilize non-conforming and overlapping families or rather neighborhoods, generally consisting of an arbitrary number of nodes. Therefore, the discretization is more flexible for the cost of higher complexity. Further, in place of Gauß points and nodes, the neighbor particles serve as integration points, as well as nodal points for the meshfree shape functions.

Within this chapter, a detailed description on the development of PG methods is given, subdivided into the following main aspects: First, the underlying spatial particle discretization together with an explanation of the discrete notation is presented in section 4.1. In section 4.2, the relation of discrete peridynamic states and their corresponding local quantities is discussed. Thereby, the classical discrete correspondence formulation is reviewed and more general shape function based approaches, bridging peridynamic and local measures, are presented that lead to the discretized weak form of the PG methods. Following, section 4.3 addresses the treatment of Dirichlet and Neumann boundary conditions. The explicit and implicit temporal discretization is performed in section 4.4. The linearization of the variational formulation as well as three different linearization procedures for implicit analyses, namely the finite difference approximation, a consistent linearization and the automatic symbolic differentiation, are presented in sections 4.5 and 4.6. Finally, section 4.7 deals with local strong form preservation properties.

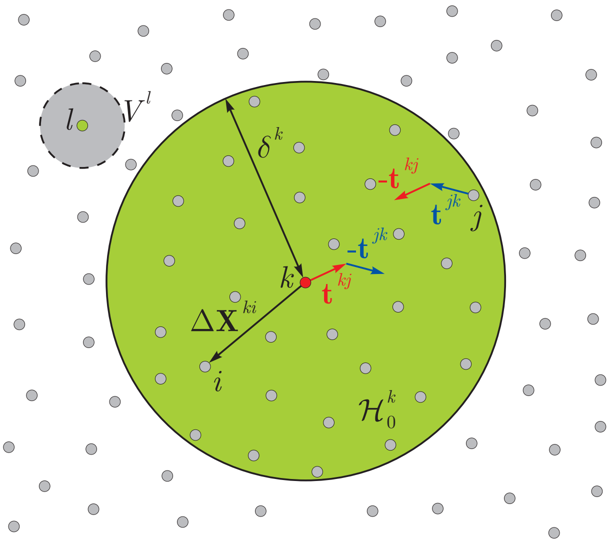

Figure 4.1. Particle discretization with the discrete connectivity and pairwise force densities acting between master particle k and its neighborhood $\mathcal{H}_0^k$.

4.1 Particle discretization

The basis for the PG methods is the particle discretization which establishes the meshfree character. Analogous to chapters 2 and 3, the region Ω_0 is separated into particles carrying the displacement $\mathbf{u}$ as the primary variable. Instead of infinitesimal particles, the spatial discretization yields a finite number of n^p discrete particles with associated volumes V and densities ρ_0. Starting from a particle k, further called master particle, the connectivity to its surrounding region is build up by the discrete family (or neighborhood) $\mathcal{H}_0^k$, consisting of a number of N^k neighbor particles (see illustration in Figure 4.1). With the collocation of the particle discretization, the integral relations from the previous chapters turn into assemblies or rather sums. A global integral over Ω_0 is therefore assembled via all n^p particle contributions and an integral over $\mathcal{H}_0^k$ is expressed as a sum on the family level:

$$\begin{aligned} \int_{\Omega_0} (\,)\ d\Omega_0 \quad &\rightarrow \quad \mathop{\mathrm{A}}_{k=1}^{n^p} \left\{ (\,)^k\, V^k \right\} \quad \text{and} \\ \int_{\mathcal{H}_0^k} (\,)\ d\mathcal{H}_0^k \quad &\rightarrow \quad \sum_{i=0}^{N^k} (\,)^i\, V^i \,, \end{aligned} \tag{4.1}$$

where $\mathop{\mathrm{A}}\limits_{k=1}^{n^p} \{\,\}$ is the assembling operator over all particles. Index $i = 0$ denotes the master particle k and all $i \neq 0$ correspond to its neighbors. Hence, when the sum $\sum_{i=1}^{N^k}$ is used, the master particle is excluded. The discrete kinematic description is made of the collective bond vectors, stored in a container, the discretized state:

$$\Delta\mathbf{X}^{kj} = \mathbf{X}^j - \mathbf{X}^k \rightarrow \underline{\Delta\mathbf{X}}^k = \begin{pmatrix} \Delta\mathbf{X}^{k0} \\ \Delta\mathbf{X}^{k1} \\ \vdots \\ \Delta\mathbf{X}^{kN^k} \end{pmatrix}. \tag{4.2}$$

In the further thesis, a single superscript refers to a quantity related to a single particle or the family of a single particle. Accordingly, $\mathbf{X}^k$ describes the position of the discrete particle k and $\underline{\Delta\mathbf{X}}^k$ stands for the discrete initial bond vector state of the family $\mathcal{H}_0^k$ of particle k. Furthermore, the combination of Δ with a double superscript, as $\Delta\mathbf{X}^{kj}$, expresses a difference with respect to the first superscript. Note, that when a double superscript is used without a Δ, like e.g. the pairwise force density $\mathbf{t}^{kj}$ or the deformation gradient $\mathbf{F}^{kj}$, this expresses generally not a difference. Instead, the first superscript belongs to a master particle that specifies the family and the second one determines the point of evaluation. Thus, $\mathbf{F}^{kj}$ expresses the deformation gradient at position $\mathbf{X}^j$ from the perspective of family $\mathcal{H}_0^k$. In the definition of shape functions, a third superscript arises that will be explained in the next section.

The underlying particle distribution can be generated in several ways (cf. CHOI & KIM (1999), KLAAS & SHEPHARD (1999), LI ET AL. (2000b) and LI ET AL. (2000a)). In peridynamics, a common approach consists in separating the region Ω_0 into (regularly structured) elements. The particle positions and volumes are then the centroids and volumes of each corresponding element. As a result, no particle is located directly on the surface of Ω_0, which makes the imposition of boundary conditions more cumbersome and less accurate in the context of correspondence models (see section 4.3). Alternatively, the particle positions and associated volumes can be gained from the nodes of a FE mesh. While the positions are predetermined by the nodal ones, their volume has to be determined by means of a lumping strategy, like e.g. row summation or nodal quadrature (see ZIENKIEWICZ ET AL. (2005)). Next to a comfortable imposition of boundary conditions, this yields the possibility to straightforwardly couple a meshfree domain with an adjacent mesh-based domain by connecting their nodes. For this purpose, the meshfree shape functions have to meet certain criteria to accomplish a smooth transition, which will be addressed in chapter 5.

While in FE methods, the shape functions on each element are defined by a specific number of nodes, PG methods use an arbitrary number of particles for their construction and hence, the shape of a family is flexible. When peridynamic constitutive models including non-local effects are used, the size can be determined by the horizon δ^k as the largest length scale on which non-local effects are present. In the utilization of local models within the PG methods, the non-local approach is aimed to be the basis for a versatile particle method, where in the limiting refinement case, the local model should be reached. Hence, with decreasing average particle spacing $\bar{h}$, the support of the neighborhood can be set proportional to $\bar{h}$. Typically, a horizon between $\delta^k = 1.51\bar{h}$ and $\delta^k = 3.01\bar{h}$ is chosen.

Spherical neighborhoods with a globally constant horizon ensure a pairwise connectivity, which means, each particle j inside family $\mathcal{H}_0^k$ has particle k in its own family $\mathcal{H}_0^j$. With irregular or partially refined particle patterns a globally fixed horizon can lead to a large number of neighbor particles in fine regions and therefore to an increased computational cost. One possibility is, to define dual-families to allow a varying horizon size (see REN ET AL. (2016) and REN ET AL. (2017)). However, the PG methods are not restrictive to spherical family shapes when based on the weak forms or a potential as later defined and collected in Table 4.1. In this work, two other possibilities are pursued. The first one, consists in a nearest neighbor search algorithm. Thereby, a family is made up of the master particle and its nearest N^k neighbor particles. To ensure pairwisity (which is not necessarily needed in PG methods), all particles j, that have particle k in their family $\mathcal{H}_0^j$ and are not part of the nearest N^k neighbors of particle k, can be added to the family $\mathcal{H}_0^k$. While for a reduced computational cost, a small number of neighbor particles is desired, a minimal number of neighbors is usually specified by the number of regression coefficients of the meshfree shape functions (see section 5.2.2). A second promising approach employs the FE discretization of which the particles are collocated. Here, the collection of nodes or rather particles belonging to the adjacent elements of a master particle form its family.

4.2 Bridging peridynamic and local quantities

As outlined in section 3.4, the application of constitutive models from the local theory within the peridynamic momentum equation requires the formulation of two bridges between the non-local measures and its local counterparts – the correspondence formulation. First, the non-local kinematics have to be related to the deformation gradient. More precisely in a discrete setting, the discrete current bond vector state $\underline{\Delta \mathbf{x}}^k$ has to be transferred into a deformation gradient $\bar{\mathbf{F}}^k$. Once the constitutive response is calculated in form of the first Piola-Kirchhoff stress $\bar{\mathbf{P}}^k$, a back-distribution has to convert the local stress tensor into the discrete pairwise force density vector state $\underline{\mathbf{t}}^k$. Classically, the first bridge is build by the discrete peridynamic reduction operation. The second one can be gained on several ways, whereby one of which is equating the peridynamic and local discrete virtual work of internal forces. In the following, the classical correspondence formulation is stated, and its proneness for low-energy modes is analyzed. Subsequently, more general shape function based correspondence formulations are presented, resulting in the discrete weak form of the PG methods.

4.2.1 Classical correspondence formulation

In the classical correspondence formulation, the peridynamic reduction (equation (3.7)) defines an averaged deformation gradient within a family. When the particle discretization is performed with equation (4.1), the discretized averaged deformation gradient yields

$$\bar{\mathbf{F}}^k = \mathcal{R}\{\underline{\Delta\mathbf{x}}^k\} = \left(\underline{\Delta\mathbf{x}}^k * \underline{\Delta\mathbf{X}}^k\right)\cdot\mathbf{K}^{k^{-1}} = \left(\sum_{j=0}^{N^k}\omega^{kj}\Delta\mathbf{x}^{kj}\otimes\Delta\mathbf{X}^{kj}V^j\right)\cdot\mathbf{K}^{k^{-1}}\,, \tag{4.3}$$

where the symmetric discrete shape tensor $\mathbf{K}^k$ computes from equations (3.5), (3.6) and (4.1) to the outer product of the discrete initial bond vector state with itself:

$$\mathbf{K}^k = \underline{\Delta\mathbf{X}}^k * \underline{\Delta\mathbf{X}}^k = \sum_{j=0}^{N^k}\omega^{kj}\Delta\mathbf{X}^{kj}\otimes\Delta\mathbf{X}^{kj}V^j\,. \tag{4.4}$$

To improve the locality of the averaged deformation gradient, a weight function (kernel) ω can be defined. Commonly, a radial weight function depending on the length of the reference bonds is used, as e.g.

$$\omega^{kj} = \begin{cases} \frac{1}{\left|\Delta\mathbf{X}^{kj}\right|^2} & \forall\, j \neq k \\ 0 & \forall\, j = k \end{cases}\,. \tag{4.5}$$

For regular particle patterns, special integration rules can alternatively be adopted to get a higher order accuracy of the discretized shape tensor and averaged deformation gradient (see YAGHOOBI & CHORZEPA (2017)). Finally, the pairwise force relation discretizes from equation (3.22) to

$$\mathbf{t}^{kj} = \omega^{kj}\bar{\mathbf{P}}^k\cdot\mathbf{K}^{k^{-1}}\cdot\Delta\mathbf{X}^{kj}\,. \tag{4.6}$$

With this linking of local and non-local measures, the resulting non-ordinary state based peridynamic method (WARREN ET AL. (2009)) is a flexible meshfree method that can handle the whole range of local material models. However, in practice, the classical correspondence formulation suffers from low-energy modes that pollute the displacement field and make the solution without further treatment useless. Next to other interpretations of this phenomenon, it can be attributed to the surjectiveness of the peridynamic reduction operation, which is further discussed.

As the use of peridynamic material models, directly depending on non-local kinematics, does not generally lead to low-energy modes, the critical point in the correspondence formulation becomes evident: During the two bridging operations between local and non-local measures, i.e. between $\underline{\Delta\mathbf{x}}^k \to \bar{\mathbf{F}}^k$ and $\bar{\mathbf{P}}^k \to \underline{\mathbf{t}}^k$, the low-energy modes arise. If both operations (equations (4.3) and (4.6)) are analyzed, it shows, that in the computation of an averaged deformation gradient, a loss of information takes place which can not be restored by the re-distribution into pairwise force densities. Mathematically, this information loss can be seen as an inadmissible linearization of the non-linear mapping of a family by means of a single second order tensor, yielding a surjective operation (see Figure 4.2). In comparison with the FEM, such an information loss occurs when elements that allow more than linear deformation modes are averaged or rather underintegrated, which results in a rank deficient element stiffness matrix with spurious zero-energy modes. The understanding

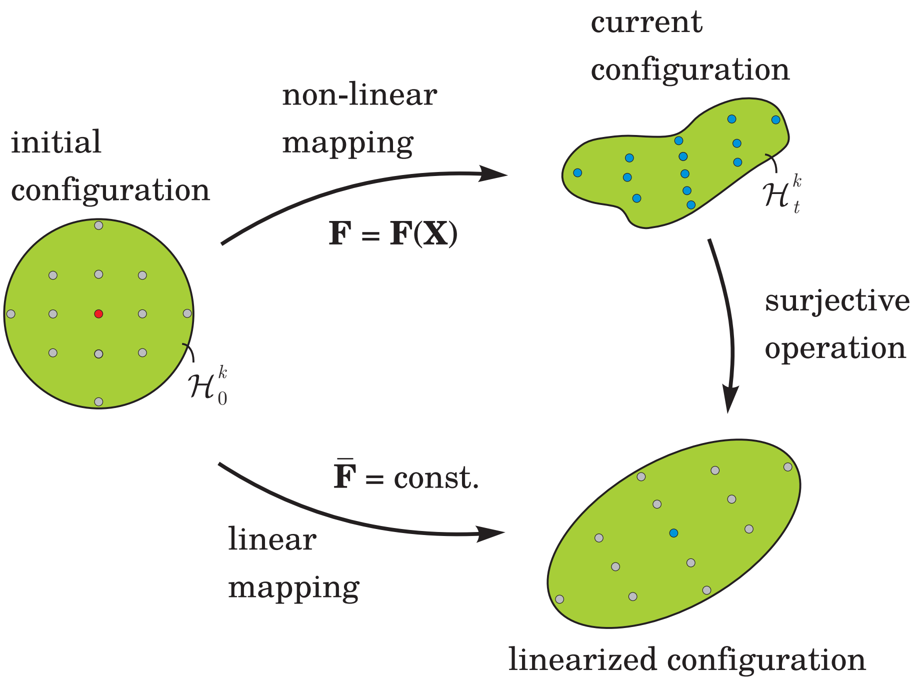

Figure 4.2. The linearization of the generally non-linear mapping of the deformation of $\mathcal{H}_0^k$ using a constant locally averaged deformation gradient $\bar{\mathbf{F}}$ leads as a surjective operation to a loss of information. Blue colored particles denote the points of evaluation.

of a single family as an overlapping kind of element provides an explanation why the low-energy modes in the classical correspondence formulation are present: If there is a more general higher order correspondence formulation, the rank deficiency will result either from an underintegration, an insufficient approximation basis or both.

4.2.2 From states to tensors: A general shape function approach

Following the considerations of section 4.2.1 with Figure 4.2, there are a couple of possibilities of how the mapping of a family from the initial to the current configuration can be done more appropriately. Since the difference between the initial and current configuration consists of the displacement of each particle, an approximation of this displacement field within the family may be performed by means of a Taylor series expansion with respect to the master particle's position $\mathbf{X}^k$:

$$\mathbf{u}\left(\Delta\mathbf{X}^{kj}\right) = \mathbf{u}^k + \left.\frac{\partial \mathbf{u}}{\partial \mathbf{X}}\right|^k \cdot \Delta\mathbf{X}^{kj} + \frac{1}{2}\left.\frac{\partial^2 \mathbf{u}}{\partial \mathbf{X}\partial \mathbf{X}}\right|^k : \Delta\mathbf{X}^{kj} \otimes \Delta\mathbf{X}^{kj} + \mathcal{O}\left(\Delta\mathbf{X} \otimes \Delta\mathbf{X} \otimes \Delta\mathbf{X}\right) , \tag{4.7}$$

where the expansion was terminated after the second derivatives. Note, that the termination after the first derivatives actually yields a linear approximation as done by the peridynamic reduction. Similarly to the Taylor series expansion, a regression analysis of the family displacement field could be executed. In here, already a set of basis functions (e.g. $(1, X, X^2)$ in 1-D) is used to fit the real displacement field by optimizing their coefficients. A more general approach, in which the upper ones can be unified, consists in the classical Galerkin shape function ansatz with respect to the master particle's position $\mathbf{X}^k$:

$$\mathbf{u}^{kj} = \mathbf{u}^k\left(\mathbf{X}^j\right) = \sum_{i=0}^{N^k} \mathbf{u}^i N^{kji} \,. \tag{4.8}$$

$\mathbf{u}^{kj}$ denotes the displacement at the position of particle j, approximated in the family of particle k, consistent with the notation described in section 4.1. In the triple index of the shape function N^{kji}, the first index stands for the family in which the shape functions are constructed, i.e. $\mathcal{H}_0^k$. Index j identifies the point of evaluation $\mathbf{X}^j$ and the third index marks the particle that is the supporting grid point of the shape function. For a closer relation to the non-local kinematics of bonds ($\Delta\mathbf{x}^{kj} = \Delta\mathbf{X}^{kj} + \Delta\mathbf{u}^{kj}$), the approximation can also be stated with respect to differences:

$$\mathbf{u}^{kj} - \mathbf{u}^k = \sum_{i=0}^{N^k} \Delta\mathbf{u}^{ki} N^{kji} \,. \tag{4.9}$$

A description of the deformation of family $\mathcal{H}_0^k$ that is invariant to rigid body translations results from the derivative of equation (4.9) as the displacement gradient with respect to the initial configuration

$$\frac{\partial \mathbf{u}^{kj}}{\partial \mathbf{X}} = \sum_{i=0}^{N^k} \Delta\mathbf{u}^{ki} \otimes \frac{\partial N^{kji}}{\partial \mathbf{X}} \,. \tag{4.10}$$

The position-dependent deformation gradient, required for the application of a material model from the local continuum mechanics theory, can therefore be expressed as a function of the deformed bond vector state and computes

$$\mathbf{F}^{kj} = \sum_{i=0}^{N^k} \Delta\mathbf{x}^{ki} \otimes \frac{\partial N_{\mathbf{u}}^{kji}}{\partial \mathbf{X}} \,, \tag{4.11}$$

where the shape functions $N_{\mathbf{u}}^{kji}$, marked with $(\ )_{\mathbf{u}}$, are called trial shape functions. Analogously, the virtual displacement gradient can be defined with respect to the virtual displacements $\delta\mathbf{u}$:

$$\delta\mathbf{F}^{kj} = \sum_{i=0}^{N^k} \Delta\delta\mathbf{u}^{ki} \otimes \frac{\partial N_{\delta\mathbf{u}}^{kji}}{\partial \mathbf{X}} \,. \tag{4.12}$$

Index $(\ )_{\delta\mathbf{u}}$ indicates the approximation of the virtual displacement gradient with the so-called test shape functions $N_{\delta\mathbf{u}}^{kji}$. Generally, the trial and test shape functions do not have to match and, in fact, the requirements that each of them should fulfill are different which will be discussed in chapter 5. The approximation of equations (4.11) and (4.12) are quite general and the locally averaged peridynamic deformation gradient, resulting from the reduction operation, can be restored by a special choice of shape functions as demonstrated in section 5.2. Note, that with the upper definition, $\mathbf{F}^{kj}$ is generally not the same as $\mathbf{F}^{jj}$, even if it denotes the deformation gradient at the position of particle j, the family in which the approximation is made differs. This shows that the resulting global approximation is non-conforming. In contrast, in case of the classical peridynamic reduction, $\mathbf{F}^{kj}$ is equal to $\mathbf{F}^{kk}$ as there is a constant deformation gradient per family.

4.2.3 Inverse non-local averaging

Now, the second relation between local and non-local measures, i.e. the dependency $\underline{\mathbf{t}}^k = \underline{\mathbf{t}}\left(\bar{\mathbf{P}}^k\right)$, is addressed. In the classical correspondence formulation of equation (4.6), the pairwise force density state depends only on a single stress tensor, averaged around master particle k. As already mentioned, this correlates with a loss of information towards the peridynamic deformation vector state. Hence, to enable the benefit of a variable approximation of the deformation gradient field inside family $\mathcal{H}_0^k$, a more general expression for this relation, like $\underline{\mathbf{t}}^k = \underline{\mathbf{t}}\left(\underline{\mathbf{P}}\right)$, is needed that includes changing stresses or rather the first Piola-Kirchhoff stress tensor state $\underline{\mathbf{P}}^k$, consisting of the collective $\mathbf{P}^{kj}\ \forall j \in \mathcal{H}_0^k$. In the following, two generalized correspondence formulations are derived via a comparison of the discrete local and peridynamic virtual work of internal forces, resulting in the Peridynamic Petrov-Galerkin (PPG) and Peridynamic Bubnov-Galerkin (PBG) methods. Therefore, the particle discretization (equation (4.1)) has to be applied to equations (2.57) and (3.13) or rather (3.14), yielding respectively the discretized weak form of the local and peridynamic linear momentum balance

$$\delta U_h = \mathop{\mathbf{A}}_{k=1}^{n^p} \left\{ \delta W_{int}^k + \left[\rho_0^k V^k \left(\ddot{\mathbf{u}}^k - \bar{\mathbf{b}}^k \right) - A^k \left(\mathbf{P}^k \cdot \mathbf{n}_0^k \right) \right] \cdot \delta \mathbf{u}^k \right\} = 0 \quad \text{and} \tag{4.13}$$

$$\delta U_h = \mathop{\mathbf{A}}_{k=1}^{n^p} \left\{ \delta \hat{W}_{int}^k + \rho_0^k V^k \left(\ddot{\mathbf{u}}^k - \tilde{\mathbf{b}}^k \right) \cdot \delta \mathbf{u}^k \right\} = 0\,. \tag{4.14}$$

Whereby the discrete virtual work of internal forces at particle level computes (see equation (3.13))

$$\delta W_{int}^k = V^k \mathbf{P}^k : \delta \mathbf{F}^k \quad \text{and} \tag{4.15}$$

$$\delta \hat{W}_{int}^k = V^k \sum_{j=0}^{N^k} \mathbf{t}^{kj} \cdot \Delta \delta \mathbf{u}^{kj} V^j = -V^k \sum_{j=0}^{N^k} \mathbf{t}^{jk} \cdot \Delta \delta \mathbf{u}^{kj} V^j = -V^k \sum_{j=0}^{N^k} \left[\mathbf{t}^{kj} - \mathbf{t}^{jk} \right] V^j \cdot \delta \mathbf{u}^k\,. \tag{4.16}$$

Petrov-Galerkin

First, a Petrov-Galerkin type correspondence formulation is derived. Therefore, the Galerkin ansatz for the virtual deformation gradient of equation (4.12) is inserted into the local virtual work of equation (4.15) as $\delta \mathbf{F}^k = \delta \mathbf{F}^{kk}$:

$$\delta W_{int}^{k} = V^{k}\mathbf{P}^{k} : \sum_{i=0}^{N^k} \Delta\delta\mathbf{u}^{ki} \otimes \frac{\partial N_{\delta\mathbf{u}}^{kki}}{\partial \mathbf{X}} \,. \tag{4.17}$$

With an increasing refinement in a nonlinear simulation, the deformation gradient within a family tends to be constant. Therefore, when the same material model is used, the virtual strain energy of the local and peridynamic form have to match for homogeneous deformations to ensure a convergence to the same solution. Equating δW_{int}^{k} and $\delta \hat{W}_{int}^{k}$ leads with the peridynamic description of the virtual work of the right part of equation (4.16) to

$$V^{k}\mathbf{P}^{k} : \sum_{i=0}^{N^k} \Delta\delta\mathbf{u}^{ki} \otimes \frac{\partial N_{\delta\mathbf{u}}^{kki}}{\partial \mathbf{X}} = -V^{k} \sum_{j=0}^{N^k} \mathbf{t}^{jk} \cdot \Delta\delta\mathbf{u}^{kj} V^{j} \,. \tag{4.18}$$

To get an expression for the pairwise force density, the left side can be rearranged in index notation, the summation index changed and extended with $-V^j / -V^j$:

$$V^{k} P_{AB}^{k} \sum_{i=0}^{N^k} \Delta\delta u_{A}^{ki} \frac{\partial N_{\delta\mathbf{u}}^{kki}}{\partial X_B} = -V^{k} \sum_{j=0}^{N^k} \left(-\frac{1}{V^j} P_{AB}^{k} \frac{\partial N_{\delta\mathbf{u}}^{kkj}}{\partial X_B} \right) \Delta\delta u_{A}^{kj} V^{j} \,. \tag{4.19}$$

Going back to symbolic notation, the pairwise force density can be read of

$$-V^{k} \sum_{j=0}^{N^k} \left(-\frac{1}{V^j} \mathbf{P}^{k} \cdot \frac{\partial N_{\delta\mathbf{u}}^{kkj}}{\partial \mathbf{X}} \right) \cdot \Delta\delta\mathbf{u}^{kj} V^{j} = -V^{k} \sum_{j=0}^{N^k} \mathbf{t}^{jk} \cdot \Delta\delta\mathbf{u}^{kj} V^{j} \,. \tag{4.20}$$

Since in the limiting case of homogeneous deformations, the stress is constant, the perspective of the approximation of the stress $\mathbf{P}^k$ at the absolute position $\mathbf{X}^k$ can be changed to the same perspective of the corresponding pairwise force density. Thus, a generalized correspondence formulation, including changing stresses can be written as

$$\mathbf{t}^{jk} = -\frac{1}{V^j} \mathbf{P}^{jk} \cdot \frac{\partial N_{\delta\mathbf{u}}^{kkj}}{\partial \mathbf{X}} \quad \text{or rather} \quad \mathbf{t}^{kj} = -\frac{1}{V^k} \mathbf{P}^{kj} \cdot \frac{\partial N_{\delta\mathbf{u}}^{jjk}}{\partial \mathbf{X}} \,. \tag{4.21}$$

So far, no properties of the test shape functions were applied or analyzed in the derivation. Some specific test function requirements (see chapter 5) will later show to be more easily satisfied with an alternative formulation. Hence, at this point, the test shape functions can be redefined: $\frac{\partial N_{\delta\mathbf{u}}^{kkj}}{\partial \mathbf{X}} \to -\frac{\partial N_{\delta\mathbf{u}}^{jjk}}{\partial \mathbf{X}}$, leading to

$$\mathbf{t}^{kj} = \frac{1}{V^k} \mathbf{P}^{kj} \cdot \frac{\partial N_{\delta\mathbf{u}}^{kkj}}{\partial \mathbf{X}} \,. \tag{4.22}$$

In the upper expressions for the pairwise force densities, the virtual deformation gradient is evaluated only once inside a family, while the actual deformation gradient is evaluated at each neighbor particle. This leads generally, i.e. in the case of nonlinear shape functions, to a Petrov-Galerkin formulation, resulting in a non-symmetric stiffness matrix. Therefore, the correspondence formulations of equations (4.21) and (4.22) are further denoted as *PPG1* and *PPG2*, respectively.

Bubnov-Galerkin

A correspondence formulation leading to a Bubnov-Galerkin method, provided that the trial and test shape functions coincide ($N_{\mathbf{u}}^{kji} = N_{\delta\mathbf{u}}^{kji} = N^{kji}$), can be derived by the following idea of smoothing the stress power by means of a least square minimization:

$$\min\left[\int_{\mathcal{H}_0^k}\left(\mathbf{P}^k : \delta\mathbf{F}^k - \mathbf{P} : \delta\mathbf{F}\right)^2 \, d\mathcal{H}_0^k\right] . \tag{4.23}$$

By taking the derivative with respect to $\mathbf{P}^k : \delta\mathbf{F}^k$, it motivates the transformation

$$\mathbf{P}^k : \delta\mathbf{F}^k \to \frac{1}{V^{\mathcal{H}_0^k}} \int_{\mathcal{H}_0^k} \mathbf{P} : \delta\mathbf{F} \, d\mathcal{H}_0^k \, . \tag{4.24}$$

Applied to the discrete virtual work of internal forces at particle level, this yields

$$\delta W_{int}^k = V^k \mathbf{P}^k : \delta\mathbf{F}^k \approx \frac{V^k}{V^{\mathcal{H}_0^k}} \sum_{j=0}^{N^k} \mathbf{P}^{kj} : \delta\mathbf{F}^{kj} V^j \tag{4.25}$$

which can also be seen as a reverse averaging within the family $\mathcal{H}_0^k$. Note, that the conversion is accurate in the limiting case of a homogeneous deformation, where the deformation gradient, as well as the stresses are constant. The volume $V^{\mathcal{H}_0^k}$ of $\mathcal{H}_0^k$ thereby computes as the sum of all particle contributions

$$V^{\mathcal{H}_0^k} = \sum_{j=0}^{N^k} V^j \, . \tag{4.26}$$

Again, the discrete virtual strain energy (4.25) can be equated with its peridynamic form of the left-hand side of equation (4.16):

$$\frac{V^k}{V^{\mathcal{H}_0^k}} \sum_{j=0}^{N^k} \mathbf{P}^{kj} : \delta\mathbf{F}^{kj} V^j = V^k \sum_{j=0}^{N^k} \mathbf{t}^{kj} \cdot \Delta\delta\mathbf{u}^{kj} V^j \, . \tag{4.27}$$

By insertion of the virtual displacement gradient (4.12) into the left part with a change of indices, it can be rearranged in index notation to

$$\frac{V^k}{V^{\mathcal{H}_0^k}} \sum_{i=0}^{N^k} P_{AB}^{ki} \delta F_{AB}^{ki} V^i = V^k \sum_{j=0}^{N^k} \frac{1}{V^j V^{\mathcal{H}_0^k}} \sum_{i=0}^{N^k} P_{AB}^{ki} \frac{\partial N_{\delta\mathbf{u}}^{kij}}{\partial X_B} V^i \Delta\delta u_A^{kj} V^j \, . \tag{4.28}$$

Hence, equation (4.27) rewrites

$$V^k \sum_{j=0}^{N^k} \left(\frac{1}{V^j V^{\mathcal{H}_0^k}} \sum_{i=0}^{N^k} V^i \mathbf{P}^{ki} \cdot \frac{\partial N_{\delta\mathbf{u}}^{kij}}{\partial \mathbf{X}} \right) \cdot \Delta\delta\mathbf{u}^{kj} V^j = V^k \sum_{j=0}^{N^k} \mathbf{t}^{kj} \cdot \Delta\delta\mathbf{u}^{kj} V^j \, . \tag{4.29}$$

Therefore, the pairwise force density can be expressed as

$$\mathbf{t}^{kj} = \frac{1}{V^j V^{\mathcal{H}_0^k}} \sum_{i=0}^{N^k} V^i \mathbf{P}^{ki} \cdot \frac{\partial N_{\delta \mathbf{u}}^{kij}}{\partial \mathbf{X}} \,, \tag{4.30}$$

which leads to a Bubnov-Galerkin formulation of the internal forces, further denoted as *PBG* formulations, and results for of hyperelastic material behavior to a symmetric global tangent stiffness matrix.

4.3 Treatment of boundary conditions

Compared to the mesh-based FEM, the imposition of Dirichlet and Neumann boundary conditions requires an increased attention within meshfree particle methods and has been suspect to extensive research in the past. Further, an incomplete overview of techniques for the imposition of both is given. Generally, it is possible to impose the boundary conditions almost analogously to mesh-based methods, if certain conditions on the shape functions are fulfilled which will be addressed in chapter 5.

4.3.1 Dirichlet boundaries

Concerning the essential (Dirichlet) boundaries, several classes of methodologies are present (FRIES ET AL., 2003). One of them consists in a modification of the weak form by adding a term that enforces the boundary conditions weakly. These include the Lagrangian multiplier method (see e.g. BELYTSCHKO ET AL. (1996) and BREZZI (1974)), the penalty method (see e.g. ZHU & ATLURI (1998) and FERNÁNDEZ-MÉNDEZ & HUERTA (2004)) and the Nitsche's method (cf. NITSCHE (1971)). Alternatively, the Dirichlet boundary conditions can be strongly imposed via shape functions that posses the Kronecker delta or rather Lagrange property. Therefore, the meshfree domain can either be coupled to Finite Elements on which the essential boundary conditions are imposed (see BELYTSCHKO ET AL. (1995) and HUERTA ET AL. (2004a)) or the Kronecker delta property has to be recovered. This can be done by means of a transformation method (cf. CHEN ET AL. (1997), CHEN & WANG (2000) and LI & LIU (2002)), the use of generalized variables via D'Alembert's principle (GÜNTHER & LIU (1998)) or using singular weighting functions in the construction of Moving Least Square shape functions (see LANCASTER & SALKAUSKAS (1981), KALJEVIĆ & SAIGAL (1997) and WU (2014)).

Within this work, the direct nodal imposition of the Dirichlet boundaries is further used. In case the particle distribution is governed by the collocation of a FE mesh (see section 4.1), it is sufficient to fulfill the Kronecker delta property of the shape functions related to the nodes that are directly on the Dirichlet boundary. Alternatively, but less accurate, additional rows of wall particles can be incorporated to account for discretizations where particles do not lie directly on the boundary or to improve the behavior for shape functions that lack the Kronecker delta property. In section 5.2.2, a special sort of meshfree shape functions will be presented, based on a concept of a moving Taylor series expansion, that allows a nodal imposition by satisfying the Kronecker delta property.

4.3.2 Neumann boundaries

By investigating the discrete classical and peridynamic weak forms (4.13) and (4.14) it stands out that the stress boundaries on the surface do not have a counterpart in the peridynamic form. Hence, the external forces have to be converted into volumetric forces acting on a particle layer near the surface. Therefore, an additional layer of particles, not part of the discretization of region Ω_0, can be added (cf. MADENCI & OTERKUS (2016a)). The surface forces act then as resulting internal forces between the additional particle layer and the particles within the discretized body. Alternatively, the Neumann boundaries can be imposed on the particles lying directly on the surface (e.g. by means of a collocated FE mesh). By equating the external forces of (4.13) and (4.14) on particle level,

$$-\rho_0^k V^k \tilde{\mathbf{b}}^k = -\rho_0^k V^k \overline{\mathbf{b}}^k - A^k \mathbf{P}^k \cdot \mathbf{n}_0^k \, , \tag{4.31}$$

the external volumetric force density acting on a particle on the Neumann boundary is composed of two parts, truly volumetric ones like the gravity and converted ones:

$$\tilde{\mathbf{b}}^k = \overline{\mathbf{b}}^k + \tilde{\mathbf{s}}^k \quad \text{with} \quad \tilde{\mathbf{s}}^k = \frac{1}{\rho_0^k V^k} \mathbf{P}^k \cdot \mathbf{A}^k \tag{4.32}$$

where $\tilde{\mathbf{s}}^k$ denotes the additional equivalent volume force density. To ensure a consistent imposition of the Neumann boundaries, the nodal outer surface normal with respect to the initial configuration $\mathbf{A}^k = A^k \mathbf{n}_0^k$ has to be in agreement with the discrete form of Gauß's theorem (see also WEISSENFELS (2019)). This is accomplished, if the condition for linear variational consistency is utilized (which is suspect to chapter 5) and computes for the correspondence formulations (4.21), (4.22) and (4.30) as

$$\text{PPG1}: \quad \mathbf{A}^k = \sum_{j=0}^{N^k} V^j \frac{\partial N_{\delta\mathbf{u}}^{jjk}}{\partial \mathbf{X}} - \sum_{j=0}^{N^k} V^k \frac{\partial N_{\delta\mathbf{u}}^{kkj}}{\partial \mathbf{X}} \, , \tag{4.33}$$

$$\text{PPG2}: \quad \mathbf{A}^k = \sum_{j=0}^{N^k} V^k \frac{\partial N_{\delta\mathbf{u}}^{jjk}}{\partial \mathbf{X}} - \sum_{j=0}^{N^k} V^j \frac{\partial N_{\delta\mathbf{u}}^{kkj}}{\partial \mathbf{X}} \quad \text{and} \tag{4.34}$$

$$\text{PBG}: \quad \mathbf{A}^k = \sum_{i=0}^{N^k} \sum_{j=0}^{N^i} \frac{V^i V^j}{V^{\mathcal{H}_0^i}} \frac{\partial N_{\delta\mathbf{u}}^{ijk}}{\partial \mathbf{X}} - \sum_{i=0}^{N^k} \sum_{j=0}^{N^k} \frac{V^k V^j}{V^{\mathcal{H}_0^k}} \frac{\partial N_{\delta\mathbf{u}}^{kji}}{\partial \mathbf{X}} \, . \tag{4.35}$$

4.4 Temporal discretization

Looking in the discretized peridynamic weak form (4.14), the structure of the virtual work of internal forces, as well as the treatment of boundary conditions have been described in sections 4.2 and 4.3, respectively. Now, the missing transient behavior is addressed, which will be separated into the evolution of inertia forces and the evolution of constitutive history variables with regard to von Mises plasticity. While the latter one is done locally at the integration points or rather neighbor particles, the former is usually globally coupled, at least via the mass matrix. However, with the particle discretization of equation (4.1), the mass matrix is by default diagonal, i.e. without further lumping. Thus, also the integration of motion becomes a decoupled problem on particle level, if specific explicit time integration schemes are used.

4.4.1 Integration of motion

For an implicit time integration of each particle's movement, the Newmark-beta method (cf. NEWMARK (1959)) can be applied. Therefore, originating from time t_n, the equilibrium is generally iteratively obtained in the new time $t_{n+1} = t_n + \Delta t_n$. With the Newmark-beta method, the new velocity $\dot{\mathbf{u}}^k_{n+1}$ and acceleration $\ddot{\mathbf{u}}^k_{n+1}$ of particle k are related to its new displacement $\mathbf{u}^k_{n+1}$ via the following expressions:

$$\dot{\mathbf{u}}^k_{n+1} = \frac{\gamma_{NM}}{\beta_{NM}\Delta t^2}\left(\mathbf{u}^k_{n+1} - \mathbf{u}^k_n\right) + \left(1 - \frac{\gamma_{NM}}{\beta_{NM}}\right)\dot{\mathbf{u}}^k_n + \Delta t\left(1 - \frac{\gamma_{NM}}{2\beta_{NM}}\right)\ddot{\mathbf{u}}^k_n \tag{4.36}$$

and

$$\ddot{\mathbf{u}}^k_{n+1} = \frac{1}{\beta_{NM}\Delta t^2}\left[\mathbf{u}^k_{n+1} - \mathbf{u}^k_n - \Delta t\dot{\mathbf{u}}^k_n - \Delta t^2\left(\frac{1}{2} - \beta_{NM}\right)\ddot{\mathbf{u}}^k_n\right]. \tag{4.37}$$

With the Newmark time integration parameters $\beta_{NM} = 0.25$ and $\gamma_{NM} = 0.5$, the resulting constant average acceleration leads to an unconditional stability. Hence, only the iterative solution procedure of the assembled discretized weak form limits the size of the time step Δt_n. However, the time step size has to be chosen small enough to capture the physical phenomena. If this required time step becomes very small, it can be advantageous to use an explicit time integration as the central difference method, where the time step size is restricted by the Courant-Friedrichs-Lewy condition (see e.g. BELYTSCHKO ET AL. (1976)). Here, the equilibrium is stated in the current time step t_n and explicitly extrapolated to the new time step t_{n+1}. The current velocity $\dot{\mathbf{u}}^k_n$ and acceleration $\ddot{\mathbf{u}}^k_n$ of particle k follow from the central differential quotients as

$$\dot{\mathbf{u}}^k_n = \frac{\mathbf{u}^k_{n+1} - \mathbf{u}^k_{n-1}}{2\Delta t} \tag{4.38}$$

and

$$\ddot{\mathbf{u}}^k_n = \frac{\mathbf{u}^k_{n+1} - 2\mathbf{u}^k_n + \mathbf{u}^k_{n-1}}{\Delta t^2}, \tag{4.39}$$

where in the zeroth time step

$$\mathbf{u}^k_{-1} = \mathbf{u}^k_0 - \Delta t\dot{\mathbf{u}}^k_0 + \frac{\Delta t^2}{2}\ddot{\mathbf{u}}^k_0. \tag{4.40}$$

Except for the use with continuously approximated mixed variables (see chapter 6) or rate-dependent behavior, the central difference time integration does not need the solution of a global system. In contrast to the implicit constant mean acceleration of equations (4.36) and (4.37), the central difference method additionally conserves as a symplectic method the momentum and energy (see also SIMO & TARNOW (1992)).

4.4.2 Evolution of plastic variables

Further on, the constitutive model can require an additional evolution of internal variables in time. In terms of the evolution of the plastic part of the inverse right Cauchy-Green tensor (2.52) for von Mises elasto-plasticity, the integration can be done via an exponential ansatz (see e.g. (KORELC & STUPKIEWICZ, 2014)) that ensures that the plastic deformation remains perfectly isochoric. If the Yield function $\mathcal{F}$ is positive in an elastic predictor step, the set of local equations that has to be solved iteratively in a Newton-Raphson procedure at each integration point (or neighbor particle) states

$$\mathbf{Q} = \left\{\mathbf{C}_p^{-1} - \mathbf{F}^{-1} \cdot e^{2\Delta\alpha\mathbf{n}} \cdot \mathbf{F} \cdot \mathbf{C}_{pn}^{-1}, \mathcal{F}\right\} = \mathbf{0} \tag{4.41}$$

with the evolution of the hardening variable $\Delta\alpha = \Delta\lambda$. While quantities with the index n belong to the current or prior time (t_n in the implicit and t_{n-1} in the explicit case), the indices referring to the new or current time (t_{n+1} in the implicit and t_n in the explicit case) are omitted for convenience. The updated history variables $\mathbf{C}_p^{-1}$ and α have to be varied to get the local tangent for the solution of the Newton iteration:

$$\mathbf{A} = \frac{\partial \mathbf{Q}}{\partial \mathbf{h}} \quad \text{with} \quad \mathbf{h} = \left\{\mathbf{C}_p^{-1}, \alpha\right\} . \tag{4.42}$$

This can generally be done via the same procedures as for the linearization of the global equations that will be presented in section 4.6. Within this work, the Automatic Differentiation tool AceGen is used to compute the local tangent (4.42).

4.5 Residual or discretized strong form

With a correspondence formulation for the pairwise force densities, the external volume and surface forces, a temporal discretization of the inertia forces and applied essential boundary conditions, the general weak form is fully defined. Table 4.1 lists the weak forms resulting from the pairwise force density expressions (4.21), (4.22) and (4.30) inserted into the discrete weak form (4.14). With the approaches of the actual and virtual deformation gradient (4.11) and (4.12), the virtual nodal displacements can be excluded from the assembled weak form:

$$\delta U_h = \mathbf{R_u} \cdot \delta\mathbf{U} = 0\,, \tag{4.43}$$

whereby $\delta\mathbf{U}$ denotes the global vector of virtual nodal displacements. The resulting global nodal residual vector $\mathbf{R_u} = \mathbf{R_u}(\mathbf{U})$ is a generally nonlinear function of the global nodal displacement vector $\mathbf{U}$ and its temporal derivatives, which are, in turn, related to the displacements via the time integration approach. It contains the internal, external and inertia forces acting on each node and can be obtained by filtering out the virtual nodal displacements by means of the derivative of the assembled weak form with respect to the virtual nodal displacements:

$$\mathbf{R}_{\mathbf{u}} = \frac{\partial \delta U_h}{\partial \delta \mathbf{U}} = \mathop{\mathbf{A}}_{k=1}^{n^p} \left\{ \mathbf{R}_{\mathbf{u}}^k \right\} , \tag{4.44}$$

with the local residual $\mathbf{R}_{\mathbf{u}}^k = \frac{\partial \delta U_h}{\partial \delta \mathbf{u}^k}$. As the virtual nodal displacements in equation (4.43) can be arbitrary apart from the essential boundary, the residual itself has to vanish for all free nodes:

$$\mathbf{R}_{\mathbf{u}}^k = 0 \, , \tag{4.45}$$

whereas for particles suspect to Dirichlet boundary conditions, the residual equals the reaction force. By evaluating $\mathbf{R}_{\mathbf{u}}^k$ with equation (4.16), it becomes apparent that within a particle discretization, the nodal residual, resulting from the weak form, is equivalent to the direct discretization of the strong form (equation (3.11)) provided that the pairwisity of the connectivity is fulfilled:

$$\mathbf{R}_{\mathbf{u}}^k = -V^k \sum_{j=0}^{N^k} V^j \left(\mathbf{t}^{kj} - \mathbf{t}^{jk} \right) + \rho_0^k V^k \left(\ddot{\mathbf{u}}^k - \tilde{\mathbf{b}}^k \right) = 0 \, . \tag{4.46}$$

The local residual or rather the discretized strong form resulting from the different approaches PPG1, PPG2 and PBG are summarized in Table 4.1.

In case Automatic Differentiation is used to generate the family-wise assembling routine of the residual and tangent matrix (see also section 4.6), it can be more convenient to formulate a pseudo potential (cf. HUDOBIVNIK ET AL. (2019)) that governs the weak form via variation. For the PBG method, the pseudo potential writes

$$U_h = \mathop{\mathbf{A}}_{k=1}^{n^p} \left\{ \frac{V^k}{V^{\mathcal{H}_0^k}} \sum_{j=0}^{N^k} V^j W^{kj} + \left[\rho_0^k V^k \left(\ddot{\mathbf{u}}^k - \overline{\mathbf{b}}^k \right) - \mathbf{P}^k \cdot \mathbf{A}^k \right] \cdot \mathbf{u}^k \right\} . \tag{4.47}$$

A variation, while holding the plastic history variables as well as the inertia and external forces fixed, leads to

$$\delta U_h = \left. \frac{\partial U_h}{\partial \mathbf{U}} \right|_{\frac{\partial \mathbf{h}}{\partial \mathbf{u}} = \mathbf{0} \, , \, \frac{\partial \ddot{\mathbf{u}}}{\partial \mathbf{u}} = \frac{\partial \overline{\mathbf{b}}}{\partial \mathbf{u}} = \frac{\partial (\mathbf{P} \cdot \mathbf{A})}{\partial \mathbf{u}} = \mathbf{0}} \cdot \delta \mathbf{U} \, , \tag{4.48}$$

equivalent to the PBG weak form in Table 4.1. The residual can then directly be derived from U_h by inserting equation (4.48) into the expression (4.44):

$$\mathbf{R}_{\mathbf{u}} = \left. \frac{\partial U_h}{\partial \mathbf{U}} \right|_{\frac{\partial \mathbf{h}}{\partial \mathbf{u}} = \mathbf{0} \, , \, \frac{\partial \ddot{\mathbf{u}}}{\partial \mathbf{u}} = \frac{\partial \overline{\mathbf{b}}}{\partial \mathbf{u}} = \frac{\partial (\mathbf{P} \cdot \mathbf{A})}{\partial \mathbf{u}} = \mathbf{0}} \tag{4.49}$$

which can efficiently be done by the use of Automatic Differentiation. Note, that pseudo potential (4.47) reduces to a real potential when static, hyperelastic behavior with displacement-independent external loads is considered.

4.6 Linearization of the global equations

The collective nodal residual vectors (4.46) construct, except for the explicit case, a coupled system of nonlinear equations $\mathbf{R}_{n+1} = \mathbf{0}$ with the nodal displacements $\mathbf{U}_{n+1}$ as unknowns. For its solution, the Newton-Raphson iterative scheme can be applied. Therefore, the residual $\mathbf{R}_{n+1}$ is linearized with respect to an initial guess of the nodal displacement vector – typically from the last time or load step $\mathbf{U}_n$ – by means of a Taylor series expansion:

$$\mathcal{L}\left\{\mathbf{R}_{n+1}\right\}\big|_{\mathbf{U}=\mathbf{U}_n} = \mathbf{R}_n + \Delta\mathbf{R}_n = \mathbf{R}_n + \frac{\partial \mathbf{R}_n}{\partial \mathbf{U}_n} \cdot \left(\mathbf{U} - \mathbf{U}_n\right) , \tag{4.50}$$

which can be set equal to the zero vector to get an estimate for the root $\mathbf{U}_{n+1}$. If the initial guess of $\mathbf{U}$ is sufficiently close to the root, the alternate linearization and its solution lead with quadratic convergence to the solution $\mathbf{U}_{n+1}$ via the following algorithm:

$$\mathbf{U}_{n+1\ i+1} = \mathbf{U}_{n+1\ i} + \Delta\mathbf{U}_{n+1\ i+1} \tag{4.51}$$

with $\Delta\mathbf{U}_{n+1\ i+1}$ as the solution of

$$\mathbf{K}_{n+1\ i} \cdot \Delta\mathbf{U}_{n+1\ i+1} = -\mathbf{R}_{n+1\ i} \, . \tag{4.52}$$

Thereby $\mathbf{K}_{n+1\ i}$ denotes the effective global tangent stiffness matrix

$$\mathbf{K}_{n+1\ i} = \frac{\partial \mathbf{R}_{n+1\ i}}{\partial \mathbf{U}_{n+1\ i}} \, . \tag{4.53}$$

The above iterative procedure can be aborted when the residual $\mathbf{R}_{n+1\ i}$ gets sufficiently small. In the special case of linear elasticity, one step of the iterative scheme is sufficient to find the solution $\mathbf{U}_{n+1}$. If the explicit time integration scheme of section 4.4.1 is conducted, the resulting system gets uncoupled and its solution can be done locally in one step.

However, within nonlinear implicit simulations, the global Newton-Raphson scheme makes up the main driving computational cost, which can further be split in two parts. First, the construction of system (4.52), and second, its solution. Concerning the construction, the tangent stiffness matrix has to be computed. In the field of Correspondence Peridynamics, this tangent matrix is usually approximated as a secant via Finite Differences, which is costly and results, according to BROTHERS ET AL. (2014), in the majority of the computation time in implicit peridynamic analyses. With the general shape function based notation of the PG methods, the much faster consistent linearization becomes less challenging, as the shape function approach decouples the nodal displacements and the displacement-independent shape functions. Therefore, also Automatic Differentiation tools can be applied. In the

Table 4.1. Discretized global weak forms and local strong forms of the different PG methods and the equivalent (pseudo-) potential of the PBG method.

Global weak form	PPG1	$\delta U_h = \underset{k=1}{\overset{n^p}{\mathbf{A}}} \left\{ -\sum_{j=0}^{N^k} \left(V^j \mathbf{P}^{kj} \cdot \frac{\partial N_{\delta\mathbf{u}}^{jjk}}{\partial \mathbf{X}} \right) \cdot \Delta\delta\mathbf{u}^{kj} + \left[\rho_0^k V^k \left(\ddot{\mathbf{u}}^k - \overline{\mathbf{b}}^k \right) - \mathbf{P}^k \cdot \mathbf{A}^k \right] \cdot \delta\mathbf{u}^k \right\} = 0$
	PPG2	$\delta U_h = \underset{k=1}{\overset{n^p}{\mathbf{A}}} \left\{ \sum_{j=0}^{N^k} \left(V^j \mathbf{P}^{kj} \cdot \frac{\partial N_{\delta\mathbf{u}}^{kkj}}{\partial \mathbf{X}} \right) \cdot \Delta\delta\mathbf{u}^{kj} + \left[\rho_0^k V^k \left(\ddot{\mathbf{u}}^k - \overline{\mathbf{b}}^k \right) - \mathbf{P}^k \cdot \mathbf{A}^k \right] \cdot \delta\mathbf{u}^k \right\} = 0$
	PBG	$\delta U_h = \underset{k=1}{\overset{n^p}{\mathbf{A}}} \left\{ \frac{V^k}{V^{\mathcal{H}_0^k}} \sum_{j=0}^{N^k} \sum_{i=0}^{N^k} \left(V^j \mathbf{P}^{kj} \cdot \frac{\partial N_{\delta\mathbf{u}}^{kji}}{\partial \mathbf{X}} \right) \cdot \Delta\delta\mathbf{u}^{ki} + \left[\rho_0^k V^k \left(\ddot{\mathbf{u}}^k - \overline{\mathbf{b}}^k \right) - \mathbf{P}^k \cdot \mathbf{A}^k \right] \cdot \delta\mathbf{u}^k \right\} = 0$
Local strong form/ local residual	PPG1	$\mathbf{R}_{\mathbf{u}}^k = \sum_{j=0}^{N^k} V^j \mathbf{P}^{kj} \cdot \frac{\partial N_{\delta\mathbf{u}}^{jjk}}{\partial \mathbf{X}} - \sum_{j=0}^{N^k} V^k \mathbf{P}^{jk} \cdot \frac{\partial N_{\delta\mathbf{u}}^{kkj}}{\partial \mathbf{X}} + \rho_0^k V^k \left(\ddot{\mathbf{u}}^k - \overline{\mathbf{b}}^k \right) - \mathbf{P}^k \cdot \mathbf{A}^k = \mathbf{0}$
	PPG2	$\mathbf{R}_{\mathbf{u}}^k = \sum_{j=0}^{N^k} V^k \mathbf{P}^{jk} \cdot \frac{\partial N_{\delta\mathbf{u}}^{jjk}}{\partial \mathbf{X}} - \sum_{j=0}^{N^k} V^j \mathbf{P}^{kj} \cdot \frac{\partial N_{\delta\mathbf{u}}^{kkj}}{\partial \mathbf{X}} + \rho_0^k V^k \left(\ddot{\mathbf{u}}^k - \overline{\mathbf{b}}^k \right) - \mathbf{P}^k \cdot \mathbf{A}^k = \mathbf{0}$
	PBG	$\mathbf{R}_{\mathbf{u}}^k = \sum_{i=0}^{N^k} \sum_{j=0}^{N^i} \frac{V^i V^j}{V^{\mathcal{H}_0^i}} \mathbf{P}^{ij} \cdot \frac{\partial N_{\delta\mathbf{u}}^{ijk}}{\partial \mathbf{X}} - \sum_{i=0}^{N^k} \sum_{j=0}^{N^k} \frac{V^k V^j}{V^{\mathcal{H}_0^k}} \mathbf{P}^{kj} \cdot \frac{\partial N_{\delta\mathbf{u}}^{kji}}{\partial \mathbf{X}} + \rho_0^k V^k \left(\ddot{\mathbf{u}}^k - \overline{\mathbf{b}}^k \right) - \mathbf{P}^k \cdot \mathbf{A}^k = \mathbf{0}$
Global (pseudo-) potential	PBG	$U_h = \underset{k=1}{\overset{n^p}{\mathbf{A}}} \left\{ \sum_{j=0}^{N^k} \frac{V^k V^j}{V^{\mathcal{H}_0^k}} W^{kj} + \left[\rho_0^k V^k \left(\ddot{\mathbf{u}}^k - \overline{\mathbf{b}}^k \right) - \mathbf{P}^k \cdot \mathbf{A}^k \right] \cdot \mathbf{u}^k \right\}$

subsequent sections, the different techniques are described in detail.

As a second part, the solution of the resulting linear system (4.52) has to be performed. Thereby, standard direct or iterative solvers and preconditioners can be chosen, as e.g. the direct solvers of the PARDISO package (SCHENK ET AL., 2001) or the iterative biconjugate gradient stabilized method (BiCGSTAB, SLEIJPEN ET AL. (1994)) combined with a Jacobi or incomplete LU preconditioner. Note, that the Petrov-Galerkin formulations lead to a non-symmetric tangent matrix which restricts the choice of appropriate solvers. Whether the construction or solution of the system dominates the computational cost depends on several factors. The part of the cost for the construction grows with increasing complexity of the constitutive relations or less efficient construction techniques (Finite Differences). On the other hand, a larger number of global degrees of freedom and an unsuitable choice of the linear solver increase the relative cost of the second part.

4.6.1 Finite Difference approximation

The Central Finite Differences can be utilized to numerically approximate the tangent stiffness matrix (see e.g. LITTLEWOOD (2015)). In doing so, each particle has to be perturbed in every dimension in positive and negative direction. The change in the residual of influenced particles has to be computed and inserted into the global stiffness matrix. Note, that the resulting tangent matrix is sparse, as in the definition of the local residual (4.46) only the nodal displacements of the collective families of each neighbor particle are present (i.e. within two times the horizon for spherical families). The concerning entry of the residual change of particle k in x-direction due to perturbation of particle i in y-direction states

$$\mathbf{K}\left(k+x, i+y\right) \approx \frac{R_x^k\left(\mathbf{U}+\boldsymbol{\epsilon}_y^i\right) - R_x^k\left(\mathbf{U}-\boldsymbol{\epsilon}_y^i\right)}{2\epsilon}\,, \tag{4.54}$$

whereby the perturbation size ϵ should be chosen as small as possible to get the best approximation, but not too small such that numerical errors decrease the accuracy. LITTLEWOOD (2015) suggests a value of about 10^{-6} times the particle spacing. Note, that despite the low efficiency of the FD approximation in contrast to a consistent linearization, it is very flexible in the sense that it can be implemented independent on the constitutive relations or the form of the residual.

4.6.2 Consistent linearization

While in the branch of nonlocal material models, which are directly dependent on a deformation state measure, also the consistent linearization based on modulus states is a common technique since SILLING (2010), in the correspondence theory, the numerical approximation is usually adopted within implicit analysis. However, with the Galerkin-type shape function approach of the actual and virtual deformation gradient (4.11) and (4.12), the linearization of the weak form can be done analogously to the FEM (see WRIGGERS (2008)). Therefore, the starting point is the linearized weak form

$$\mathcal{L}\left\{\delta U_h\right\}\Big|_{\mathbf{u}=\bar{\mathbf{u}}} = \delta\bar{U}_h + \Delta\delta\bar{U}_h\,. \tag{4.55}$$

The goal is now, to eliminate the global vector of virtual displacements on the left and the actual displacements on the right, to end up in the separated form of the increment of the weak form

$$\Delta\delta\bar{U}_h = \delta\mathbf{U}\cdot\mathbf{K}\cdot\mathbf{U}\,, \tag{4.56}$$

where $\mathbf{K}$ denotes the effective global tangent stiffness matrix of equation (4.53). With the assumption of non-changing connectivity within a load step, the global tangent matrix can be assembled from particle-wise or family-wise contributions:

$$\mathbf{K} = \mathop{\mathbf{A}}\limits_{k=1}^{n^p}\left\{\mathbf{K}^k\right\}\,. \tag{4.57}$$

Exemplarily, the linearization is performed in detail for the PPG1 correspondence formulation within appendix A. Assuming displacement-independent loads, the particle-wise tangent stiffness matrix for the static case can be expressed as

$$\mathbf{K}^k = \sum_{j=1}^{N^k}\sum_{i=0}^{N^k}\left(G_1^{ji}\mathbf{1} + \mathbf{M}_1^{ji}\right) + \sum_{j=1}^{N^k}\sum_{i=0}^{N^j}\left(G_2^{ji}\mathbf{1} + \mathbf{M}_2^{ji}\right) \tag{4.58}$$

where it is split into the pairwise geometric parts

$$G_1^{ji} = -V^j\frac{\partial N_u^{kji}}{\partial\mathbf{X}}\cdot\bar{\mathbf{S}}^{kj}\cdot\frac{\partial N_{\delta\mathbf{u}}^{jjk}}{\partial\mathbf{X}} \quad\text{and}\quad G_2^{ji} = V^k\frac{\partial N_u^{jki}}{\partial\mathbf{X}}\cdot\bar{\mathbf{S}}^{jk}\cdot\frac{\partial N_{\delta\mathbf{u}}^{kkj}}{\partial\mathbf{X}}\,. \tag{4.59}$$

and the substantial parts in Voigt notation

$$\mathbf{M}_1^{ji} = -V^j\bar{\mathbf{F}}^{kj}\cdot\left(\mathbf{B}_{\delta\mathbf{u}}^{jjk^T}\cdot\bar{\mathbf{D}}^{kj}\cdot\mathbf{B}_u^{kji}\right)\cdot\bar{\mathbf{F}}^{kj^T} \quad\text{and}\quad \mathbf{M}_2^{ji} = V^k\bar{\mathbf{F}}^{jk}\cdot\left(\mathbf{B}_{\delta\mathbf{u}}^{kkj^T}\cdot\bar{\mathbf{D}}^{jk}\cdot\mathbf{B}_{\mathbf{u}}^{jki}\right)\cdot\bar{\mathbf{F}}^{jk^T}\,. \tag{4.60}$$

Analogously, the particle-wise tangent stiffness matrices of the PPG2 and PBG formulations can be derived.

4.6.3 Automatic Differentiation

Both the efficiency of the consistent linearization and the flexibility of the FD approximation can be joined by means of Automatic Differentiation (AD) (see KORELC (2009), KORELC & STUPKIEWICZ (2014) and KORELC & WRIGGERS (2016)). The software AceGen combines expression optimization (KORELC, 1997) and AD with the symbolic notation of Mathematica and can compute element or family-wise residual and tangent contributions of arbitrary size. Compatible with FE environments, as e.g. AceFEM, Ansys and Abaqus, AceGen provides a relatively easy way of implementing the PG methods into existing FE software. Thereby, the family contribution of the weak form or a (pseudo) potential in the form of Table 4.1 is differentiated with respect to the collective nodal displacements within the family:

$$\mathbf{R}^{\mathcal{H}_0^k} = \frac{\hat{\delta}\delta U_h^k}{\hat{\delta}\delta\mathbf{u}^{\mathcal{H}_0^k}} \quad \text{or rather} \quad \mathbf{R}^{\mathcal{H}_0^k} = \left.\frac{\hat{\delta}U_h^k}{\hat{\delta}\mathbf{u}^{\mathcal{H}_0^k}}\right|_{\frac{\hat{\delta}\mathbf{h}}{\hat{\delta}\mathbf{u}}=\mathbf{0}\,,\,\frac{\hat{\delta}\ddot{\mathbf{u}}}{\hat{\delta}\mathbf{u}}=\frac{\hat{\delta}\overline{\mathbf{b}}}{\hat{\delta}\mathbf{u}}=\frac{\hat{\delta}(\mathbf{P}\cdot\mathbf{A})}{\hat{\delta}\mathbf{u}}=\mathbf{0}}\,, \tag{4.61}$$

where $\hat{\delta}$ denotes the computational derivative. The family-wise tangent stiffness matrix is computed from the second derivative:

$$\mathbf{K}^{\mathcal{H}_0^k} = \left.\frac{\hat{\delta}\mathbf{R}^{\mathcal{H}_0^k}}{\hat{\delta}\mathbf{u}^{\mathcal{H}_0^k}}\right|_{\frac{D\mathbf{h}}{D\mathbf{F}}=-\mathbf{A}^{-1}\cdot\frac{\hat{\delta}\mathbf{Q}}{\hat{\delta}\mathbf{F}}}\,. \tag{4.62}$$

In case of an internal Newton iteration (like for equations (4.41)), the computational derivative directly leads to the algorithmic tangent and therefore leads to a quadratic convergence of the global Newton method. By adding the differentiation exception of equation (4.62) the local tangent $\mathbf{A}$ of the converged local system can be used to improve the efficiency of the optimized code generation (KORELC, 2009). When AD tools are used that are not able to efficiently deal with the derivation with respect to a vector of unknown length, the chain rule can be applied to separate the differentiation process in two parts without loss of generality in the chose of constitutive models. One material dependent AD part up to the deformation gradient and one correspondence formulation dependent self-derived part.

4.7 Local conservation properties

In section 4.5 it was demonstrated that due to the particle discretization, the local residual of the corresponding weak form is equivalent to the direct discretization of the original strong form. As a result, the linear momentum is preserved locally between each two particles. This can be seen from the momentum exchange $\frac{D\mathbf{I}}{Dt}$ between two particles k and j:

$$\frac{D\mathbf{I}^{kj}}{Dt} = \left(\mathbf{t}^{kj} - \mathbf{t}^{jk}\right) V^k V^j = -\left(\mathbf{t}^{jk} - \mathbf{t}^{kj}\right) V^j V^k = -\frac{D\mathbf{I}^{jk}}{Dt}\,. \tag{4.63}$$

While the local preservation of linear momentum is fulfilled independent on the structure of $\mathbf{t}$, the local preservation of angular momentum is not a priori fulfilled. Therefore, it has to be shown, that for a specific formulation of $\mathbf{t}$, the resulting moment of the force state vanishes, cf. BONET & LOK (1999) and SILLING ET AL. (2007):

$$\sum_{j=0}^{N^k} \Delta\mathbf{x}^{kj} \times \mathbf{t}^{kj} V^j = \mathbf{0}\,. \tag{4.64}$$

In the discrete setting of the PPG1 and PPG2 formulations, equation (4.64) does not generally hold. However, for the PBG formulation (equation (4.30)), the preservation can be proofed. By insertion of the correspondence formulation in the discrete index form of condition (4.64), the net moment vanishes, provided that the test and trial functions coincide:

$$
\begin{aligned}
\sum_{j=0}^{N^k} \epsilon_{ABC} \Delta x_B^{kj} t_C^{kj} V^j &= \sum_{j=0}^{N^k} \epsilon_{ABC} \Delta x_B^{kj} \sum_{i=0}^{N^k} \frac{V^i}{V^j V^{\mathcal{H}_0^k}} P_{CD}^{ki} \frac{\partial N_{\delta \mathbf{u}}^{kij}}{\partial X_D} V^j \\
&= \sum_{i=0}^{N^k} \frac{V^i}{V^{\mathcal{H}_0^k}} \epsilon_{ABC} P_{CD}^{ki} \sum_{j=0}^{N^k} \Delta x_B^{kj} \frac{\partial N_{\mathbf{u}}^{kij}}{\partial X_D} \\
&= \sum_{i=0}^{N^k} \frac{V^i}{V^{\mathcal{H}_0^k}} \epsilon_{ABC} P_{CD}^{ki} F_{BD}^{ki} \\
&= \sum_{i=0}^{N^k} \frac{V^i J^{ki}}{V^{\mathcal{H}_0^k}} \epsilon_{ABC} \sigma_{BC}^{ki} = 0 \, ,
\end{aligned}
\tag{4.65}
$$

with the Levi-Civita symbol ϵ_{ABC}. In the second line a reordering was performed and the test and trial shape functions substituted, in line three the discrete deformation gradient of equation (4.11) was inserted and in line four the reference of the first Piola-Kirchhoff stress was pushed forward and the symmetry of the Cauchy stress tensor exploited.

Chapter 5

The role of shape functions

In the general presentation of the PG methods in chapter 4, the shape function approaches of the actual and virtual deformation gradient equations (4.11) and (4.12) were conducted without a specific choice of shape functions. In fact, the choice of shape functions for the test and trial functions is a crucial point that defines the numerical properties of the resulting methods. Among other characteristics, it can decide over rank deficiency, stability, robustness, the accurate imposition of Dirichlet and Neumann boundaries or the convergence rate. Also, special linear shape function choices reduce the general PG methods to the classical peridynamic correspondence formulation or the total Lagrangian corrected SPH.

Howsoever, the freedom in the choice of shape functions should be used to gain the most desirable properties for which the following strategy is adopted. In a first step, certain criteria have to be isolated that ensure the requested properties. These requirements on the shape functions are prepared in section 5.1. Second, section 5.2 reviews existing meshfree shape functions and checks them on the fulfillment of the aforementioned criteria. Further, the concept of Weighted and Moving Least Squares is derived from an integral formulation of the regression of peridynamic states and extended towards a Moving Taylor series expansion, leading to interpolating shape functions. Finally, two modification procedures are presented in section 5.3 that restore those requirements that are generally not met a priori.

5.1 Requirements on test and trial shape functions

For the examination of shape function conditions, some technical terms are introduced, before the conditions are elaborated. It is noted, that the nomenclature in literature is not always the same and the defined terminology is used in the following. First, the *reproducibility* of shape functions defines whether they can capture certain (polynomial) fields accurately. In terms of shape functions resulting from a regression analysis, the underlying basis space (the regression ansatz) will be reproducible, i.e. the error of the regression goes to zero. In case of a polynomial basis, where a complete set of monomials up to an order n is used, the resulting shape functions possess the *completeness* up to order n, which means, the polynomial basis space is *complete* up to order n. Further, the shape functions posses the *consistency*, if its approximation of the underlying field is exact. Considering e.g. an accurate approximation of any linear field, then the shape functions are called *first order* or *linearly consistent*. Despite being consistent, a shape function approach may not be accurate at the supporting points. If they are, the shape functions are of *interpolating* character. Further, *bond-conforming* shape function derivatives ensure the precise mapping of bonds into the approximated configuration, leading to a *configurational consistency*.

Even though first order consistent shape functions are used for the trial and test space, the resulting discretization method is possibly not able to capture linear fields exactly. As a consequence, suboptimal convergence rates or a convergence to an erroneous solution can occur. The reason for this is, that the numerical integration of the shape functions is either not accurate, or the ansatz space is not conforming. As a result, the *Galerkin orthogonality* (error is orthogonal to solution space), is disturbed which would guarantee the reproducibility of the chosen shape function spaces. This reproducibility of the discretization method up to an order n is denoted as *Galerkin exactness* or *variational consistency* of order n and enables the fulfillment of the linear or n-th order polynomial patch test as well as the convergence in optimal rates. Further, the criterion that has to hold to gain variational consistency is termed *integration constraint*, also referred to as *divergence criterion*. In the following subsections, the conditions, necessary to fulfill the above-mentioned properties, are stated.

5.1.1 Consistency criteria

Referring to KRONGAUZ & BELYTSCHKO (1997), one key ingredient for convergence is consistency of the trial functions. As mentioned earlier, linear or first order consistency of the classical shape function approach (as in equation (4.8)), guarantees the exact approximation of a linear function. Consider the scalar function $f\,(X,Y) = a_0 + a_1(X - X^k) + a_2(Y - Y^k)$ in 2-D within family $\mathcal{H}_0^k$. Then any neighbor particle i holds the nodal value

$$f^i = a_0 + a_1 \Delta X^{ki} + a_2 \Delta Y^{ki} \,. \tag{5.1}$$

If the shape function approximation is linearly consistent, it is able to approximate the linear function f accurately. Therefore, the linearly consistent shape function approximation $f^{kj} = \sum_{i=0}^{N^k} f^i N^{kji}$ (see also equation (4.8)) can be expressed as

$$f^{kj} = a_0 + a_1 \Delta X^{kj} + a_2 \Delta Y^{kj} \,. \tag{5.2}$$

Inserting equations (5.1) and (5.2) into the shape function approach gives, cf. KRONGAUZ & BELYTSCHKO (1997),

$$a_0 + a_1 \Delta X^{kj} + a_2 \Delta Y^{kj} = \sum_{i=0}^{N^k} a_0 N^{kji} + a_1 \Delta X^{ki} N^{kji} + a_2 \Delta Y^{ki} N^{kji} \,, \tag{5.3}$$

A comparison of the coefficients of a_0, a_1 and a_2 leads to the following expressions which are the properties of the linearly consistent shape functions:

$$\sum_{i=0}^{N^k} N^{kji} = 1\,, \quad \sum_{i=0}^{N^k} N^{kji} \Delta X^{ki} = \Delta X^{kj} \quad \text{and} \quad \sum_{i=0}^{N^k} N^{kji} \Delta Y^{ki} = \Delta Y^{kj}\,. \tag{5.4}$$

In the other way round, if the conditions (5.4) hold for the set of shape functions N^{kji}, then the shape functions are linearly consistent. More generally, the following difference-based criteria can be formulated for 3-D. Shape functions are called zeroth order consistent, implying a reproducibility of constant fields, when

$$\sum_{i=0}^{N^k} N^{kji} = 1\,, \tag{5.5}$$

also known as the partition of unity. Further, they are linearly consistent, meaning they can reproduce linear fields, if, in addition to (5.5),

$$\sum_{i=0}^{N^k} N^{kji} \Delta \mathbf{X}^{ki} = \Delta \mathbf{X}^{kj}\,. \tag{5.6}$$

Analogously, the additional criterion for second order consistency states

$$\sum_{i=0}^{N^k} N^{kji} \Delta \mathbf{X}^{ki} \otimes \Delta \mathbf{X}^{ki} = \Delta \mathbf{X}^{kj} \otimes \Delta \mathbf{X}^{kj}\,. \tag{5.7}$$

leading to a reproducibility of second order polynomials. Whenever the shape function approach is only used to approximate the derivatives of a field, as done in equation (4.11), the fulfillment of the derivatives of the above criteria, i.e.

$$\sum_{i=0}^{N^k} \frac{\partial N^{kji}}{\partial \mathbf{X}} = \mathbf{0}\,, \tag{5.8}$$

$$\sum_{i=0}^{N^k} \Delta \mathbf{X}^{ki} \otimes \frac{\partial N^{kji}}{\partial \mathbf{X}} = \mathbf{1} \quad \text{and} \tag{5.9}$$

$$\sum_{i=0}^{N^k} \Delta \mathbf{X}^{ki} \otimes \Delta \mathbf{X}^{ki} \otimes \frac{\partial N^{kji}}{\partial \mathbf{X}} = 2 \Delta \mathbf{X}^{kj} \otimes \mathbf{1}\,, \tag{5.10}$$

respectively, is sufficient to ensure an accurate approximation of the gradient field of a constant, linear or quadratic function. Note, that in case the difference-based ansatz of equation (4.11) is utilized, the fulfillment of equation (5.8) is no longer necessary.

5.1.2 Interpolation condition

In the preceding subsection, the accordance of nodal values and the shape function approximation was utilized for certain polynomial fields to derive the consistency criteria. In practice, the field that is to be approximated can be non-linear and even a consistent shape function approximation does not generally match the nodal values. However, for an accurate strong imposition of Dirichlet boundary conditions, this is necessary. According to the principle of virtual displacements, only geometrically possible virtual displacements are allowed, which means that the virtual displacement has to vanish on the Dirichlet boundary. If the Dirichlet boundary conditions are further strongly imposed via nodal or rather particle positions, the shape function contribution of those particles that are not part of the Dirichlet boundary has to be zero. This can be ensured, by means of the Kronecker delta property

$$N_{\delta \mathbf{u}}^{kji} = \delta^{ji} \,, \tag{5.11}$$

also denoted as Lagrange property. A consequence of the Kronecker delta property is that the shape function approximation (4.8) has an interpolative character, i.e. the approximation function equals the nodal values at the nodal positions. Note that condition (5.11) is actually more restrictive than necessary, as only the shape functions of inner particles would have to be zero on the essential boundary. Furthermore, due to the particle integration in the present method, the Kronecker delta property is implicitly assumed. Therefore equation (5.11) is not a strict requirement since only shape function derivatives are needed.

5.1.3 Bond mapping criterion

Similar to the Kronecker delta property that ensures a shape function approximation to be interpolating, a criterion can be defined that ensure an accurate mapping of the shape function derivatives. Although the deformation gradient, as a linear mapping operator, is only supposed to map incremental distance vectors accurately from the initial into the current configuration, it can be useful to enable them to map also vectors of finite length, particularly the bonds. By means of an accurate mapping of the initial bond $\Delta \mathbf{X}^{kj}$ to the deformed bond $\Delta \mathbf{x}^{kj}$ via the deformation gradient $\mathbf{F}^{kj}$, the collapsing of bonds can be prevented, provided that an appropriate constitutive law is used. With the discrete deformation gradient (4.11), the accurate linear mapping can be ensured if the trial shape function derivatives fulfill the following bond mapping criterion

$$\Delta \mathbf{x}^{kj} = \mathbf{F}^{kj} \cdot \Delta \mathbf{X}^{kj} = \sum_{i=0}^{N^k} \Delta \mathbf{x}^{ki} \otimes \frac{\partial N_{\mathbf{u}}^{kji}}{\partial \mathbf{X}} \cdot \Delta \mathbf{X}^{kj}, \quad \forall \Delta \mathbf{x}^{ki}, \Delta \mathbf{x}^{kj} \in \mathbb{R}^{n_{dim}} \,. \tag{5.12}$$

Considering the description of the deformation of a family in Figure 4.2, a state of bond-conforming deformation gradients leads to a reversible bijective mapping. Hence, the shape functions can be termed configurationally consistent, meaning that any actual deformation lies in the trial function space of the family. This is likely the reason why an increased stability in dynamic and updated Lagrangian simulations can be observed when criterion (5.12) holds for linearly consistent shape functions. However, the bond mapping criterion generally contradicts the consistency criteria of orders higher than one. Hence, criterion (5.12) can be seen as an improvement only of linearly consistent shape functions and one can decide either for a bijective mapping of the non-local kinematics or a higher order consistency allowing higher convergence rates. Higher order configurational consistency that does not affect the consistency itself could be obtained via higher order mappings, including not only the deformation gradient, but also higher order derivatives.

5.1.4 Integration constraints

While in conforming FE methods, the linear consistency of the trial and test functions, together with an accurate Gauß integration is sufficient to pass the linear patch test, this is generally not the case for meshfree particle methods with overlapping supports. The reason for this lies in the fact that the numerical integration of the mostly non-linear meshless shape functions is inaccurate, destroys the smoothness or is based on local approximation spaces that are globally non-conforming. As a consequence, the Galerkin orthogonality is disturbed and the computed coefficients or rather nodal displacements $\mathbf{U}$ do not belong anymore to the quasi-best Galerkin approximation (see Céa (1964)). In Krongauz & Belytschko (1997) and Belytschko et al. (1998) an integrability condition on the test functions, later termed integration constraint and Galerkin exactness, was presented, which has to be fulfilled to satisfy the linear patch test. Later, Chen et al. (2013) generalized it to conditions for variational consistency (VC) of n-th order, which is the counterpart to the consistency of the trial functions.

Concerning the VC of the discrete general weak forms of Table 4.1, the zeroth order is automatically fulfilled, as a constant displacement field (i.e. rigid body modes) leads to vanishing stresses and thus no internal forces are acting on any particle. However, first and second order Galerkin exactness are not generally met. For the first order VC, consider a linear displacement field leading to a constant stress field $\mathbf{P}^{kj} = \mathbf{P}$. This leads, with $\overline{\mathbf{b}}^k = \ddot{\mathbf{u}}^k = \mathbf{0}$, for the PPG1, PPG2 and PBG correspondence formulations to the local residuals

$$\text{PPG1}: \quad \mathbf{R}_{\mathbf{u}}^k = \sum_{j=0}^{N^k} V^j \mathbf{P} \cdot \frac{\partial N_{\delta\mathbf{u}}^{jjk}}{\partial \mathbf{X}} - \sum_{j=0}^{N^k} V^k \mathbf{P} \cdot \frac{\partial N_{\delta\mathbf{u}}^{kkj}}{\partial \mathbf{X}} - \mathbf{P} \cdot \mathbf{A}^k = \mathbf{0}\,, \tag{5.13}$$

$$\text{PPG2}: \quad \mathbf{R}_{\mathbf{u}}^k = \sum_{j=0}^{N^k} V^k \mathbf{P} \cdot \frac{\partial N_{\delta\mathbf{u}}^{jjk}}{\partial \mathbf{X}} - \sum_{j=0}^{N^k} V^j \mathbf{P} \cdot \frac{\partial N_{\delta\mathbf{u}}^{kkj}}{\partial \mathbf{X}} - \mathbf{P} \cdot \mathbf{A}^k = \mathbf{0} \quad \text{and} \tag{5.14}$$

$$\text{PBG}: \quad \mathbf{R}_{\mathbf{u}}^k = \sum_{i=0}^{N^k} \sum_{j=0}^{N^i} \frac{V^i V^j}{V^{\mathcal{H}_0^i}} \mathbf{P} \cdot \frac{\partial N_{\delta\mathbf{u}}^{ijk}}{\partial \mathbf{X}} - \sum_{i=0}^{N^k} \sum_{j=0}^{N^k} \frac{V^k V^j}{V^{\mathcal{H}_0^k}} \mathbf{P} \cdot \frac{\partial N_{\delta\mathbf{u}}^{kji}}{\partial \mathbf{X}} - \mathbf{P} \cdot \mathbf{A}^k = \mathbf{0}\,, \tag{5.15}$$

respectively. As $\mathbf{P}$ can be arbitrary, it reduces to the test shape function requirement for first order VC or rather the peridynamic integration constraint

$$\text{PPG1}: \quad \sum_{j=0}^{N^k} V^j \frac{\partial N_{\delta\mathbf{u}}^{jjk}}{\partial \mathbf{X}} - \sum_{j=0}^{N^k} V^k \frac{\partial N_{\delta\mathbf{u}}^{kkj}}{\partial \mathbf{X}} = \begin{cases} \mathbf{0} & \text{on } \Omega \backslash \partial\Omega \\ \mathbf{A}^k & \text{on } \partial\Omega \end{cases} , \tag{5.16}$$

$$\text{PPG2}: \quad \sum_{j=0}^{N^k} V^k \frac{\partial N_{\delta\mathbf{u}}^{jjk}}{\partial \mathbf{X}} - \sum_{j=0}^{N^k} V^j \frac{\partial N_{\delta\mathbf{u}}^{kkj}}{\partial \mathbf{X}} = \begin{cases} \mathbf{0} & \text{on } \Omega \backslash \partial\Omega \\ \mathbf{A}^k & \text{on } \partial\Omega \end{cases} \quad \text{and} \tag{5.17}$$

$$\text{PBG}: \quad \sum_{i=0}^{N^k} \sum_{j=0}^{N^i} \frac{V^i V^j}{V^{\mathcal{H}_0^i}} \frac{\partial N_{\delta\mathbf{u}}^{ijk}}{\partial \mathbf{X}} - \sum_{i=0}^{N^k} \sum_{j=0}^{N^k} \frac{V^k V^j}{V^{\mathcal{H}_0^k}} \frac{\partial N_{\delta\mathbf{u}}^{kji}}{\partial \mathbf{X}} = \begin{cases} \mathbf{0} & \text{on } \Omega \backslash \partial\Omega \\ \mathbf{A}^k & \text{on } \partial\Omega \end{cases} , \tag{5.18}$$

where the second sum in the PPG1 and PBG formulation vanish, provided that the test shape functions fulfill additionally the zeroth order consistency condition of equation (5.8). Analogously, for second order VC a quadratic displacement field can be considered which results in the range of linear elasticity to a linear stress distribution. Originating at particle k, the stress in $\mathcal{H}_0^k$, $\mathcal{H}_0^i$ or $\mathcal{H}_0^j$ computes

$$\begin{aligned} &\mathbf{P}^{kj} = \mathbf{P}^{ij} = \mathbf{P}^k + \mathrm{Grad}^k \, \mathbf{P} \cdot \Delta\mathbf{X}^{kj} \quad \text{and} \\ &\mathbf{P}^{jk} = \mathbf{P}^k \, . \end{aligned} \tag{5.19}$$

With the corresponding volume force $\rho_0 V^k \overline{\mathbf{b}}^k = -V^k \, \mathrm{Div}^k \, \mathbf{P}$, the insertion into the local residuals results in

$$\begin{aligned} \text{PPG1}: \quad \mathbf{R}_{\mathbf{u}}^k = & \sum_{j=0}^{N^k} V^k \mathbf{P}^k \cdot \frac{\partial N_{\delta\mathbf{u}}^{kkj}}{\partial \mathbf{X}} - \sum_{j=0}^{N^k} V^j \mathbf{P}^k \cdot \frac{\partial N_{\delta\mathbf{u}}^{jjk}}{\partial \mathbf{X}} \\ & - \sum_{j=0}^{N^k} V^j \, \mathrm{Grad}^k \, \mathbf{P} \cdot \Delta\mathbf{X}^{kj} \cdot \frac{\partial N_{\delta\mathbf{u}}^{jjk}}{\partial \mathbf{X}} - V^k \, \mathrm{Div}^k \, \mathbf{P} + \mathbf{P}^k \cdot \mathbf{A}^k = \mathbf{0} \, , \end{aligned} \tag{5.20}$$

$$\begin{aligned} \text{PPG2}: \quad \mathbf{R}_{\mathbf{u}}^k = & \sum_{j=0}^{N^k} V^j \mathbf{P}^k \cdot \frac{\partial N_{\delta\mathbf{u}}^{kkj}}{\partial \mathbf{X}} - \sum_{j=0}^{N^k} V^k \mathbf{P}^k \cdot \frac{\partial N_{\delta\mathbf{u}}^{jjk}}{\partial \mathbf{X}} \\ & + \sum_{j=0}^{N^k} V^j \, \mathrm{Grad}^k \, \mathbf{P} \cdot \Delta\mathbf{X}^{kj} \cdot \frac{\partial N_{\delta\mathbf{u}}^{kkj}}{\partial \mathbf{X}} - V^k \, \mathrm{Div}^k \, \mathbf{P} + \mathbf{P}^k \cdot \mathbf{A}^k = \mathbf{0} \quad \text{and} \end{aligned} \tag{5.21}$$

$$\begin{aligned}\text{PBG}: \quad \mathbf{R}_{\mathbf{u}}^{k} = & \sum_{i=0}^{N^k}\sum_{j=0}^{N^k} \frac{V^k V^j}{V^{\mathcal{H}_0^k}} \mathbf{P}^k \cdot \frac{\partial N_{\delta\mathbf{u}}^{kji}}{\partial \mathbf{X}} - \sum_{i=0}^{N^k}\sum_{j=0}^{N^i} \frac{V^i V^j}{V^{\mathcal{H}_0^i}} \mathbf{P}^k \cdot \frac{\partial N_{\delta\mathbf{u}}^{ijk}}{\partial \mathbf{X}} \\ & + \sum_{i=0}^{N^k}\sum_{j=0}^{N^k} \frac{V^k V^j}{V^{\mathcal{H}_0^k}} \operatorname{Grad}^k \mathbf{P} \cdot \Delta \mathbf{X}^{kj} \cdot \frac{\partial N_{\delta\mathbf{u}}^{kji}}{\partial \mathbf{X}} \\ & - \sum_{i=0}^{N^k}\sum_{j=0}^{N^i} \frac{V^i V^j}{V^{\mathcal{H}_0^i}} \operatorname{Grad}^k \mathbf{P} \cdot \Delta \mathbf{X}^{kj} \cdot \frac{\partial N_{\delta\mathbf{u}}^{ijk}}{\partial \mathbf{X}} - V^k \operatorname{Div}^k \mathbf{P} + \mathbf{P}^k \cdot \mathbf{A}^k = \mathbf{0}\,. \end{aligned} \tag{5.22}$$

Since both $\mathbf{P}^k$ and $\operatorname{Grad}^k \mathbf{P}$ are arbitrary constants, equation (5.20) leads in addition to the first order constraint, to the condition for second order VC, written in Einstein notation as

$$-\frac{\partial^k P_{AB}}{\partial X_C} \sum_{j=0}^{N^k} V^j \Delta X_C^{kj} \frac{\partial N_{\delta\mathbf{u}}^{jjk}}{\partial X_B} = V^k \frac{\partial^k P_{AB}}{\partial X_B} = V^k \frac{\partial^k P_{AB}}{\partial X_C} 1_{BC}\,, \tag{5.23}$$

or rather symbolically

$$\text{PPG1}: \quad \sum_{j=0}^{N^k} -V^j \Delta \mathbf{X}^{kj} \otimes \frac{\partial N_{\delta\mathbf{u}}^{jjk}}{\partial \mathbf{X}} = V^k \mathbf{1}\,, \tag{5.24}$$

which has to hold for all interior and surface particles. The conditions for second order VC of the PPG2 and PBG formulation can be derived analogously. They state

$$\text{PPG2}: \quad \sum_{j=0}^{N^k} V^j \Delta \mathbf{X}^{kj} \otimes \frac{\partial N_{\delta\mathbf{u}}^{kkj}}{\partial \mathbf{X}} = V^k \mathbf{1} \quad \text{and} \tag{5.25}$$

$$\text{PBG}: \quad \sum_{i=0}^{N^k}\sum_{j=0}^{N^k} \frac{V^k V^j}{V^{\mathcal{H}_0^k}} \Delta \mathbf{X}^{kj} \otimes \frac{\partial N_{\delta\mathbf{u}}^{kji}}{\partial \mathbf{X}} - \sum_{i=0}^{N^k}\sum_{j=0}^{N^i} \frac{V^i V^j}{V^{\mathcal{H}_0^i}} \Delta \mathbf{X}^{kj} \otimes \frac{\partial N_{\delta\mathbf{u}}^{ijk}}{\partial \mathbf{X}} = V^k \mathbf{1}\,, \tag{5.26}$$

where the first term in the condition for the PBG formulation vanishes with zeroth order consistent test shape functions.

5.2 Specific meshfree shape functions

In isoparametric FE methods, the shape functions are constructed on a reference element, having both a defined shape and a fixed number of nodes. In contrast, meshfree shape functions usually have to deal with an arbitrary number of arbitrarily distributed nodes which makes the fulfillment of above defined requirements more challenging.

One class of shape functions that is compatible with an arbitrary number of nodes builds on the barycentric coordinates (WACHSPRESS (1975) and WARREN (1996)), which underlies a geometric description of a convex polygon. With MALSCH & DASGUPTA (2003), FLOATER (2003) and HORMANN & FLOATER (2006) an extension to concave polygons was introduced and also interior nodes were addressed (MALSCH & DASGUPTA, 2004). It is distinguished, inter alia, between Wachspress, mean value, metric and natural neighbor-based coordinates. An overview on their specific properties can be found in SUKUMAR & MALSCH (2006). Further developments include the maximum entropy coordinates (see SUKUMAR (2004) and SUKUMAR (2013)), the harmonic coordinates (JOSHI ET AL., 2007), bi-harmonic coordinates (WEBER ET AL., 2012) and cubic mean value coordinates (LI ET AL., 2013), to name a few.

Barycentric coordinates are usually based on a geometric construction, other meshfree shape functions are defined only by nodal positions by means of an optimization problem. For instance, the least square shape functions lead back to the least-squares (LS) method of Gauss and Legendre and can be defined by a minimization of a least squared error functional. In LANCASTER & SALKAUSKAS (1981) the approximation and interpolation of curves and surfaces was discussed where the least squared errors were combined with a weighting function. A continuous counterpart inspired by the wavelet theory consists in the reproducing kernel shape functions used in the RKPM (LIU ET AL., 1995b). Further developments on least square based interpolations include KUNLE (2001), PLENGKHOM & KANOK-NUKULCHAI (2005), NETUZHYLOV (2008), GRECO & SUKUMAR (2013) and LI & WANG (2016). In the Local Maximum Entropy (LME) approximants, cf. ARROYO & ORTIZ (2006), as a local counter part of the maximum entropy coordinates with radial basis functions, a constrained optimization problem is solved to gain the consistency.

While many meshfree shape functions fulfill the zeroth and first order consistency, the other requirements of section 5.1 are more demanding. Most barycentric coordinate-based shape functions, as well as the LME approximants, posses at least a weak Kronecker delta property, i.e. on the convex boundary. Also the least square based shape functions can have an interpolating character when combined with singular weighting functions. However, the bond mapping criterion and the integration constraint are usually not met a priori. Nevertheless, correction techniques of the shape function derivatives can be utilized to obtain a posteriori bond-conforming and variationally consistent shape functions. Within this thesis, the basis for these corrections consists in a special kind of least square based shape functions. In the following subsection, an introduction to the LS concept is given with an relation to the peridynamic reduction. Subsequently, the shape function derivatives resulting from an interpolating LS approach are derived.

5.2.1 Shape functions of least square regressions

Weighted Least Squares (WLS) and Moving Least Squares (MLS) are fitting techniques for arbitrary point clouds. Within these techniques, a field is approximated by a linear combination of basis functions, like for instance monomials. The coefficients are determined in such a way that the summed squared error is minimized. In case of WLS the errors are weighted statically and in case of MLS dependent on the point of evaluation. Further, specific WLS shape function states are derived with respect to continuous peridynamic states, resulting from a regression of a peridynamic state. The classical discrete formulation of WLS and MLS shape functions can e.g. be found in LANCASTER & SALKAUSKAS (1981) and will be deduced as the discrete counterpart of the peridynamic regression.

Peridynamic regression

Now, consider a scalar state $\underline{f}^k$ within family $\mathcal{H}_0^k$, spanned by the position vector state $\underline{\mathbf{X}}^k$ (see section 3.1 for state notation). The n-th order polynomial regression of $\underline{f}^k$ is defined as

$$\hat{f}^k(\mathbf{X}) = \mathbf{a}^k \cdot \mathbf{p}(\mathbf{X}) \,, \tag{5.27}$$

where $\mathbf{p}$ is a vector containing the complete set of polynomial monomials, e.g. $\mathbf{p}_1 = (1, X, Y, Z)^T$, up to order n, and $\mathbf{a}^k$ denotes its coefficients. Since $\underline{f}^k$ is not generally polynomial, an error state $\underline{\epsilon}^k$ can be computed, specifying the regression error field within $\mathcal{H}_0^k$:

$$\underline{\epsilon}^k = \hat{f}^k\left(\underline{\mathbf{X}}^k\right) - \underline{f}^k \,. \tag{5.28}$$

According to the method of least-squares, the coefficients $\mathbf{a}^k$ can be determined by minimization of the positive weighted squared error integral

$$E^k = \left(\underline{\omega\epsilon}^k\right) \bullet \underline{\epsilon}^k \,. \tag{5.29}$$

The minimization with respect to $\mathbf{a}^k$ yields

$$\min\left(E^k\right) \quad \rightarrow \quad \frac{\partial E^k}{\partial \mathbf{a}^k} = 2\frac{\partial \underline{\epsilon}^k}{\partial \mathbf{a}^k} * \underline{\epsilon}^k = 2\underline{\mathbf{p}}^k * \underline{\epsilon}^k = \mathbf{0} \,. \tag{5.30}$$

By inserting the error state (5.28) and the regression function (5.27) it rewrites

$$\underline{\mathbf{p}}^k * \underline{\mathbf{p}}^k \cdot \mathbf{a}^k - \underline{\mathbf{p}}^k * \underline{f}^k = \mathbf{0} \,. \tag{5.31}$$

Finally, the coefficients compute as the root of equation (5.31) to

$$\mathbf{a}^k = \mathbf{M}^{k^{-1}} \cdot \underline{\mathbf{p}}^k * \underline{f}^k \,, \tag{5.32}$$

with the symmetric positive definite (higher order) shape tensor

$$\mathbf{M}^k = \underline{\mathbf{p}}^k * \underline{\mathbf{p}}^k \,. \tag{5.33}$$

Therefore, the regression function (5.27) is now defined and, by insertion of the coefficients $\mathbf{a}^k$, it can be rewritten analogous to the classical shape function approach in the continuous state notation as

$$\hat{f}^k(\mathbf{X}) = \underline{n}^k(\mathbf{X}) * \underline{f}^k \quad \text{with} \quad \underline{n}^k(\mathbf{X}) = \underline{\mathbf{p}}^k \cdot \mathbf{M}^{k^{-1}} \cdot \mathbf{p}(\mathbf{X}) \,. \tag{5.34}$$

Here, $\underline{n}^k(\mathbf{X})$ denotes a specific shape function state that can be seen as kind of a double state due to its dependency on the position $\mathbf{X}$.

General peridynamic reduction

Analogous to the above derivation of the peridynamic regression, a vector or tensor valued regression can be defined, whereby the order of the coefficient matrix increases. The derivative of this regression function can then be seen as a general peridynamic reduction. Hence, an n-th order reduction of the vector state $\underline{\mathbf{f}}^k$ yields

$$ {}^{n}\mathcal{R}\{\underline{\mathbf{f}}^k\}\,(\mathbf{X}) = \underline{\mathbf{f}}^k * \underline{\mathbf{p}}^k \cdot {\mathbf{M}^k}^{-1} \cdot \frac{\partial \mathbf{p}}{\partial \mathbf{X}} \,. \tag{5.35} $$

where the n-th order complete polynomial basis and a static weighting was implied. Note, that the locally averaged deformation gradient from equation (4.3) which is used in the classical peridynamic correspondence formulation can be gained by the use of linear (difference-based) regression ($\mathbf{p} = \Delta\mathbf{X}$):

$$ {}^{1}\mathcal{R}\{\underline{\Delta\mathbf{x}}^k\} = \Delta\underline{\mathbf{x}}^k * \Delta\underline{\mathbf{X}}^k \cdot {\mathbf{K}^k}^{-1} \cdot \mathbf{1} = \overline{\mathbf{F}}^k \,. \tag{5.36} $$

Discrete WLS and MLS shape functions

For its numerical usage within the PG methods, the peridynamic regression has to be discretized, to fit into the definition of the discretized actual and virtual deformation gradients (4.11) and (4.12). Therefore, the regression function of equation (5.34) can be written in its integral form, evaluated at the position of particle j:

$$ \hat{f}^k\left(\mathbf{X}^j\right) = \int_{\mathcal{H}_0} \underline{\omega}\,(X')\,\mathbf{p}^k\,(X') \cdot {\mathbf{M}^k}^{-1} \cdot \mathbf{p}\left(\mathbf{X}^j\right) f\,(X')\;\, d\mathcal{H}_0 \,. \tag{5.37} $$

The application of the particle discretization of (4.1) leads then to

$$ \hat{f}^k\left(\mathbf{X}^j\right) = \sum_{i=0}^{N^k} \omega^{ki}\mathbf{p}^{ki} \cdot {\mathbf{M}^k}^{-1} \cdot \mathbf{p}^{kj} f^i V^i = \sum_{i=0}^{N^k} N^{kji} f^i \,, \tag{5.38} $$

where all data-independent quantities can be collected with the shape functions

$$ N^{kji}_{WLS} = \omega^{ki}\mathbf{p}^{ki} \cdot {\mathbf{M}^k}^{-1} \cdot \mathbf{p}^{kj} V^i \,. \tag{5.39} $$

As outlined in section 4.2.2, k stands thereby for the family in which the regression is performed and j denotes the evaluation point of the shape function that corresponds to node i. The discrete (higher order) shape tensor, also called mass or moment matrix, follows analogously:

$$ \mathbf{M}^k = \sum_{i=0}^{N^k} \omega^{ki}\, \mathbf{p}^{ki} \otimes \mathbf{p}^{ki} V^i \,. \tag{5.40} $$

Within equation (5.39), the weights ω^{ki} do not depend on the evaluation point $\mathbf{X}^j$. Hence, the regression function as well as its shape functions will generally be a polynomial of the order of the basis ansatz. Since the shape functions arise from a weighted least squared error functional, they are called WLS shape functions and in case of the constant weight $\omega^{ki} = 1$ LS shape functions. With the choice of the weight function, the influence of the nodal values can be regulated via their distances or rather bond lengths:

$$\omega^{ki} = \begin{cases} \frac{1}{\Delta\mathbf{X}^{ki}\cdot\Delta\mathbf{X}^{ki}} & \forall\, i \neq k \\ 0 & \forall\, i = k \end{cases}, \tag{5.41}$$

In such a way, the regression function will fit nodal values near the master particle k more precisely and in case of regular particle distributions, the locality of the weight function can even be increased by potentiating the denominator. Further, the concept of MLS involves a movement of this weight function perspective with the evaluation point $\mathbf{X}^j$ of the shape functions:

$$\omega^{ji} = \begin{cases} \frac{1}{\Delta\mathbf{X}^{ji}\cdot\Delta\mathbf{X}^{ji}} & \forall\, i \neq j \\ 0 & \forall\, i = j \end{cases}, \tag{5.42}$$

Thereby, the regression function becomes the form

$$N^{kji}_{MLS} = \omega^{ji}\mathbf{p}^{ki} \cdot \mathbf{M}^{kj^{-1}} \cdot \mathbf{p}^{kj} V^i\,. \tag{5.43}$$

Note, that due to the moving weight function, also the shape tensor becomes evaluation point dependent:

$$\mathbf{M}^{kj} = \sum_{i=0}^{N^k} \omega^{ji}\, \mathbf{p}^{ki} \otimes \mathbf{p}^{ki} V^i\,. \tag{5.44}$$

Thanks to the particle discretization, only shape function derivatives occur in the discretized weak forms of Table 4.1. Considering WLS shape functions, its derivative can be gained simply by differentiation of the monomials:

$$\frac{\partial N^{kji}_{WLS}}{\partial \mathbf{X}} = \omega^{ki}\mathbf{p}^{ki} \cdot \mathbf{M}^{k^{-1}} \cdot \frac{\partial \mathbf{p}^{kj}}{\partial \mathbf{X}} V^i\,. \tag{5.45}$$

Within the MLS shape functions, the coefficients $\mathbf{a}^k$ are also a function of the position and have to be taken into account. However, in the scope of collocation combined with singular weight functions it can also be reduced to a differentiation of the basis, cf. LANCASTER & SALKAUSKAS (1986):

$$\frac{\partial N^{kji}_{MLS}}{\partial \mathbf{X}} = \omega^{ji}\mathbf{p}^{ki} \cdot \mathbf{M}^{kj^{-1}} \cdot \frac{\partial \mathbf{p}^{kj}}{\partial \mathbf{X}} V^i\,. \tag{5.46}$$

Note, that due to the collocation, the weight function also has to be evaluated at the respective point, i.e. at the singularity. This fact causes numerical troubles (see LI & WANG (2016)) and can e.g. be treated by means of an augmentation of the denominator or (like above) by an numerical exception that sets the weight to zero at the concerning particle. The latter destroys the interpolative character and equation (5.46) is no longer valid. Therefore, the AD tool AceGen is further used to derive the shape function derivatives whenever MLS shape functions are used:

$$\frac{\partial N^{kji}_{MLS}}{\partial \mathbf{X}} = \frac{\hat{\delta} N^{kji}_{MLS}}{\hat{\delta} \mathbf{X}} \,. \tag{5.47}$$

5.2.2 A Moving Taylor Expansion

To circumvent the ill-conditioning while using singular weight functions in a MLS approximation, one can define a reference position around which the regression is performed. When moving this reference position, an interpolating function can be set up where the derivative can be calculated directly from differences. Consider the following Taylor expansion with the reference position $\mathbf{X}^j$:

$$\hat{f}^k\left(\mathbf{X}\right) = a^k_0 1 + \mathbf{a}^k_\Delta \cdot \left(\mathbf{X} - \mathbf{X}^j\right) + \dots = a^k_0 1 + \mathbf{a}^k_\Delta \cdot \mathbf{p}_\Delta\left(\mathbf{X} - \mathbf{X}^j\right) \,, \tag{5.48}$$

where the difference-based monomials of order $n > 0$ are stored within the vector $\mathbf{p}_\Delta$ and the corresponding coefficients in $\mathbf{a}^k_\Delta$. Direct evaluation at the reference position $\mathbf{X}^j$ yields

$$\hat{f}^k\left(\mathbf{X}^j\right) = a^k_0 1 + \mathbf{a}^k_\Delta \cdot \mathbf{0} = f^j \quad \rightarrow \quad a^k_0 = f^j \,. \tag{5.49}$$

where it was set to the nodal value to imply an a priori interpolation property. The remaining coefficients can now be determined in a least square sense by minimizing the squared error

$$E^{kj} = \sum_{i=0}^{N^k} \omega^{ji} \left[f^i - \left(f^j + \mathbf{a}^k_\Delta \cdot \mathbf{p}^{ji}_\Delta \right) \right]^2 V^i \,. \tag{5.50}$$

In analogy to equation (5.32), the remaining coefficients compute as

$$\mathbf{a}^k_\Delta = \sum_{i=0}^{N^k} \omega^{ji} \mathbf{M}^{kj^{-1}}_\Delta \cdot \mathbf{p}^{ji}_\Delta V^i \Delta f^{ji} \quad \text{with} \quad \mathbf{M}^{kj}_\Delta = \sum_{i=0}^{N^k} \omega^{ji} \mathbf{p}^{ji}_\Delta \otimes \mathbf{p}^{ji}_\Delta V^i \,. \tag{5.51}$$

By insertion of the coefficients into the Taylor expansion (5.48), differentiation with respect to $\mathbf{X}$ and elimination of the nodal values, the shape function derivatives can be computed as

$$\frac{\partial N^{kji}_{MTE}}{\partial \mathbf{X}} = \begin{cases} \omega^{ji} V^i \mathbf{p}^{ji}_\Delta \cdot \mathbf{M}^{kj^{-1}}_\Delta \cdot \frac{\partial \mathbf{p}^{jj}_\Delta}{\partial \mathbf{X}} & \forall\, i \neq j \\ -\sum_{l=0, l\neq j}^{N^k} \frac{\partial N^{kjl}_{MTE}}{\partial \mathbf{X}} & \forall\, i = j \end{cases} \,, \tag{5.52}$$

where the derivative of the shape function at the evaluation point is computed by means of the zeroth order consistency condition (5.8). The derivatives (5.52) of the moved Taylor expansion will further be denoted as the derivatives of Moving Taylor Expansion (MTE) shape functions. Analogously, Weighted Taylor Expansion (WTE) shape functions can be gained by setting the reference point statically to the position of the master particle $\mathbf{X}^k$.

Since the derivation of the WLS, MLS, WTE and MTE shape functions are based on the minimization of a squared error potential, they guarantee consistency up to the order of completeness of their basis ansatz. In other words, the error (5.50) minimizes to zero in case

Table 5.1. Abbreviations of Weighted and Moving Least Square and Taylor Expansion shape functions and their exemplary polynomial basis in two dimensions.

Abbreviation	Exemplary basis for 2-D
MTE1	$\mathbf{p}_{\Delta}^{ji} = (\Delta X^{ji}, \Delta Y^{ji})^T$
MLS1	$\mathbf{p}^{ji} = (1, \Delta X^{ji}, \Delta Y^{ji})^T$
WTE1	$\mathbf{p}_{\Delta}^{ji} = \mathbf{p}_{\Delta}^{ki} = \left(\Delta X^{ki}, \Delta Y^{ki}\right)^T$
WLS1	$\mathbf{p}^{ji} = \mathbf{p}^{ki} = \left(1, \Delta X^{ki}, \Delta Y^{ki}\right)^T$
WTE2	$\mathbf{p}_{\Delta}^{ji} = \mathbf{p}_{\Delta}^{ki} = \left(\Delta X^{ki}, \Delta Y^{ki}, \Delta X^{ki2}, \Delta X^{ki}\Delta Y^{ki}, \Delta Y^{ki2}\right)^T$
WLS2	$\mathbf{p}^{ji} = \mathbf{p}^{ki} = \left(1, \Delta X^{ki}, \Delta Y^{ki}, \Delta X^{ki2}, \Delta X^{ki}\Delta Y^{ki}, \Delta Y^{ki2}\right)^T$

the nodal values can be represented by the basis. To ensure the invertibility of the shape tensor it is necessary to have a sufficient large number of neighbor particles within each dimensional direction. If, for instance, a linear basis is considered, the convex hull of all family members has at least to be a simplex of the corresponding dimension. In the further work, different combinations of the shape functions are utilized that can be summarized by the exemplary set of basis listed in Table 5.1, combined with the static weights (5.41) (WLS and WTE) or moving weights (5.42) (MLS and MTE).

5.3 Modification of shape function derivatives

In contrast to the consistency criteria and the Kronecker delta property, the bond mapping criterion and integration constraints for the fulfillment of the configurational and VC are not met by the previously derived shape functions. Therefore, correction techniques can be designed to obtain these properties by manipulating the shape function derivatives. In Bubnov-Galerkin formulations, the challenging aspect in achieving such shape function derivatives is to preserve the other properties while doing the correction. In the following, methodologies are presented in which the uncorrected shape functions $\hat{N}$ are enforced to be bond-conforming. In a second step, the variationally inconsistent functions $\tilde{N}$ are modified to be variationally consistent.

5.3.1 Restoration of bond mapping

Considering a linear deformation field, the deformation gradient resulting from a first order consistent shape function approximation is constant and accurate. Further, within this linear deformation, the deformation gradient approximation maps any distance vector accurately from the initial to the current configuration. Within a nonlinear deformation field, the deformation gradient does not guarantee an accurate mapping of the bonds and the mapped bond will generally deviate from the current bond. In BREITZMAN & DAYAL (2018), a correction of an averaged deformation gradient was presented in which it is modified only in the direction of the bond by removing the error of the homogeneous deformation assumption in the direction of the bond $\Delta \mathbf{X}^{kj}$ and adding the correctly mapped bond:

$$\begin{aligned}
\Delta \mathbf{x}^{kj} &= \mathbf{F}^{kj} \cdot \Delta \mathbf{X}^{kj} = \Delta \mathbf{x}^{kj}_{pred} - \Delta \mathbf{x}^{kj}_{pred} + \Delta \mathbf{x}^{kj} \\
&= \mathbf{F}^{kj}_{pred} \cdot \Delta \mathbf{X}^{kj} - \mathbf{F}^{kj}_{pred} \cdot \Delta \mathbf{X}^{kj} + \Delta \mathbf{x}^{kj} \\
&= \mathbf{F}^{kj}_{pred} \cdot \Delta \mathbf{X}^{kj} - \mathbf{F}^{kj}_{pred} \cdot \Delta \mathbf{X}^{kj} \left(\frac{\Delta \mathbf{X}^{kj}}{|\Delta \mathbf{X}^{kj}|} \cdot \frac{\Delta \mathbf{X}^{kj}}{|\Delta \mathbf{X}^{kj}|} \right) + \Delta \mathbf{x}^{kj} \left(\frac{\Delta \mathbf{X}^{kj}}{|\Delta \mathbf{X}^{kj}|} \cdot \frac{\Delta \mathbf{X}^{kj}}{|\Delta \mathbf{X}^{kj}|} \right) \\
&= \left[\mathbf{F}^{kj}_{pred} \cdot \left(\mathbf{1} - \frac{\Delta \mathbf{X}^{kj}}{|\Delta \mathbf{X}^{kj}|} \otimes \frac{\Delta \mathbf{X}^{kj}}{|\Delta \mathbf{X}^{kj}|} \right) + \frac{\Delta \mathbf{x}^{kj}}{|\Delta \mathbf{X}^{kj}|} \otimes \frac{\Delta \mathbf{X}^{kj}}{|\Delta \mathbf{X}^{kj}|} \right] \cdot \Delta \mathbf{X}^{kj} \,,
\end{aligned} \tag{5.53}$$

where in the third line, the identity $\frac{\Delta \mathbf{X}^{kj}}{|\Delta \mathbf{X}^{kj}|} \cdot \frac{\Delta \mathbf{X}^{kj}}{|\Delta \mathbf{X}^{kj}|} = 1$ is exploited and reordered in line four. The singular tensor $\left(\mathbf{1} - \frac{\Delta \mathbf{X}^{kj}}{|\Delta \mathbf{X}^{kj}|} \otimes \frac{\Delta \mathbf{X}^{kj}}{|\Delta \mathbf{X}^{kj}|} \right)$ removes the information of the predicted deformation gradient, while $\frac{\Delta \mathbf{x}^{kj}}{|\Delta \mathbf{X}^{kj}|} \otimes \frac{\Delta \mathbf{X}^{kj}}{|\Delta \mathbf{X}^{kj}|}$ adds the accurate mapping in the direction of the concerning bond. This procedure can be shifted to a manipulation of shape functions, independent on the deformation field which yields the following bond-conforming deformation gradient

$$\begin{aligned}
\mathbf{F}^{kj} &= \sum_{i=0}^{N^k} \Delta \mathbf{x}^{ki} \otimes \frac{\partial \tilde{N}^{kji}}{\partial \mathbf{X}} \\
&= \sum_{i=0}^{N^k} \left(\Delta \mathbf{x}^{ki} \otimes \frac{\partial \hat{N}^{kji}}{\partial \mathbf{X}} \right) \cdot \left(\mathbf{1} - \frac{\Delta \mathbf{X}^{kj}}{|\Delta \mathbf{X}^{kj}|} \otimes \frac{\Delta \mathbf{X}^{kj}}{|\Delta \mathbf{X}^{kj}|} \right) + \Delta \mathbf{x}^{kj} \otimes \frac{\Delta \mathbf{X}^{kj}}{|\Delta \mathbf{X}^{kj}|^2} \,.
\end{aligned} \tag{5.54}$$

Here, $\hat{N}^{kji}$ are the uncorrected shape functions and

$$\frac{\partial \tilde{N}^{kji}}{\partial \mathbf{X}} = \left(\mathbf{1} - \frac{\Delta \mathbf{X}^{kj}}{|\Delta \mathbf{X}^{kj}|} \otimes \frac{\Delta \mathbf{X}^{kj}}{|\Delta \mathbf{X}^{kj}|} \right) \cdot \frac{\partial \hat{N}^{kji}}{\partial \mathbf{X}} + \delta^{ji} \frac{\Delta \mathbf{X}^{kj}}{|\Delta \mathbf{X}^{kj}|^2} \tag{5.55}$$

denote the corrected ones. As the above procedure is driven by an error, it can be shown that the linear consistency is preserved, even though the formal zeroth order consistency condition of equation (5.8) is violated, which restricts the Galerkin-ansatz to the difference-based form of equation (4.11). However, for higher order consistency, the approximated deformation gradient at a neighbor particle does not necessarily have to map the distance vector to it correctly and the high order consistency would be disturbed by the upper linear bond mapping correction. Hence, the bond correction will further only be used in the case of a linear basis. Alternatively, a higher order bond correction may be derived where also the second order shape function derivatives would have to be considered.

5.3.2 Restoration of variational consistency

The variational inconsistency of the PG methods stems from the inaccurate numerical integration of the weak form. On the one hand, this comes from the non-conforming shape of the meshfree particles and, on the other hand, from the predetermined integration point positions due to the collocation. In order to regain the VC, the discrete shape function derivatives can be modified to compensate the integration error and restore the Galerkin orthogonality by fulfilling the integration constraints (see e.g. BONET & KULASEGARAM (2000) in the context of SPH). In view of the peridynamic integration constraints of equations (5.16), (5.17) and (5.18), such a correction has to be made on the global level, since the pairwise local residual depends also on the shape functions of its neighboring families. Note, that the globally coupled problem can be transferred to a set of larger local problems as outlined in section 8.2. Further on, a correction is proposed that is structured as follows: First, the correction approach is stated, based on a combination of correction shape functions and correction factor unknowns. Then follows the derivation of preservation conditions to maintain consistency and bond conformity. Further on, correction functions are constructed that are in agreement with the prior defined preservation conditions. And finally, the determination of the correction factors is addressed to solve the integration constraints.

Correction approaches

As already mentioned, the local conditions for VC, derived in section 5.1.4, are globally coupled due to the pairwise formulation. One way to perform a correction of the VC is to define an additive ansatz for the corrected shape function derivatives and insert it in the integration constraints. By using a linear combination of correction shape functions and correction factor unknowns for each integration constraint, the resulting set of equations form a linear system of equations that can be solved for the correction factor unknowns. Starting with variationally inconsistent (though possibly bond-conforming) shape functions $\tilde{\mathbf{N}}$, the correction ansatz can be written

$$\frac{\partial \hat{N}^{kji}}{\partial \mathbf{X}} = \frac{\partial \tilde{N}^{kji}}{\partial \mathbf{X}} + \sum_{d=1}^{n_{dim}} \alpha^{k}_{1\,d} \Phi^{kji}_{d} \mathbf{e}_{d} + \sum_{d=1}^{n_{dim}} \sum_{e=1}^{n_{dim}} \alpha^{k}_{2\,de} \Delta X^{kj}_{e} \Phi^{kji}_{d} \mathbf{e}_{d} \,. \tag{5.56}$$

While linear VC can be obtained with the first correction term, for second order VC the second one has to be added. Thereby, $\mathbf{\Phi}^{kji}$ stands for the correction shape functions, $\mathbf{e}_d$ is the Cartesian basis and $\alpha^{k}_{1\,d}$ and $\alpha^{k}_{2\,de}$ denote the correction factor unknowns.

Preservation conditions

Within PPG formulations, the test and trial functions are generally independent on each other, and whereas consistency is a matter of trial functions, the test shape functions are suspect to the integration constraints. However, in case of PBG formulations or the mixed methods introduced in chapter 6, the trial and test functions have to coincide. Therefore, the correction of VC must not interfere with the consistency criteria in these cases. This can be ensured, by inserting the correction ansatz (5.56) into the consistency criteria (5.8), resulting in preservation conditions on the correction shape functions. When considering the VC correction of first order, the following constraints apply for a conservation of zeroth, first and second order consistency, respectively:

$$\sum_{i=0}^{N^k} \boldsymbol{\Phi}^{kji} = \mathbf{0}\,, \quad \sum_{i=0}^{N^k} \Delta\mathbf{X}^{ki} \otimes \boldsymbol{\Phi}^{kji} = \mathbf{0} \quad \text{and} \tag{5.57}$$

$$\sum_{i=0}^{N^k} \Delta\mathbf{X}^{ki} \otimes \Delta\mathbf{X}^{ki} \otimes \boldsymbol{\Phi}^{kji} = \mathbf{0}\,. \tag{5.58}$$

Additionally, the linear configurational consistency (equation (5.12)) can be preserved if the correction shape functions satisfy

$$\left(\sum_{i=0}^{N^k} \Delta\mathbf{u}^{ki} \otimes \boldsymbol{\Phi}^{kji} \right) \cdot \Delta\mathbf{X}^{kj} = \mathbf{0}\,, \quad \forall \Delta\mathbf{u}^{ki} \in \mathbb{R}^{n_{dim}}\,. \tag{5.59}$$

Construction of correction functions

When setting up the correction shape functions, the similarity between the preservation conditions (5.57) and (5.58) with the consistency conditions (5.1), (5.2) and (5.4) can be exploited. A straightforward choice in the scope of Petrov-Galerkin methods would be a constant correction function (see e.g. CHEN ET AL. (2013)). By adding an exception at the master particle, the zeroth order consistency can be restored:

$$\boldsymbol{\Phi}^{kji}_{V1} = \left(1 - \delta^{kj} N^k\right) \sum_{d=1}^{n_{dim}} \mathbf{e}_d\,. \tag{5.60}$$

A second possibility consists in the usage of second order derivatives of linearly consistent shape functions (cf. PUSO ET AL. (2008)), as e.g.

$$\boldsymbol{\Phi}^{kji}_{V2} = \frac{\partial^2 N^{kji}_{WLS2}}{\partial \mathbf{X}^2}\,, \tag{5.61}$$

where this version conserves also the first order consistency which can be seen when differentiating the derivatives of the consistency conditions (5.6). Further, a linearly consistent shape function can be utilized for the correction of the derivatives. Therefore, to fulfill also the zeroth order preservation condition, the Kronecker delta has to be subtracted, leading to the correction function

$$\boldsymbol{\Phi}^{kji}_{V3} = \left(N^{kki}_{MLS1} - \delta^{ki}\right) \sum_{d=1}^{n_{dim}} \mathbf{e}_d\,. \tag{5.62}$$

If the preservation of second order consistency (5.58) is needed for the correction of linear VC, the same approach can be used with second order consistent shape functions as

$$\mathbf{\Phi}_{V4}^{kji} = \left(N_{WLS2}^{kki} - \delta^{ki}\right) \sum_{d=1}^{n_{dim}} \mathbf{e}_d \,. \tag{5.63}$$

Further, the approach (5.62) can be modified, analogously to (5.55), to conserve also the accurate mapping of bonds. In this case, the correction function computes

$$\mathbf{\Phi}_{V5}^{kji} = \left(\mathbf{1} - \frac{\Delta\mathbf{X}^{kj} \otimes \Delta\mathbf{X}^{kj}}{|\Delta\mathbf{X}^{kj}|^2}\right) \cdot \left(N_{MLS1}^{kki} - \delta^{ki}\right) \sum_{d=1}^{n_{dim}} \mathbf{e}_d \,. \tag{5.64}$$

Calculation of correction degrees of freedom

With the definition of the correction ansatz (5.56) and the selection of suitable correction shape functions, the global set of integration constraints can be assembled. Therefore, the integration constraints of section 5.1.4 are treated as the residual

$$\hat{\mathbf{R}}_\beta = \mathop{\mathbf{A}}_{k=1}^{n_p} \left\{\hat{\mathbf{R}}_\beta^k\right\} , \tag{5.65}$$

where $\hat{\mathbf{R}}_\beta^k$ denotes the local residual of the VC correction. In case of a correction of linear VC ($\beta = 1$), the local residual for the PBG methods computes

$$\hat{\mathbf{R}}_1^k = \sum_{i=0}^{N^k} \sum_{j=0}^{N^i} \frac{V^i V^j}{V^{\mathcal{H}_0^i}} \frac{\partial \hat{N}_{\delta\mathbf{u}}^{ijk}}{\partial \mathbf{X}} - \sum_{i=0}^{N^k} \sum_{j=0}^{N^k} \frac{V^k V^j}{V^{\mathcal{H}_0^k}} \frac{\partial \hat{N}_{\delta\mathbf{u}}^{kji}}{\partial \mathbf{X}} - \mathbf{A}^k \tag{5.66}$$

and for second order VC ($\beta = 2$) additionally

$$\hat{\mathbf{R}}_2^k = \sum_{i=0}^{N^k} \sum_{j=0}^{N^k} \frac{V^k V^j}{V^{\mathcal{H}_0^k}} \Delta\mathbf{X}^{kj} \otimes \frac{\partial \hat{N}_{\delta\mathbf{u}}^{kji}}{\partial \mathbf{X}} - \sum_{i=0}^{N^k} \sum_{j=0}^{N^i} \frac{V^i V^j}{V^{\mathcal{H}_0^i}} \Delta\mathbf{X}^{kj} \otimes \frac{\partial \hat{N}_{\delta\mathbf{u}}^{ijk}}{\partial \mathbf{X}} - V^k \mathbf{1} \,. \tag{5.67}$$

Now, the correction factor unknowns have to be varied, such that the error in the integration constraints goes to zero. Since the correction ansatz (5.56) is based on a linear combination of correction factors and correction functions, the resulting system is linear. Hence, the collective nodal unknowns can be determined by the solution of

$$\frac{\partial \hat{\mathbf{R}}_\beta}{\partial \boldsymbol{\alpha}_\beta} \cdot \boldsymbol{\alpha}_\beta = -\hat{\mathbf{R}}_\beta \tag{5.68}$$

where $\hat{\mathbf{R}}_\beta$ is the error of the variationally inconsistent shape functions. Thereby, the tangent matrix $\frac{\partial \hat{\mathbf{R}}_\beta}{\partial \boldsymbol{\alpha}_\beta}$ can be derived analogous to the tangent matrix of the weak form of section 4.6. However, an eigen mode analysis of the resulting tangent matrix of equation shows that zero eigen values can occur. In fact, for the correction of linear VC, as many zero eigen values are present as consistency conditions are preserved in the correction. This means, independent of the discretization, there exist e.g. $2 + 4 = 6$ zero eigen values for the preservation of

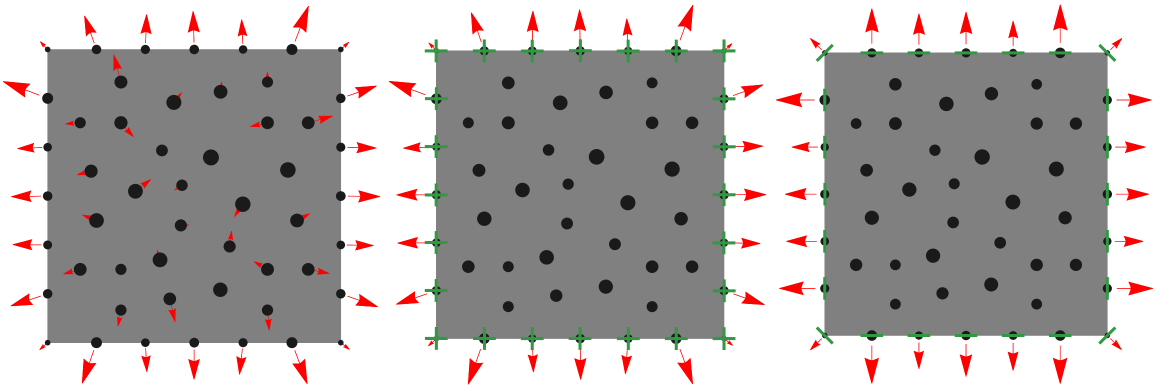

(a) Variationally inconsistent (b) Fixed correction factors at surface (c) Fixed correction factors perpendicular to surface

Figure 5.1. On the left: Spurious surface approximations at interior nodes resulting from variationally inconsistent test functions. On the right: The correction of VC forces the surface vectors to be zero apart from nodes on the surface. The boundary conditions of the correction are represented by green lines.

linear consistency in 2-D during the correction of linear VC.

Therefore, the solution of the concerning system needs particular consideration in the application of boundary conditions such that the tangent matrix does not get singular, cf. PUSO ET AL. (2008). A straightforward elimination of a certain number of zero eigen modes would be the fixing of the same number of degrees of freedom at selected particles. However, with increasing refinement, such boundary conditions act like a singularity which decreases the condition of the correction system. A possibility to circumvent this issue consists in the fixing of the degrees of freedom at the entire surface $\partial\Omega_0$, though as a reaction, the normals at the according particles do not match those of Finite Elements anymore. This is generally not a problem, but if the particles shall be coupled with Finite Element nodes, the normals should match. Therefore, a feasible compromise is the fixing of the correction factor only in normal direction at the surface by means of nodal Lagrangian multipliers.

The effect of the resulting correction can be seen in Figure 5.1 where the nodal surface normals are computed using the PPG1 first order VC criterion as in equation (4.33). The nodal imposition of boundary conditions for the correction procedure is visualized by green lines perpendicular to the fixed correction factor unknown. Whereas the uncorrected test shape functions lead to erroneous normals, the variationally consistent ones produce reasonable normals. Note, that within a total Lagrangian framework, the correction factors do not change during the simulation and their computation and thus also the construction of variationally consistent and bond-conforming shape functions can be done as part of the preprocessing.

Chapter 6

Specific Peridynamic-Galerkin formulations

With the different correspondence formulations presented in section 4.2 and the choice of shape functions with their optional correction, various possible combinations arise. In the following section, the most relevant displacement-based combinations are presented. Further on, two techniques will be introduced that are directed towards the modeling within the presence of volumetric geometric constraints: The construction of mixed displacement–pressure–dilation approaches is addressed in section 6.2, whereupon the underintegration of the weak form and its subsequent stabilization follows in section 6.3.

6.1 Displacement based formulations

The general peridynamic weak form (4.14) with (4.16) offers a wide scope for the design of a specific formulation and therefore also the setting of its properties. By means of a Galerkin approach, three different correspondence formulations were derived, leading to the weak forms of the PPG1, PPG2 and PBG methods, which then still require a definition of shape functions. On the one hand, the Petrov-Galerkin methods differentiate between trial and test functions. This makes it easier to fulfill the conditions of both test and trial shape functions, respectively. However, as a result, the tangent stiffness matrix is not anymore symmetric, even in modeling a hyperelastic material response. The symmetry which is actually intrinsic to conservative systems can be achieved through a Bubnov-Galerkin approach with an equivalence of the trial and test functions. This, in turn, leads to a more cumbersome treatment of the shape functions in order to satisfy their requested properties.

As for the trial functions, the consistency plays and important role for their expectable convergence rate. A straightforward possibility to achieve optimal consistency with respect to the number of basis monomials consists in the usage of n-th order WTE shape functions for the approximation of the actual displacements. In this case, the same local trial space is spanned as in n-th order triangle or rather tetrahedron elements and it will further be denoted as an Un approach. The fully integrated Un PG formulations generally posses a full rank of the global stiffness matrix, independent on the number of neighbor particles, which is due to its overlapping supports. Exceptions are the U1 formulations that are suspect to global low-energy modes. In fact, the U1 formulations can be reduced to the classical peridynamic correspondence formulation or the total Lagrangian corrected SPH.

Accompanied with an increase of the order of consistency, the neighborhood size has to enlarge which increase both the number of integration points per family and the density of the tangent stiffness matrix. An effective way in constructing a stable low-order formulation consists in moving weight functions. Thereby, the linear basis of the MTE1 shape functions can be used to construct nonlinear shape functions, which lead to Unl (nonlinear displacement) formulations. Additionally, the bond-mapping correction (5.55) can enhance the behavior of the trial space in correlating the deformation of each bond directly with a strain energy and employing a bijective peridynamic reduction.

Within the scope of PBG formulations, the test and trial functions have to coincide. Therefore, also the trial shape functions have to posses the linear VC to ensure a proper convergence. To not disturb the consistency and bond-mapping properties, the shape functions of the PBG Unl formulation can be constructed as follows: Starting with the MTE1 shape functions and the bond-mapping correction (5.55), the correction of VC has to be performed with the Φ_{V5} correction shape functions (5.64). On the other hand, a PBG U2 formulation can be gained using WTE2 shape functions combined with the Φ_{V4} correction shape functions (5.63) in a linear VC correction. If second order VC is requested, a WLS3 basis for the correction function would be needed.

The chose of a Petrov-Galerkin method simplifies the treatment of the test functions, as they generally do not have to be consistent and bond-conforming anymore, and they are only once evaluated within the PPG1 and PPG2 correspondence formulations. Thus, the correction of VC has to be performed only on the test shape functions, such that also constant correction functions can be applied. Furthermore, it is possible to construct arbitrary trial-test function combinations. Some possible combinations include the U2 formulations WTE2-WTE1 and WTE2-LME or the Unl formulations MTE1-WTE1 and MTE1-LME. As already mentioned, the drawbacks of the PPG formulations are the loss of symmetry of the tangent stiffness matrix, the violation of the local preservation of angular momentum and the decreased robustness compared to its Bubnov-Galerkin relatives.

6.2 Mixed displacement–pressure–dilation approaches

Although the formulations presented in section 6.1 can obtain optimal rates of convergence, provided that they are variationally consistent, they exhibit the phenomenon of volumetric locking, which is known from displacement based Finite Elements. A classical technique to circumvent this issue consists in the separate treatment of the isochoric and volumetric parts in terms of a Hu-Washizu potential (see section 2.4.2). Thereby, only the isochoric part of the deformation is handled by the mere displacement based approach via an isochoric strain energy function. The dilation and the resulting pressure are taken into account by means of the additional potential (2.59), whereby the pressure and dilation are implemented as degrees of freedom, leading to a mixed $\mathbf{u}$–p–Θ formulation. The discretization of the three field variational principle of equation (2.59) follows in the sense of the PPG and PBG methods with equation (4.1) to

$$\Pi_h = \mathop{\mathbf{A}}_{k=1}^{n_p} \left\{\Pi^k\right\} \quad \text{with} \tag{6.1}$$

$$\text{PPG:} \quad \Pi^k = V^k \left[\frac{K}{4}\left(\Theta^{k2} - 1 - 2\ln\Theta^k\right) + p^k\left(J^k - \Theta^k\right)\right] \quad \text{or} \tag{6.2}$$

$$\text{PBG:} \quad \Pi^k = \frac{V^k}{V^{\mathcal{H}_0^k}} \sum_{j=0}^{N^k} V^j \left[\frac{K}{4}\left(\Theta^{kj2} - 1 - 2\ln\Theta^{kj}\right) + p^{kj}\left(J^{kj} - \Theta^{kj}\right)\right] , \tag{6.3}$$

where for the PBG methods the inverse averaging, analogous to equation (4.24), was conducted. Note here, that the additional Hu-Washizu potential of the PPG formulations can be gained by a selective underintegration of the the additional PBG Hu-Washizu potential. Within equations (6.2) and (6.3), the approximations for the family dilation, pressure and Jacobian field have still to be specified which is suspect to the subsequent subsections. Independent on the approximation, the additional family-wise residual and tangent contribution due to the Hu-Washizu potential can be derived by analogy with equation (2.60) as

$$\mathbf{R}_{\Pi}^{\mathcal{H}_0^k} = \frac{\hat{\delta}\Pi^k}{\hat{\delta}\mathbf{p}^{\mathcal{H}_0^k}} \quad \text{and} \quad \mathbf{K}_{\Pi}^{\mathcal{H}_0^k} = \frac{\hat{\delta}\mathbf{R}_{\Pi}^{\mathcal{H}_0^k}}{\hat{\delta}\mathbf{p}^{\mathcal{H}_0^k}} \quad \text{with} \quad \mathbf{p}^{\mathcal{H}_0^k} = \left[\mathbf{u}^{\mathcal{H}_0^k T}, \mathbf{p}^{\mathcal{H}_0^k T}, \mathbf{\Theta}^{\mathcal{H}_0^k T}\right]^T , \tag{6.4}$$

with the use of Automatic Differentiation and the collective unknowns $\mathbf{p}^{\mathcal{H}_0^k}$. The structure of the resulting family-wise tangent matrix for weakly compressible and incompressible ($\Theta = 1$) material behavior states

$$\mathbf{K}_{\Pi}^{\mathcal{H}_0^k} = \begin{pmatrix} \mathbf{K_{uu}} & \mathbf{K_{up}} & \mathbf{0} \\ \mathbf{K_{pu}} & \mathbf{0} & \mathbf{K_{p\Theta}} \\ \mathbf{0} & \mathbf{K_{\Theta p}} & \mathbf{K_{\Theta\Theta}} \end{pmatrix} \quad \text{or rather} \quad \mathbf{K}_{\Pi}^{\mathcal{H}_0^k} = \begin{pmatrix} \mathbf{K_{uu}} & \mathbf{K_{up}} \\ \mathbf{K_{pu}} & \mathbf{0} \end{pmatrix} . \tag{6.5}$$

In case of local pressure and dilation unknowns, the weakly compressible problem can be statically condensed to the displacement degrees of freedom, cf. GUYAN (1965). This leads to the effective displacement based tangent matrix

$$\mathbf{K}_{eff} = \mathbf{K_{uu}} + \mathbf{K_{up}} \cdot \mathbf{K}_{\mathbf{\Theta p}}^{-1} \cdot \mathbf{K_{\Theta\Theta}} \cdot \mathbf{K}_{\mathbf{p\Theta}}^{-1} \cdot \mathbf{K_{pu}} . \tag{6.6}$$

The separation of the isochoric and volumetric strain energy leads also to an additive split of the pairwise force density into an isochoric and volumetric part ($\mathbf{t}^{kj} = \mathbf{t}_{iso}^{kj} + \mathbf{t}_{vol}^{kj}$). Since the internal forces can be expressed with pairwise force densities, the preservation of the local conservation of linear momentum is satisfied. In appendix B, the expression of the volumetric correspondence formulations are derived which write

$$\text{PPG:} \quad \mathbf{t}^{kj}_{vol} = -\frac{1}{V^k}\mathbf{P}^{j}_{vol} \cdot \frac{\partial N^{jjk}}{\partial \mathbf{X}} \quad \text{and} \tag{6.7}$$

$$\text{PBG:} \quad \mathbf{t}^{kj}_{vol} = \frac{1}{V^j V^{\mathcal{H}^k_0}} \sum_{i=0}^{N^k} V^i \mathbf{P}^{ki}_{vol} \cdot \frac{\partial N^{kij}}{\partial \mathbf{X}} \,. \tag{6.8}$$

that are in analogy to equations (4.21) and (4.30). Furthermore, the local preservation of angular momentum is conserved within the Bubnov-Galerkin methods as the structure of the pairwise force expression does not change (see equation (4.65)). In the following, some classically used function spaces for the local displacement pressure and dilation field are exploited for the use in the PG methods.

6.2.1 Constant pressure and dilation

First of all, a peridynamic analogon of the Q1P0 element of SIMO ET AL. (1985) is presented. Therefore, the displacement field is set to be equivalent to the fully integrated stable Unl formulation, i.e. it is interpolated with the MTE1 shape functions. In case of the PPG version, the trial shape functions are bond-corrected, while the test shape functions are corrected to be variationally consistent. For the PBG counterpart, the trial and test shape functions coincide and both corrections are performed. The pressure and dilation field, on the other hand, are approximated as constants within each family:

$$p^{kj} = p^k \quad \text{and} \quad \Theta^{kj} = \Theta^k \,. \tag{6.9}$$

Since the family-wise pressure and dilation approximation do not directly depend on the values at its neighboring particles, they can be treated as local unknowns. Hence, a static condensation according to equation (6.6) eliminates the additional set of equations arising from the pressure and dilation variation. The resulting formulation with a local nonlinear displacement field (with linear basis) and constant pressure and dilation will further be termed UnlP0. In case of incompressible material behavior, i.e. $\nu = 0.5$, the dilation equals one, which yields the IUnlP0 formulations, where the local pressures can not be eliminated due to the vanishing $\mathbf{K}_{pp}$ term in the family stiffness matrix.

The behavior of the UnlP0 formulation shows, similar to the related Q1P0 or H1P0 Finite Elements, no locking and great robustness. However, like in its FE counterparts, unphysical pressure modes can occur which possibly result in certain situations in hourglass-like modes. This can be explained for the PBG formulation by the violation of the inf-sup condition and for the PPG formulation by the selective underintegration of the volumetric terms. This intrinsic underintegration makes it impossible to profit from higher order approximations of the pressure and dilation field within the PPG methods. However, within the PBG potential all fields are evaluated at each neighbor particle and, therefore, the formulation of higher order pressure and dilation approximations can be done to prevent spurious pressure oscillations.

6.2.2 Higher order approaches

In terms of second order displacement and linear pressure and dilation fields, two general approximation possibilities are present. First, a locally linear pressure field can be constructed by means of a Taylor series expansion, and second, a linear approximation of a nodal field via shape functions can be defined. In the former case, the pressure and dilation at a neighbor particle j within family $\mathcal{H}_0^k$ yields

$$p^{kj} = p^k + \frac{\partial^k p}{\partial \mathbf{X}} \cdot \Delta \mathbf{X}^{kj} \quad \text{and} \quad \Theta^{kj} = \Theta^k + \frac{\partial^k \Theta}{\partial \mathbf{X}} \cdot \Delta \mathbf{X}^{kj} . \tag{6.10}$$

Here, the pressure and dilation gradient $\frac{\partial^k p}{\partial \mathbf{X}}$ and $\frac{\partial^k \Theta}{\partial \mathbf{X}}$ are considered as additional local unknowns that are eliminated on family-level. To satisfy the inf-sup condition, the displacement field is usually set to be one order higher as the pressure space, since the derivative order in the weak form is also one order higher. Therefore, the U2P1 formulation forms by combining the linear pressure and dilation field with the second order WTE2 shape functions for the displacement approximation. The correction of at least linear variational consistency has to be performed to enable a convergence for irregular particle patterns. To profit from the second order displacement approximation in terms of higher convergence rates, the second order variational consistency would be needed which is not addressed here. Alternative to the treatment as unknowns, the pressure and dilation gradient in the Taylor series expansion (6.10) can be computed via a WTE shape function approach:

$$\frac{\partial^k p}{\partial \mathbf{X}} = \sum_{i=0}^{N^k} \Delta p^{ki} \frac{\partial N_p^{kki}}{\partial \mathbf{X}} \quad \text{and} \quad \frac{\partial^k \Theta}{\partial \mathbf{X}} = \sum_{i=0}^{N^k} \Delta \Theta^{ki} \frac{\partial N_\Theta^{kki}}{\partial \mathbf{X}} \tag{6.11}$$

with the differences $\Delta p^{ki} = p^i - p^k$ and $\Delta \Theta^{ki} = \Theta^i - \Theta^k$. The shape functions for the pressure and dilation approximation for this U2P1C formulation are chosen the same as those for the displacements, but only once evaluated at the master particle: $N_p^{kki} = N_\Theta^{kki} = N_\mathbf{u}^{kki}$. While in case of the U2P1 formulation the additional degrees of freedom can be statically condensed, the U2P1C formulation leads to a larger global system of equations, i.e. $\mathbf{u}$, p and Θ instead of $\mathbf{u}$ at each particle. However, numerical observations show, in contrast to their FE counterparts, that neither of the formulations prevent both locking and unphysical pressure patterns. On the one hand, the U2P1 formulation exhibits volumetric locking and on the other hand, the U2P1C formulation can produce unphysical pressure modes.

6.2.3 A bubble-enriched formulation

An alternative approach to circumvent volumetric locking by fulfilling the LBB condition consists in the enrichment of the displacement field with a cubic bubble function, based on an equal order approximation of the displacement, pressure and dilation field, called MINI element (cf. ARNOLD ET AL. (1984)). A peridynamic reconstruction can be based on the MTE1 shape functions for the interpolation of the displacement field, like in the Unl formulation, and the same pressure and dilation approximation that is used in the U2P1C formulation (equation (6.11)). As for each field a linear basis is used, the resulting formulation is expected to either lock or produce unphysical pressure patterns which can be numerically verified. Therefore, the displacement space is locally enriched with a bubble-like function which leads to the following approximations of the actual and virtual deformation gradient that surrogate the definitions of equation (4.11) and (4.12):

$$\mathbf{F}^{kj} = \sum_{i=0}^{N^k} \Delta\mathbf{x}^{ki} \otimes \frac{\partial N_{\mathbf{u}}^{kji}}{\partial \mathbf{X}} + \mathbf{u}_b^k \otimes \frac{\partial N_b^{kj}}{\partial \mathbf{X}} \quad \text{and} \tag{6.12}$$

$$\delta\mathbf{F}^{kj} = \sum_{i=0}^{N^k} \Delta\delta\mathbf{u}^{ki} \otimes \frac{\partial N_{\delta\mathbf{u}}^{kji}}{\partial \mathbf{X}} + \delta\mathbf{u}_b^k \otimes \frac{\partial N_b^{kj}}{\partial \mathbf{X}} \tag{6.13}$$

where $\mathbf{u}_b^k$ denote the additional local bubble-mode unknowns that can be statically condensed and $\frac{\partial N_b^{kj}}{\partial \mathbf{X}}$ is the gradient of the bubble-like enrichment function. The construction of the bubble function which is defined to be zero outside the scope of a particles neighborhood has to be done carefully to not disturb the fulfillment of the linear patch test. Here, the meshfree bubble-like function derivatives are directly constructed while taking into account the following condition that is needed to preserve the variational consistency:

$$\frac{V^k}{V^{\mathcal{H}_0^k}} \sum_{j=0}^{N^k} V^j \frac{\partial N_b^{kj}}{\partial \mathbf{X}} = \mathbf{0}\,. \tag{6.14}$$

A straightforward construction lies in the usage of bonds, i.e. the distance vectors

$$\frac{\partial N_b^{kj}}{\partial \mathbf{X}} = \Delta\mathbf{X}^{cj} = \mathbf{X}^j - \mathbf{X}^c\,, \tag{6.15}$$

where the perspective, the barycenter $\mathbf{X}^c$, ensures the fulfillment of equation (6.14):

$$\mathbf{X}^c = \frac{1}{V^{\mathcal{H}_0^k}} \sum_{j=0}^{N^k} V^j \mathbf{X}^j\,. \tag{6.16}$$

Within numerical tests, the resulting enriched Unl+P1C formulation showed to have superior behavior against all other tested formulations regarding stability, robustness and localization in the presence of volumetric constraints. In the range of solids, the global pressure field is smooth and no volumetric locking could be observed. Nevertheless, due to the shape function based pressure approximation, even for explicit time integration a global system with the pressure and dilation as unknowns has to be solved. This is why, further, two stabilized underintegrated formulations are also presented which have a reduced computational cost, especially in explicit algorithms.

6.3 Underintegration and stabilization

When explicit time integration schemes are used, the evaluation of the plastic evolution equations that requires a local Newton-Raphson procedure is the main driving computational cost in displacement based formulations as the solution of a global system is not needed. Therefore, the computation time depends almost linearly on the number of evaluation points within a neighborhood. A popular treatment of this lies in the concept of underintegration which also hinders the volumetric locking to occur. Though efficient, an underintegration leads to a decrease of detectable local deformation modes and hence to unphysical global low-energy modes that manifest in hourglass-like particle oscillations. Hence, an additional stabilization is needed which, on the other hand, can itself lead to volumetric locking.

In the PBG method, the underintegration of the virtual strain energy can be performed by skipping the reverse averaging of equation (4.25), which can also be interpreted as a fully integrated WTE1 approach. This leads to the underintegrated potential of the U1 formulation that coincides, except from shape function corrections, with the classical rank deficient peridynamic correspondence formulation:

$$U_h = \mathop{\mathbf{A}}_{k=1}^{n^p} \left\{ V^k W^{kk} + \left[\rho_0^k V^k \left(\ddot{\mathbf{u}}^k - \overline{\mathbf{b}}^k\right) - \mathbf{P}^k \cdot \mathbf{A}^k\right] \cdot \mathbf{u}^k \right\} \,. \tag{6.17}$$

To avoid the presence of spurious low-energy modes, the spurious modes have to be stiffened, whereby the following aspects have to be considered: First, the stabilization should not disturb the variational consistency such that the additional strain energy does not effect the converged solution. Second, the locking behavior of the fully integrated displacement based formulations should not be restored due to the stabilization. And finally, the reduced computational cost due to the single evaluation of the local evolution laws within each family should be maintained. Further, two stabilization schemes are presented that mostly fulfill the above-listed requirements.

6.3.1 Full integration stabilization

In a first approach, the underintegrated strain energy is extended by a pseudo strain energy to penalize the error of the linear displacement field approximation compared to the MTE1 interpolation (see Nadler & Rubin (2003), Krysl (2015) and Wriggers et al. (2017)). Thereby, the stabilization energy is integrated via the full Unl formulation and the underintegrated stabilization energy is subtracted to ensure a convergence to the accurate solution. The resulting potential for this U1SUnl formulation states

$$U_h = \mathop{\mathbf{A}}_{k=1}^{n^p} \left\{ V^k (W^{kk} - \tilde{W}^{kk}) + \frac{V^k}{V^{\mathcal{H}_0^k}} \sum_{j=0}^{N^k} V^j \tilde{W}^{kj} + \left[\rho_0^k V^k \left(\ddot{\mathbf{u}}^k - \overline{\mathbf{b}}^k\right) - \mathbf{P}^k \cdot \mathbf{A}^k\right] \cdot \mathbf{u}^k \right\} \,, \tag{6.18}$$

where the pseudo energy

$$\tilde{W}^{kj} = W^{kj}\left(\tilde{E}, \tilde{\nu}, \mathbf{h}^{kk}\right) \tag{6.19}$$

is computed with the plastic variables $\mathbf{h}^{kk}$ of the underintegrated strain energy. In this way, the local evolution laws have to be evaluated only once. To circumvent a volumetric locking of the stabilization pseudo energy and to trigger the plastic localization, the material parameters are modified as

$$\tilde{E} = \min\left[E, \max\left(\eta E, \left|\frac{\sigma_{vM}}{\alpha}\right|\right)\right] \quad \text{and} \quad \tilde{\nu} = \min\left(0.49, \nu\right) \tag{6.20}$$

with $\eta = 10^{-3}$. On the one hand, in the case of elasticity with $\nu \leq 0.49$, the U1SUnl formulation reduces to the Unl formulation. On the other hand, with an increasing refinement, the displacement field in a family tends to be linear and the stabilization vanishes in the limiting case. Thus, the converged solution is not affected. As a drawback, the correction of VC has to be performed twice, for the WTE1 and MTE1 shape functions.

6.3.2 Stabilization with implicit gradients

Alternatively to the error between the WLS1 approximation and the MTE1 interpolation of the displacement field, the curvature can be utilized to define a stabilization. Based on this, an implicit gradient based natural stabilization, similar to the one used in HILLMAN & CHEN (2016) for Stabilized Non-conforming Nodal Integration (SNNI) and combined with a plastic localization trigger is presented. The starting point is a first order Taylor series expansion of the actual and virtual deformation gradient with respect to the position and an expansion of the first Piola-Kirchhoff stress with respect to the deformation gradient:

$$\begin{aligned} \mathbf{F}^{'} &= \mathbf{F}^{k} + \frac{\partial^{k}\mathbf{H}}{\partial \mathbf{X}} \cdot \Delta\mathbf{X}^{k'} \,, \\ \delta\mathbf{F}^{\prime} &= \delta\mathbf{F}^{k} + \frac{\partial^{k}\delta\mathbf{H}}{\partial \mathbf{X}} \cdot \Delta\mathbf{X}^{k'} \quad \text{and} \\ \mathbf{P}^{'} &= \mathbf{P}^{k} + \tilde{\mathbb{A}}^{k} : \left(\mathbf{F}^{'} - \mathbf{F}^{k}\right) \end{aligned} \tag{6.21}$$

with the difference vector $\Delta\mathbf{X}^{k'} = \mathbf{X}^{'} - \mathbf{X}^{k}$, the gradient of the actual and virtual displacement gradient at the master particle $\frac{\partial^{k}\mathbf{H}}{\partial \mathbf{X}}$ and $\frac{\partial^{k}\delta\mathbf{H}}{\partial \mathbf{X}}$, and the fourth order incremental material tangent with respect to the deformation gradient:

$$\tilde{\mathbb{A}}^{k} = \left.\frac{\partial^{k2}\tilde{W}}{\partial \mathbf{F}^{2}}\right|_{\frac{\partial \mathbf{h}}{\partial \mathbf{u}}=\mathbf{0}} \tag{6.22}$$

where only the elastic part of the tangent is considered for the sake of simplicity. Instead, to improve the plastic localization, the same modification of the stabilization strain energy $\tilde{W}$ is used as as in the U1SUnl formulation (equation (6.19) and (6.20)). Inserting the Taylor expansions in the integral form of the local virtual work (4.25) yields

$$\int_{V^k} \mathbf{P} : \delta\mathbf{F}\, dV^k = \int_{V^k} \left(\delta\mathbf{F}^{k} + \frac{\partial^{k}\delta\mathbf{H}}{\partial \mathbf{X}} \cdot \Delta\mathbf{X}^{k'}\right) : \left(\mathbf{P}^{k} + \mathbb{A}^{k} : \frac{\partial^{k}\mathbf{H}}{\partial \mathbf{X}} \cdot \Delta\mathbf{X}^{k'}\right) dV^k \,. \tag{6.23}$$

A simplification in index notation excluding constant terms leads to

$$\begin{aligned}\int_{V^k} P_{AB} : \delta F_{AB}\, dV^k = {} & V^k P^k_{AB} \delta F^k_{AB} + P^k_{AB} \frac{\partial^k \delta H_{AB}}{\partial X_C} \int_{V^k} \Delta X^{k'}_C \, dV^k \\ & + \delta F^k_{AB} \mathbb{A}^k_{ABCD} \frac{\partial^k H_{CD}}{\partial X_E} \int_{V^k} \Delta X^{k'}_E \, dV^k \\ & + \frac{\partial \delta H^k_{AB}}{\partial X_E} \mathbb{A}^k_{ABCD} \frac{\partial H^k_{CD}}{\partial X_F} \int_{V^k} \Delta X^{k'}_E \Delta X^{k'}_F \, dV^k \, .\end{aligned} \tag{6.24}$$

Under the assumption of spherical particle shapes with volume V^k, the first order moments, i.e. the second and third part on the right side, vanish. Therefore, the discretized local virtual work of inner forces computes to

$$\int_{V^k} \mathbf{P} : \delta \mathbf{F} \, dV^k = V^k \mathbf{P}^k : \delta \mathbf{F}^k + \mathbf{S}^k_m : \mathbf{M}^k_2 \tag{6.25}$$

which can be interpreted as an U1 underintegration with an additional natural stabilization where

$$\mathbf{S}^k_m = \frac{\partial^k \delta \mathbf{H}}{\partial \mathbf{X}} : \tilde{\mathbb{A}}^k : \frac{\partial^k \mathbf{H}}{\partial \mathbf{X}} \tag{6.26}$$

is a stabilization matrix spanned in the tangent room of the current configuration with a modified elastic strain energy and

$$\mathbf{M}^k_2 = \begin{pmatrix} M^k_{xx} & 0 & 0 \\ 0 & M^k_{xx} & 0 \\ 0 & 0 & M^k_{xx} \end{pmatrix} \quad \text{with} \quad M^k_{xx} = \frac{\left(\frac{3}{\pi}\right)^{2/3}}{10 \cdot 2^{1/3}} V^{k^{5/3}} \tag{6.27}$$

is the second moment of volume of the spherically assumed particle. The gradient of the actual and virtual deformation gradient can be approximated via the following MLS approach:

$$\frac{\partial^k \delta \mathbf{H}}{\partial \mathbf{X}} = \frac{\partial^k \mathbf{H}}{\partial \mathbf{X}} = \sum_{i=0}^{N^k} \Delta \delta \mathbf{u}^{ki} \otimes \frac{\partial^2 N^{kki}_{MLS1}}{\partial \mathbf{X}^2} \tag{6.28}$$

with the modified weight function exception of 1000 times the particle spacing (see equation (5.42)). The resulting U1SIG formulation is an efficient and very robust alternative for explicit simulations in the range of finite elasto-plasticity as no global system of equations has to be solved and the local iterative Newton-Raphson scheme is only processed at one point per family. In case of implicit analyses, $\tilde{\mathbb{A}}^k$ is frozen in the beginning of each time or load step to preserve the Bubnov-Galerkin character.

Chapter 7

Numerical illustrations, verifications and examples

In the following chapter, the performance of the proposed PG formulations is investigated. Therefore, it is first demonstrated that an improper choice of shape functions, like in other meshfree methods, can lead in practice to poor or even useless solutions. Subsequently, a selection of numerical tests is presented which isolate the reasons of failure in practice and which served as a guideline in the development of the proposed formulations. The shape function conditions of chapter 5 ensure the accurate solution of these tests and provide a sound basis for the nonlinear benchmarks in which an extraordinary robustness of certain PG formulations can be observed.

To distinguish between the presented formulations, a generative code is used which is composed of the successive abbreviations of Table 7.1. Hereby, some abbreviations are marked as default, meaning that they are always used whenever they are not specifically analyzed in a numerical problem. Exemplarily, the code VCBCPBG V5sn Unl+P1C TL stands for a total Lagrangian, variationally consistent and bond conforming Unl+P1C formulation, while the fifth choice of correction functions combined with fixed normal correction factors on the surface was used to restore the variational consistency. When not distinguished between the presence of BC, the choice of the VC correction and the reference frame, VCPBG Unl+P1C indicates the same formulation as the above mentioned. The implementation of the presented numerical examples has mainly been done in the FE environment AceFEM. For demonstration purposes, different visualization possibilities are utilized: Single colored particles (Mathematica) and first order interpolations on the original FE meshes of the particle distributions (AceFEM).

7.1 Errors in practice

In the following, the 2- and 3-D Cook's membranes serve as a first example to demonstrate the importance of the choice of shape functions in Galerkin methods. Thereby, Cook's membrane (see e.g. WRIGGERS ET AL. (2017)), a tapered cantilever beam as depicted

Table 7.1. Overview of used abbreviations

	Abbreviation	**Description**
Shape function corrections	VC	first order variational consistency is restored
	VC2	first and second order variational consistency are restored, based on PPG2 formulation
	BC	Bond correction is performed, equation (5.55) (default for all first order formulations)
Method	PPG/PBG/FEM	Peridynamic Petrov-/Bubnov-Galerkin and Finite Element Method
VC correction function	V1	Φ_{V1}^{kji}, equation (5.60)
	V2	Φ_{V2}^{kji}, equation (5.61)
	V3	Φ_{V3}^{kji}, equation (5.62) (default for PPG)
	V4	Φ_{V4}^{kji}, equation (5.63)
	V5	Φ_{V5}^{kji}, equation (5.64) (default for PBG)
Boundary conditions for VC correction	p	Correction factor fixed at selected particles
	s	Correction factor fixed at all surface particles
	sn	Correction factor fixed in normal direction at all surface particles (default)
Formulation	Unl	Displacement based, nonlinear first order MTE shape functions (with BC)
	UnlP0	Mixed approach, nonlinear first order MTE shape functions (with BC) for displacements, constant pressure and dilation
	U2	Displacement based, second order WTE shape functions
	U2P1	U2 with local linear pressure and dilation field as degrees of freedom
	U2P1C	U2 with local linear pressure and dilation field as shape function approximation
	Unl+P1C	Unl with bubble-like enrichment and linear pressure and dilation field as shape function approximation
	U1SUnl	Underintegration with stabilization of Unl
	U1SIG	Underintegration with implicit gradient stabilization
	T1/O1	2d/3d Finite Element with linear displacement field
	Q1/H1	2d/3d Finite Element with bi-/tri-linear displacement field
	Q1P0/H1P0	Q1/H1 with local constant pressure
	H2	3d Finite Element with tri-quadratic displacement field
Reference configuration	TL	Total Lagrangian description (default)
	UL	Updated Lagrangian description

in Figure 7.1, is clamped on the left and loaded at the right. The block is modeled as a neo-Hookean solid with the Lame constants $\mu = 40\,\frac{\mathrm{N}}{\mathrm{m}^2}$ and $\lambda = 100\,\frac{\mathrm{N}}{\mathrm{m}^2}$, according to a Young's modulus of $E = 108.571\,\frac{\mathrm{N}}{\mathrm{m}^2}$ and a Poisson's ratio of $\nu = 0.357$. Its spatial particle discretization is generated by the collocation of a regularly structured Finite Element mesh (see section 4.1). In order to increase the effect of improper shape functions, the connectivity is made up of a relatively large number of at least $N = 50$ nearest particles. The clamping on the left is imposed by fixing the displacement of all particles at $X = 0$ and the line load on the right end is applied via the x-components of the particle-wise surface normals, computed via integration constraint (5.18). Within an implicit quasistatic simulation, the load is applied in 10 load steps to decrease the path dependency of the unstable solutions.

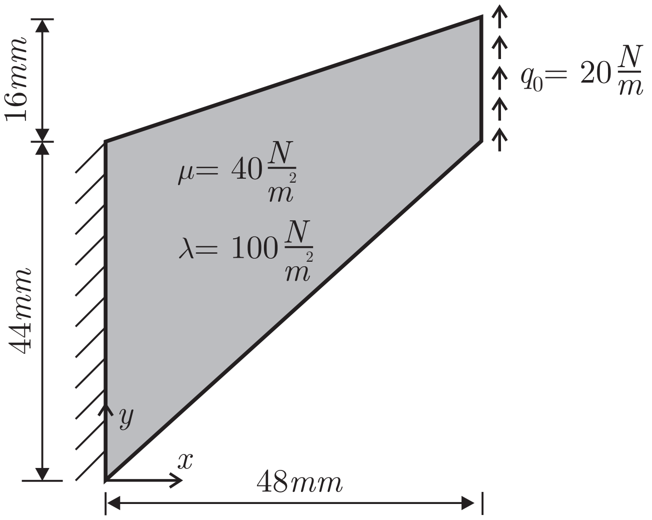

Figure 7.1. Geometry, material data and boundary conditions of 2-D Cook's membrane benchmark.

The final configuration of the PBG Unl formulation is visualized in Figure 7.2 for different sorts of original shape functions and correction techniques. Each particle is represented by a filled circle while the x-y-component of the deformation gradient is colored. Using WLS1 shape functions, the PBG Unl formulation coincides with the common peridynamic correspondence formulation or rather the total Lagrangian corrected SPH. Severe displacement oscillations can be observed which are a result of spurious low-energy modes. As will be shown in an eigen mode analysis later on, the low-energy modes are a consequence of a linear shape function approximation or rather underintegration where the deformation of a family is averaged to a constant deformation gradient. The mere movement of the weighting function by means of MLS1 shape functions remedies the presence of spurious modes in the interior. However, in the absence of low-energy modes, inaccuracies along the surface become apparent, especially at the displacement and force boundary. The more localized interpolating MTE1 shape functions alleviate these issues, but still are suspect to slight oscillations, stemming from the inaccuracy in the integration constraint near the surface. Both the correction of variational and configurational consistency improve the solution, while both are necessary to ensure a good behavior at the weak singularity in the upper

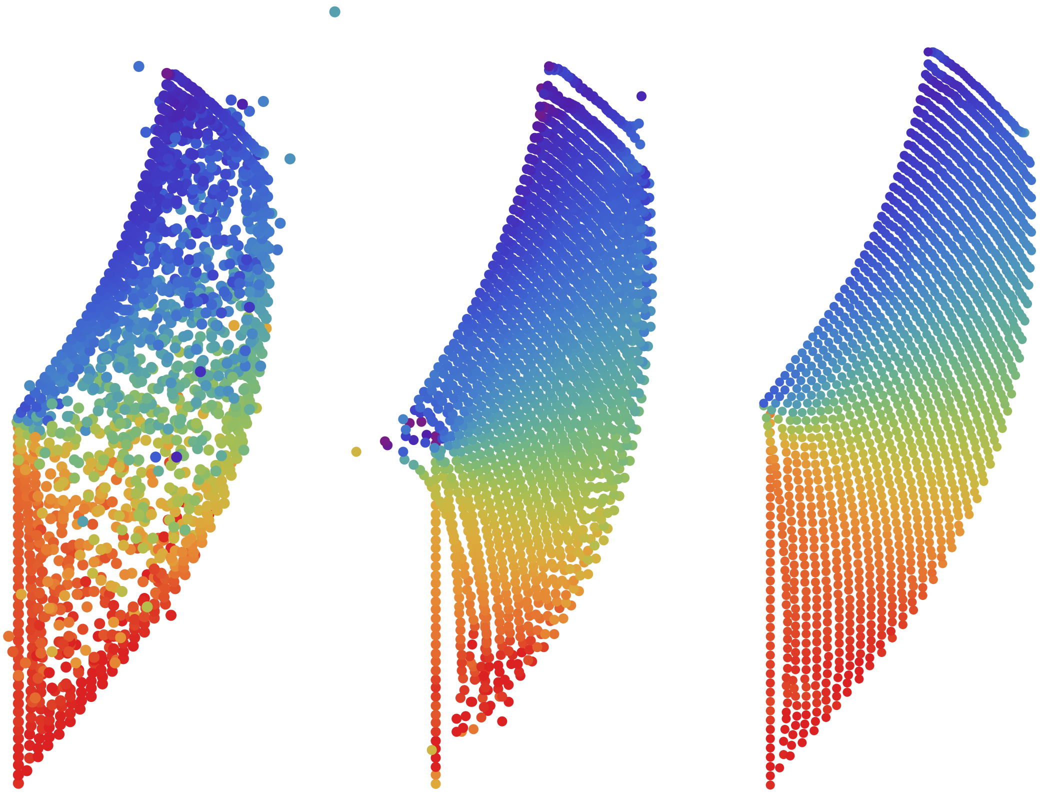

(a) PBG Unl, WLS1 (U1) (b) PBG Unl, MLS1 (c) PBG Unl, MTE1

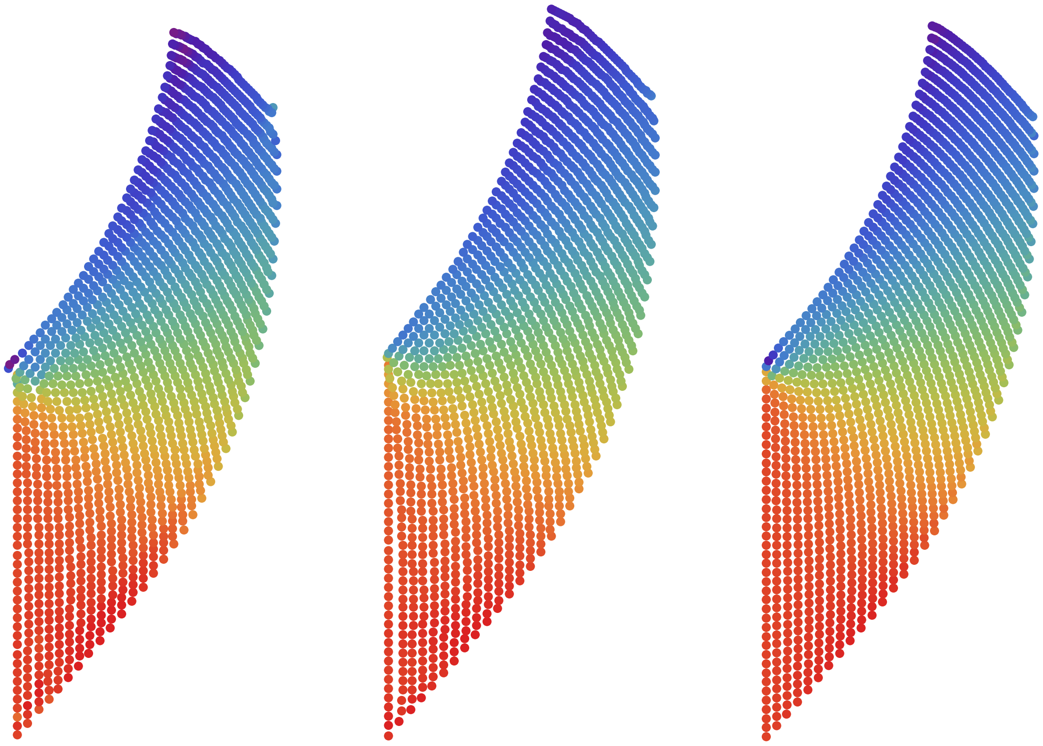

(d) VCPBG Unl, MTE1 (e) BCPBG Unl, MTE1 (f) VCBCPBG Unl, MTE1

Figure 7.2. Impact of different original shape functions and subsequent correction techniques on the solution of the 2-D Cook's membrane problem with the PBG Unl formulation.

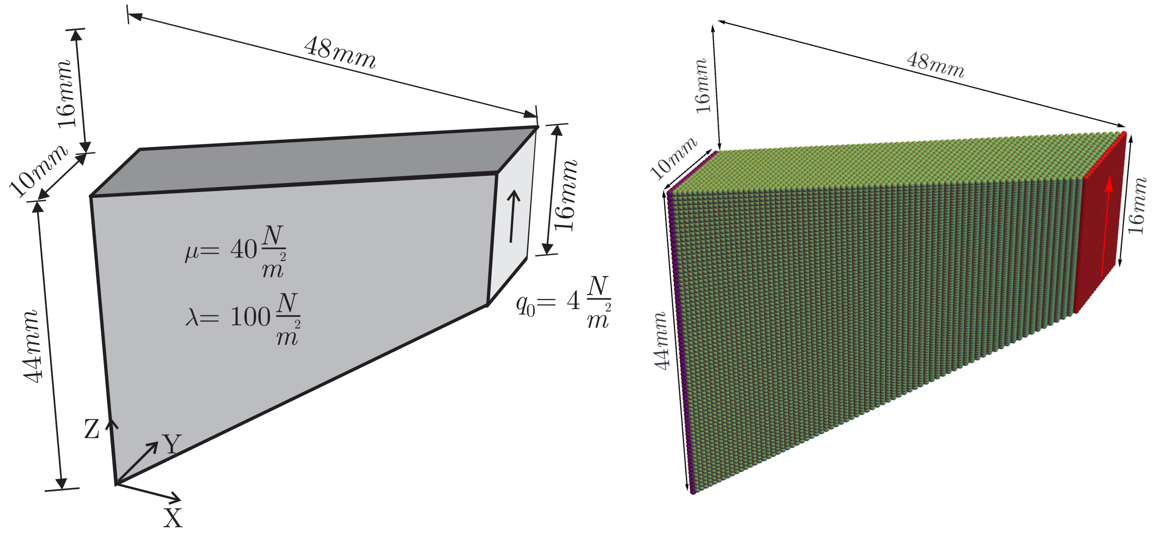

(a) Model problem (b) Discretization

Figure 7.3. On the left: Geometry, material data and boundary conditions of the three dimensional Cook's membrane problem. On the right: Particle discretization consisting of free moving (green), fixed (purple) and force applied (red) particles in case of the regular distribution into $72 \times 72 \times 18$ free moving particles.

left edge and near the force transmission. Note, that in practice the number of neighboring particles should be chosen smaller and the resulting error may not be as apparent, such that even the MLS1 shape functions can lead to acceptable solutions in certain situations.

Nevertheless, also smaller families can suffer from inappropriate shape functions as will be demonstrated next. Therefore, the convergence behavior of a 3-D Cook's membrane is examined by a series of regular and distorted (-d) particle discretizations. In this example, instead of a collocated Finite Element mesh, the particle discretization is made up of the centroids of H1 elements which is also a common technique (cf. MADENCI & OTERKUS (2016a)). As no particles lie directly on the surface, an additional layer of particles is used to model the wall on the left and to impose the force at the right (see Figure 7.3). In a single load step, an area load of $q = 4\,\frac{\mathrm{N}}{\mathrm{m}^2}$ is exerted in positive z-direction. For the study, the PPG UnlP0 formulation is combined with different weighting functions $\omega_n^{ji} = 1/\left(\Delta\mathbf{X}^{ji} \cdot \Delta\mathbf{X}^{ji}\right)^n$. The von Mises stress is colored exemplarily for the finest regular and distorted discretization on the deformed configuration for ω_2 in Figure 7.4. In a convergence study, depicted in Figure 7.5, the vertical displacement of the upper right front corner is compared to regularly structured H1P0 Finite Elements. Although the macroscopic behavior exhibits overall a smooth stress field and the rate of convergence is comparable to those of Finite Elements, a discrepancy in the edge displacement can be observed even for about 100000 particles. Only the highly localized weight function ω_5 leads to an accurate converged solution which is impractical for irregular particle distributions. This inaccuracy is mainly caused by the variational inconsistency of the test functions which leads to an erroneous surface approximation.

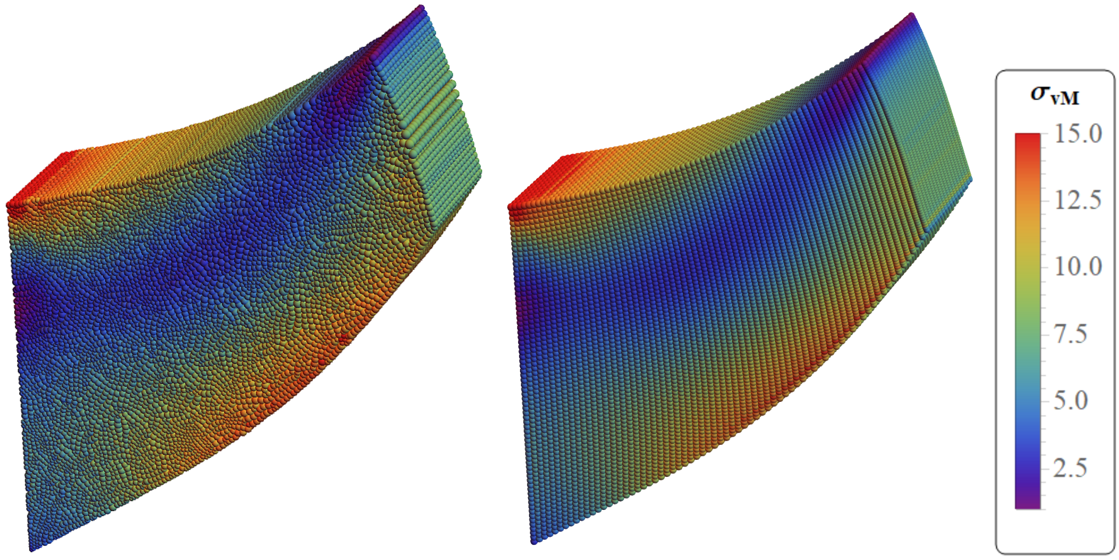

(a) $n_p = 101726$ (b) $n_p = 95904$ (c) Legend

Figure 7.4. Deformed configuration of the Cook's membrane for the finest irregular and regular discretization using n_p particles. The contours of the von Mises stress in Newton per square meter are depicted by the particle colors.

7.2 Isolation of pitfalls and verifications

The failures that can happen in practical PG simulations, as demonstrated in the previous section, are strongly influenced and can be lead back to the choice of shape functions. In order to study the influence of shape functions and to construct shape functions leading to an accurate solution, it is useful to define certain numerical test cases that differ their specific properties. Petrov-Galerkin formulations are well suited for this investigation, as manipulations can be done separately on the test and trial functions. In the further section, the stability is first addressed in terms of an eigen mode analysis. Subsequently, the patch tests and convergence analysis are exploited to examine the variational consistency. Further, a comparison of a total Lagrangian and updated Lagrangian description is used to show the influence of an accurate bond mapping. Finally, a numerical inf-sup test is performed to assess the behavior of certain formulations within the presence of incompressibility constraints.

7.2.1 Eigen mode analysis

The stability of a discretization scheme is, along with consistency, important for the convergence properties, cf. BELYTSCHKO ET AL. (2013). To investigate the stability of

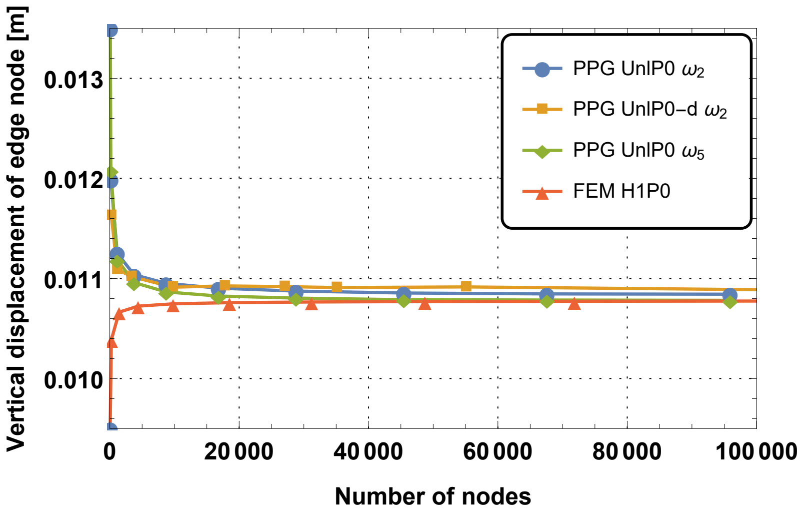

Figure 7.5. Convergence study: The vertical displacement at the upper right front edge of Cook's membrane is plotted over the number of nodes. Different discretizations and weight functions of the PPG UnlP0 formulation are compared to the mixed H1P0 Finite Elements.

a specific discretization, an analysis of the eigenvalues of its tangent stiffness matrix can be performed. In the context of Finite Elements, such an analysis can be done on element level which gives precise information which element deformation modes are associated with internal energy (see e.g. WRIGGERS (2008)). Concerning the PG methods, it is generally possible to construct the global stiffness matrix by assembling particle-wise or family-wise contributions in several ways, resulting in rectangular (equation (4.58)) or even quadratic (equation (4.62)) local tangent contributions.

However, although quadratic local matrices can be used for a local eigen mode analysis, their practical relevance is limited as they do not fully represent the stiffness of a discrete region. In fact, an increased number of zero eigenvalues in a local family stiffness matrix, i.e. more than the rigid body modes, does not necessarily lead to unphysical global modes. In any 2-D family, all presented PG formulations posses three zero eigen values – two translational and one rotatory rigid body mode. The number of eigenvalues with associated strain energy counts three in case of the U1 formulation and nine in case of the U2 and U1SIG formulations that both contain a complete second order polynomial trial space. All formulations that are based on moving weights, as the Unl formulations, occupy no further zero eigen values apart from the rigid body motions, independent on the size of its family.

As already mentioned, the eigen modes of the global discretization are more relevant in practice, since the overlapping coupling of the families leads to the fact that a rank deficiency of family stiffness matrices does not have to be inherited from the global stiffness matrix. Therefore, the global tangent stiffness matrix ix exemplarily analyzed for an unloaded free moving 2-D block of $20\,\mathrm{mm}$ length and $10\,\mathrm{mm}$ height with a Young's modulus of $100\,\frac{\mathrm{N}}{\mathrm{mm}^2}$ and a Poisson's ratio of $\nu = 0.4$. The block is discretized into 20×10 elements and collocated to get the particle discretization, while the connectivity is generated from the

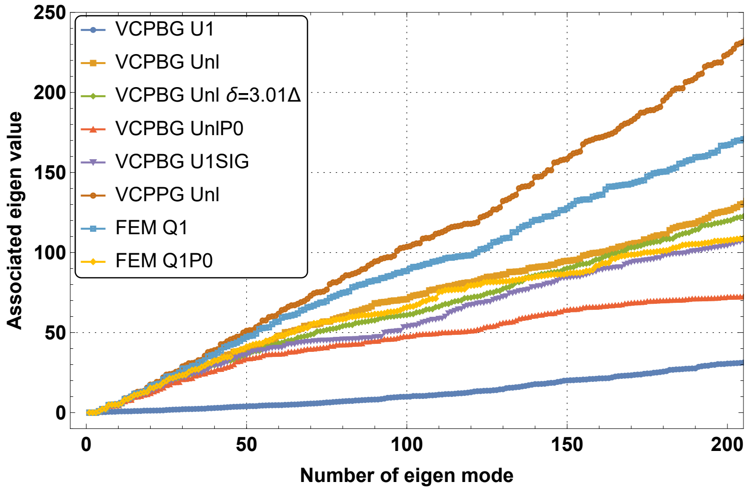

Figure 7.6. The eigen values of the global tangent stiffness matrix of a free moving bloc are plotted in ascending order for several PG and FEM formulations.

original Q1 mesh. Next to three rigid body modes, which are present to all formulations, the smallest 200 eigen values of the global tangent stiffness matrices are depicted in Figure 7.6 in ascending order for several formulations. While the U1 formulation which is known to suffer from spurious oscillations exhibits plenty of eigen modes with low associated energy, the other formulations are in good agreement to the FEM Q1 eigen values in the range of low stiffness. Note, that the enlargement of the family size to 3.01 times the nodal spacing in the VCPBG Unl formulation shows a very small effect on its eigenvalues. In Figure 7.7, the eigen modes of lowest stiffness are visualized for several PG formulations which show a reasonable shape. In case of the variationally consistent classical correspondence formulation, the two lowest and first physical mode (which is the 100-th) are displayed.

7.2.2 Patch tests

Although not always necessary, the ability to exactly reproduce a linear or even higher order polynomial field is an important condition for a discretization method to achieve convergence. The fulfillment of this condition can be verified by means of a patch test.

Linear patch test

Regarding the linear patch test, the reproducibility of a linear displacement field by the discretization method has to hold, which was the basis for the derivation of the linear variational consistency criterion. Following CHEN ET AL. (2013), an isotropic linear elastic material with a Young's modulus $E = 100\,\frac{kN}{m^2}$ and a Poison's ratio of $\nu = 0.3$ is subject to the linear displacement field

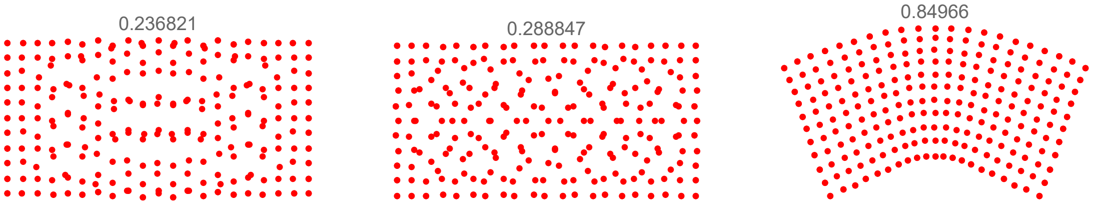
0.236821
0.288847
0.84966

(a) VCPBG U1: first two non-zero low energy modes and first physical mode

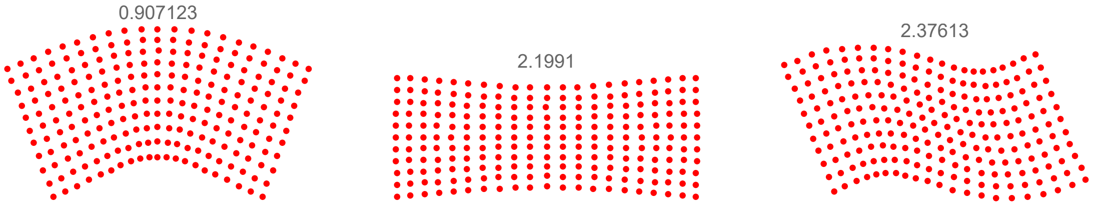
0.907123
2.1991
2.37613

(b) VCPPG Unl

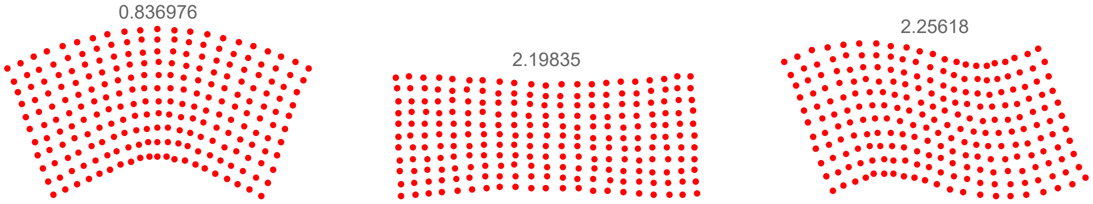
0.836976
2.19835
2.25618

(c) VCPBG Unl

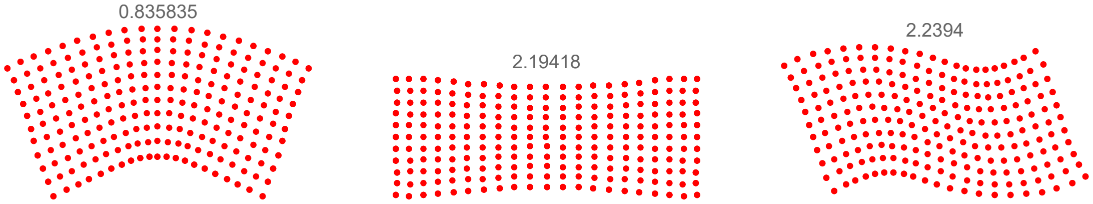
0.835835
2.19418
2.2394

(d) VCPBG U1SIG

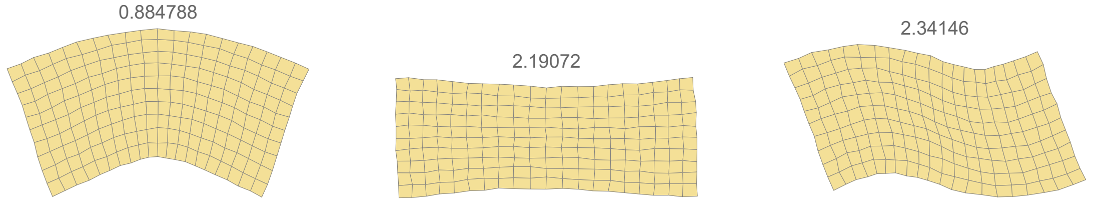
0.884788
2.19072
2.34146

(e) FEM Q1

Figure 7.7. First three non-zero eigen modes of a free moving bloc for different proposed formulations.

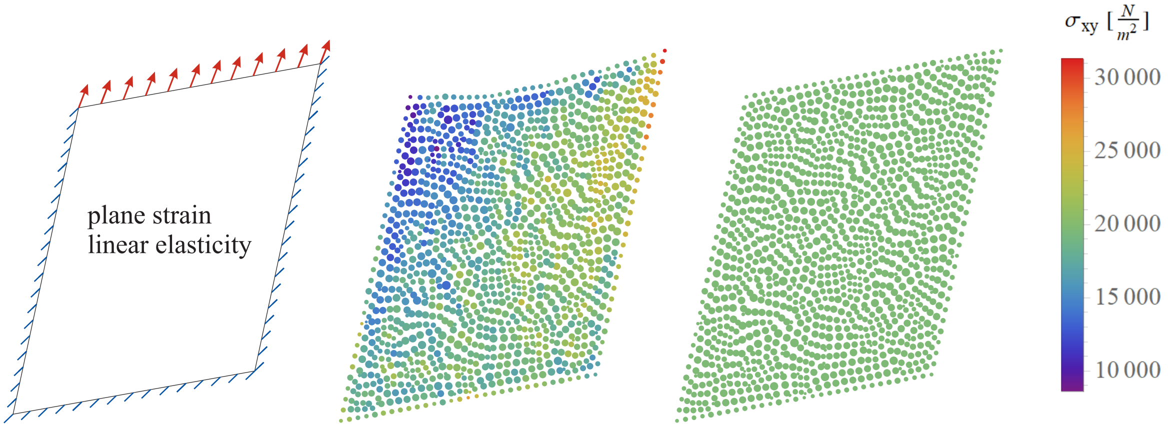

(a) Illustration (b) PPG Unl (c) VCPPG Unl (d) Legend

Figure 7.8. The resulting shear stress field is colored over the deformed particle configuration. Whereas the classical PG methods fail the patch test, it is passed by their variationally consistent counterparts.

$$\mathbf{u} = \begin{pmatrix} 0.1X + 0.3Y \\ 0.2X + 0.4Y \end{pmatrix} \quad \text{with} \quad \frac{\partial \mathbf{u}}{\partial \mathbf{X}} = \begin{pmatrix} 0.1 & 0.3 \\ 0.2 & 0.4 \end{pmatrix} \tag{7.1}$$

in $\{X \times Y\} \in \{[-1\,\mathrm{m}, 1\,\mathrm{m}] \times [-1\,\mathrm{m}, 1\,\mathrm{m}]\}$. At the left, bottom and right edge Dirichlet boundary conditions and at the upper edge Neumann boundary conditions are applied that are consistent with the displacement field (see illustration in Figure 7.8), i.e.

$$\mathbf{P} = \begin{pmatrix} 0.2\mu + 0.5\lambda & 0.5\mu \\ 0.5\mu & 0.8\mu + 0.5\lambda \end{pmatrix} \tag{7.2}$$

where the Lame parameters λ and μ are computed from E and ν. Therefore, the nodal displacements on the Dirichlet boundary are directly prescribed according to equation (7.1) and the surface forces on the Neumann boundary are applied via the equivalent volume force $\tilde{\mathrm{s}}$ of equation (4.32). Figure 7.8 depicts the resulting shear stress field – which should be constant – for an uncorrected and a variationally consistent PPG Unl formulation with 1345 irregularly distributed particles. The displacement and energy error norms

$$\begin{aligned} \epsilon_{L^2} &= \sqrt{\int_{\Omega_0} ||\mathbf{u} - \mathbf{u}^h||_2^2 \, d\Omega_0} \quad \text{and} \\ \epsilon_{H^1} &= \sqrt{\int_{\Omega_0} \sum_{i,j} \left|\left| \frac{\partial \left(u - u^h\right)_i}{\partial X_j} \right|\right|_2^2 d\Omega_0} \end{aligned} \tag{7.3}$$

are displayed in Table 7.2 where $\mathbf{u}^h$ stands for the discrete displacement field. As expected, the linear patch test is not fulfilled for the uncorrected PG formulations but is accurate for each of the VC corrected PPG formulations. Concerning the mixed displacement–pressure–dilation and PBG formulations, only the first order consistency preserving correction

Table 7.2. Error norms in L^2 and H^1 for the linear patch test

Method	ϵ_{L^2}	ϵ_{H^1}
PPG Unl	$9.532 * 10^{-2}$	$2.336 * 10^{-1}$
VCPPG V1sn Unl	$2.146 * 10^{-15}$	$2.330 * 10^{-14}$
VCPPG V2sn Unl	$7.596 * 10^{-16}$	$8.125 * 10^{-15}$
VCPPG V3p Unl	$9.602 * 10^{-17}$	$1.013 * 10^{-15}$
VCPPG V3s Unl	$7.629 * 10^{-17}$	$9.868 * 10^{-16}$
VCPPG V3sn Unl	$6.489 * 10^{-17}$	$9.974 * 10^{-16}$
PPG UnlP0	$8.557 * 10^{-2}$	$2.513 * 10^{-1}$
VCPPG V1sn UnlP0	$6.040 * 10^{-3}$	$2.299 * 10^{-2}$
VCPPG V2sn UnlP0	$1.652 * 10^{-15}$	$1.353 * 10^{-14}$
VCPPG V3sn UnlP0	$4.370 * 10^{-14}$	$4.117 * 10^{-13}$
PBG Unl	$8.563 * 10^{-3}$	$1.284 * 10^{-1}$
VCPBG V5sn Unl	$2.518 * 10^{-14}$	$1.154 * 10^{-12}$

functions lead to a fulfillment of the patch test.

Quadratic patch test

Analogously to the linear patch test, a quadratic one can be set up on the basis of a quadratic displacement field (Chen et al., 2013):

$$\begin{aligned} \mathbf{u} &= \begin{pmatrix} 0.12X + 0.14Y + 0.16X^2 + 0.18XY + 0.2Y^2 \\ 0.11X + 0.13Y + 0.15X^2 + 0.1XY + 0.21Y^2 \end{pmatrix} \quad \text{with} \\ \frac{\partial \mathbf{u}}{\partial \mathbf{X}} &= \begin{pmatrix} 0.12 + 0.32X + 0.18Y & 0.14 + 0.18X + 0.4Y \\ 0.11 + 0.3X + 0.1Y & 0.13 + 0.1X + 0.42Y \end{pmatrix} . \end{aligned} \tag{7.4}$$

The same domain and material parameters are chosen as in the linear case which lead, for linear elasticity, to a linear stress field with

$$\begin{aligned} \mathbf{P}_{XX} &= \lambda\,(0.25 + 0.42X + 0.6Y) + \mu\,(0.24 + 0.64X + 0.36Y) \\ \mathbf{P}_{YY} &= \lambda\,(0.25 + 0.42X + 0.6Y) + \mu\,(0.26 + 0.2X + 0.84Y) \\ \mathbf{P}_{XY} &= \mathbf{P}_{YX} = \mu\,(0.25 + 0.48X + 0.5Y) . \end{aligned} \tag{7.5}$$

Consistent with the stress field, a source term is needed which computes

$$\rho_0 \overline{\mathbf{b}} = - \begin{pmatrix} 0.42\lambda + 1.14\mu \\ 0.6\lambda + 1.32\mu \end{pmatrix} . \tag{7.6}$$

Again, Dirichlet boundary conditions are applied at the left, bottom and right edge while there are Neumann boundaries at the top. The resulting shear stress distribution is colored in Figure 7.9 on the deformed configuration of an uncorrected, a first and a second order variationally consistent PPG formulation. Table 7.3 shows the error norms in L^2 and H^1.

Table 7.3. Error norms in L^2 and H^1 for the quadratic patch test

Method	ϵ_{L^2}	ϵ_{H^1}
PPG Unl	$1.757 * 10^{-1}$	$3.658 * 10^{-1}$
VCPPG V3sn Unl	$5.950 * 10^{-4}$	$1.861 * 10^{-2}$
VC2PPG V1s U2	$6.674 * 10^{-16}$	$1.075 * 10^{-14}$

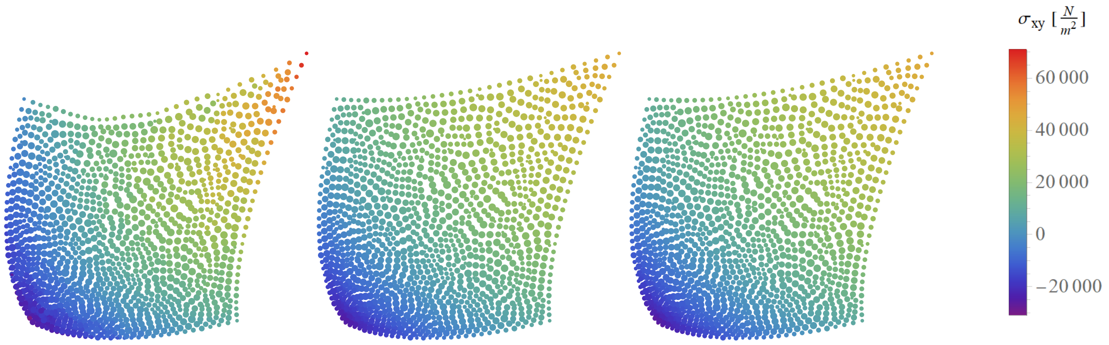

(a) PPG Unl (b) VCPPG V3sn Unl (c) VC2PPG V1s U2 (d) Legend

Figure 7.9. The resulting shear stress field is colored over the deformed particle configuration. Even if only the second order corrected test functions lead to the passing of the quadratic patch test, the linearly corrected one produces reasonable results and a smooth stress field.

As expected, second order variational consistency with a trial function of second order basis is needed to pass the quadratic patch test. However, the first order correction already improves the performance of the patch test and yields reasonable macroscopic behavior. Due to the increase of degrees of freedom for the second order correction, the generally larger neighborhood and the complexity to construct a second order variationally consistent PBG formulation, it is proposed to stick to the first order VC correction until more efficient local correction techniques are available.

7.2.3 Convergence in a manufactured 2-D problem

Next, the convergence rates resulting from the choice of the correction shape functions and correction boundary conditions are investigated. Therefore, the manufactured solution of HILLMAN ET AL. (2019) with the following displacement field is utilized:

$$\mathbf{u} = \begin{pmatrix} \sin\left(\frac{\pi}{2}X\right)\cos\left(\frac{\pi}{2}Y\right) \\ \cos\left(\frac{\pi}{2}X\right)\sin\left(\frac{\pi}{2}Y\right) \end{pmatrix} . \tag{7.7}$$

in $\{X \times Y\} \in \{[-1\,\mathrm{m}, 1\,\mathrm{m}] \times [-1\,\mathrm{m}, 1\,\mathrm{m}]\}$ with Dirichlet boundary conditions at the entire surface. Considering the linear elastic regime, with $E = 100\,\frac{kN}{m^2}$ and $\nu = 0.3$, the consistent body force writes

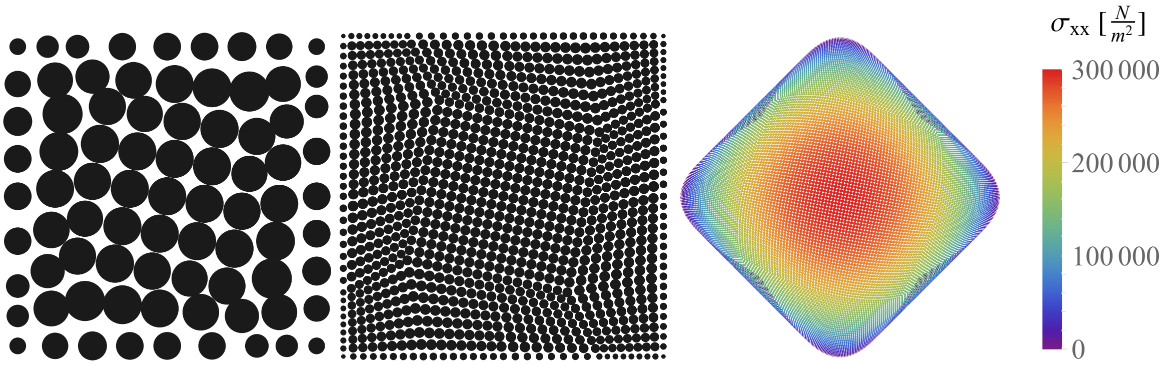

(a) $N = 4$ (b) $N = 16$ (c) $N = 64$ (d) Legend

Figure 7.10. On the left: Refining discretizations for the manufactured 2-D solution in the initial configuration. On the right: the normal stress in x-direction is colored over the deformed configuration.

$$\rho_0 \overline{\mathbf{b}} = -\frac{E\,(1-\nu)\,\pi^2}{2\,(2\nu^2+\nu-1)} \begin{pmatrix} \sin\left(\frac{\pi}{2}X\right)\cos\left(\frac{\pi}{2}Y\right) \\ \cos\left(\frac{\pi}{2}X\right)\sin\left(\frac{\pi}{2}Y\right) \end{pmatrix} . \tag{7.8}$$

For a series of refining discretizations with $N + 1$ particles per meter in each dimension the displacement and energy error norms are computed. Figure 7.10 depicts the undeformed configuration for $N = 4$ and $N = 16$ and the deformed configuration with $N = 64$ of a variationally consistent formulation with colored normal stress.

In Figure 7.11, the error norms with the averaged convergence rate are plotted for different PG formulations and correction shape functions. Due to the refinement, the actually variationally inconsistent formulations still exhibit a stable convergence behavior, as the error in the integration constraint decreases steadily. However, the optimal rates of 2 in the L^2 norm and 1 in the H^1 norm for linear basis are not reached. While the correction of VC reduces the error in each tested case, the stability of the rate with increasing refinement differs. The V3 and V5 correction functions perform most reliable for the PPG and PBG methods and restore the expected rates. In case of the convergence in energy norm, even slightly higher rates can be observed. For the VC correction of mixed formulations, the same behavior can generally be observed, where it is noted, that also for the PPG formulations, the shape functions should maintain the trial function consistency (which is not the case for V1).

7.2.4 Comparison of total and updated Lagrange

Meshfree methods are oftentimes used in situations where large deformations would otherwise require a remeshing. Instead of a remeshing, a neighbor search in the deformed configuration is performed in meshfree methods. The updated Lagrangian perspective in which the weak form of the momentum equation is stated is then based on the last dynamic equilibrium or, in case of explicit time integration, updated every n_u time steps. Along with

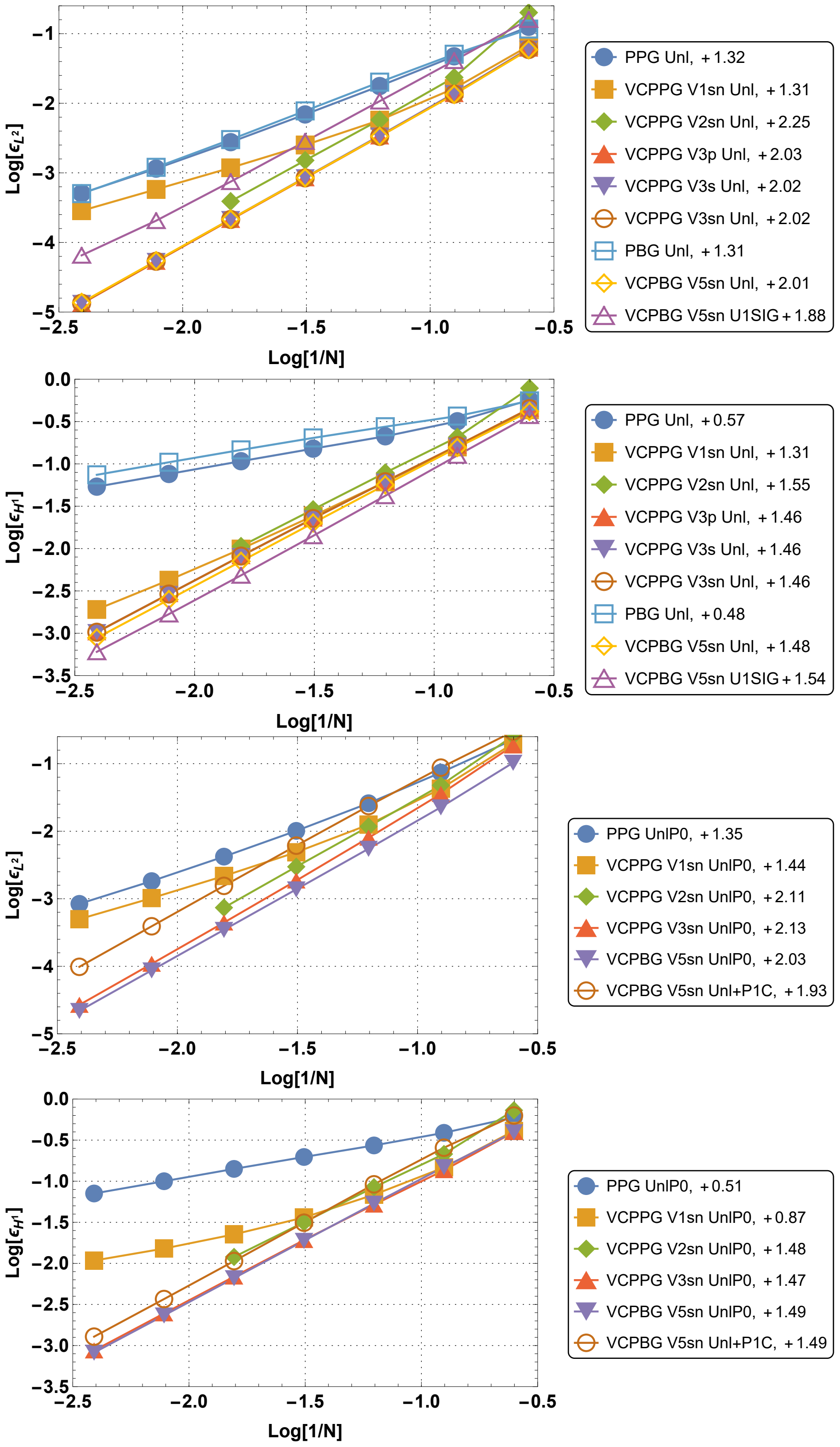

Figure 7.11. Convergence of the displacement and energy error norms with increasing refinement for different correction shape functions and correction boundary conditions with displacement based and mixed formulations.

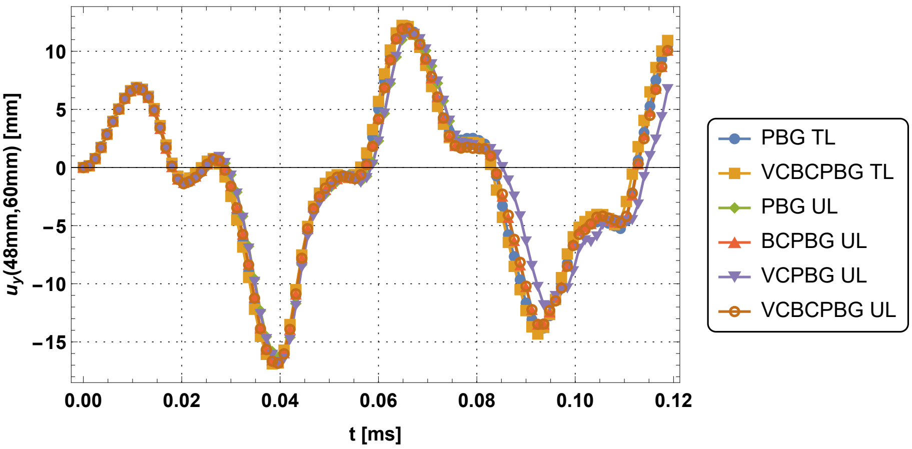

Figure 7.12. Vertical displacement response of the upper right corner of the dynamic Cook's membrane problem for different combinations of shape function correction within the total and updated Lagrangian PBG Unl formulation.

the necessary re-computation of shape functions, a numerical tensile instability oftentimes arises (see e.g. BELYTSCHKO ET AL. (2000)), even for small deformations. To ensure a reliable update in extreme deformations, the comparison of a total Lagrangian and updated Lagrangian simulation can reveal inconsistencies arising from such an update. Therefore, a dynamic Cook's membrane problem similar to the one in CIHAN ET AL. (2020) is used to examine the influence of the Lagrange update on the transient behavior for the satisfaction of different shape function corrections in the PBG Unl formulation. The geometry and Dirichlet boundary are used as in Figure 7.1 with a Young's modulus of $E = 210\,\mathrm{GPa}$ and a Poisson's ratio of $\nu = 0.3$. Being initially at rest, the load is dynamically applied on the right hand side with

$$q\left(t\right) = 10000\,\frac{\mathrm{kN}}{\mathrm{mm}} \cdot \sin\left(\frac{\pi\,t}{0.01\,\mathrm{ms}}\right) \quad \text{for} \quad 0\,\mathrm{ms} \leq t \leq 0.02\,\mathrm{ms}\,. \tag{7.9}$$

With Newmark time integration, the response within $0.12\,\mathrm{ms}$ is computed in a number of 500 time steps. To trigger a possible tensile instability, an updated is performed in every time step for the updated Lagrangian (UL) simulations. The deformed configuration of selected frames is exemplarily visualized in Figure 7.13 for the VCBCPBG UL formulation. The displacement of the upper right edge is displayed in Figure 7.12. While the difference resulting from the VC and BC corrections is marginal in case of the total Lagrangian (TL) descriptions, for UL formulations it has an important effect. Indeed, the PBG UL formulation crashes at about $0.08\,\mathrm{ms}$ and the mere correction of VC shows still a visual deviation in time. The configurational consistency, established by the BC correction, removes this discrepancy and yields a very good agreement to the TL response.

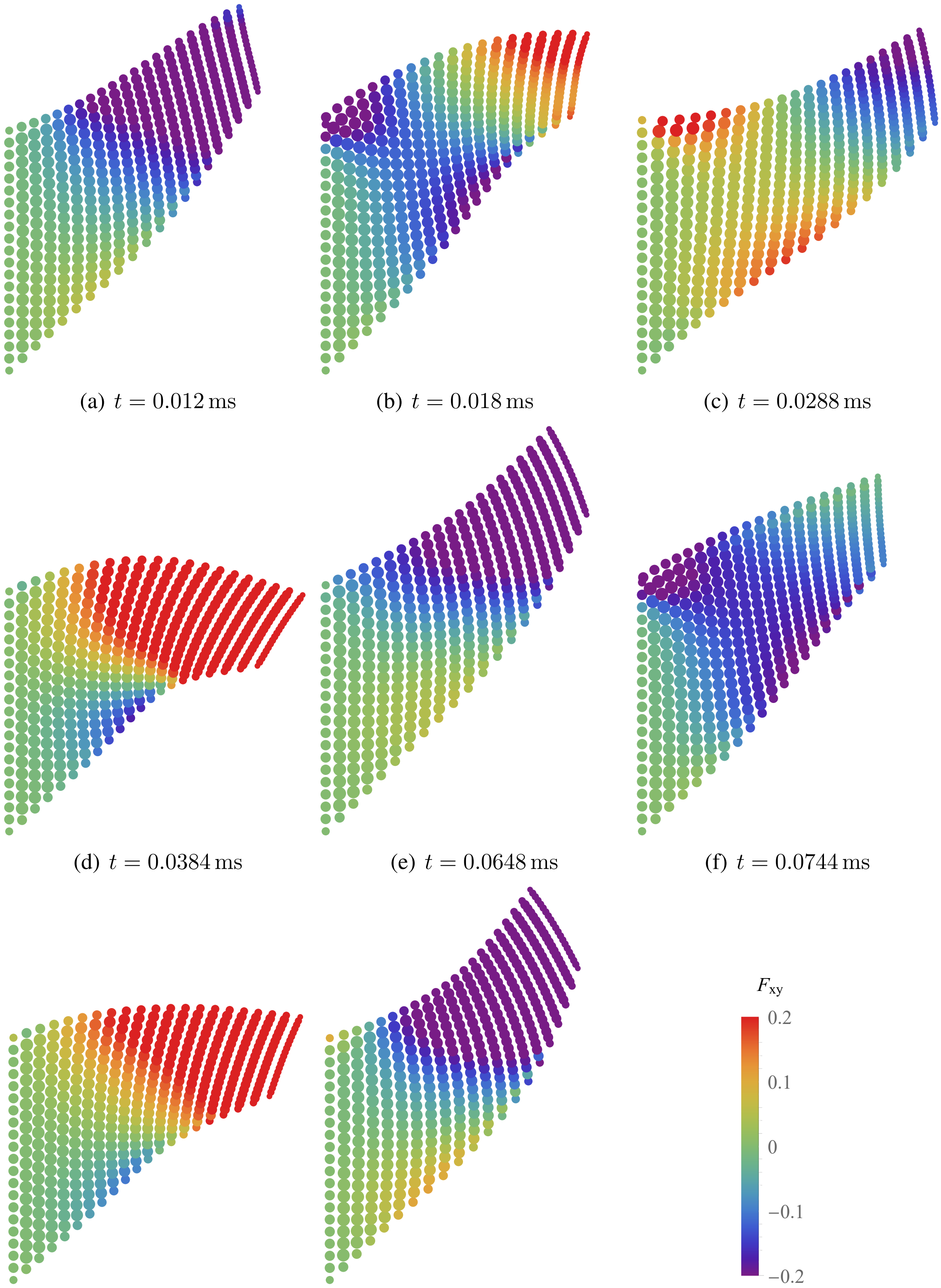

(a) $t = 0.012\,\mathrm{ms}$ (b) $t = 0.018\,\mathrm{ms}$ (c) $t = 0.0288\,\mathrm{ms}$

(d) $t = 0.0384\,\mathrm{ms}$ (e) $t = 0.0648\,\mathrm{ms}$ (f) $t = 0.0744\,\mathrm{ms}$

(g) $t = 0.0912\,\mathrm{ms}$ (h) $t = 0.12\,\mathrm{ms}$ (i) Legend

Figure 7.13. Deformed configuration of selected frames of the dynamic Cook's membrane problem for the case of VCBCPBG UL, colored x-y-component of the deformation gradient.

7.2.5 Numerical inf-sup test

In mixed FE methods, the inf-sup or Ladyzhenskaya-Babuška-Brezzi (LBB) condition ensures together with the ellipticity condition the existence, uniqueness and stability of the regarding discretization. For nearly incompressible material behavior in linear elasticity, the inf-sup condition (see FORTIN & BREZZI (1991)) states

$$\inf_{p_h \in P_h} \sup_{\mathbf{u}_h \in U_h} \frac{\int_{\Omega_0} p_h \operatorname{Div} \mathbf{u}_h \, d\Omega_0}{||p_h||_{L^2} \; ||\mathbf{u}_h||_{H^1}} \geq \beta > 0 \,, \tag{7.10}$$

where P_h and U_h are finite dimensional spaces of trial pressure and displacement fields, respectively. Due to the complexity of meshless shape functions, an analytical proof whether the condition is satisfied is difficult to state. However, CHAPELLE & BATHE (1993) proposed a numerical test which can give a prediction for the satisfaction (see also QUAK ET AL. (2011) for the application to meshfree methods). Therefore, a bloc of material with the applied essential boundaries as shown in Figure 7.14(a) is discretized by a series of refining regular and distorted particle distributions consisting of $N \times N$ particles or elements with $N = \{2, 4, 8, 16, 32\}$ (see Figures 7.14(b) and 7.14(c)), where a family is build up by all particles within a radius of 2.51 times the particle spacing. As the inf-sup condition deals with the trial spaces, no variational consistency correction is used. The limit β of the inf-sup condition of equation (7.10) can be computed from the following generalized eigenvalue problem:

$$\mathbf{T}_h \cdot \mathbf{U}_h = \lambda \mathbf{S}_h \cdot \mathbf{U}_h \,, \tag{7.11}$$

where $\mathbf{U}_h$ is the global vector of nodal displacements. Matrix $\mathbf{S}_h$ results from the H_1 norm of the discrete displacement field

$$||\mathbf{u}_h||^2_{H_1} = \mathbf{U}_h \cdot \mathbf{S}_h \cdot \mathbf{U}_h \tag{7.12}$$

and $\mathbf{T}_h$ corresponds to the discrete pressure projection:

$$||p_h||^2_{L_2} = \mathbf{U}_h \cdot \mathbf{T}_h \cdot \mathbf{U}_h \,. \tag{7.13}$$

For the numerical evaluation, the following procedure can be adopted to take profit from existing implicit frameworks. In case static condensation can be used to reduce the degrees of freedom at family level to only displacement ones, $\mathbf{T}_h$ can simply be computed as the global tangent stiffness matrix in the static and unloaded initial configuration with a bulk and shear modulus of $K = 1$ and $\mu = 0$. Accordingly, $\mathbf{S}_h$ can be determined with $K = 0$ and $\mu = 1$ with the modified strain energy density potential $W = \frac{\mu}{2} \operatorname{tr} \left[\mathbf{F}^T \cdot \mathbf{F} \right] - 3$. If a continuous pressure approximation is used, the condensation has to be performed on the global level. Alternatively, β can more efficiently be calculated from the eigen value problem with respect to the pressure space (cf. CHAPELLE & BATHE (1993)).

The inf-sup value of a particular resolution computes to the smallest non-zero eigenvalue of the generalized eigenvalue problem defined in equation (7.11):

$$\tilde{\beta} = \sqrt{\lambda_k} \,. \tag{7.14}$$

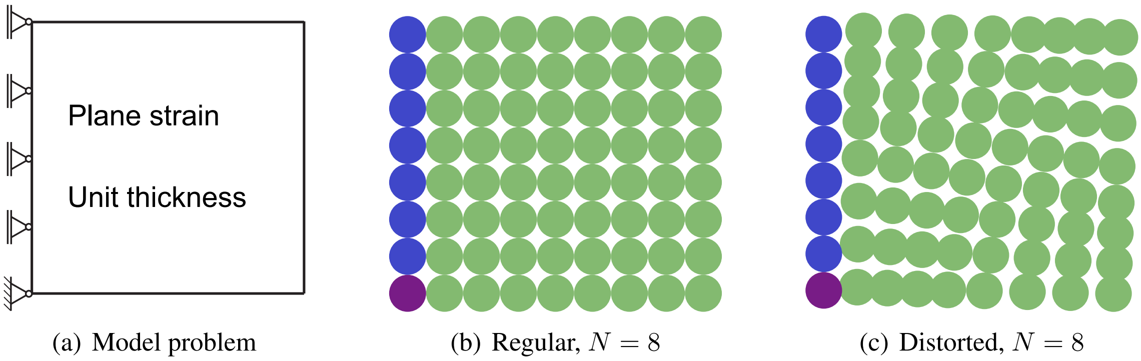

(a) Model problem (b) Regular, $N = 8$ (c) Distorted, $N = 8$

Figure 7.14. On the left: Model problem for numerical inf-sup test. On the right: Exemplary discretizations for regular and irregular particle distributions. The Dirichlet boundary conditions are applied by an additional layer of wall particles. The displacements of blue colored particles are fixed horizontally and the purple particle is fixed in both horizontal and vertical direction.

where $k-1$ is the number of zero-eigenvalues. The number of spurious pressure modes can be determined from

$$k_{pm} = k - (n_u - n_p + 1) \tag{7.15}$$

with the number of global displacement and pressure degrees of freedom n_u and n_p. Figure 7.15 depicts the inf-sup values of the model problem of Figure 7.14. For validation, the curves for the Q1P0 and MINI Finite Element are computed which are in agreement with those of CHAPELLE & BATHE (1993). Concerning the PBG formulations, it can be seen that the fully integrated displacement based formulations exhibit volumetric locking, as their inf-sup value decreases linearly in the log–log plot. In contrast, the inf-sup value of the underintegrated U1 formulation is bounded from below and the number of spurious pressure modes equals zero. Therefore, it passes the numerical inf-sup test which indicates that the formulation is not suspect to volumetric locking or spurious pressure modes. Hence, the numerical inf-sup test is not able to detect spurious modes resulting from an underintegration. This gives also an explanation why, despite having pressure oscillations, the volumetric underintegrated PPG UnlP0 formulation also passes the numerical inf-sup test (see BODE ET AL. (2020b)). By doing a full integration also of the volumetric terms, the resulting PBG UnlP0 formulation does not anymore fulfill the numerical inf-sup test as pressure oscillations can occur. Further, the inf-sup test predicts the U2P1 and U2P1C formulations not to fulfill the LBB condition. Solely the Unl+P1C formulation satisfies the numerical inf-sup test as a fully integrated PBG formulation.

7.3 Numerical benchmarks

In the following section, the effectiveness of the proposed PG methods with a proper choice of shape functions is demonstrated in a series of solid mechanics benchmark problems.

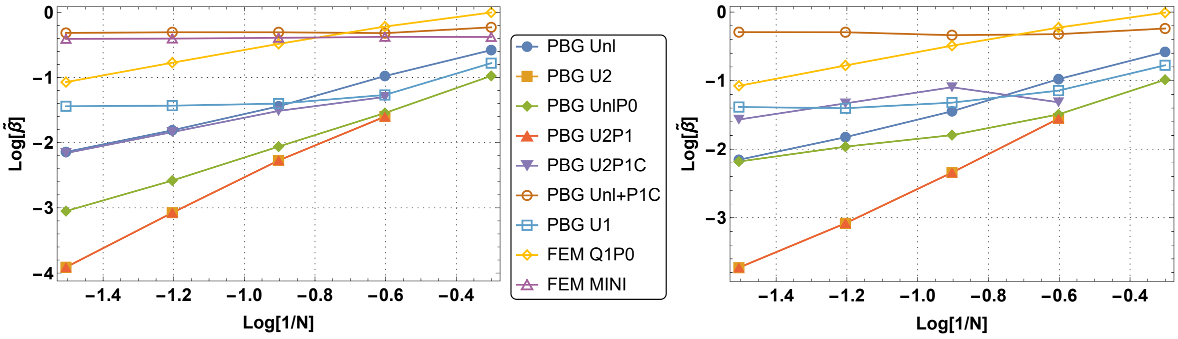

(a) Regular (b) Irregular

Figure 7.15. Inf-sup values of the model problem of Figure 7.14, where the logarithm of the inf-sup value is plotted over the logarithm of the inverse of the number of particles in each dimension for regular and distorted particle and node distributions, respectively.

First, the robustness is shown in a 2-D punch and a 3-D torsion test in the range of nonlinear elasticity. Second, the convergence behavior is investigated for regular and irregular particle patterns in a 3-D punch test and Cook's membrane problem. Subsequently, three elasto-plastic examples show the applicability in plastic localization, severely distorted particle distributions and impact events. Finally, the usage of symmetry boundary conditions and possible coupling with the FEM is shown on a 2-D plate with hole.

7.3.1 2-D punch problem

One of the difficulties in mesh-based methods lies in the need of a remeshing when elements get non-convex or even of negative volume. In these situations, meshfree methods as the PG methods are oftentimes less sensitive due to their overlapping connectivities. To generate a situation that pushes the FEM to its limits, the 2-D punch test of Wriggers et al. (2017) with modified boundary conditions is conducted. As depicted in Figure 7.16, a block of material is compressed on the left side by adaptively decreasing $\bar{u} \rightarrow -1\,\mathrm{mm}$ until failure of convergence. Using the same set of nodes originating from a regular mesh of 64×32 quadrilaterals, the maximal displacement in x-direction is plotted against the minimal displacement in y-direction for the Q1 Finite Element and the variationally consistent PPG and PBG Unl formulations with linear basis (see Figure 7.16). While the FEM simulation crashes at a compression to 39% of the initial thickness, the PPG and PBG formulations allow a compression up to 28% and 1.3%, respectively. The final deformed configurations of the FEM and PBG simulation are displayed in Figure 7.17 where the material was squeezed out to the right and around the applied Dirichlet boundary, resulting in self-penetrating elements which cause the failure of convergence in the FEM.

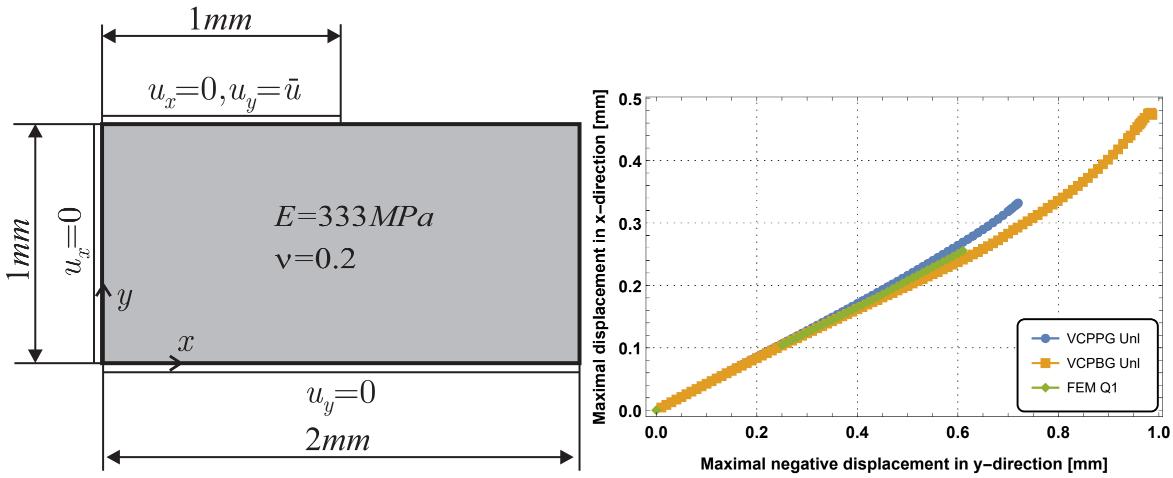

Figure 7.16. On the left: Geometry, material data and boundary conditions of the two dimensional punch problem. On the right: Maximal displacement in x-direction is plotted over the maximal negative displacement in y-direction for the displacement based FE and PG methods with linear basis.

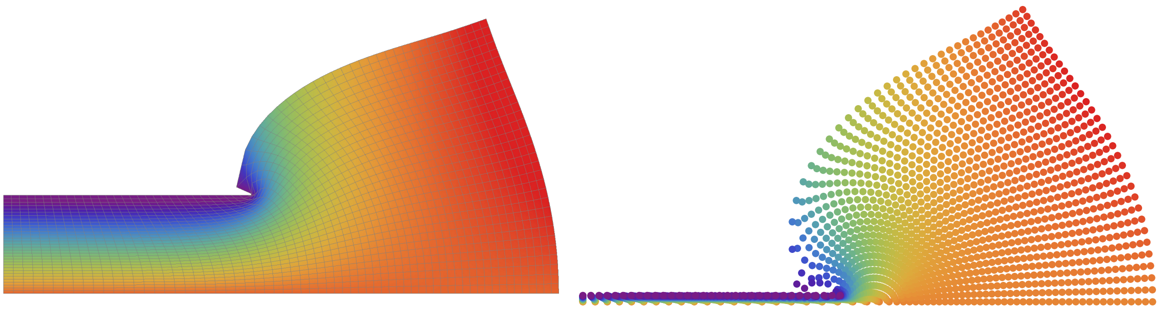

(a) FEM Q1 (b) VCPBG Unl

Figure 7.17. Maximal compressed configurations of the two dimensional punch test. The severe mesh distortion near the singularity at the right end of the upper Dirichlet boundary causes the divergence in the FE simulation.

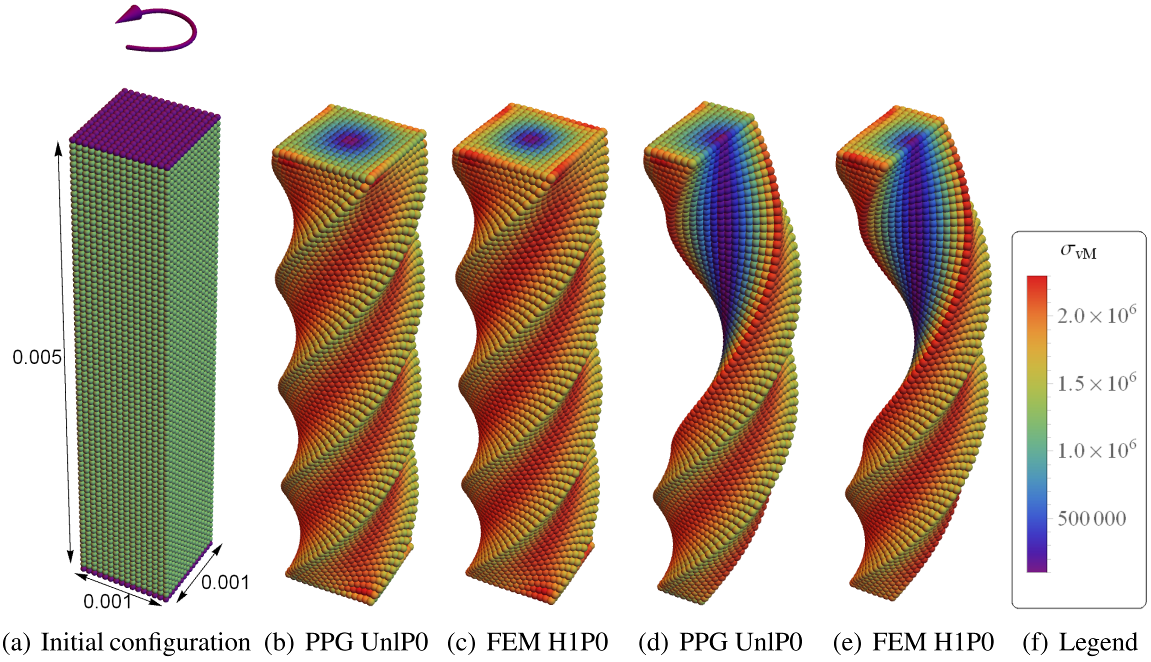

(a) Initial configuration (b) PPG UnlP0 (c) FEM H1P0 (d) PPG UnlP0 (e) FEM H1P0 (f) Legend

Figure 7.18. On the left: Geometry of the torsion problem where particles underlying displacement boundary conditions are colored purple and free moving particles green. On the right: Exemplary configuration for a twisting angle of 360 degrees with the mixed PPG UnlP0 and FEM H1P0 formulations. The von Mises stress in Newton per square meter are colored.

7.3.2 Torsion of square hyperelastic prism

In FE methods, it is known that the usage of mixed displacement–pressure–dilation formulations can considerably increase the robustness in terms of maximal possible step sizes within an implicit simulation. The influence of different PG formulations on the maximal step size is therefore demonstrated in a torsion test similar to the one in KADAPA ET AL. (2016). A squared prism of dimensions $0.001\,\mathrm{m}\times0.001\,\mathrm{m}\times0.005\,\mathrm{m}$ is clamped at the top and bottom and rotated at the top end (see Figure 7.18). As material parameters a bulk modulus of $K=5\cdot10^8\,\frac{N}{m^2}$ and a shear modulus of $\mu=1.61148\cdot10^8\,\frac{N}{m^2}$ are used. In Figure 7.18 the von Mises stress is exemplarily depicted for a rotation angle of 360 degrees both for the PPG UnlP0 and FEM H1P0 solutions. The stress distribution looks very similar and has a minimum in the center and maximal values in the middle of each side.

The particle discretization for the PPG formulations is gained as the centroids of the elements with additional wall particles for the application of the Dirichlet boundary and a horizon size of 1.51 times the particle spacing. The largest possible twisting angle within one load step as well as the minimum number of load steps for a rotation of 360 degrees are shown in Table 7.4 for a discretization into $16\times16\times5\cdot16$ original elements. Both measures show that the superiority of the mixed formulations over the pure displacement based approaches accounts in the PG methods similarly as in the FEM. The stabilized PBG U1SIG formulation appears to have a relatively small maximal step size. However, the

Table 7.4. Robustness study: Maximal converging angle in a single load step in degrees and minimum number of load steps need for one full rotation for displacement based and mixed PG and FE approaches.

Method	Maximal step $[°]$	Steps/$360°$
FEM H1	7	72
FEM H1P0	42	9
PPG Unl	17	60
PPG UnlP0	64	6
PBG Unl	12	72
PBG U2	4	90
PPG UnlP0	54	7
PBG U2P1	58	7
PBG U2P1C	47	8
PBG Unl+P1C	49	8
PBG U1SIG	4	90

formulation is especially efficient for explicit schemes which reduces the significance of this limitation.

7.3.3 3-D Punch problem

To verify the convergence within nonlinear deformations and the behavior in near incompressibility, a punch into a block of solid material as shown in Figure 7.19 (cf. WRIGGERS (2016)) is analyzed. The block has the dimensions $0.1\,m \times 0.1\,m \times 0.05\,m$ and a Young's modulus of $E = 4.8293\,\frac{N}{m^2}$. The convergence or rather locking behavior is investigated for two different Poisson's ratios of $\nu = \{0.4, 0.49999\}$. For the PPG formulations, the particles are generated by means of the centroids of regularly structured Finite Elements. A load of $q = 9\,\frac{N}{m^2}$ is applied in negative z-direction on an additional layer of particles (red). To prevent localization problems due to the force boundaries in the deformed configuration, the horizontal positions of the concerning particles are fixed. At the bottom, an additional layer of wall particles (purple) is used to model a wall where the z-direction is constrained. Free moving particles are colored green. The PBG discretizations, on the other hand, are as the collocated nodes of an FE mesh, where the boundary conditions are directly imposed at the surface particles. When applying the load, the block undergoes large deformations. In Figure 7.19 the final configuration as well as a cross section is exemplarily depicted for an incompressible PPG IUnlP0 formulation for a discretization into 24948 particles. The displacement in z-direction is colored, see legend in Figure 7.19(d).

The convergence of the minimal displacement in z-direction is analyzed by a series of regular discretizations with decreasing particle spacing. Figure 7.20 depicts the convergence behavior for the different PG formulations compared to FEM overkill solutions which are visualized as the horizontal black lines. Thanks to the regular particle distribution, the error in the integration constraints decrease with an increasing number of particles and also the

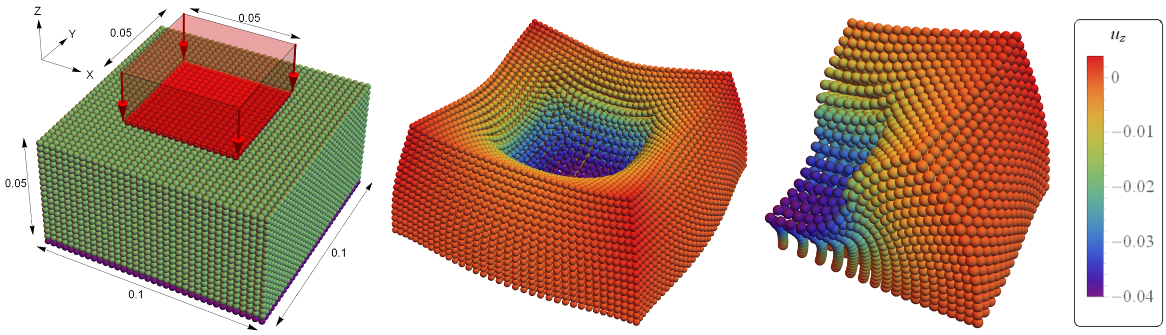

(a) Initial configuration (b) Final configuration (c) Cross section (d) Legend

Figure 7.19. On the left: Geometry and boundary conditions of the punch problem. Dirichlet boundary conditions are prescribed for purple particles and external forces are applied to the red particles. On the right: Exemplary deformed configuration and cross section for an incompressible PPG IUnlP0 formulation. The vertical displacement in meter is colored.

variationally inconsistent formulation observe a convergence in about the same rate as the H1 Finite Element for the case of $\nu = 0.4$. Concerning the range of near incompressibility, an over-stiff behavior of the displacement based formulations can be observed which is demonstrated by means of the VCPBG Unl formulation. The mixed UnlP0 formulations do not show a locking behavior, but the two finest VCPBG UnlP0 simulations crashed at about 90% of the applied load. This is probably caused by the violation of the inf-sup test leading to unphysical pressure patterns and could be improved by a stronger localization of the weight function or by using irregular particle patterns as will be shown in the following example. However, the mixed PBG Unl+P1C formulation shows very good results in the incompressible limit even for a very low number of particles.

7.3.4 Cook's membrane

One of the promising applications of meshfree particle methods include the modeling of large deformations including phase changes (see e.g. WESSELS ET AL. (2018)). A key condition for the accurate simulation of such processes that require a Lagrange update consists in the capability to converge with arbitrarily distributed particle distributions resulting from the large deformation. To test this, the 3-D Cook's membrane problem of section 7.1 is again conducted with a series of irregular particle distributions converted from tetrahedral FE meshes by means of collocation. The resulting displacement in z-direction of the right upper front corner for different displacement based and mixed formulations is displayed in Figure 7.21 (a) - (b) for the material parameters of Figure 7.3 and a modified Poisson's ratio of $\nu = 0.4999999$. The black horizontal lines denote overkill FE solutions. As already mentioned, a deviation from the Finite Element solution or even unstable behavior can be observed for irregular particle patterns with the variationally inconsistent PG formulations. On the other hand, the VC corrected counterparts converge to the FE benchmark, where the

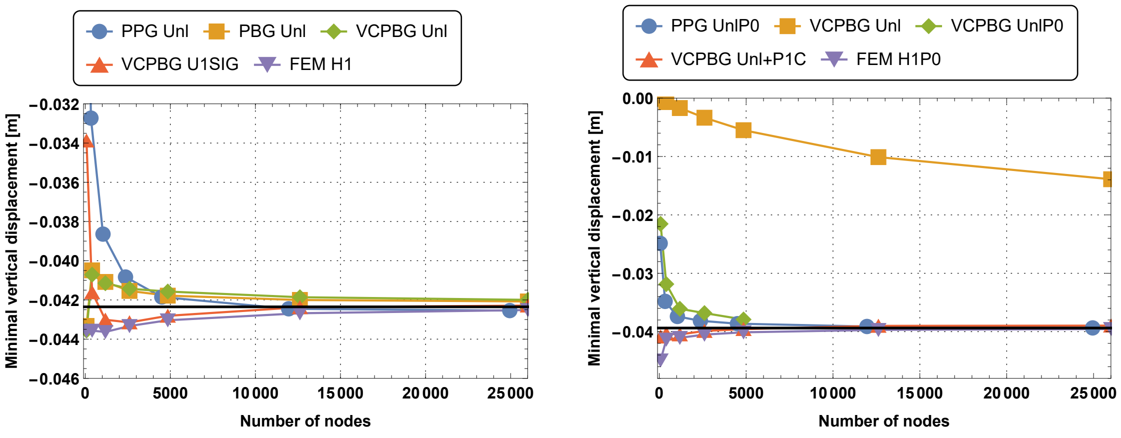

(a) $\nu = 0.4$ (b) $\nu = 0.49999$

Figure 7.20. Convergence study: The minimal vertical displacement is plotted over the number of nodes. Different approaches of the PPG method are compared to the mixed H1P0 Finite Element for two different Poisson's ratios.

PBG formulations generally exhibit a softer response and faster convergence but with a less monotonic convergence in comparison to the irregular FEM O1 solutions.

The computational time needed for the VCPBG Unl and FEM O1 simulations, using the Conjugate Gradient method for the solution of the global linear system in the Newton Raphson method, is visualized in Figure 7.21 (c) - (d). Whereas in the range of fewer degrees of freedom the assembling of the system plays the major role for the computational time, for larger numbers of particles the solution of the linear system dominates. Hence, the increase of computational time for smaller systems is caused by an increased number of evaluations of the constitutive equations and for larger systems by the less sparse tangent matrix resulting from overlapping families. For the finest discretization into 1.2 million degrees of freedom, the total computation time of the PG simulation is about 56% larger compared to the corresponding FE simulation. However, the deviation of the edge displacement from the FE overkill solution amounts only 23% of the deviation of the FE O1 solution.

7.3.5 Cylindrical necking

Next, the localization of the proposed formulations is examined in a practical problem. Therefore, the quasistatic necking of a cylinder is performed in accordance with HUDOBIVNIK ET AL. (2019). Figure 7.22 depicts the model problem and inital discretization, where the cylinder is clamped at both sides and elongated at the right by a displacement of $\bar{u} = 5\,\mathrm{mm}$ in x-direction. Its material parameters state $E = 206.9\,\frac{\mathrm{kN}}{\mathrm{mm}^2}$, $\nu = 0.29$, $\sigma_{y0} = 0.45\,\frac{\mathrm{kN}}{\mathrm{mm}^2}$, $\sigma_{y\infty} = 1.165\,\frac{\mathrm{kN}}{\mathrm{mm}^2}$, $H = 0.13\,\frac{\mathrm{kN}}{\mathrm{mm}^2}$ and $\delta = 16.93$. The discretization is made up of the nodes of a refining collocated FE mesh, where each element of the original mesh is divided into $N \times N \times N$ elements. To trigger the plastic necking, the radius is reduced to $d_c = 0.99d$ at the center of the cylinder. Without further shifting of nodes, the

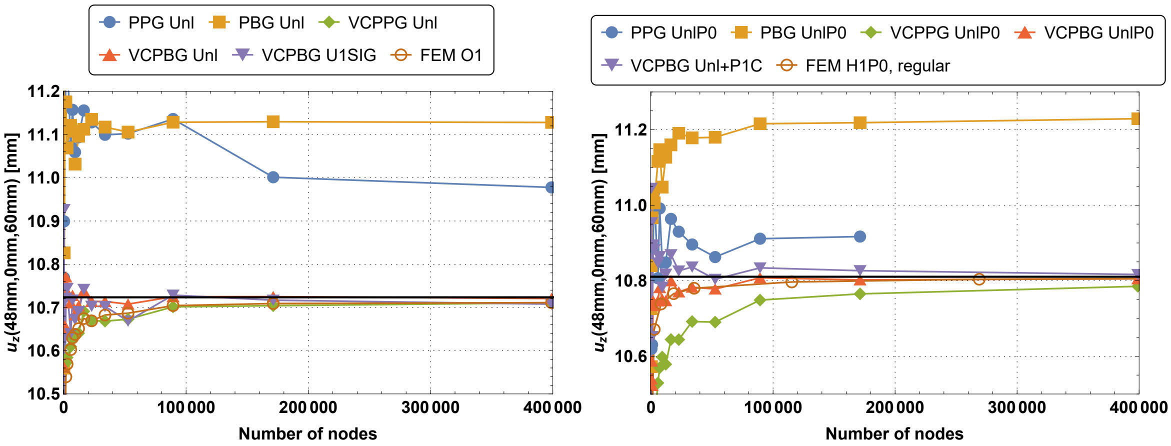

(a) Displacement based approaches, $\nu \approx 0.36$ (b) Mixed $\mathbf{u}$-p-Θ approaches, $\nu = 0.4999999$

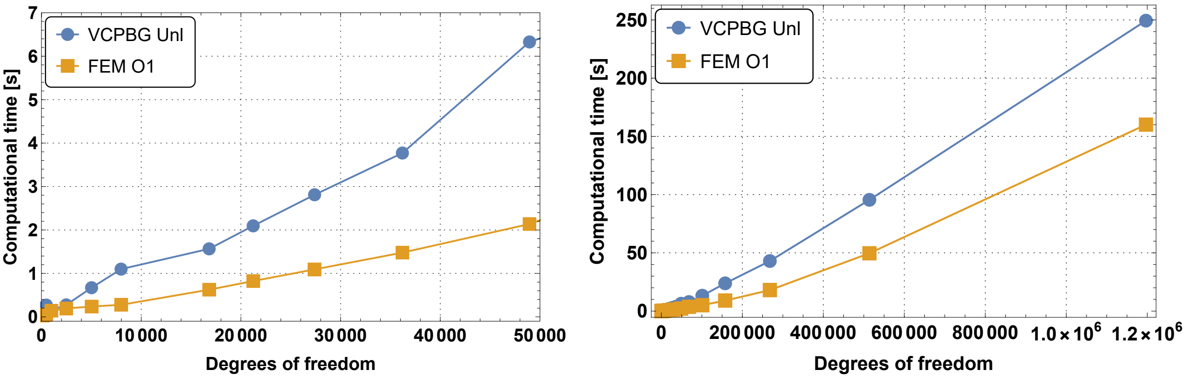

(c) Computational time for two load steps using Conjugate Gradient method

Figure 7.21. Convergence study: The displacement in z-direction of the upper right front corner of Cook's membrane is plotted over a series of 18 irregular particle distributions. A Finite element comparison is performed with a displacement based tetrahedral mesh with the same node distribution and a regular refining H1P0 Finite Element mesh.

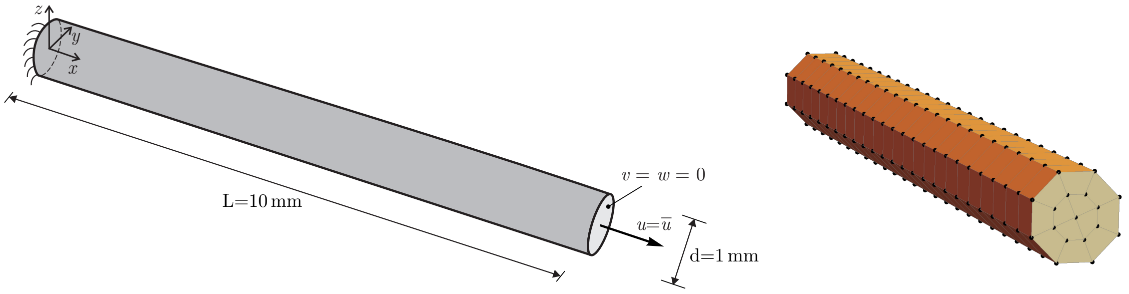

Figure 7.22. On the left: Geometry and boundary conditions of the quasistatic cylindrical necking problem. On the right: Initial collocated FE mesh for discretization $N = 1$.

volume of the surface particles is simply scaled such that the collective particle volume exactly matches the cylinder's one.

The residual force at the left clamping over the displacement at the right end is plotted at the top of Figure 7.23 for $N = 6$. Until the plastic localization manifests in a necking which reduces the applicable force, all curves lie on top of each other. While the necking continues, the volumetric locking of some of the formulations restricts the further localization. Whereas the Unl+P1C formulation is in the best agreement to the H1P0 FEM solution, the UnlP0 and underintegrated stabilized formulations lead also to good results. Figure 7.24 displays the accumulated plastic strain at the final configuration. The inaccurate force displacement curve of the U2P1 formulation is here explained, as the localization did not take place in the center, but almost simultaneously at two places. Furthermore, the U2P1C formulation aborted, likely due to pressure oscillations. Note, that even though the force displacement curve of the Unl+P1C and UnlP0 formulation lie above the FEM H1P0 curve, the maximal accumulated plastic strain is stronger localized. The maximal residual force for a series of refining discretizations is shown at the bottom of Figure 7.23. The superior convergence of the PG solutions can be explained by the simple volume scaling of the surface particles which accounts for the exact volume of the curvilinear cylinder.

7.3.6 Dynamic torsion of square elasto-plastic prism

The robustness towards strongly irregular particle distributions is one of the major advantages of meshfree methods. Therefore, the implicit dynamic response of a twisted square prism with the geometry as in section 7.3.2 is evaluated for the proposed formulations with two distorted original meshes, while Newmark time integration is applied. In Figure 7.25, the geometry of the squared specimen is depicted, as well as the cross section of the two discretizations and, as a benchmark, the FEM H1P0 solution with 320000 regularly structured elements. The prism, initially at rest, is clamped at the bottom and rotated at the top with a speed of one rotation per $10\,\mu\mathrm{s}$. Its material parameters are the same as those of the previous example with an initial density of $\rho_0 = 7.85\,\frac{\mathrm{g}}{\mathrm{cm}^3}$. The two discretizations, consisting of 1715 elements, are distorted by perturbing the interior nodes in each direction

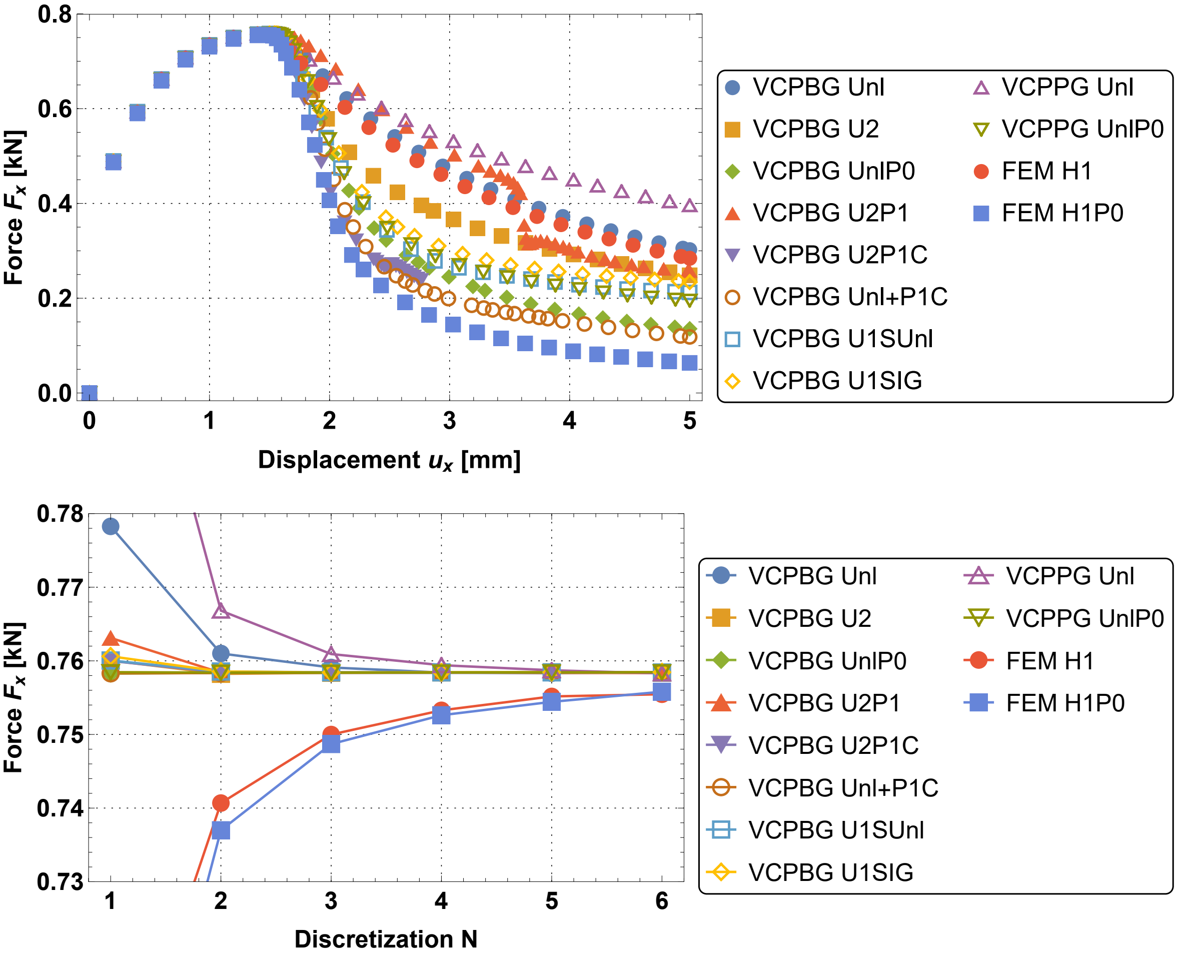

Figure 7.23. At the top: The residual force at the left clamping is plotted over the applied displacement on the right end. At the bottom: Convergence of maximal residual force at the left clamping for various formulations.

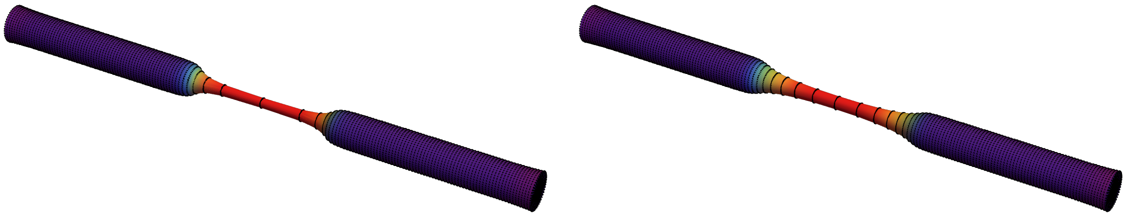

(a) VCPBG Unl, $\bar{e}^p_{max} = 1.95$

(b) VCPBG U2, $\bar{e}^p_{max} = 2.23$

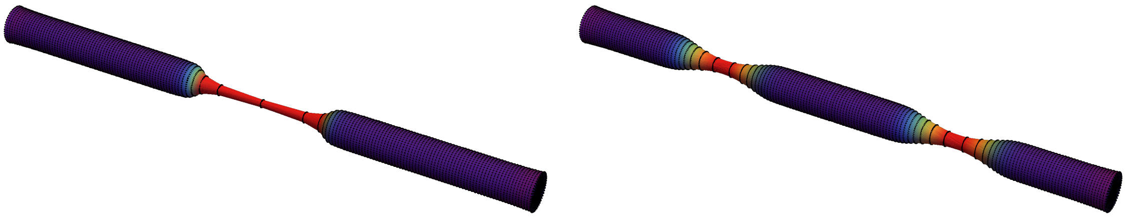

(c) VCPBG UnlP0, $\bar{e}^p_{max} = 5.30$

(d) VCPBG U2P1, $\bar{e}^p_{max} = 2.07$

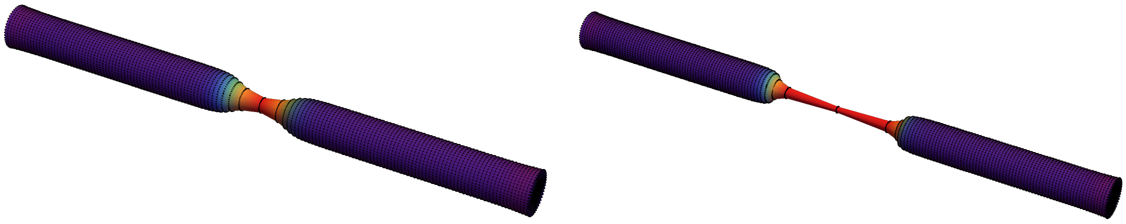

(e) VCPBG U2P1C, $\bar{e}^p_{max} = 2.10$

(f) VCPBG Unl+P1C, $\bar{e}^p_{max} = 6.09$

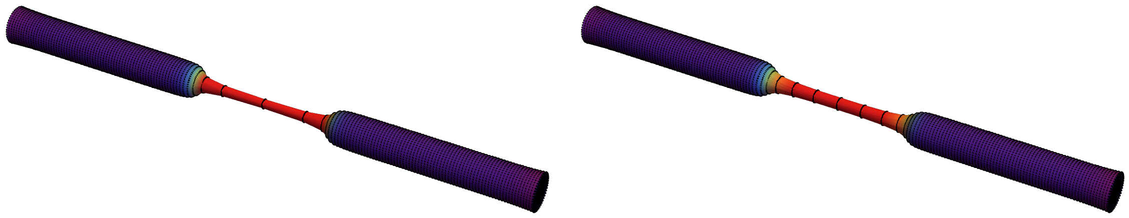

(g) VCPBG U1SUnl, $\bar{e}^p_{max} = 2.94$

(h) VCPBG U1SIG, $\bar{e}^p_{max} = 2.37$

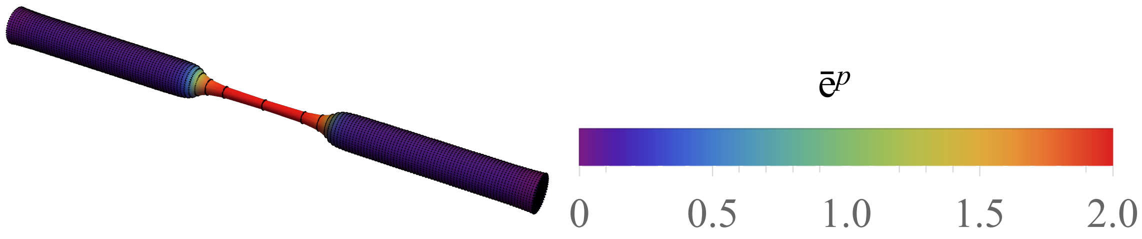

(i) VCPPG UnlP0, $\bar{e}^p_{max} = 2.94$

(j) Legend

Figure 7.24. The accumulated plastic strain for quasistatic cylindrical necking problem is colored on the deformed configuration for the presented formulations. The maximal accumulated plastic strain of the comparative FEM H1P0 solution is $\bar{e}^p_{max} = 3.71$

Table 7.5. Maximal accumulated plastic strain as a measure for the plastic localization within irregular particle patterns and failure angle for the highly irregularly discretized squared prism for all presented approaches.

Formulation	Maximal accumulated plastic strain at 360 degrees (D1)	Failure angle in degree (D2)
VCPBG Unl	0.92	1076.7
VCPBG U2	0.91	641.5
VCPBG UnlP0	1.97	1150.0
VCPBG U2P1	1.29	872.9
VCPBG U2P1C	2.32	460.0
VCPBG Unl+P1C	10.86	1364.2
VCPBG U1SUnl	1.24	1351.6
VCPBG U1SIG	1.3	2119.1
VCPPG Unl	$-$	2.9
VCPPG UnlP0	1.52	45.1
FEM H1	1.05	11.0
FEM H1P0	1.33	97.2
FEM H1P0, fine regular mesh	18.81	

randomly by a value in the interval $(-0.25, 0.25)$ (D1) or $(-0.5, 0.5)$ (D2) times the particle spacing, respectively. By means of collocation, the particle positions and volumes are then determined.

First, with the moderately distorted discretization (D1), a twisting up to 360 degrees is performed and the visual deformation (see Figure 7.26) as well as the maximal accumulated plastic strain (see Table 7.5) are examined. As can be seen, all formulations except the PPG Unl converge, but the localization of the plastic deformation, which should accumulate at the outer top, varies. The best matching results, compared to the FE benchmark, can be gained via the enriched Unl+P1C approach, followed from the other mixed formulations. Due to a slight locking of the stabilization, the localization of the underintegrated approaches is disturbed, but the visual deformations are still agreeable. In a second step, for the highly distorted discretization (D2), the rotation is continued until the adaptive time stepping could not converge for a further rotation of 0.1 degrees. The maximal rotation angle is displayed in Table 7.5. While the mesh-based FEM H1P0 solution already fails at 97.2 degrees, the PBG approaches can deal with rotations up to 15 times as large. Especially the underintegrated stabilized U1SIG formulation exhibits an excellent robustness. Furthermore, the mere displacement based PBG formulation with linear basis outperforms its FE counterpart by a factor of almost 100.

7.3.7 Taylor anvil impact benchmark

Subsequently, the classical Taylor anvil benchmark for impact simulations of KAMOULAKIS (1990) is implemented. Thereby, a copper rod with an initial velocity of $227\,\frac{\mathrm{m}}{\mathrm{s}}$ is shot

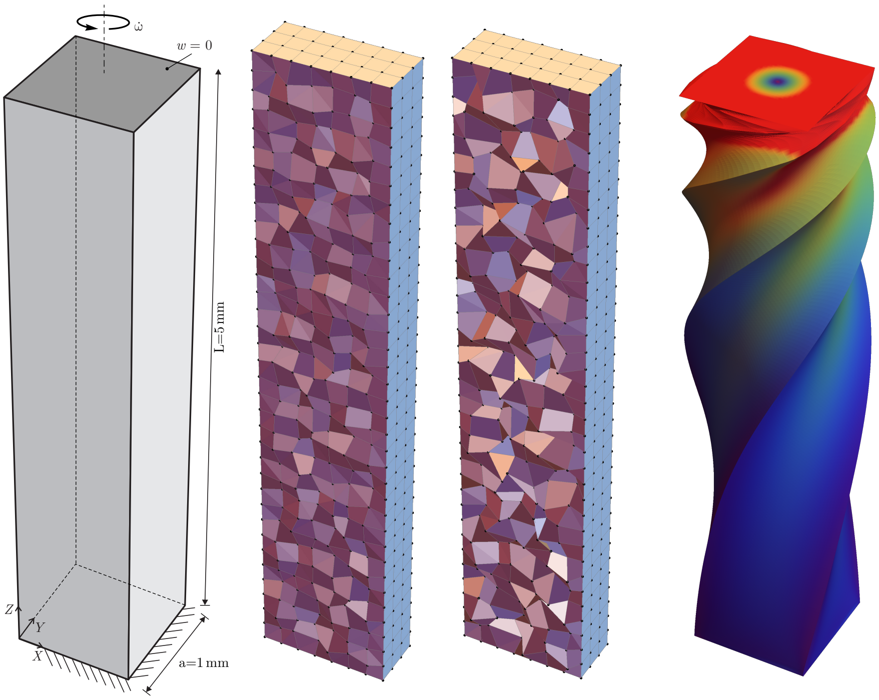

(a) Geometry (b) D1 (c) D2 (d) H1P0 benchmark

Figure 7.25. Geometry, discretization of collocated irregular meshes and benchmark solution with 360 000 H1P0 Finite Elements of the dynamic torsion problem with the same color legend as in Figure 7.26.

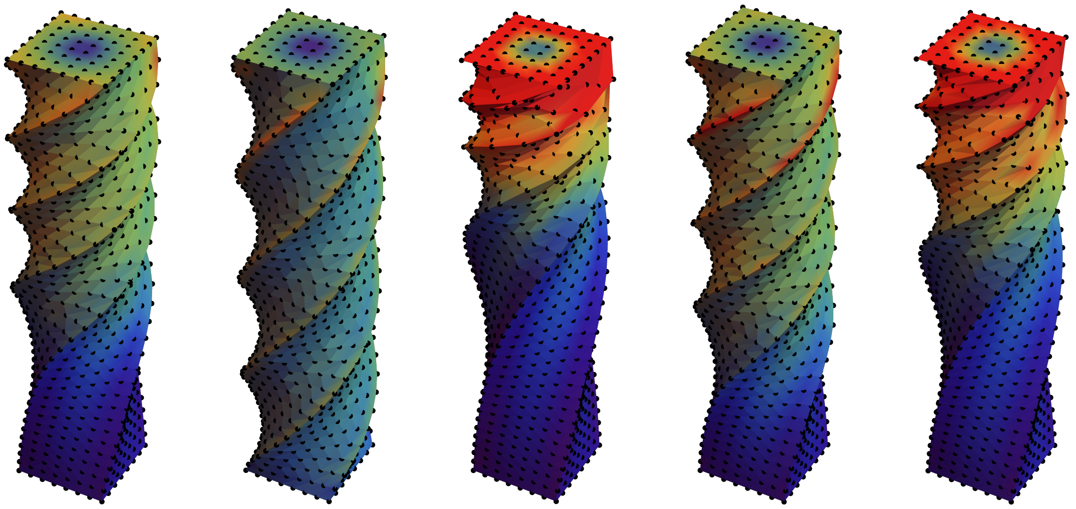

(a) VCPBG Unl (b) VCPBG U2 (c) VCPBG UnlP0 (d) VCPBG U2P1 (e) VCPBG U2P1C

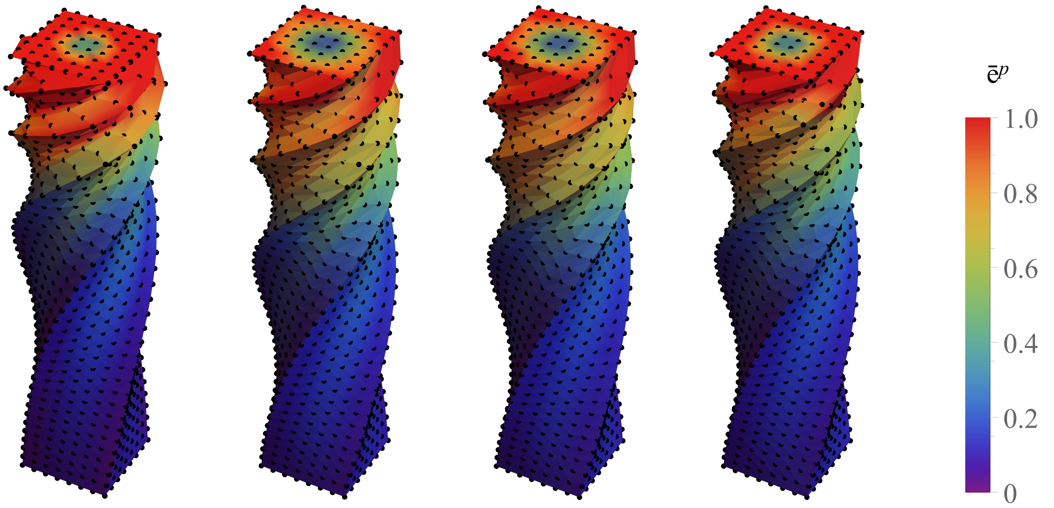

(f) VCPBG Unl+P1C (g) VCPBG U1SUnl (h) VCPBG U1SIG (i) VCPPG UnlP0 (j) Legend

Figure 7.26. The accumulated plastic strain for the problem of the dynamic torsion of a square prism is colored on the deformed configuration for the presented formulations.

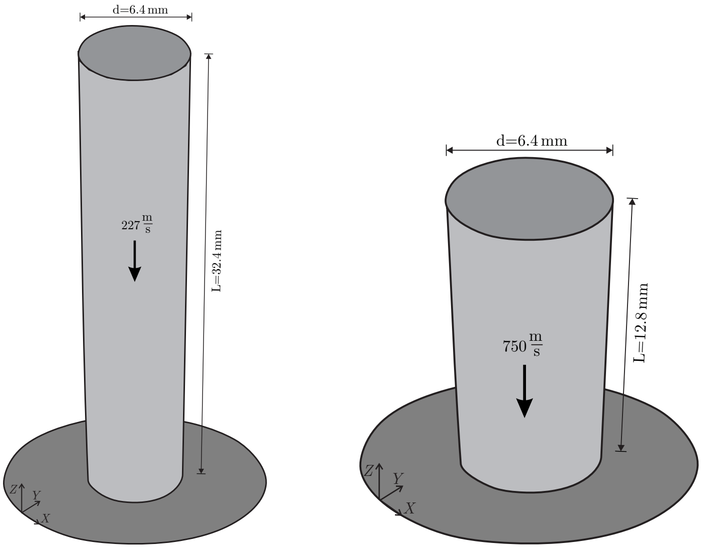
d=6.4 mm
$227\,\frac{\mathrm{m}}{\mathrm{s}}$
L=32.4 mm
Z
Y
X
d=6.4 mm
$750\,\frac{\mathrm{m}}{\mathrm{s}}$
L=12.8 mm
Z
Y
X

(a) Geometry A (b) Geometry B

Figure 7.27. Geometry and initial conditions of the two versions of the Taylor anvil benchmark.

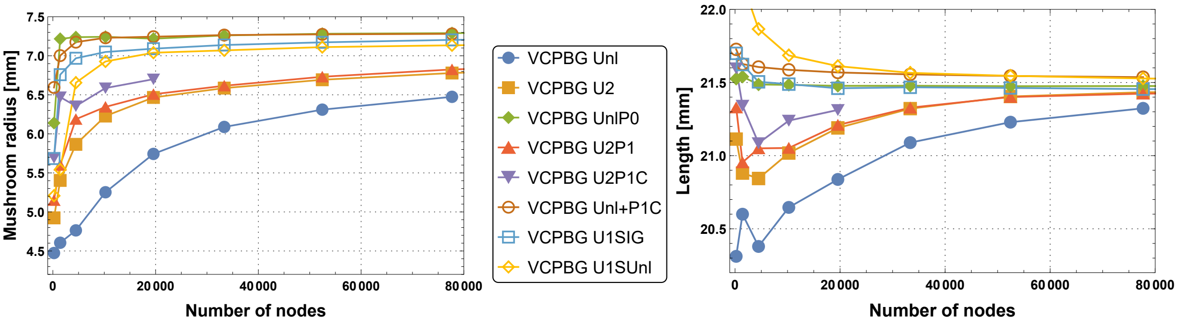

Figure 7.28. On the left: Final mushroom radius at the impacting end over number of particles. On the right: Final length in the center of the specimen over number of particles.

against a rigid, frictionless wall (see Figure 7.27(a)). The material parameters are set to be $E = 117.0\,\frac{\mathrm{kN}}{\mathrm{mm}^2}$, $\nu = 0.35$, $\sigma_{y0} = 0.4\,\frac{\mathrm{kN}}{\mathrm{mm}^2}$, $\sigma_{y\infty} = 0.4\,\frac{\mathrm{kN}}{\mathrm{mm}^2}$, $H = 0.1\,\frac{\mathrm{kN}}{\mathrm{mm}^2}$, $\delta = 0$ and $\rho_0 = 8.93\,\frac{\mathrm{g}}{\mathrm{cm}^3}$. With the impact of the bar, an elastic and plastic wave start to propagate from the bottom of the rod and form a characteristic mushroom-like deformation. Classically, the final length, the radius of the mushroom at the bottom and the maximal accumulated plastic strain at a time of $80\,\mu\mathrm{s}$ after impact when most of the initial kinetic energy dissipated are taken for comparison. Here, a series of refining discretizations is used for each of the presented PBG formulations, where the Unl, UnlP0, U1SUnl and U1SIG approaches are temporally explicitly integrated with the central difference method, and the U2, U2P1, U2P1C and Unl+P1C formulations utilize the Newmark-beta method with 1000 time steps. The contact zone at the bottom is simplified as a Dirichlet boundary condition which is, in case of the explicit integration, adopted to apply only compressive forces.

Table 7.6. Comparison of final length, mushroom radius and maximal total equivalent plastic strain of the literature and selected PBG approaches (extension of KUMAR ET AL. (2019)).

	Final length [mm]	Mushroom radius [mm]	$\bar{e}^p_{max}$
KAMOULAKIS (1990), FEM	$21.47 - 21.66$	$7.02 - 7.12$	$2.47 - 3.24$
ZHU & CESCOTTO (1995), FEM	$21.26 - 21.49$	$6.89 - 7.18$	$2.75 - 3.03$
CAMACHO & ORTIZ (1997), FEM	$21.42 - 21.44$	$7.21 - 7.24$	$2.97 - 3.25$
BELYTSCHKO ET AL. (2000), EFG	21.46	7.13	3.33
KUMAR ET AL. (2019), OTM	21.45	6.84	2.69
CIHAN ET AL. (2021), VEM H1JP	$21.36 - 21.45$	$6.99 - 7.01$	3.15
CIHAN ET AL. (2021), VEM VOJP	$21.56 - 21.65$	$7.17 - 7.18$	4.06
VCPBG Unl	21.32	6.47	2.81
VCPBG U2	21.44	6.85	2.94
VCPBG UnlP0	21.48	7.30	3.56
VCPBG U2P1	21.43	6.88	3.03
VCPBG U2P1C	21.31	6.70	2.49
VCPBG Unl+P1C	21.54	7.28	3.35
VCPBG U1SIG	21.45	7.26	4.46
VCPBG U1SUnl	21.52	7.16	3.73

The convergence of the mushroom radius and the final length of the copper rod against the number of particles are displayed in Figure 7.28. Apparently, the Unl, U2 and U2P1 formulations are suspect to volumetric locking. While the underintegrated and stabilized approaches U1SUnl and U1SIG also converge relatively fast, the best rates can be achieved with the mixed UnlP0 and Unl+P1C formulations. The reference values of the finest discretization are in agreement to those of previous literature (see Table 7.6). Figure 7.29 depicts the total equivalent plastic strain on the deformed configuration at a time of $80\,\mu\mathrm{s}$ for a discretization into 33361 particles. The locking behavior of some of the formulations can be recognized by the shape of the plastified mushroom region. When comparing the pressure field of the two best performing mixed approaches, an explanation for the outcome of the numerical inf-sup tests becomes visible. The UnlP0 formulation which not passed the inf-sup test shows checkerboard-like modes while the Unl+P1C formulation which satisfied the inf-sup test exhibits a smooth pressure field.

To demonstrate the capability in modeling extreme events, KUMAR ET AL. (2019) adopted the benchmark by increasing the initial velocity to $750\,\frac{\mathrm{m}}{\mathrm{s}}$ and decreasing the specimen length to $12.8\,\mathrm{mm}$ and the simulation time to $15\,\mu\mathrm{s}$. Figure 7.31 shows the deformed configuration of two intermediate, the final and extended $30\,\mu\mathrm{s}$ configuration of the U1SIG approach with explicit time integration and adaptive Dirichlet boundary conditions at the bottom. In the cross section after $3\,\mu\mathrm{s}$, it can be seen, that a cavity forms during the formation of the mushroom. This physically meaningful behavior could already be observed for high impact velocities in an experimental setting of an aluminum rod (CHAPMAN ET AL. (2005)) or numerically with a different geometry and speed with copper (FORDE ET AL. (2009)).

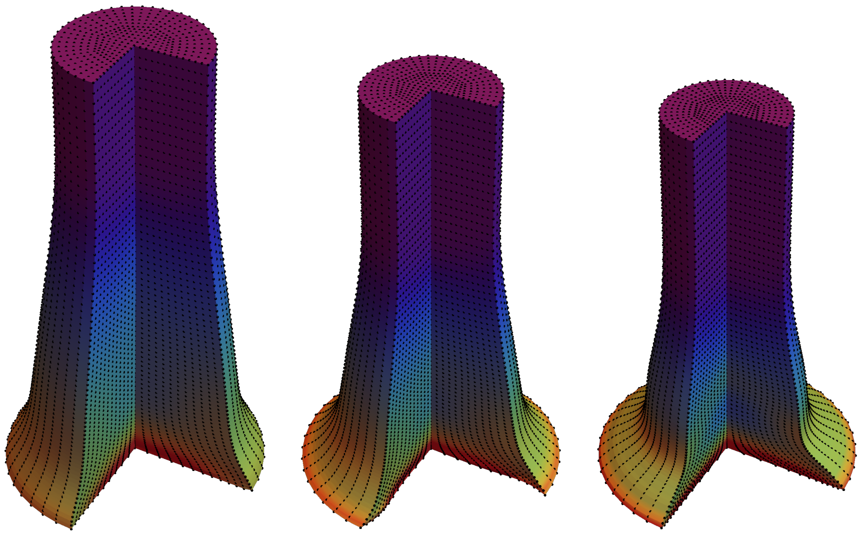

(a) VCPBG Unl (b) VCPBG U2 (c) VCPBG UnlP0

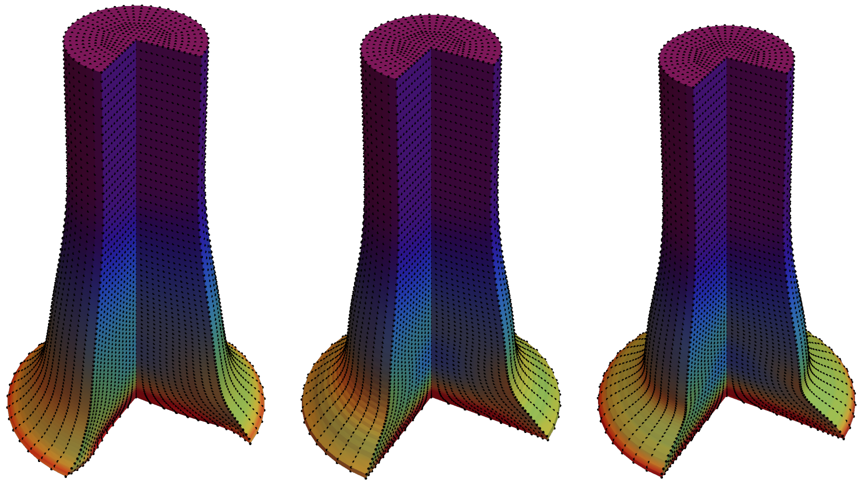

(d) VCPBG U2P1 (e) VCPBG U2P1C (f) VCPBG Unl+P1C

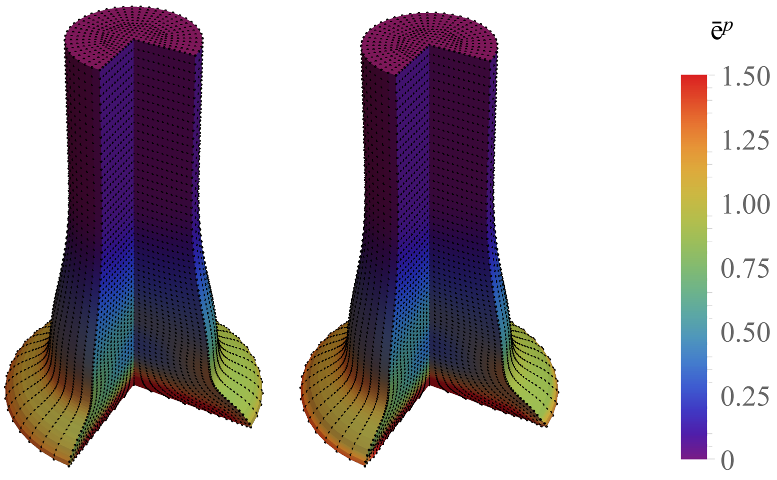
$\bar{\varepsilon}^p$
1.50
1.25
1.00
0.75
0.50
0.25
0

(g) VCPBG U1SUnl (h) VCPBG U1SIG (i) Legend

Figure 7.29. The accumulated plastic strain for the Taylor anvil benchmark is colored on the deformed configuration for the presented PBG formulations.

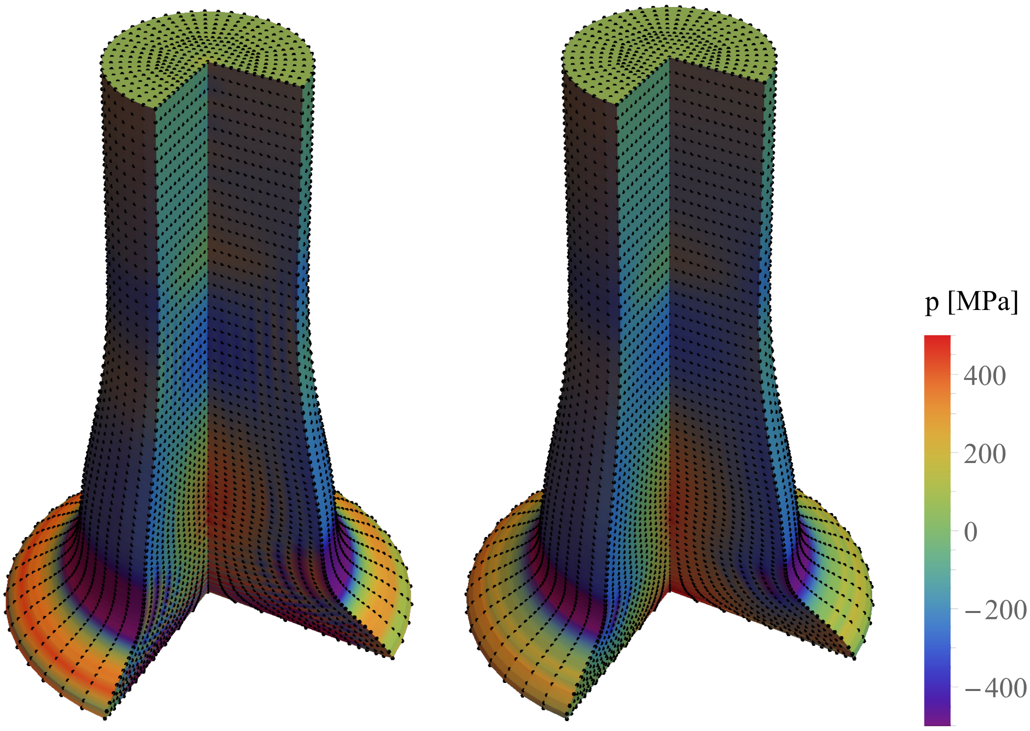

(a) VCPBG UnlP0 (b) VCPBG Unl+P1C (c) Legend

Figure 7.30. The pressure distribution of the two best performing mixed PBG approaches is visualized on the deformed configuration.

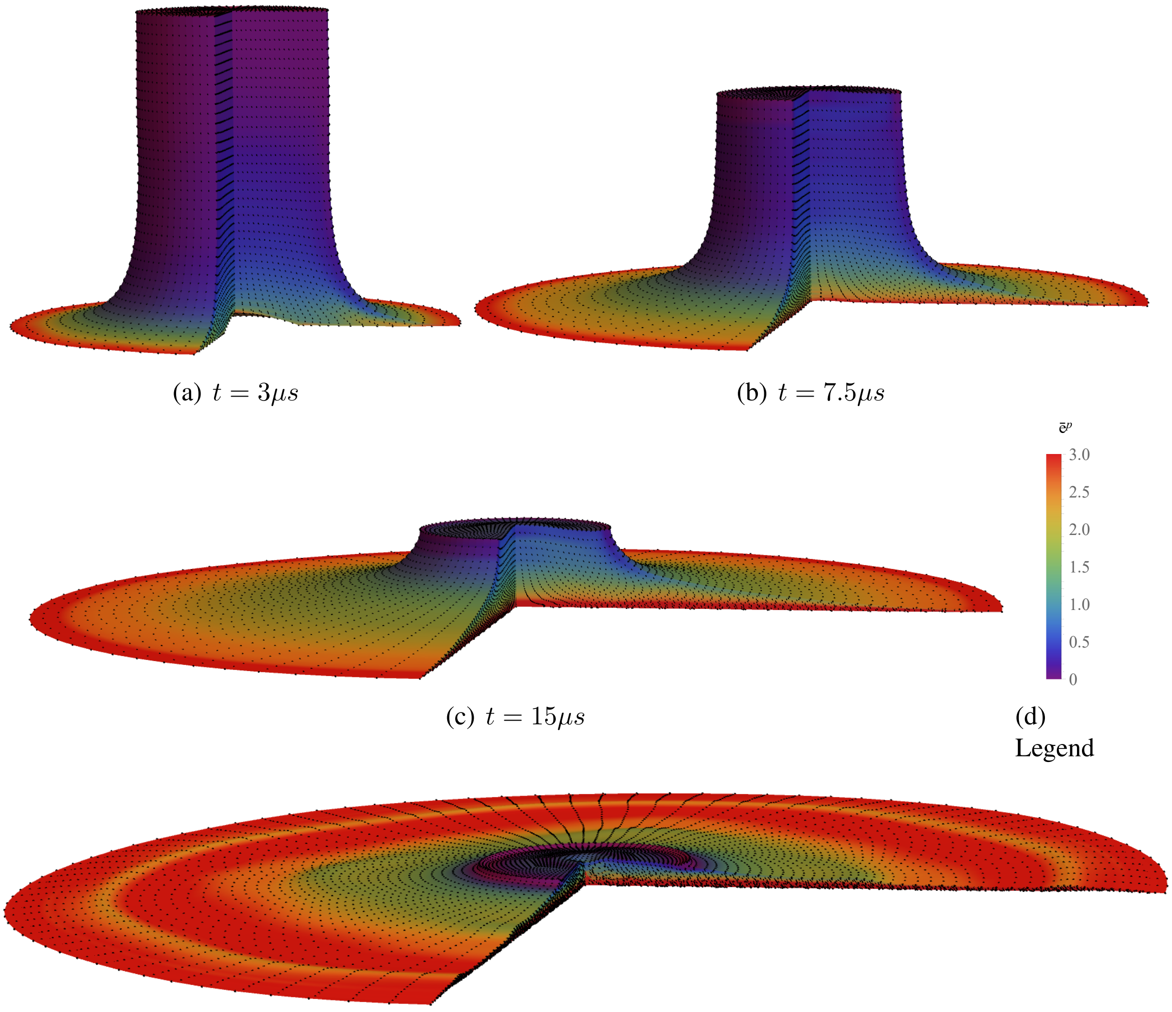

(a) $t = 3\mu s$

(b) $t = 7.5\mu s$

(c) $t = 15\mu s$

(d) Legend

(e) $t = 30\mu s$

Figure 7.31. The accumulated plastic strain is colored on two intermediate configurations, the final and extended configuration of the high velocity Taylor anvil impact test using the VCPBG U1SIG formulation.

7.3.8 Coupling with Finite Elements and symmetry boundary conditions

With the satisfaction of the patch test and the imposition of Dirichlet boundaries on a single layer of particles directly at the surface, the coupling with Finite Elements and the application of symmetry boundary conditions become straightforward. To demonstrate this, a plate with a circular hole (cf. YAGHOOBI & CHORZEPA (2018)) is used to test these possibilities. As depicted in Figure 7.32 the symmetry of the problem is utilized to model only the bottom left quarter (see also geometry and material parameters). PPG particles are used in the right area where high stresses are expected. The left part is modeled with

Q1 Finite Elements to further reduce the computational cost. Both domains are coupled simply by having the same nodes at the coupling interface. The FEM-PPG coupling is tested using an uncorrected and a first order variationally consistent formulation, both with 73728 elements and 21857 particles. As a benchmark, a Q1 Finite Element solution with 1523712 elements is used. In Figure 7.33, the normal stress in horizontal direction is plotted along the symmetry lines. For the variationally inconsistent formulation, strong oscillations occur near the coupling zone and at the boundary. In contrast, the first order variationally consistent version with fixed correction factors at the surface in normal direction agrees very well with the FE solution. Further, in the displacement and stress contours, displayed in Figure 7.34, smooth distributions with strongly localized stresses at the expected areas are observed.

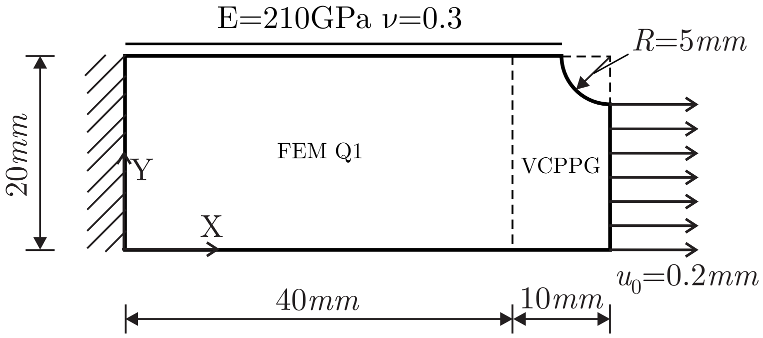

Figure 7.32. Geometry, material data and boundary conditions of the quarter of the plate with hole.

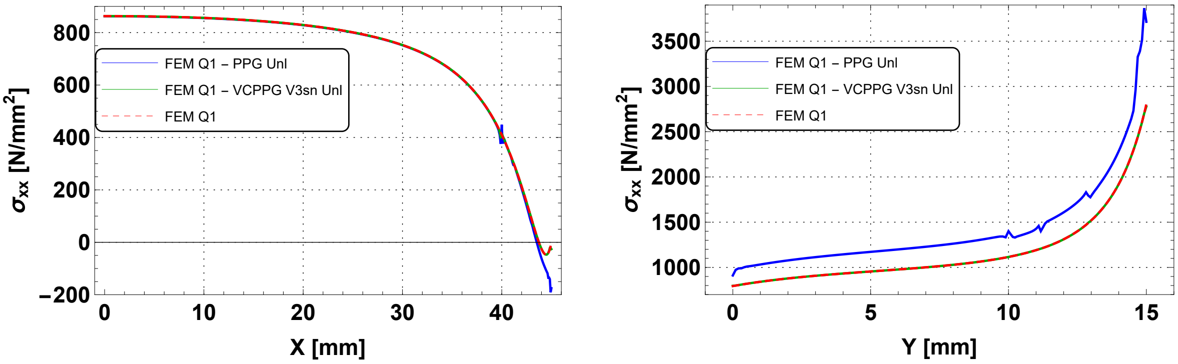

Figure 7.33. Normal stress in x-direction along the symmetry axis of the plate with hole problem for the FEM coupled uncorrected and first order variationally consistent PPG method compared to a Finite Element reference solution.

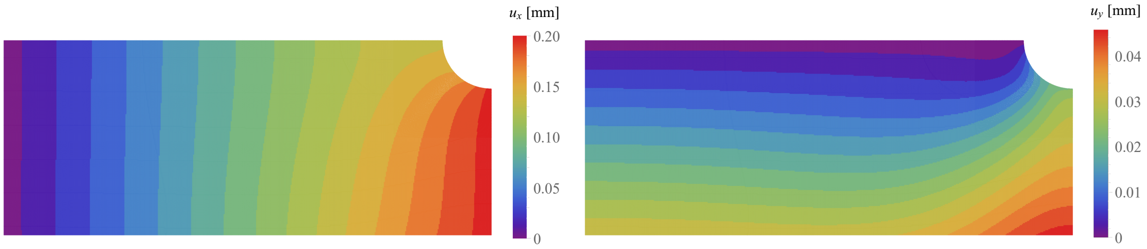

(a) Displacement in x-direction

(b) Displacement in y-direction

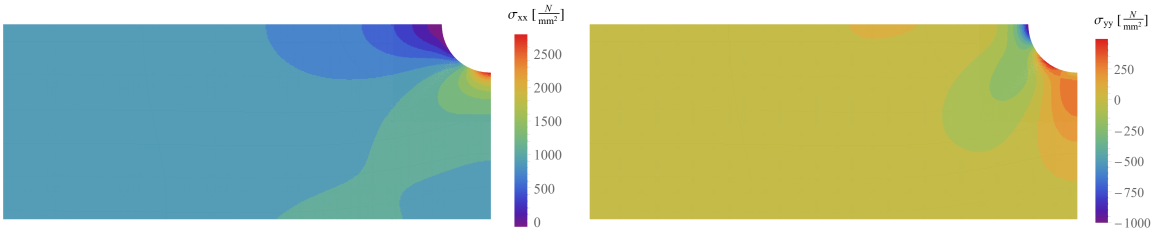

(c) Normal stress in x-direction

(d) Normal stress in y-direction

Figure 7.34. Displacement and stress contours of the plate with hole problem for the first order variationally consistent VCPPG V3sn Unl formulation, coupled with Finite Elements.

Chapter 8

Conclusion and outlook

In the presented work, the PG methods were introduced as a class of meshfree formulations based on particle discretizations as a generalization of the common peridynamic correspondence formulation and the corrected SPH. The Galerkin type approach provides the basis for developing more stable, robust, convergent and efficient correspondence formulations. Petrov-Galerkin formulations were found to offer a convenient tool to analyze the specific needs of shape functions and with which a set of crucial properties were identified. These include the interpolation property, trial function consistency, configurational consistency and variational consistency. Based on an essential inverse averaging, a powerful Bubnov-Galerkin method can be designed when constructing shape functions that fulfill all the mentioned conditions. Besides, with the option of full neighbor particle integration, it is possible to derive higher order, mixed and enriched peridynamic analogons to those known from FE technology. Noteworthy are on the one hand the VCPBG Unl formulation in simulations without geometric constraints and the VCPBG UnlP0 and especially VCPBG Unl+P1C approaches in the range of incompressibility and plastic isochoric flow within implicit simulations. When physical phenomena require small time steps, the VCPBG U1SIG formulation is a great alternative to utilize the central differences explicit time stepping where no global system of equations has to be solved and the constitutive laws are only once evaluated.

Compared to the FEM, the PBG method exhibits an extraordinary robustness against severely distorted original meshes for the cost of increased computational time, depending on the degree of non-locality. Its similar structure makes it possible to be implemented into existing FE environments as e.g. AceFEM, where neighborhoods take the place of elements and the particles are generated as collocated FE nodes. Compared, on the other hand, to the common peridynamic correspondence formulation, next to an increased stability, accuracy and convergence rate, a massive speed up can be realized for implicit frameworks which is based on the presented consistent linearization options in contrast to the classical numerical tangent approximation. However, the theory of the proposed PG methods is by no means complete and a vast range of possible extensions require for extensive research. Next to the volumetric locking that was addressed in chapter 6, other types of over-stiffening as e.g. shear locking should be examined in future. The development of error estimates should also be addressed to increase the reliability of the PG methods. Further, the extension to multi-field problems as e.g. a chemo-mechanical coupling (c.f. HAJIKHANI (2021)) could be analyzed. In the following, two possible proceeding research fields are presented, namely the modeling of fracture and fluid flows.

8.1 Back to the origin of peridynamics: Fracture

Although peridynamics originates with its integro-differential formulation from the modeling of discontinuities, the simple breakage of bonds gets less intrinsic and straightforward when utilizing state-based correspondence material models, cf. SILLING (2016). Nevertheless, as it is possible to use constitutive laws from the local theory within a correspondence framework, one can also incorporate continuum damage models like done in TUPEK ET AL. (2013), LIU ET AL. (2018) and BEHZADINASAB & FOSTER (2019). Using the PG methods, this technique can analogously pursued which is demonstrated in the following plate with tho holes problem using the VCPBG U1SIG formulation and explicit central difference time integration. Without going into further detail, the Johnson-Cook ductile damage and fracture model of JOHNSON & COOK (1983) and JOHNSON & COOK (1985) was exploited, where the thermal softening and rate dependency were neglected. As material parameters, a density of $\rho_0 = 7830\,\frac{\mathrm{kg}}{\mathrm{m}^3}$, Young's modulus of $E = 200\,\mathrm{GPa}$, Poisson's ratio of $\nu = 0.29$, strength constants $A = 792\,\mathrm{MPa}$, $B = 510\,\mathrm{MPa}$ and $n = 0.26$ and fracture constants $D_1 = 0.05$, $D_2 = 3.44$, $D_3 = -2.12$ and $D_c = 0.3$ were used as in BROUMAND & KHOEI (2015). The geometry of the problem is depicted in Figure 8.1 (a) and is modeled in plane strain. In the transient simulation, the steel plate is fixed at the bottom and pulled up at the top with a constant speed of $\bar{v} = 2000\,\frac{\mathrm{mm}}{\mathrm{s}}$. As visualized in Figure 8.1 (b) - (f), the plate starts to rupture in two places in the middle of the plate in the shear band. The crack paths join and propagate towards the circular cutouts. Finally the two outer bridges tear apart in a 45 degree angle to the tension direction. The force response at the bottom end and stored elastic energy are plotted in Figures 8.1 (g) and (h). The strong dynamics lead to an increase of force and energy which soon drops down in consequence of the failure. While the residual force at the bottom clamping oscillates around the x-axis, the stored energy decreases to an amount denoting the internal residual deformation.

Note, that the demonstrated simulation was performed in a total Lagrangian setting and the connectivity of the lower and upper part of the plate are still connected. While in this academic test case this causes no harm, in a complex practical crash event, it may be preferable to separating also the connectivity when a fracture zone occurs. This could be realized either in a semi-total Lagrangian or an updated Lagrangian manner. Neighbor particles that move away to far, meaning they are on the other side of the fracture, could be deleted from the original family and the shape functions recomputed in the initial or current configuration in case of semi-total and updated Lagrange, respectively. In the subsequent correction of variational consistency, it must be noted that with the fracture a surface arises which has to be taken into account. Since the computation of the VC correction requires the solution of a global system, such an update should not be performed in each time step and only when needed as it would otherwise ruin the computational speed of an explicit simulation. An alternative technique could consist in the use of local VC correction schemes which will further be explained in section 8.2.

8.2 Fluid flows

Next to the simulation of solid mechanics problems, meshfree methods are often used to model fluids in an updated Lagrangian description. To extend the PG methods for simulating fluids, some prerequisites should be noted. One of it consists in the absence of volumetric locking since many fluids behave almost incompressible. With respect to this, several strategies have been pursued as fractional step schemes (see e.g. CUMMINS & RUDMAN (1999) and NITHIARASU ET AL. (2006)) or pseudo divergence free shape functions (cf. HUERTA ET AL. (2004b)), but also the mixed displacement–pressure–dilation approaches can be used when fulfilling the LBB condition. To demonstrate this, in Figure 8.2, a 2-D Poiseuille flow was simulated using the VCPBG Unl+P1C formulation and Newmark time integration. While initially at rest, the water-like Newtonian fluid (density $\rho = 10^3\,\frac{\mathrm{kg}}{\mathrm{m}^3}$, bulk modulus $K = 2.08\,\mathrm{GPa}$, dynamic viscosity $\eta = 10^{-3}\,\mathrm{Pa\,s}$) underlies a gravity of $g = 2 \cdot 10^{-4}\,\frac{\mathrm{m}}{\mathrm{s}^2}$ in horizontal direction (x-axis) and accelerates until a parabolic velocity distribution between the upper and lower wall sets in. In contrast to the PBG Unl formulation (where the water does not flow at all), no locking effects could be observed here, which is in accordance with the numerical inf-sup test of section 7.2.5.

Nevertheless, in its present setting, the Unl+P1C formulation is still not applicable for complex flow problems which can be seen in situations where the accurate approximation of the pressure field becomes important. Therefore, in a second example, the classical dam break problem is simulated as depicted in Figure 8.3 (a) with an inviscid water-like fluid. Again, the VCPBG Unl+P1C formulation with Newmark time integration is used within a discretization of 50×100 regularly distributed particles in a total Lagrangian simulation. Both the shape of the water as well as the pressure distribution within it look reasonable at the selected time frames in Figures 8.3 (b) - (g). However, when performing the same simulation using an irregular particle distribution, severe oscillations would soon arise. The reason for this lies in the fact, that the variational consistency correction is only performed with respect to the test function of the displacements. Even though any linear displacement field can be captured accurately, a linear pressure field may not. Hence, additional integration constraints have to hold for the virtual pressure field. A global correction scheme was investigated to correct this inconsistency, but seemed not to be appropriate due to a rank deficiency of the global correction matrix that could not be eliminated as done in section 5.3.2. To circumvent the issue of finding boundary conditions for the VC correction and to accelerate the correction procedure, the development of local VC corrections as outlined below should be pursued. Although the condition for first order VC of the displacement field is globally coupled, it can be decoupled to a set of (larger) local conditions. By introducing a sum over volume fractions on the right hand side of equation (5.18) (PBG), it rewrites considering zeroth order consistency (i.e. no bond correction is performed)

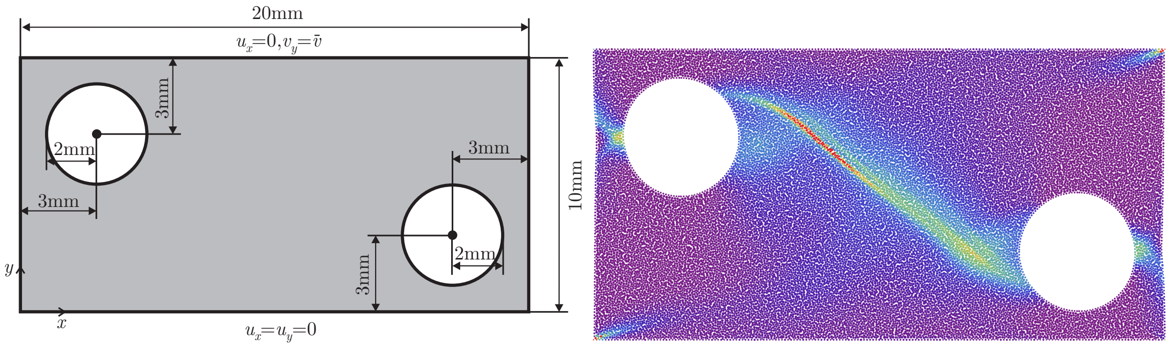
20mm
u_x=0,v_y=$\bar{v}$
3mm
2mm
3mm
3mm
2mm
3mm
10mm
y
x
u_x=u_y=0

(a) Geometry and boundary conditions (b) $t = 8\,\mu$s

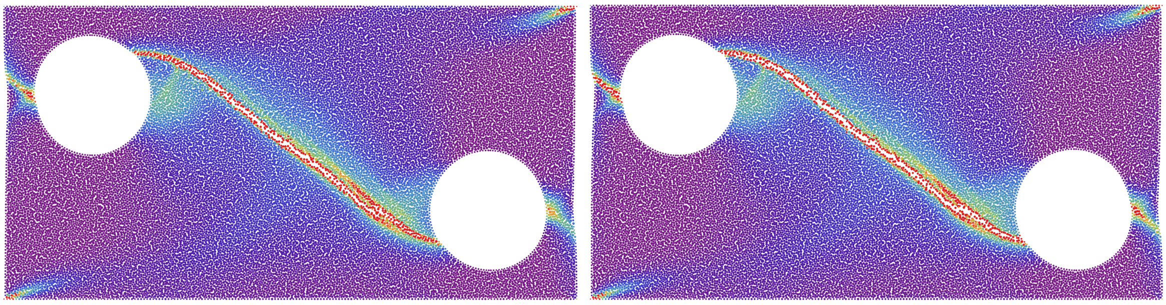

(c) $t = 10\,\mu$s (d) $t = 12\,\mu$s

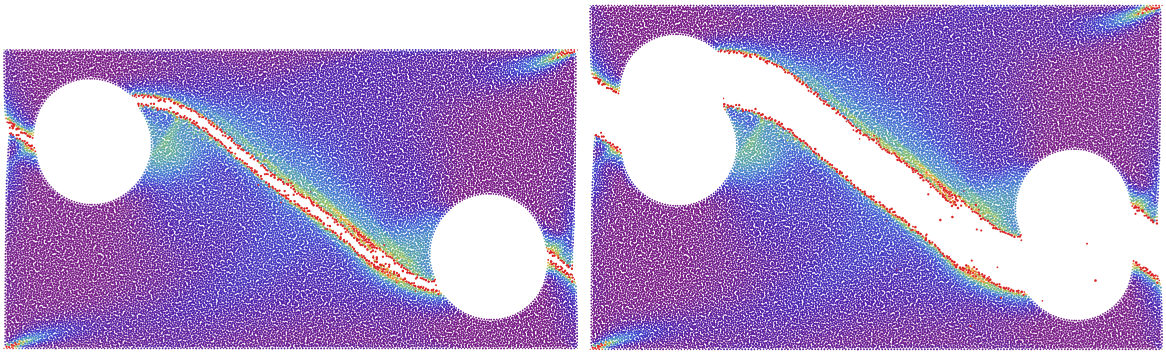

(e) $t = 20\,\mu$s (f) $t = 100\,\mu$s

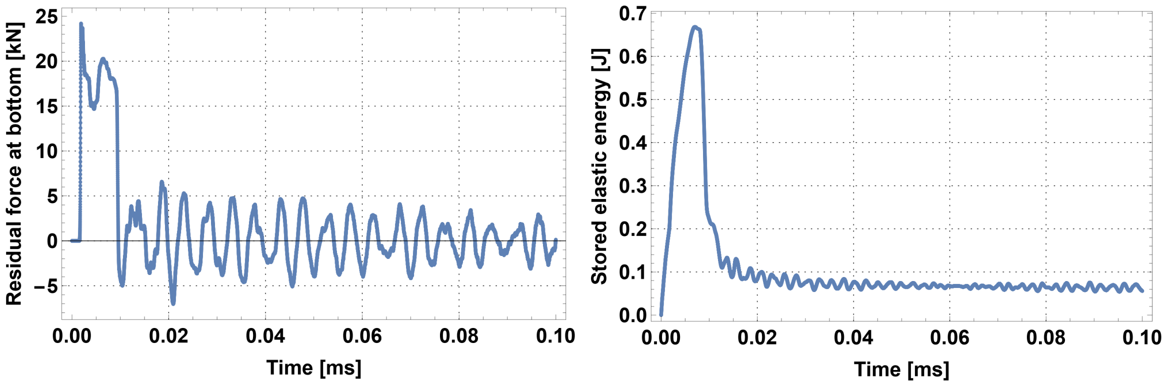

(g) Force response (h) Elastic energy

Figure 8.1. Plate with two hole ductile fracture test case: For the discretization a collocated T1-FE mesh resulting into 27936 particles is used with the inherited FE-connectivity.

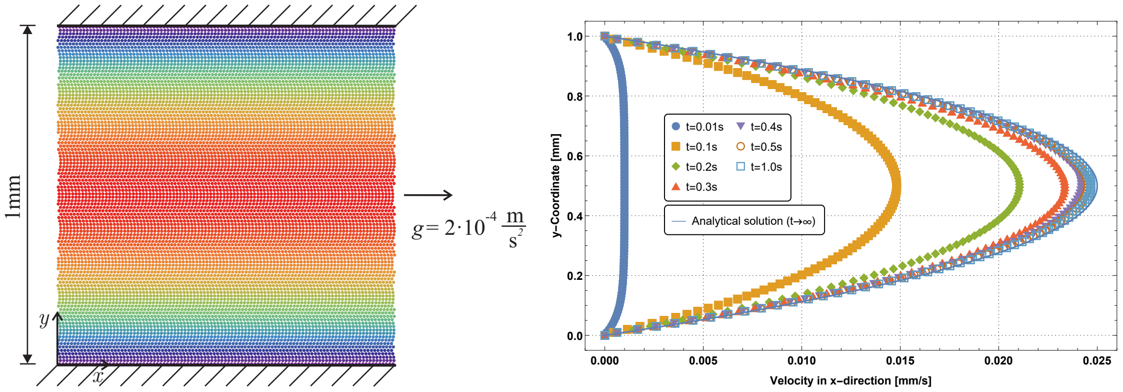

(a) $t = 10\,\mathrm{s}$ (b) Horizontal velocity profile for certain time frames

Figure 8.2. Geometry, discretization and dynamic response of the 2-D Poiseuille flow using 100 × 100 VCPBG Unl+P1C particles.

$$\sum_{i=0}^{N^k}\sum_{j=0}^{N^i}\frac{V^iV^j}{V^{\mathcal{H}_0^i}}\frac{\partial N_{\delta\mathbf{u}}^{ijk}}{\partial\mathbf{X}} = \begin{cases}\sum\limits_{i=0}^{N^k}\mathbf{0} & \text{on } \Omega\backslash\partial\Omega\\ \sum\limits_{i=0}^{N^k}\frac{V^i}{V^{\mathcal{H}_0^k}}\mathbf{A}^k & \text{on } \partial\Omega\end{cases} \tag{8.1}$$

which is valid whenever for each neighbor particle $i \in \mathcal{H}_0^k$ applies

$$\sum_{j=0}^{N^i}\frac{V^iV^j}{V^{\mathcal{H}_0^i}}\frac{\partial N_{\delta\mathbf{u}}^{ijk}}{\partial\mathbf{X}} = \begin{cases}\mathbf{0} & \text{on } \Omega\backslash\partial\Omega\\ \frac{V^i}{V^{\mathcal{H}_0^k}}\mathbf{A}^k & \text{on } \partial\Omega\end{cases} \tag{8.2}$$

As equation (8.2) has to hold for each neighborhood in a global pairwise discretization, the indices can be changed yielding

$$\sum_{j=0}^{N^k}V^j\frac{\partial N_{\delta\mathbf{u}}^{kji}}{\partial\mathbf{X}} = \frac{V^{\mathcal{H}_0^k}}{V^{\mathcal{H}_0^i}}\begin{cases}\mathbf{0} & i \text{ on } \Omega\backslash\partial\Omega\\ \mathbf{A}^i & i \text{ on } \partial\Omega\end{cases} \quad \forall i \in \mathcal{H}_0^k\,, \tag{8.3}$$

which is a set of local conditions. At this point, a local correction ansatz can be introduced to modify the test function derivatives in conformity with section 5.3.2. Thereby, either special correction shape functions conditions or additional constraint equations have to be defined such that the consistency properties listed in section 5.1.1 are preserved.

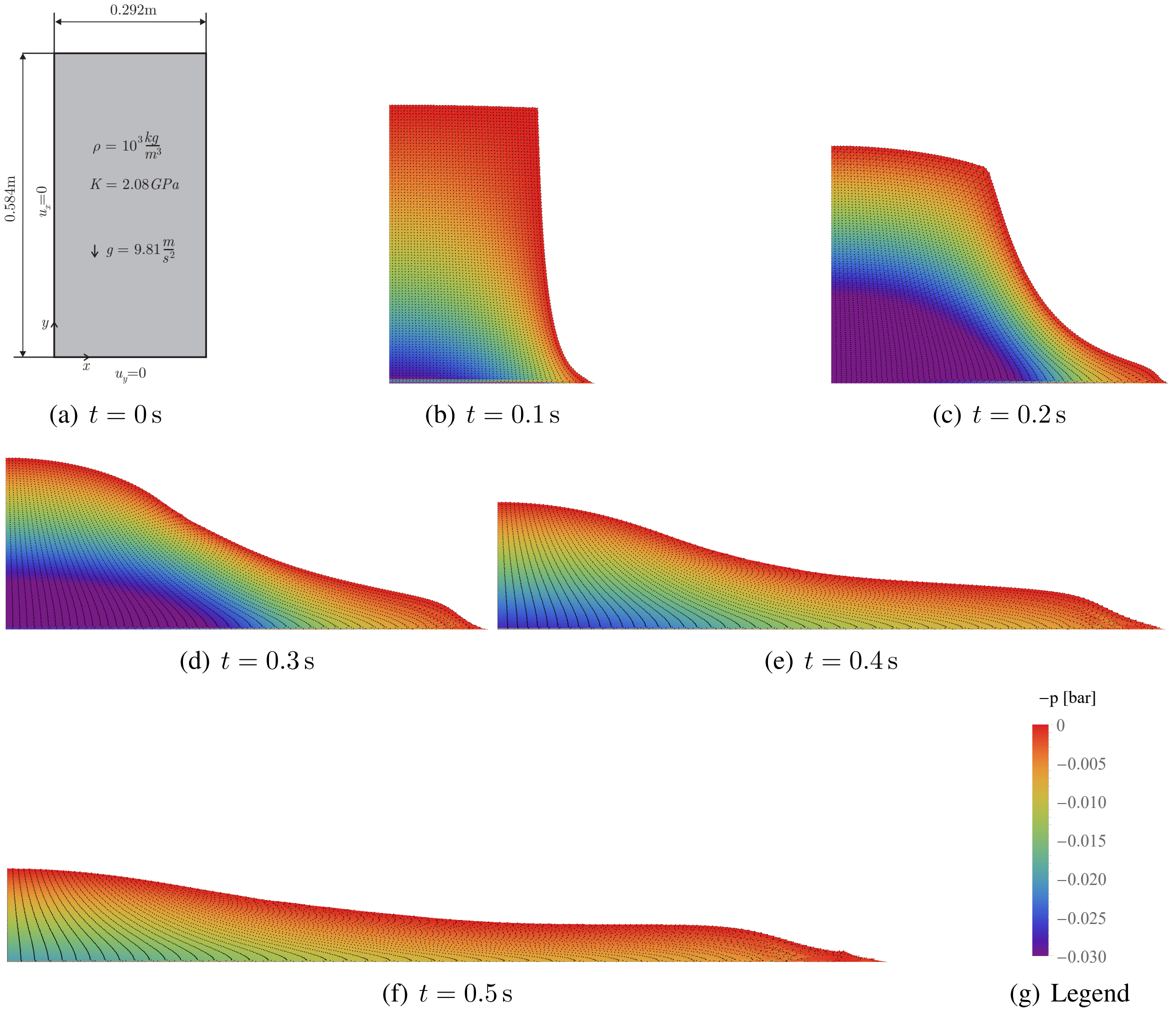

(a) $t = 0\,\mathrm{s}$ (b) $t = 0.1\,\mathrm{s}$ (c) $t = 0.2\,\mathrm{s}$

(d) $t = 0.3\,\mathrm{s}$ (e) $t = 0.4\,\mathrm{s}$

(f) $t = 0.5\,\mathrm{s}$ (g) Legend

Figure 8.3. Geometry, boundary conditions, material data and exemplary deformed configurations of the dam break problem.

Appendix A

Exemplary derivation of the global tangent stiffness matrix

Considering only displacement-independent loads and a non changing discretization, the discretized weak form of equation (4.14) is linearized as follows:

$$\Delta\delta\bar{U}_h = \mathop{\mathbf{A}}_{k=1}^{n^p} \Delta \left\{ -V^k \sum_{j=0}^{N^k} \left[\bar{\mathbf{t}}^{kj} - \bar{\mathbf{t}}^{jk}\right] V^j \cdot \delta\mathbf{u}^k \right\} . \tag{A.1}$$

Taking into account that the pairwise force densities are defined to be zero outside of H_0^k, equation (A.1) can be rewritten analogously to equations (3.13) as

$$\Delta\delta\bar{U}_h = \mathop{\mathbf{A}}_{k=1}^{n^p} \Delta \left\{ V^k \sum_{j=0}^{N^k} \left[\bar{\mathbf{t}}^{kj} - \bar{\mathbf{t}}^{jk}\right] V^j \cdot \delta\mathbf{u}^j \right\} . \tag{A.2}$$

It follows the particle-wise view under the assumption of constant initial particle volumes and actual displacement independent virtual displacements:

$$\Delta\delta\bar{U}_h^k = V^k \sum_{j=0}^{N^k} \Delta \left[\bar{\mathbf{t}}^{kj} - \bar{\mathbf{t}}^{jk}\right] V^j \cdot \delta\mathbf{u}^j . \tag{A.3}$$

By inserting the correspondence formulation of equation (4.21) (PPG1) it changes to

$$\Delta\delta\bar{U}_h^k = \sum_{j=0}^{N^k} \Delta \left[-V^j \bar{\mathbf{P}}^{kj} \cdot \frac{\partial N_{\delta\mathbf{u}}^{jjk}}{\partial\mathbf{X}} + V^k \bar{\mathbf{P}}^{jk} \cdot \frac{\partial N_{\delta\mathbf{u}}^{kkj}}{\partial\mathbf{X}} \right] \cdot \delta\mathbf{u}^j . \tag{A.4}$$

Since the test functions are defined in the reference configuration and are therefore displacement independent, it simplifies to

$$\Delta\delta\bar{U}_h^k = \sum_{j=1}^{N^k} \left[-V^j \Delta\bar{\mathbf{P}}^{kj} \cdot \frac{\partial N_{\delta\mathbf{u}}^{jjk}}{\partial\mathbf{X}} + V^k \Delta\bar{\mathbf{P}}^{jk} \cdot \frac{\partial N_{\delta\mathbf{u}}^{kkj}}{\partial\mathbf{X}} \right] \cdot \delta\mathbf{u}^j . \tag{A.5}$$

Substituting the first Piola-Kirchhoff stress for $\bar{\mathbf{P}} = \bar{\mathbf{F}} \cdot \bar{\mathbf{S}}$ and the linearized second Piola-Kirchhoff stress for $\Delta\bar{\mathbf{S}} = \bar{\mathbb{C}} : \Delta\bar{\mathbf{E}}$ yields via the product rule

$$\begin{aligned}\Delta\delta\bar{U}_h^k = \sum_{j=1}^{N^k} \Bigg[& -V^j \left(\Delta\bar{\mathbf{F}}^{kj} \cdot \bar{\mathbf{S}}^{kj} + \bar{\mathbf{F}}^{kj} \cdot \bar{\mathbb{C}}^{kj} : \Delta\bar{\mathbf{E}}^{kj}\right) \cdot \frac{\partial N_{\delta\mathbf{u}}^{jjk}}{\partial\mathbf{X}} \\ & + V^k \left(\Delta\bar{\mathbf{F}}^{jk} \cdot \bar{\mathbf{S}}^{jk} + \bar{\mathbf{F}}^{jk} \cdot \bar{\mathbb{C}}^{jk} : \Delta\bar{\mathbf{E}}^{jk}\right) \cdot \frac{\partial N_{\delta\mathbf{u}}^{kkj}}{\partial\mathbf{X}} \Bigg] \cdot \delta\mathbf{u}^j \\ = {} & T_1 + T_2 + T_3 + T_4\end{aligned} \tag{A.6}$$

with the fourth order material tangent $\mathbb{C}$ and the Green-Lagrange strain $\bar{\mathbf{E}} = \frac{1}{2}\left(\bar{\mathbf{F}}^T \cdot \bar{\mathbf{F}} - \mathbf{1}\right)$. The further breakdown of the above expression is separated into a geometric (T_1 and T_3) and a substantial part (T_2 and T_4).

Geometric Part

Using the shape function approach of equation (4.11) and the derivative of the partition of unity condition (bond correction is not considered here), the linearization of the deformation gradient $\Delta\bar{\mathbf{F}}^{kj}$ gets

$$\Delta\bar{\mathbf{F}}^{kj} = \Delta\bar{\mathbf{H}}^{kj} = \sum_{i=0}^{N^k} \Delta\mathbf{u}^{ki} \otimes \frac{\partial N_{\mathbf{u}}^{kji}}{\partial\mathbf{X}} = \sum_{i=0}^{N^k} \mathbf{u}^i \otimes \frac{\partial N_{\mathbf{u}}^{kji}}{\partial\mathbf{X}}\,. \tag{A.7}$$

Thereby, the first geometric part writes

$$T_1 = \sum_{j=1}^{N^k}\sum_{i=0}^{N^k} -V^j \mathbf{u}^i \otimes \frac{\partial N_{\mathbf{u}}^{kji}}{\partial\mathbf{X}} \cdot \bar{\mathbf{S}}^{kj} \cdot \frac{\partial N_{\delta\mathbf{u}}^{jjk}}{\partial\mathbf{X}} \cdot \delta\mathbf{u}^j\,. \tag{A.8}$$

Rearranging this leads to

$$T_1 = \sum_{j=1}^{N^k}\sum_{i=0}^{N^k} \delta\mathbf{u}^j \cdot \left(-V^j \frac{\partial N_{\mathbf{u}}^{kji}}{\partial\mathbf{X}} \cdot \bar{\mathbf{S}}^{kj} \cdot \frac{\partial N_{\delta\mathbf{u}}^{jjk}}{\partial\mathbf{X}}\right) \mathbf{1} \cdot \mathbf{u}^i = \sum_{j=1}^{N^k}\sum_{i=0}^{N^k} \delta\mathbf{u}^j \cdot G_1^{ji} \mathbf{1} \cdot \mathbf{u}^i \tag{A.9}$$

with the geometrical scalar

$$G_1^{ji} = -V^j \frac{\partial N_{\mathbf{u}}^{kji}}{\partial\mathbf{X}} \cdot \bar{\mathbf{S}}^{kj} \cdot \frac{\partial N_{\delta\mathbf{u}}^{jjk}}{\partial\mathbf{X}}\,. \tag{A.10}$$

Analogously, the second geometric part T_3 is treated by changing the indices of the linearized deformation gradient (equation (A.7)):

$$T_3 = \sum_{j=1}^{N^k}\sum_{i=0}^{N^j} V^k \mathbf{u}^i \otimes \frac{\partial N_{\mathbf{u}}^{jki}}{\partial\mathbf{X}} \cdot \bar{\mathbf{S}}^{jk} \cdot \frac{\partial N_{\delta\mathbf{u}}^{kkj}}{\partial\mathbf{X}} \cdot \delta\mathbf{u}^j\,. \tag{A.11}$$

Again, a rearrangement leads to

$$T_3 = \sum_{j=1}^{N^k} \sum_{i=0}^{N^j} \delta \mathbf{u}^j \cdot \left(V^k \frac{\partial N_{\mathbf{u}}^{jki}}{\partial \mathbf{X}} \cdot \bar{\mathbf{S}}^{jk} \cdot \frac{\partial N_{\delta \mathbf{u}}^{kkj}}{\partial \mathbf{X}} \right) \mathbf{1} \cdot \mathbf{u}^i = \sum_{j=1}^{N^k} \sum_{i=0}^{N^j} \delta \mathbf{u}^j \cdot G_2^{ji} \mathbf{1} \cdot \mathbf{u}^i \tag{A.12}$$

with

$$G_2^{ji} = V^k \frac{\partial N_{\mathbf{u}}^{jki}}{\partial \mathbf{X}} \cdot \bar{\mathbf{S}}^{jk} \cdot \frac{\partial N_{\delta \mathbf{u}}^{kkj}}{\partial \mathbf{X}} \, . \tag{A.13}$$

Substantial Part

By using the linearized deformation gradient of equation (A.7) and considering the product rule, the linearized Green-Lagrange strain can be written as

$$\Delta \bar{\mathbf{E}}^{kj} = \frac{1}{2} \left(\Delta \bar{\mathbf{F}}^{kj^T} \cdot \bar{\mathbf{F}}^{kj} + \bar{\mathbf{F}}^{kj^T} \cdot \Delta \bar{\mathbf{F}}^{kj} \right) = \sum_{i=0}^{N^k} \frac{1}{2} \left(\frac{\partial N_{\mathbf{u}}^{kji}}{\partial \mathbf{X}} \otimes \mathbf{u}^i \cdot \bar{\mathbf{F}}^{kj} + \bar{\mathbf{F}}^{kj^T} \cdot \mathbf{u}^i \otimes \frac{\partial N_{\mathbf{u}}^{kji}}{\partial \mathbf{X}} \right) . \tag{A.14}$$

Inserting this into the first substantial part T_2 leads to

$$\begin{aligned} T_2 = & \sum_{j=1}^{N^k} \sum_{i=0}^{N^k} -\frac{1}{2} V^j \bar{\mathbf{F}}^{kj} \cdot \bar{\mathbb{C}}^{kj} : \left(\frac{\partial N_{\mathbf{u}}^{kji}}{\partial \mathbf{X}} \otimes \mathbf{u}^i \cdot \bar{\mathbf{F}}^{kj} \right) \cdot \frac{\partial N_{\delta \mathbf{u}}^{jjk}}{\partial \mathbf{X}} \cdot \delta \mathbf{u}^j \\ & + \sum_{j=1}^{N^k} \sum_{i=0}^{N^k} -\frac{1}{2} V^j \bar{\mathbf{F}}^{kj} \cdot \bar{\mathbb{C}}^{kj} : \left(\bar{\mathbf{F}}^{kj^T} \cdot \mathbf{u}^i \otimes \frac{\partial N_{\mathbf{u}}^{kji}}{\partial \mathbf{X}} \right) \cdot \frac{\partial N_{\delta \mathbf{u}}^{jjk}}{\partial \mathbf{X}} \cdot \delta \mathbf{u}^j \, . \end{aligned} \tag{A.15}$$

Written in index notation and considering the symmetries of $\bar{\mathbb{C}}$, the two parts can be merged as follows:

$$\begin{aligned} & \sum_{j=1}^{N^k} \sum_{i=0}^{N^k} -\frac{1}{2} V^j \bar{F}_{FA}^{kj} \bar{\mathbb{C}}_{ABCD}^{kj} \frac{\partial N_{\mathbf{u}}^{kji}}{\partial X_C} u_E^i \bar{F}_{ED}^{kj} \frac{\partial N_{\delta \mathbf{u}}^{jjk}}{\partial X_B} \delta u_F^j \\ & + \sum_{j=1}^{N^k} \sum_{i=0}^{N^k} -\frac{1}{2} V^j \bar{F}_{FA}^{kj} \bar{\mathbb{C}}_{ABCD}^{kj} \bar{F}_{DE}^{kj^T} u_E^i \frac{\partial N_{\mathbf{u}}^{kji}}{\partial X_C} \frac{\partial N_{\delta \mathbf{u}}^{jjk}}{\partial X_B} \delta u_F^j \\ & = \sum_{j=1}^{N^k} \sum_{i=0}^{N^k} -\delta u_F^j V^j \bar{F}_{FA}^{kj} \frac{\partial N_{\delta \mathbf{u}}^{jjk}}{\partial X_B} \mathbb{C}_{BADC}^{kj} \frac{\partial N_{\mathbf{u}}^{kji}}{\partial X_C} \bar{F}_{DE}^{kj^T} u_E^i \, . \end{aligned} \tag{A.16}$$

Rewriting this in matrix notation yields

$$T_2 = \sum_{j=1}^{N^k} \sum_{i=0}^{N^k} \delta \mathbf{u}^j \cdot \left[-V^j \bar{\mathbf{F}}^{kj} \cdot \left(\frac{\partial N_{\delta \mathbf{u}}^{jjk}}{\partial \mathbf{X}} \cdot \bar{\mathbb{C}}^{kj} \cdot \frac{\partial N_{\mathbf{u}}^{kji}}{\partial \mathbf{X}} \right) \cdot \bar{\mathbf{F}}^{kj^T} \right] \cdot \mathbf{u}^i = \sum_{j=1}^{N^k} \sum_{i=0}^{N^k} \delta \mathbf{u}^j \cdot \mathbf{M}_1^{ji} \cdot \mathbf{u}^i \tag{A.17}$$

with the substantial matrix

$$\mathbf{M}_1^{ji} = -V^j \bar{\mathbf{F}}^{kj} \cdot \left(\frac{\partial N_{\delta \mathbf{u}}^{jjk}}{\partial \mathbf{X}} \cdot \bar{\mathbb{C}}^{kj} \cdot \frac{\partial N_{\mathbf{u}}^{kji}}{\partial \mathbf{X}} \right) \cdot \bar{\mathbf{F}}^{kj^T} . \tag{A.18}$$

Utilizing the Voigt notation for equation (A.18), it can be written as

$$\mathbf{M}_1^{ji} = -V^j \bar{\mathbf{F}}^{kj} \cdot \left(\mathbf{B}_{\delta \mathbf{u}}^{jjk^T} \cdot \bar{\mathbf{D}}^{kj} \cdot \mathbf{B}_u^{kji} \right) \cdot \bar{\mathbf{F}}^{kj^T} \tag{A.19}$$

with the B matrix in 2-D

$$\mathbf{B}^{kji} = \begin{pmatrix} \frac{\partial N^{kji}}{\partial X} & 0 \\ 0 & \frac{\partial N^{kji}}{\partial Y} \\ \frac{\partial N^{kji}}{\partial Y} & \frac{\partial N^{kji}}{\partial X} \end{pmatrix} . \tag{A.20}$$

Analogously to the first substantial part, the second one can be handled by changing the indices k and j of the linearized Green-Lagrange strain tensor (equation (A.14)) and inserting it into T_4:

$$\begin{aligned} T_4 = & \sum_{j=1}^{N^k} \sum_{i=0}^{N^j} \frac{1}{2} V^k \bar{\mathbf{F}}^{jk} \cdot \bar{\mathbb{C}}^{jk} : \left(\frac{\partial N_{\mathbf{u}}^{jki}}{\partial \mathbf{X}} \otimes \mathbf{u}^i \cdot \bar{\mathbf{F}}^{jk} \right) \cdot \frac{\partial N_{\delta \mathbf{u}}^{kkj}}{\partial \mathbf{X}} \cdot \delta \mathbf{u}^j \\ + & \sum_{j=1}^{N^k} \sum_{i=0}^{N^j} \frac{1}{2} V^k \bar{\mathbf{F}}^{jk} \cdot \bar{\mathbb{C}}^{jk} : \left(\bar{\mathbf{F}}^{jk^T} \cdot \mathbf{u}^i \otimes \frac{\partial N_{\mathbf{u}}^{jki}}{\partial \mathbf{X}} \right) \cdot \frac{\partial N_{\delta \mathbf{u}}^{kkj}}{\partial \mathbf{X}} \cdot \delta \mathbf{u}^j . \end{aligned} \tag{A.21}$$

Note, that the inner sum operates on the family of particle j from the outer sum which leads to a rectangular particle-wise stiffness matrix. Like before, a rearrangement in index notation merges the two occurring terms:

$$T_4 = \sum_{j=1}^{N^k} \sum_{i=0}^{N^j} \delta \mathbf{u}^j \cdot \left[V^k \bar{\mathbf{F}}^{jk} \cdot \left(\frac{\partial N_{\delta \mathbf{u}}^{kkj}}{\partial \mathbf{X}} \cdot \bar{\mathbb{C}}^{jk} \cdot \frac{\partial N_{\mathbf{u}}^{jki}}{\partial \mathbf{X}} \right) \cdot \bar{\mathbf{F}}^{jk^T} \right] \cdot \mathbf{u}^i = \sum_{j=1}^{N^k} \sum_{i=0}^{N^j} \delta \mathbf{u}^j \cdot \mathbf{M}_2^{ji} \cdot \mathbf{u}^i , \tag{A.22}$$

with the second substantial matrix

$$\mathbf{M}_2^{ji} = V^k \bar{\mathbf{F}}^{jk} \cdot \left(\frac{\partial N_{\delta \mathbf{u}}^{kkj}}{\partial \mathbf{X}} \cdot \bar{\mathbb{C}}^{jk} \cdot \frac{\partial N_{\mathbf{u}}^{jki}}{\partial \mathbf{X}} \right) \cdot \bar{\mathbf{F}}^{jk^T} \tag{A.23}$$

or in Voigt notation

$$\mathbf{M}_2^{ji} = V^k \bar{\mathbf{F}}^{jk} \cdot \left(\mathbf{B}_{\delta\mathbf{u}}^{kkj^T} \cdot \bar{\mathbf{D}}^{jk} \cdot \mathbf{B}_{\mathbf{u}}^{jki} \right) \cdot \bar{\mathbf{F}}^{jk^T} . \tag{A.24}$$

With the pairwise geometric and substantial parts, the particle-wise tangent stiffness matrix can be assembled as in equation (4.58).

Appendix B

Momentum preservation of mixed approaches

The preservation of linear momentum is ensured by the concept of pairwise forces. As the isochoric part of the strain energy is handled in the standard purely displacement based way, the momentum preservation is automatically fulfilled and it remains to show that the volumetric part of the residual can also be written in terms of pairwise force densities. Thus, starting from the local volumetric potential of equation (6.2) and (6.3), the residual contribution to a neighbor particle l can be computed as the derivative with respect to the particles displacement

$$\text{PPG:} \quad \frac{\partial \Pi^k}{\partial \mathbf{u}^j} = V^k p^k \frac{\partial J^k}{\partial \mathbf{F}^k} : \frac{\partial \mathbf{F}^k}{\partial \mathbf{u}^j} \quad \text{or} \tag{B.1}$$

$$\text{PBG:} \quad \frac{\partial \Pi^k}{\partial \mathbf{u}^j} = \frac{V^k}{V^{\mathcal{H}_0^k}} \sum_{j=0}^{N^k} V^j p^{kj} \frac{\partial J^{kj}}{\partial \mathbf{F}^{kj}} : \frac{\partial \mathbf{F}^{kj}}{\partial \mathbf{u}^j} \tag{B.2}$$

where the chain rule is used. Inserting the deformation gradient approach (4.11) and switching to index notation yields

$$\text{PPG:} \quad \frac{\partial \Pi^k}{\partial u_A^l} = V^k p^k J^k {F_{BC}^k}^{-T} \sum_{i=0}^{N^k} \frac{\partial u_B^i}{\partial u_A^l} \frac{\partial N^{kki}}{\partial X_C} \quad \text{or} \tag{B.3}$$

$$\text{PBG:} \quad \frac{\partial \Pi^k}{\partial u_A^l} = \frac{V^k}{V^{\mathcal{H}_0^k}} \sum_{j=0}^{N^k} V^j p^{kj} J^{kj} {F_{BC}^{kj}}^{-T} \sum_{i=0}^{N^k} \frac{\partial u_B^i}{\partial u_A^l} \frac{\partial N^{kji}}{\partial X_C} \, . \tag{B.4}$$

The resulting pull-back of the volumetric Cauchy-stress can be exchanged by the first Piola-Kirchhoff stress tensor:

$$\text{PPG:}\quad \frac{\partial \Pi^k}{\partial \mathbf{u}^l} = V^k p^k J^k \mathbf{F}^{k-T} \cdot \frac{\partial N^{kkl}}{\partial \mathbf{X}} = V^k \mathbf{P}^k_{vol} \cdot \frac{\partial N^{kkl}}{\partial \mathbf{X}} \quad \text{or} \tag{B.5}$$

$$\text{PBG:}\quad \frac{\partial \Pi^k}{\partial \mathbf{u}^l} = \frac{V^k}{V^{\mathcal{H}_0^k}} \sum_{j=0}^{N^k} V^j \mathbf{P}^{kj}_{vol} \cdot \frac{\partial N^{kjl}}{\partial \mathbf{X}} \,. \tag{B.6}$$

Analogous to the contribution to the nodal residual of particle j, the corresponding contribution to particle k follows

$$\text{PPG:}\quad \frac{\partial \Pi^k}{\partial \mathbf{u}^k} = V^k \mathbf{P}^k_{vol} \cdot \frac{\partial N^{kkk}}{\partial \mathbf{X}} = -\sum_{j=1}^{N^k} V^k \mathbf{P}^k_{vol} \cdot \frac{\partial N^{kkj}}{\partial \mathbf{X}} \quad \text{or} \tag{B.7}$$

$$\text{PBG:}\quad \frac{\partial \Pi^k}{\partial \mathbf{u}^k} = \frac{V^k}{V^{\mathcal{H}_0^k}} \sum_{j=0}^{N^k} V^j \mathbf{P}^{kj}_{vol} \cdot \frac{\partial N^{kjk}}{\partial \mathbf{X}} = -\frac{V^k}{V^{\mathcal{H}_0^k}} \sum_{j=0}^{N^k} \sum_{i=1}^{N^k} V^j \mathbf{P}^{kj}_{vol} \cdot \frac{\partial N^{kji}}{\partial \mathbf{X}} \,, \tag{B.8}$$

utilizing the zeroth order consistency condition of equation (5.5). The internal force acting on particle k can now be assembled from the potentials of its neighboring particles and rearranged to

$$\text{PPG:}\quad \mathbf{R}^k_{\mathbf{u}\,vol} = \sum_{j=1}^{N^k} \left[V^j \mathbf{P}^j_{vol} \cdot \frac{\partial N^{jjk}}{\partial \mathbf{X}} - V^k \mathbf{P}^k_{vol} \cdot \frac{\partial N^{kkj}}{\partial \mathbf{X}} \right] = -V^k \sum_{j=1}^{N^k} \left[\mathbf{t}^{kj}_{vol} - \mathbf{t}^{jk}_{vol} \right] V^j \quad \text{or} \tag{B.9}$$

$$\text{PBG:}\quad \mathbf{R}^k_{\mathbf{u}\,vol} = \sum_{i=1}^{N^k} \left[\sum_{j=0}^{N^i} \frac{V^i V^j}{V^{\mathcal{H}_0^i}} \mathbf{P}^{ij}_{vol} \cdot \frac{\partial N^{ijk}}{\partial \mathbf{X}} - \sum_{j=0}^{N^k} \frac{V^k V^j}{V^{\mathcal{H}_0^k}} \mathbf{P}^{kj}_{vol} \cdot \frac{\partial N^{kji}}{\partial \mathbf{X}} \right] \,, \tag{B.10}$$

where the volumetric pairwise force densities state

$$\text{PPG:}\quad \mathbf{t}^{kj}_{vol} = -\frac{1}{V^k} \mathbf{P}^j_{vol} \cdot \frac{\partial N^{jjk}}{\partial \mathbf{X}} \quad \text{or} \tag{B.11}$$

$$\text{PBG:}\quad \mathbf{t}^{kj}_{vol} = \frac{1}{V^j V^{\mathcal{H}_0^k}} \sum_{i=0}^{N^k} V^i \mathbf{P}^{ki}_{vol} \cdot \frac{\partial N^{kij}}{\partial \mathbf{X}} \,. \tag{B.12}$$

As the inner forces acting on a particle can be expressed with pairwise force densities, the linear momentum preservation holds.

Bibliography

ARNOLD D., BREZZI F. & FORTIN M. A stable finite element for the stokes equations. *Calcolo*, 21 (1984) (4): 337–344.

ARROYO M. & ORTIZ M. Local maximum-entropy approximation schemes: a seamless bridge between finite elements and meshfree methods. *International journal for numerical methods in engineering*, 65 (2006) (13): 2167–2202.

BATHE K.J. *Finite element procedures*. Klaus-Jurgen Bathe, 2006.

BECKER E. & BÜRGER W. *Kontinuumsmechanik: eine Einführung in die Grundlagen und einfache Anwendungen*, volume 20. Springer-Verlag, 2013.

BEHZADINASAB M. & FOSTER J. The third sandia fracture challenge: peridynamic blind prediction of ductile fracture characterization in additively manufactured metal. *International Journal of Fracture*, 218 (2019) (1-2): 97–109.

BELYTSCHKO T., CHIAPETTA R. & BARTEL H. Efficient large scale non-linear transient analysis by finite elements. *International Journal for Numerical Methods in Engineering*, 10 (1976) (3): 579–596.

BELYTSCHKO T., GUO Y., LIU W. & XIAO S. A unified stability analysis of meshless particle methods. *International Journal for Numerical Methods in Engineering*, 48 (2000) (9): 1359–1400.

BELYTSCHKO T., KRONGAUZ Y., DOLBOW J. & GERLACH C. On the completeness of meshfree particle methods. *International Journal for Numerical Methods in Engineering*, 43 (1998) (5): 785–819.

BELYTSCHKO T., KRONGAUZ Y., ORGAN D., FLEMING M. ET AL. Meshless methods: an overview and recent developments. *Computer methods in applied mechanics and engineering*, 139 (1996) (1-4): 3–47.

BELYTSCHKO T., LIU W., MORAN B. & ELKHODARY K. *Nonlinear finite elements for continua and structures*. John wiley & sons, 2013.

BELYTSCHKO T., LU Y. & GU L. Element-free galerkin methods. *International journal for numerical methods in engineering*, 37 (1994) (2): 229–256.

BELYTSCHKO T., ORGAN D. & KRONGAUZ Y. A coupled finite element-element-free galerkin method. *Computational Mechanics*, 17 (1995) (3): 186–195.

BESSA M., FOSTER J., BELYTSCHKO T. & LIU W. A meshfree unification: reproducing kernel peridynamics. *Computational Mechanics*, 53 (2014) (6): 1251–1264.

BOBARU F., FOSTER J., GEUBELLE P. & SILLING S. *Handbook of peridynamic modeling*. CRC press, 2016.

BODE T., WEISSENFELS C. & WRIGGERS P. Peridynamic petrov–galerkin method: A generalization of the peridynamic theory of correspondence materials. *Computer Methods in Applied Mechanics and Engineering*, 358 (2020a): 112 636.

BODE T., WEISSENFELS C. & WRIGGERS P. Mixed peridynamic formulations for compressible and incompressible finite deformations. *Computational Mechanics*, (2020b): 1–12.

BODE T., WEISSENFELS C. & WRIGGERS P. A consistent peridynamic formulation for arbitrary particle distributions. *Computer Methods in Applied Mechanics and Engineering*, 374 (2021): 113 605.

BONET J. & KULASEGARAM S. Correction and stabilization of smooth particle hydrodynamics methods with applications in metal forming simulations. *International journal for numerical methods in engineering*, 47 (2000) (6): 1189–1214.

BONET J. & KULASEGARAM S. Remarks on tension instability of eulerian and lagrangian corrected smooth particle hydrodynamics (csph) methods. *International Journal for Numerical Methods in Engineering*, 52 (2001) (11): 1203–1220.

BONET J. & LOK T.S. Variational and momentum preservation aspects of smooth particle hydrodynamic formulations. *Computer Methods in applied mechanics and engineering*, 180 (1999) (1-2): 97–115.

BREITENFELD M., GEUBELLE P., WECKNER O. & SILLING S. Non-ordinary state-based peridynamic analysis of stationary crack problems. *Computer Methods in Applied Mechanics and Engineering*, 272 (2014): 233–250.

BREITZMAN T. & DAYAL K. Bond-level deformation gradients and energy averaging in peridynamics. *Journal of the Mechanics and Physics of Solids*, 110 (2018): 192–204.

BREZZI F. On the existence, uniqueness and approximation of saddle-point problems arising from lagrangian multipliers. *Publications mathématiques et informatique de Rennes*, S4 (1974): 1–26.

BROTHERS M., FOSTER J. & MILLWATER H. A comparison of different methods for calculating tangent-stiffness matrices in a massively parallel computational peridynamics code. *Computer Methods in Applied Mechanics and Engineering*, 279 (2014): 247–267.

BROUMAND P. & KHOEI A. X-fem modeling of dynamic ductile fracture problems with a nonlocal damage-viscoplasticity model. *Finite Elements in Analysis and Design*, 99 (2015): 49–67.

CAMACHO G. & ORTIZ M. Adaptive lagrangian modelling of ballistic penetration of metallic targets. *Computer methods in applied mechanics and engineering*, 142 (1997) (3-4): 269–301.

CÉA J. Approximation variationnelle des problèmes aux limites. In *Annales de l'institut Fourier*, volume 14, pages 345–444. 1964.

CHAPELLE D. & BATHE K.J. The inf-sup test. *Computers & structures*, 47 (1993) (4-5): 537–545.

CHAPMAN D., RADFORD D., REYNOLDS M. & CHURCH P. Shock induced void nucleation during taylor impact. *International journal of fracture*, 134 (2005) (1): 41–57.

CHEN H. Bond-associated deformation gradients for peridynamic correspondence model. *Mechanics Research Communications*, 90 (2018): 34–41.

CHEN H. & SPENCER B. Peridynamic bond-associated correspondence model: Stability and convergence properties. *International Journal for Numerical Methods in Engineering*, 117 (2019) (6): 713–727.

CHEN J.S., HILLMAN M. & CHI S.W. Meshfree methods: progress made after 20 years. *Journal of Engineering Mechanics*, 143 (2017) (4): 04017 001.

CHEN J.S., HILLMAN M. & RÜTER M. An arbitrary order variationally consistent integration for galerkin meshfree methods. *International Journal for Numerical Methods in Engineering*, 95 (2013) (5): 387–418.

CHEN J.S., PAN C. & WU C.T. Large deformation analysis of rubber based on a reproducing kernel particle method. *Computational Mechanics*, 19 (1997) (3): 211–227.

CHEN J.S. & WANG H.P. New boundary condition treatments in meshfree computation of contact problems. *Computer methods in applied mechanics and engineering*, 187 (2000) (3-4): 441–468.

CHEN J.S., YOON S., WANG H.P. & LIU W. An improved reproducing kernel particle method for nearly incompressible finite elasticity. *Computer methods in applied mechanics and engineering*, 181 (2000) (1-3): 117–145.

CHOI Y. & KIM S. Node generation scheme for meshfree method by voronoi diagram and weighted bubble packing. In *Fifth us national congress on computational mechanics, Boulder, CO*. 1999.

CHOWDHURY S., ROY P., ROY D. & REDDY J. A modified peridynamics correspondence principle: Removal of zero-energy deformation and other implications. *Computer Methods in Applied Mechanics and Engineering*, 346 (2019): 530–549.

CIARLET P. *Mathematical Elasticity: Volume I: three-dimensional elasticity*. North-Holland, 1988.

CIHAN M., ALDAKHEEL F., HUDOBIVNIK B. & WRIGGERS P. Virtual element formulation for finite strain elastodynamics. *arXiv preprint arXiv:2002.02680*, (2020).

CIHAN M., HUDOBIVNIK B., ALDAKHEEL F. & WRIGGERS P. 3d mixed virtual element formulation for dynamic elasto-plastic analysis. *Computational Mechanics*, (2021): 1–18.

CUMMINS S. & RUDMAN M. An sph projection method. *Journal of computational physics*, 152 (1999) (2): 584–607.

DOLBOW J. & BELYTSCHKO T. Volumetric locking in the element free galerkin method. *International Journal for numerical methods in engineering*, 46 (1999) (6): 925–942.

DUAN Q., GAO X., WANG B., LI X. ET AL. Consistent element-free galerkin method. *International Journal for Numerical Methods in Engineering*, 99 (2014) (2): 79–101.

FERNÁNDEZ-MÉNDEZ S., BONET J. & HUERTA A. Continuous blending of sph with finite elements. *Computers & structures*, 83 (2005) (17-18): 1448–1458.

FERNÁNDEZ-MÉNDEZ S. & HUERTA A. Imposing essential boundary conditions in meshfree methods. *Computer methods in applied mechanics and engineering*, 193 (2004) (12-14): 1257–1275.

FLOATER M. Mean value coordinates. *Computer aided geometric design*, 20 (2003) (1): 19–27.

FORDE L., PROUD W. & WALLEY S. Symmetrical taylor impact studies of copper. *Proceedings of the Royal Society A: Mathematical, Physical and Engineering Sciences*, 465 (2009) (2103): 769–790.

FORTIN M. & BREZZI F. *Mixed and hybrid finite element methods*. New York: Springer-Verlag, 1991.

FOSTER J. Constitutive modeling in peridynamics. In *Handbook of Peridynamic Modeling*, pages 181–216. Chapman and Hall/CRC, 2016.

FOSTER J., SILLING S. & CHEN W. Viscoplasticity using peridynamics. *International journal for numerical methods in engineering*, 81 (2010) (10): 1242–1258.

FRIES T.P., MATTHIES H. ET AL. Classification and overview of meshfree methods. *Department of Mathematics and Computer Science, Technical University of Braunschweig*, (2003).

FÜRSTENAU J.P. *Particle-based Simulation of the Selective Laser Melting Process*. Dissertation, Institut für Kontinuumsmechanik at Leibniz Universität Hannover (2021).

GANZENMÜLLER G., HIERMAIER S. & MAY M. On the similarity of meshless discretizations of peridynamics and smooth-particle hydrodynamics. *Computers & Structures*, 150 (2015): 71–78.

GERSTLE W.H. *Introduction to practical peridynamics: computational solid mechanics without stress and strain*, volume 1. World Scientific Publishing Company, 2015.

GINGOLD R. & MONAGHAN J. Smoothed particle hydrodynamics: theory and application to non-spherical stars. *Monthly notices of the royal astronomical society*, 181 (1977) (3): 375–389.

GRECO F. & SUKUMAR N. Derivatives of maximum-entropy basis functions on the boundary: Theory and computations. *International journal for numerical methods in engineering*, 94 (2013) (12): 1123–1149.

GU X., ZHANG Q., MADENCI E. & XIA X. Possible causes of numerical oscillations in non-ordinary state-based peridynamics and a bond-associated higher-order stabilized model. *Computer Methods in Applied Mechanics and Engineering*, 357 (2019): 112 592.

GÜNTHER F. & LIU W. Implementation of boundary conditions for meshless methods. *Computer Methods in Applied Mechanics and Engineering*, 163 (1998) (1-4): 205–230.

GUYAN R. Reduction of stiffness and mass matrices. *AIAA journal*, 3 (1965) (2): 380–380.

HABRAKEN A. & CESCOTTO S. An automatic remeshing technique for finite element simulation of forming processes. *International Journal for Numerical Methods in Engineering*, 30 (1990) (8): 1503–1525.

HAJIKHANI A. *Chemo-Mechanical Modeling of Polymeric Hydrogels*. Ph.D. thesis, Garbsen: Institut für Kontinuumsmechanik (2021).

HARTMANN P. *Simulation of Thermo-chemo-mechanical Coupled Additive Manufacturing Processes Using Peridynamics*. Dissertation, Institut für Kontinuumsmechanik at Leibniz Universität Hannover (2019).

HARTMANN P., WEISSENFELS C. & WRIGGERS P. Application of enhanced peridynamic correspondence formulation for three-dimensional simulations at large strains. In *Virtual Design and Validation*, pages 81–104. Springer, 2020.

HARTMANN P., WEISSENFELS C. & WRIGGERS P. A curing model for the numerical simulation within additive manufacturing of soft polymers using peridynamics. *Computational Particle Mechanics*, 8 (2021) (2): 369–388.

HILLMAN M. & CHEN J.S. An accelerated, convergent, and stable nodal integration in galerkin meshfree methods for linear and nonlinear mechanics. *International Journal for Numerical Methods in Engineering*, 107 (2016) (7): 603–630.

HILLMAN M., CHEN J.S. & CHI S.W. Stabilized and variationally consistent nodal integration for meshfree modeling of impact problems. *Computational Particle Mechanics*, 1 (2014) (3): 245–256.

HILLMAN M., PASETTO M. & ZHOU G. Generalized reproducing kernel peridynamics: unification of local and non-local meshfree methods, non-local derivative operations, and an arbitrary-order state-based peridynamic formulation. *Computational Particle Mechanics*, (2019): 1–35.

HOLZAPFEL G. Nonlinear solid mechanics: a continuum approach for engineering science. *Meccanica*, 37 (2002) (4): 489–490.

HORMANN K. & FLOATER M. Mean value coordinates for arbitrary planar polygons. *ACM Transactions on Graphics (TOG)*, 25 (2006) (4): 1424–1441.

HUANG D. *Meshfree modelling of metal cutting using phenomenological and data-driven material models*. Dissertation, Hannover: Institutionelles Repositorium der Leibniz Universität Hannover (2020).

HUDOBIVNIK B., ALDAKHEEL F. & WRIGGERS P. A low order 3d virtual element formulation for finite elasto–plastic deformations. *Computational Mechanics*, 63 (2019) (2): 253–269.

HUERTA A., FERNÁNDEZ-MÉNDEZ S. & LIU W. A comparison of two formulations to blend finite elements and mesh-free methods. *Computer Methods in Applied Mechanics and Engineering*, 193 (2004a) (12-14): 1105–1117.

HUERTA A., VIDAL Y. & VILLON P. Pseudo-divergence-free element free galerkin method for incompressible fluid flow. *Computer methods in applied mechanics and engineering*, 193 (2004b) (12-14): 1119–1136.

JAVILI A., MORASATA R., OTERKUS E. & OTERKUS S. Peridynamics review. *Mathematics and Mechanics of Solids*, (2018).

JOHNSON G. & COOK W. A constitutive model and data for metals subjected to large strains, high strain rates and high temperatures. In *Proceedings of the 7th International Symposium on Ballistics*, volume 21, pages 541–547. The Netherlands, 1983.

JOHNSON G. & COOK W. Fracture characteristics of three metals subjected to various strains, strain rates, temperatures and pressures. *Engineering fracture mechanics*, 21 (1985) (1): 31–48.

JOSHI P., MEYER M., DEROSE T., GREEN B. ET AL. Harmonic coordinates for character articulation. *ACM Transactions on Graphics (TOG)*, 26 (2007) (3): 71–es.

KADAPA C., DETTMER W. & PERIĆ D. Subdivision based mixed methods for isogeometric analysis of linear and nonlinear nearly incompressible materials. *Computer Methods in Applied Mechanics and Engineering*, 305 (2016): 241–270.

KALJEVIĆ I. & SAIGAL S. An improved element free galerkin formulation. *International Journal for numerical methods in engineering*, 40 (1997) (16): 2953–2974.

KAMOULAKIS A. A simple benchmark for impact. *Benchmark*, (1990): 31–35.

KLAAS O. & SHEPHARD M. An octree based partition of unity method for three dimensional problems. In *Fifth us national congress on computational mechanics, Boulder, CO*. 1999.

KORELC J. Automatic generation of finite-element code by simultaneous optimization of expressions. *Theoretical Computer Science*, 187 (1997) (1-2): 231–248.

KORELC J. Automation of primal and sensitivity analysis of transient coupled problems. *Computational mechanics*, 44 (2009) (5): 631–649.

KORELC J., ŠOLINC U. & WRIGGERS P. An improved eas brick element for finite deformation. *Computational mechanics*, 46 (2010) (4): 641–659.

KORELC J. & STUPKIEWICZ S. Closed-form matrix exponential and its application in finite-strain plasticity. *International Journal for Numerical Methods in Engineering*, 98 (2014) (13): 960–987.

KORELC J. & WRIGGERS P. *Automation of Finite Element Methods*. Springer, 2016.

KRONGAUZ Y. & BELYTSCHKO T. Consistent pseudo-derivatives in meshless methods. *Computer methods in applied mechanics and engineering*, 146 (1997) (3-4): 371–386.

KRYSL P. Mean-strain eight-node hexahedron with optimized energy-sampling stabilization for large-strain deformation. *International Journal for Numerical Methods in Engineering*, 103 (2015) (9): 650–670.

KUMAR S., DANAS K. & KOCHMANN D. Enhanced local maximum-entropy approximation for stable meshfree simulations. *Computer Methods in Applied Mechanics and Engineering*, 344 (2019): 858–886.

KUNLE M. *Entwicklung und Untersuchung von moving least square Verfahren zur numerischen Simulation hydrodynamischer Gleichungen*. Dissertation, Universität Tübingen (2001).

LANCASTER P. & SALKAUSKAS K. Surfaces generated by moving least squares methods. *Mathematics of computation*, 37 (1981) (155): 141–158.

LANCASTER P. & SALKAUSKAS K. *Curve and surface fitting: an introduction*. Academic press, 1986.

LE Q., CHAN W. & SCHWARTZ J. A two-dimensional ordinary, state-based peridynamic model for linearly elastic solids. *International Journal for Numerical Methods in Engineering*, 98 (2014) (8): 547–561.

LI S. & LIU W. Meshfree and particle methods and their applications. *Appl. Mech. Rev.*, 55 (2002) (1): 1–34.

LI X. & WANG Q. Analysis of the inherent instability of the interpolating moving least squares method when using improper polynomial bases. *Engineering Analysis with Boundary Elements*, 73 (2016): 21–34.

LI X.Y., JU T. & HU S.M. Cubic mean value coordinates. *ACM Trans. Graph.*, 32 (2013) (4): 126–1.

LI X.Y., TENG S.H. & UNGOR A. Biting: Advancing front meets sphere packing. *International Journal for Numerical Methods in Engineering*, 49 (2000a) (1-2): 61–81.

LI X.Y., TENG S.H. & UNGOR A. Point placement for meshless methods using sphere packing and advancing front methods. *ICCES'00, Los Angeles, USA*, 20 (2000b): 25.

LITTLEWOOD D. Simulation of dynamic fracture using peridynamics, finite element modeling, and contact. In *ASME 2010 International Mechanical Engineering Congress and Exposition*, pages 209–217. American Society of Mechanical Engineers, 2010.

LITTLEWOOD D. Roadmap for peridynamic software implementation. *SAND Report, Sandia National Laboratories, Albuquerque, NM and Livermore, CA*, (2015).

LITTLEWOOD D., MISH K. & PIERSON K. Peridynamic simulation of damage evolution for structural health monitoring. In *ASME International Mechanical Engineering Congress and Exposition*, volume 45240, pages 1–8. American Society of Mechanical Engineers, 2012.

LIU G.R. *Meshfree methods: moving beyond the finite element method*. CRC press, 2009.

LIU G.R. & GU Y.T. *An introduction to meshfree methods and their programming*. Springer Science & Business Media, 2005.

LIU W., JUN S., LI S., ADEE J. ET AL. Reproducing kernel particle methods for structural dynamics. *International Journal for Numerical Methods in Engineering*, 38 (1995a) (10): 1655–1679.

LIU W., JUN S. & ZHANG Y. Reproducing kernel particle methods. *International journal for numerical methods in fluids*, 20 (1995b) (8-9): 1081–1106.

LIU W., YANG G. & CAI Y. Modeling of failure mode switching and shear band propagation using the correspondence framework of peridynamics. *Computers & Structures*, 209 (2018): 150–162.

LUCY L. A numerical approach to the testing of the fission hypothesis. *The astronomical journal*, 82 (1977): 1013–1024.

LUO J. & SUNDARARAGHAVAN V. Stress-point method for stabilizing zero-energy modes in non-ordinary state-based peridynamics. *International Journal of Solids and Structures*, 150 (2018): 197–207.

MADENCI E., DORDUNCU M., PHAN N. & GU X. Weak form of bond-associated non-ordinary state-based peridynamics free of zero energy modes with uniform or non-uniform discretization. *Engineering Fracture Mechanics*, 218 (2019): 106 613.

MADENCI E. & OTERKUS E. *Peridynamic theory and its applications*. Springer, 2016a.

MADENCI E. & OTERKUS S. Ordinary state-based peridynamics for plastic deformation according to von mises yield criteria with isotropic hardening. *Journal of the Mechanics and Physics of Solids*, 86 (2016b): 192–219.

MALSCH E. & DASGUPTA G. Algebraic construction of smooth interpolants on polygonal domains. In *Challenging The Boundaries Of Symbolic Computation: (With CD-ROM)*, pages 81–88. World Scientific, 2003.

MALSCH E. & DASGUPTA G. Shape functions for polygonal domains with interior nodes. *International Journal for Numerical Methods in Engineering*, 61 (2004) (8): 1153–1172.

MALVERN L. *Introduction to the Mechanics of a Continuous Medium*. Englewood Cliffs, 1969.

MONAGHAN J. Sph without a tensile instability. *Journal of Computational Physics*, 159 (2000) (2): 290–311.

NADLER B. & RUBIN M. A new 3-d finite element for nonlinear elasticity using the theory of a cosserat point. *International Journal of Solids and Structures*, 40 (2003) (17): 4585–4614.

NETUZHYLOV H. Enforcement of boundary conditions in meshfree methods using interpolating moving least squares. *Engineering analysis with boundary elements*, 32 (2008) (6): 512–516.

NEWMARK N. A method of computation for structural dynamics. *Journal of the engineering mechanics division*, 85 (1959) (3): 67–94.

NITHIARASU P., CODINA R. & ZIENKIEWICZ O. The characteristic-based split (cbs) scheme—a unified approach to fluid dynamics. *International Journal for Numerical Methods in Engineering*, 66 (2006) (10): 1514–1546.

NITSCHE J. Über ein variationsprinzip zur lösung von dirichlet-problemen bei verwendung von teilräumen, die keinen randbedingungen unterworfen sind. In *Abhandlungen aus dem mathematischen Seminar der Universität Hamburg*, volume 36, pages 9–15. Springer, 1971.

OGDEN R. *Non-linear elastic deformations*. Courier Corporation, 1997.

PLENGKHOM K. & KANOK-NUKULCHAI W. An enhancement of finite element method with moving kriging shape functions. *International Journal of Computational Methods*, 2 (2005) (04): 451–475.

PUSO M.A., CHEN J.S., ZYWICZ E. & ELMER W. Meshfree and finite element nodal integration methods. *International Journal for Numerical Methods in Engineering*, 74 (2008) (3): 416–446.

QUAK W., VAN DEN BOOGAARD A., GONZÁLEZ D. & CUETO E. A comparative study on the performance of meshless approximations and their integration. *Computational mechanics*, 48 (2011) (2): 121–137.

REN H., ZHUANG X., CAI Y. & RABCZUK T. Dual-horizon peridynamics. *International Journal for Numerical Methods in Engineering*, 108 (2016) (12): 1451–1476.

REN H., ZHUANG X. & RABCZUK T. Dual-horizon peridynamics: A stable solution to varying horizons. *Computer Methods in Applied Mechanics and Engineering*, 318 (2017): 762–782.

SCHENK O., GÄRTNER K., FICHTNER W. & STRICKER A. Pardiso: a high-performance serial and parallel sparse linear solver in semiconductor device simulation. *Future Generation Computer Systems*, 18 (2001) (1): 69–78.

ŠILHAVÝ M. Higher gradient expansion for linear isotropic peridynamic materials. *Mathematics and Mechanics of Solids*, 22 (2017) (6): 1483–1493.

SILLING S. Reformulation of elasticity theory for discontinuities and long-range forces. *Journal of the Mechanics and Physics of Solids*, 48 (2000) (1): 175–209.

SILLING S. Dynamic fracture modeling with a meshfree peridynamic code. In *Computational Fluid and Solid Mechanics 2003*, pages 641–644. Elsevier, 2003.

SILLING S. Linearized theory of peridynamic states. *Journal of Elasticity*, 99 (2010) (1): 85–111.

SILLING S. Introduction to peridynamics. In *Handbook of Peridynamic Modeling*, pages 63–98. Chapman and Hall/CRC, 2016.

SILLING S. Stability of peridynamic correspondence material models and their particle discretizations. *Computer Methods in Applied Mechanics and Engineering*, 322 (2017): 42–57.

SILLING S. & ASKARI E. A meshfree method based on the peridynamic model of solid mechanics. *Computers & structures*, 83 (2005) (17-18): 1526–1535.

SILLING S., EPTON M., WECKNER O., XU J. ET AL. Peridynamic states and constitutive modeling. *Journal of Elasticity*, 88 (2007) (2): 151–184.

SIMO J. A framework for finite strain elastoplasticity based on maximum plastic dissipation and the multiplicative decomposition: Part i. continuum formulation. *Computer methods in applied mechanics and engineering*, 66 (1988) (2): 199–219.

SIMO J. & HUGHES T. *Computational inelasticity*, volume 7. Springer Science & Business Media, 2006.

SIMO J. & TARNOW N. The discrete energy-momentum method. conserving algorithms for nonlinear elastodynamics. *Zeitschrift für angewandte Mathematik und Physik ZAMP*, 43 (1992) (5): 757–792.

SIMO J., TAYLOR R. & PISTER K. Variational and projection methods for the volume constraint in finite deformation elasto-plasticity. *Computer methods in applied mechanics and engineering*, 51 (1985) (1-3): 177–208.

SLEIJPEN G., VAN DER VORST H. & FOKKEMA D. Bicgstab (l) and other hybrid bi-cg methods. *Numerical Algorithms*, 7 (1994) (1): 75–109.

SUKUMAR N. Construction of polygonal interpolants: a maximum entropy approach. *International journal for numerical methods in engineering*, 61 (2004) (12): 2159–2181.

SUKUMAR N. Quadratic maximum-entropy serendipity shape functions for arbitrary planar polygons. *Computer Methods in Applied Mechanics and Engineering*, 263 (2013): 27–41.

SUKUMAR N. & MALSCH E. Recent advances in the construction of polygonal finite element interpolants. *Archives of Computational Methods in Engineering*, 13 (2006) (1): 129.

SULSKY D., CHEN Z. & SCHREYER H. A particle method for history-dependent materials. *Computer methods in applied mechanics and engineering*, 118 (1994) (1-2): 179–196.

SUN S. & SUNDARARAGHAVAN V. A peridynamic implementation of crystal plasticity. *International Journal of Solids and Structures*, 51 (2014) (19-20): 3350–3360.

TRUESDELL C. & TOUPIN R. The classical field theories. In *Principles of classical mechanics and field theory/Prinzipien der Klassischen Mechanik und Feldtheorie*, pages 226–858. Springer, 1960.

TUPEK M. & RADOVITZKY R. An extended constitutive correspondence formulation of peridynamics based on nonlinear bond-strain measures. *Journal of the Mechanics and Physics of Solids*, 65 (2014): 82–92.

TUPEK M., RIMOLI J. & RADOVITZKY R. An approach for incorporating classical continuum damage models in state-based peridynamics. *Computer methods in applied mechanics and engineering*, 263 (2013): 20–26.

WACHSPRESS E. *A rational finite element basis.*. Elsevier, 1975.

WARREN J. Barycentric coordinates for convex polytopes. *Advances in Computational Mathematics*, 6 (1996) (1): 97–108.

WARREN T., SILLING S., ASKARI A., WECKNER O. ET AL. A non-ordinary state-based peridynamic method to model solid material deformation and fracture. *International Journal of Solids and Structures*, 46 (2009) (5): 1186–1195.

WASHIZU K. Variational methos in elasticity and plasticity. *International Series of Monographs in Aeronautics and Astronautics*, (1968).

WEBER O., PORANNE R. & GOTSMAN C. Biharmonic coordinates. In *Computer Graphics Forum*, volume 31, pages 2409–2422. Wiley Online Library, 2012.

WEISSENFELS C. Direct nodal imposition of surface loads using the divergence theorem. *Finite Elements in Analysis and Design*, 165 (2019): 31–40.

WEISSENFELS C. & WRIGGERS P. Stabilization algorithm for the optimal transportation meshfree approximation scheme. *Computer Methods in Applied Mechanics and Engineering*, 329 (2018): 421–443.

WESSELS H. *Thermo-mechanical modeling for selective laser melting*. Dissertation, Institut für Kontinuumsmechanik at Leibniz Universität Hannover (2019).

WESSELS H., BODE T., WEISSENFELS C., WRIGGERS P. ET AL. Investigation of heat source modeling for selective laser melting. *Computational Mechanics*, (2018): 1–22.

WRIGGERS P. *Nonlinear finite element methods*. Springer Science & Business Media, 2008.

WRIGGERS P. Discretization methods for solids undergoing finite deformations. In *Advanced Finite Element Technologies*, pages 17–51. Springer, 2016.

WRIGGERS P., REDDY B., RUST W. & HUDOBIVNIK B. Efficient virtual element formulations for compressible and incompressible finite deformations. *Computational Mechanics*, 60 (2017) (2): 253–268.

WU C. Kinematic constraints in the state-based peridynamics with mixed local/nonlocal gradient approximations. *Computational Mechanics*, 54 (2014) (5): 1255–1267.

YAGHOOBI A. & CHORZEPA M. Higher-order approximation to suppress the zero-energy mode in non-ordinary state-based peridynamics. *Computers & Structures*, 188 (2017): 63–79.

YAGHOOBI A. & CHORZEPA M. Formulation of symmetry boundary modeling in non-ordinary state-based peridynamics and coupling with finite element analysis. *Mathematics and Mechanics of Solids*, 23 (2018) (8): 1156–1176.

ZHANG Q., LI S., ZHANG A., PENG Y. ET AL. A peridynamic reissner-mindlin shell theory. *International Journal for Numerical Methods in Engineering*, (2020).

ZHU T. & ATLURI S. A modified collocation method and a penalty formulation for enforcing the essential boundary conditions in the element free galerkin method. *Computational Mechanics*, 21 (1998) (3): 211–222.

ZHU Y. & CESCOTTO S. Unified and mixed formulation of the 4-node quadrilateral elements by assumed strain method: application to thermomechanical problems. *International journal for numerical methods in engineering*, 38 (1995) (4): 685–716.

ZIENKIEWICZ O., TAYLOR R. & ZHU J. *The finite element method: its basis and fundamentals*. Elsevier, 2005.

List of Figures

2.1 Motion of body $\mathcal{B}$ from initial to current configuration. 6

2.2 At the top: Superposition of isochoric plastic, isochoric elastic and volumetric plastic deformation with intermediate configurations. At the bottom: Updated Lagrangian decomposition of the deformation gradient mapping. The successive deformation of an infinitesimal spherical region by a single multiplicatively split deformation gradient is shown in gray. 8

3.1 The infinitesimal master particle X with volume dV_X interacts with each neighbor particle X' within its family $\mathcal{H}_0$. 17

3.2 The current bond vector state $\underline{\Delta \mathbf{x}}$ performs a generally nonlinear and possibly non-smooth mapping of the initial family $\mathcal{H}_0$ into the current configuration, while its reduction $\bar{\mathbf{F}}$ is its linearized weighted average. 18

4.1 Particle discretization with the discrete connectivity and pairwise force densities acting between master particle k and its neighborhood $\mathcal{H}_0^k$. 24

4.2 The linearization of the generally non-linear mapping of the deformation of $\mathcal{H}_0^k$ using a constant locally averaged deformation gradient $\bar{\mathbf{F}}$ leads as a surjective operation to a loss of information. Blue colored particles denote the points of evaluation. 28

5.1 On the left: Spurious surface approximations at interior nodes resulting from variationally inconsistent test functions. On the right: The correction of VC forces the surface vectors to be zero apart from nodes on the surface. The boundary conditions of the correction are represented by green lines. 62

7.1 Geometry, material data and boundary conditions of 2-D Cook's membrane benchmark. 75

7.2 Impact of different original shape functions and subsequent correction techniques on the solution of the 2-D Cook's membrane problem with the PBG Unl formulation. 76

7.3 On the left: Geometry, material data and boundary conditions of the three dimensional Cook's membrane problem. On the right: Particle discretization consisting of free moving (green), fixed (purple) and force applied (red) particles in case of the regular distribution into $72 \times 72 \times 18$ free moving particles. 77

7.4 Deformed configuration of the Cook's membrane for the finest irregular and regular discretization using n_p particles. The contours of the von Mises stress in Newton per square meter are depicted by the particle colors. 78
7.5 Convergence study: The vertical displacement at the upper right front edge of Cook's membrane is plotted over the number of nodes. Different discretizations and weight functions of the PPG UnlP0 formulation are compared to the mixed H1P0 Finite Elements. 79
7.6 The eigen values of the global tangent stiffness matrix of a free moving bloc are plotted in ascending order for several PG and FEM formulations. 80
7.7 First three non-zero eigen modes of a free moving bloc for different proposed formulations. 81
7.8 The resulting shear stress field is colored over the deformed particle configuration. Whereas the classical PG methods fail the patch test, it is passed by their variationally consistent counterparts. 82
7.9 The resulting shear stress field is colored over the deformed particle configuration. Even if only the second order corrected test functions lead to the passing of the quadratic patch test, the linearly corrected one produces reasonable results and a smooth stress field. 84
7.10 On the left: Refining discretizations for the manufactured 2-D solution in the initial configuration. On the right: the normal stress in x-direction is colored over the deformed configuration. 85
7.11 Convergence of the displacement and energy error norms with increasing refinement for different correction shape functions and correction boundary conditions with displacement based and mixed formulations. 86
7.12 Vertical displacement response of the upper right corner of the dynamic Cook's membrane problem for different combinations of shape function correction within the total and updated Lagrangian PBG Unl formulation. . . . 87
7.13 Deformed configuration of selected frames of the dynamic Cook's membrane problem for the case of VCBCPBG UL, colored x-y-component of the deformation gradient. 88
7.14 On the left: Model problem for numerical inf-sup test. On the right: Exemplary discretizations for regular and irregular particle distributions. The Dirichlet boundary conditions are applied by an additional layer of wall particles. The displacements of blue colored particles are fixed horizontally and the purple particle is fixed in both horizontal and vertical direction. 90
7.15 Inf-sup values of the model problem of Figure 7.14, where the logarithm of the inf-sup value is plotted over the logarithm of the inverse of the number of particles in each dimension for regular and distorted particle and node distributions, respectively. 91
7.16 On the left: Geometry, material data and boundary conditions of the two dimensional punch problem. On the right: Maximal displacement in x-direction is plotted over the maximal negative displacement in y-direction for the displacement based FE and PG methods with linear basis. 92

7.17 Maximal compressed configurations of the two dimensional punch test. The severe mesh distortion near the singularity at the right end of the upper Dirichlet boundary causes the divergence in the FE simulation. 92
7.18 On the left: Geometry of the torsion problem where particles underlying displacement boundary conditions are colored purple and free moving particles green. On the right: Exemplary configuration for a twisting angle of 360 degrees with the mixed PPG UnlP0 and FEM H1P0 formulations. The von Mises stress in Newton per square meter are colored. 93
7.19 On the left: Geometry and boundary conditions of the punch problem. Dirichlet boundary conditions are prescribed for purple particles and external forces are applied to the red particles. On the right: Exemplary deformed configuration and cross section for an incompressible PPG IUnlP0 formulation. The vertical displacement in meter is colored. 95
7.20 Convergence study: The minimal vertical displacement is plotted over the number of nodes. Different approaches of the PPG method are compared to the mixed H1P0 Finite Element for two different Poisson's ratios. 96
7.21 Convergence study: The displacement in z-direction of the upper right front corner of Cook's membrane is plotted over a series of 18 irregular particle distributions. A Finite element comparison is performed with a displacement based tetrahedral mesh with the same node distribution and a regular refining H1P0 Finite Element mesh. 97
7.22 On the left: Geometry and boundary conditions of the quasistatic cylindrical necking problem. On the right: Initial collocated FE mesh for discretization $N = 1$. 98
7.23 At the top: The residual force at the left clamping is plotted over the applied displacement on the right end. At the bottom: Convergence of maximal residual force at the left clamping for various formulations. 99
7.24 The accumulated plastic strain for quasistatic cylindrical necking problem is colored on the deformed configuration for the presented formulations. The maximal accumulated plastic strain of the comparative FEM H1P0 solution is $\bar{e}^p_{max} = 3.71$ 100
7.25 Geometry, discretization of collocated irregular meshes and benchmark solution with $360\,000$ H1P0 Finite Elements of the dynamic torsion problem with the same color legend as in Figure 7.26. 102
7.26 The accumulated plastic strain for the problem of the dynamic torsion of a square prism is colored on the deformed configuration for the presented formulations. 103
7.27 Geometry and initial conditions of the two versions of the Taylor anvil benchmark. 104
7.28 On the left: Final mushroom radius at the impacting end over number of particles. On the right: Final length in the center of the specimen over number of particles. 104
7.29 The accumulated plastic strain for the Taylor anvil benchmark is colored on the deformed configuration for the presented PBG formulations. 106

7.30 The pressure distribution of the two best performing mixed PBG approaches is visualized on the deformed configuration. 107
7.31 The accumulated plastic strain is colored on two intermediate configurations, the final and extended configuration of the high velocity Taylor anvil impact test using the VCPBG U1SIG formulation. 108
7.32 Geometry, material data and boundary conditions of the quarter of the plate with hole. 109
7.33 Normal stress in x-direction along the symmetry axis of the plate with hole problem for the FEM coupled uncorrected and first order variationally consistent PPG method compared to a Finite Element reference solution. 109
7.34 Displacement and stress contours of the plate with hole problem for the first order variationally consistent VCPPG V3sn Unl formulation, coupled with Finite Elements. 110

8.1 Plate with two hole ductile fracture test case: For the discretization a collocated T1-FE mesh resulting into 27936 particles is used with the inherited FE-connectivity. 114
8.2 Geometry, discretization and dynamic response of the 2-D Poiseuille flow using 100×100 VCPBG Unl+P1C particles. 115
8.3 Geometry, boundary conditions, material data and exemplary deformed configurations of the dam break problem. 116

List of Tables

4.1 Discretized global weak forms and local strong forms of the different PG methods and the equivalent (pseudo-) potential of the PBG method. 39

5.1 Abbreviations of Weighted and Moving Least Square and Taylor Expansion shape functions and their exemplary polynomial basis in two dimensions. . 57

7.1 Overview of used abbreviations 74
7.2 Error norms in L^2 and H^1 for the linear patch test 83
7.3 Error norms in L^2 and H^1 for the quadratic patch test 84
7.4 Robustness study: Maximal converging angle in a single load step in degrees and minimum number of load steps need for one full rotation for displacement based and mixed PG and FE approaches. 94
7.5 Maximal accumulated plastic strain as a measure for the plastic localization within irregular particle patterns and failure angle for the highly irregularly discretized squared prism for all presented approaches. 101
7.6 Comparison of final length, mushroom radius and maximal total equivalent plastic strain of the literature and selected PBG approaches (extension of KUMAR ET AL. (2019)). 105

Curriculum vitae

Tobias Bode
born April 4, 1994 in Hannover, Germany

Education and scientific experience

since 12.2017	Research assistant at the Institute of Continuum Mechanics, Leibniz University Hannover
2017	Preparation of master thesis at the Lab of Prof. T.I. Zhodi, University of California, Berkeley.
2015 - 2017	Mechanical Engineering: M. Sc., Leibniz University Hannover
2013 - 2014	Scientific assistant at the Institute of Algebraic Geometry, Leibniz University Hannover
2012 - 2015	Mechanical Engineering: B. Sc., Leibniz University Hannover
2000 - 2012	Elementary education at the Grundschule Saturnring, Garbsen Secondary education at the Johannes-Kepler-Gymnasium, Garbsen

Awards and scholarships

2018	Ernst Blickle-Study-Award of the SEW-EURODRIVE Foundation
2017	Master of Science awarded with distinction
2016	Dr.-Jürgen-Ulderup-Award of the Dr. Jürgen and Irmgard Ulderup Foundation
2015	Bachelor of Science awarded with distinction
2013 - 2016	Scholarship ’Deutschlandstipendium’
2012	Scholarship ’Niedersachsenstipendium’
2012	Abitur Award of the German Mathematical Society
2012	Abitur Award of the German Physical Society